NUMERICAL SIMULATION OF THE SHOCK COMPRESSION OF MICROSCALE REACTIVE PARTICLE SYSTEMS

A Thesis
Presented to
The Academic Faculty

By

Ryan A. Austin

In Partial Fulfillment
of the Requirements for the Degree
Master of Science in Mechanical Engineering

Georgia Institute of Technology
August, 2005

NUMERICAL SIMULATION OF THE SHOCK COMPRESSION OF MICROSCALE REACTIVE PARTICLE SYSTEMS

Approved by:

Dr. David L. McDowell
G.W. Woodruff School of Mechanical Engineering
Georgia Institute of Technology

Dr. Min Zhou
G.W. Woodruff School of Mechanical Engineering
Georgia Institute of Technology

Dr. Naresh N. Thadhani
School of Materials Science & Engineering
Georgia Institute of Technology

Date Approved: July 15, 2005

ACKNOWLEDGEMENTS

It has been an honor to carry out this research at the Georgia Institute of Technology. I thank the G.W. Woodruff School of Mechanical Engineering for providing an opportunity to work in a department that distinguishes itself as one of the very best of this institution.

I acknowledge my advisor, Dr. David L. McDowell, for guiding this research with an 'invisible hand'–thank you for your relentless energy and expertise in our collaborative efforts and for affording me the independence to pursue my own ideas.

I thank an essential collaborator, Dr. Naresh N. Thadhani, for the careful experimental work of his research group and for his insightful discussions of shock compression processes. I thank Dr. Min Zhou for serving on this thesis committee.

I acknowledge Dr. David J. Benson of the University of California, San Diego for making his state-of-the-art finite element code available for this research.

I thank my colleagues, Laurent Capolungo and James Shepherd, for their thoughtful advice directed towards this research and their shared enthusiasm in the field of solid mechanics.

Finally, I thank my parents, Kenneth and Gertrude Austin, for their unwavering support in all of my academic endeavors.

TABLE OF CONTENTS

LIST OF TABLES

LIST OF FIGURES

LIST OF SYMBOLS

Microstructure Reconstruction

$\mathbb{X}$, $\mathbb{Y}$	planar dimensions of the statistical volume element
V_f	volume fraction
R	particle radius
μ	mean (normal distribution)
σ	standard deviation (normal distribution)
m	location parameter (lognormal distribution)
s	shape parameter (lognormal distribution)
u_i	random uniform deviate on the interval [0,1]
v_i	random normal deviate on the interval [0,1]
d_{ij}	centroid-centroid distance from particle *i* to particle *j*
d	centroid-centroid distance from a given particle to its closest neighboring particle
Δd	width of the bins used to discretized the nearest-neighbor distribution
$\hat{\delta}$	parameter used in microstructure reconstruction
$\hat{\delta}_G$	parameter used in microstructure reconstruction
α	parameter used in microstructure reconstruction
β	parameter used in microstructure reconstruction
a_{NN}	scaling parameter used to normalize the discrete nearest-neighbor distribution
e_{NN}	cumulative measure of deviation of the synthetic nearest-neighbor distribution
T_v	virtual temperature
N_{succ}	number of successful configuration shifts
β_T	scaling factor used in the simulated annealing algorithm
N_{att}	maximum permissible number of configuration shift attempts
N_{dec}	maximum permissible number of virtual temperature decrements

The Finite Element Method

$\boldsymbol{x}$	position of a point in the current configuration
$\boldsymbol{X}$	position of a point in the reference configuration
$\boldsymbol{u}$	displacement field
$\dot{\boldsymbol{u}}$	velocity field
$\ddot{\boldsymbol{u}}$	acceleration field
$\boldsymbol{\sigma}$	Cauchy stress tensor
$\boldsymbol{\sigma}'$	deviatoric part of the Cauchy stress tensor
$\bar{\boldsymbol{\sigma}}$	mean elemental stress tensor
$\boldsymbol{\varepsilon}$	strain tensor
$\dot{\boldsymbol{\varepsilon}}$	strain rate tensor (rate of deformation tensor)
$\dot{\boldsymbol{\varepsilon}}'$	deviatoric strain rate tensor
$\dot{\boldsymbol{\varepsilon}}'^{p}$	plastic (inelastic) part of the deviatoric strain rate tensor
$\dot{\varepsilon}^{v}$	volumetric strain rate
t	current time
Δt	current time step
$\boldsymbol{F}$	force
$\boldsymbol{b}$	specific body force (per unit mass)
$\boldsymbol{t}$	surface traction
$\boldsymbol{n}$	surface normal
$\boldsymbol{h}$	vector of internal state variables
$\boldsymbol{I}$	second-order identity tensor
$\boldsymbol{q}$	heat flux vector
ϕ	generalized solution variable
Φ	generalized source term
V	integration volume
∂V	bounding surface of the integration volume
Ω	generalized domain
$\partial\Omega$	bounding contour of a generalized domain
Γ_u	boundary with a specified displacement
Γ_t	boundary with a specified traction

ρ	mass density
T	absolute temperature
P	pressure
E	specific energy (per unit volume)
E_C	cold compression energy (per unit volume)
e	specific energy (per unit mass)
e_s	specific shock energy (per unit mass)
e_{th}	specific thermal energy (per unit mass)
e_d	specific plastic deformation energy (per unit mass)
v	specific volume
U_P	particle velocity
$\tilde{U}_P$	blended particle velocity profile
U_S	shock wave velocity
S_1	slope of the linear $U_S - U_P$ relation
T_μ	microkinetic energy
δ_{ij}	the Kronecker delta
δu_i	virtual displacement
$\delta\varepsilon_{ij}$	virtual strain variation
ξ^i	isoparametric coordinates
N_α	interpolation function of node α
J	Jacobian matrix
q	artificial shock viscosity
c_ℓ	linear artificial shock viscosity coefficient
c_q	quadratic artificial shock viscosity coefficient
$B_{ij\alpha k}$	discrete gradient operator
$M^c_{\alpha i\beta j}$	consistent mass matrix
$M_{\alpha i\beta j}$	diagonal lumped mass matrix
M_α	mass at node α

$\boldsymbol{x}^0$	position of the centroid of an element
ℓ	shortest edge of an element
A	area
$s_{(j-1/2)}$	slope of the piece-wise linear approximation of a solution variable in an element
ΔV	transport volume
C	acoustic wave speed
$\overline{C}$	mean acoustic wave speed in an element
C_P	specific heat at constant pressure
C_V	specific heat at constant volume
μ	shear modulus
K	bulk modulus
$\tilde{K}$	corrected bulk modulus
κ	thermal conductivity
E_H	latent heat of melting
T_m	melting temperature
F_{ij}	deformation gradient
L_{ij}	velocity gradient
D_{ij}	rate of deformation tensor
W_{ij}	spin (vorticity) tensor
σ	uniaxial stress
ε	uniaxial strain
τ	shear stress
γ	shear strain (engineering)
γ^p	plastic (inelastic) shear strain (engineering)
$\overline{\sigma}$	effective stress
$\overline{\varepsilon}$	effective strain
$\overline{\varepsilon}^p$	effective plastic strain
$\overline{\tau}$	effective shear stress
$\overline{\gamma}$	effective shear strain (engineering)

$\bar{\gamma}^p$ effective plastic (inelastic) shear strain (engineering)

t_{term} time at which the simulation is terminated

t_{ramp} time over which the velocity boundary condition is ramped up to its full value

$N_{\mathbb{X}}$ number of elements in the Eulerian mesh that span the $\mathbb{X}$-dimension

$N_{\mathbb{Y}}$ number of elements in the Eulerian mesh that span the $\mathbb{Y}$-dimension

N_c number of reactant contact sites

P_c centerline pressure

$\bar{P}_j$ transversely-averaged pressure on the centerline at node j

$P_{j,k}$ pressure value at the node (j,k)

P_{st} stationary pressure

x_s position of the shock front

Constitutive Models

η compression (Gruneisen equation of state)

Γ Gruneisen parameter

K' pressure derivative of the bulk modulus (Murnaghan equation of state)

Γ^M material constant (Murnaghan equation of state)

k Boltzmann's constant

$\hat{\rho}$ dislocation density

b Burgers vector

ν_D Debye frequency

λ mean free path

τ_u internal (athermal) shear stress (Klepaczko model)

τ^* effective (thermally-activated) shear stress (Klepaczko model)

τ_0^* thermally-activated part of the threshold stress (Klepaczko model)

α_i dislocation/obstacle interaction coefficient (Klepaczko model)

μ_0 shear modulus at 0 K (Klepaczko model)

θ_* material constant (Klepaczko model)

ν_0 attempt frequency factor at 0 K (Klepaczko model)

ΔG_0	activation energy at 0 K (Klepaczko model)
p , q	constants that describe the shape of the energy barrier (Klepaczko model)
a	activation distance (Klepaczko model)
f	fraction of mobile dislocations (Klepaczko model)
M_{II}	dislocation generation term (Klepaczko model)
k_a	dislocation annihilation factor (Klepaczko model)
M_0	dislocation generation at reference strain rate (Klepaczko model)
$\dot{\gamma}_m$	reference strain rate (Klepaczko model)
A , B , C	material constants (Klepaczko model)
k_0	dislocation annihilation factor at 0 K (Klepaczko model)
m_0	strain-hardening rate-sensitivity constant (Klepaczko model)
$\dot{\gamma}_0$	threshold strain rate (Klepaczko model)
ω	effective frequency of local shear transformations (Hasan-Boyce model)
ω_0	fundamental frequency of transformation attempts (Hasan-Boyce model)
ΔG_f	activation energy for forward shear transformations (Hasan-Boyce model)
ΔG_b	activation energy for backward shear transformations (Hasan-Boyce model)
Ψ	fraction of material available for shear transformations (Hasan-Boyce model)
ψ	pseudo-Gaussian distribution of Ψ (Hasan-Boyce model)
ϖ	parameter in the Hasan-Boyce model
a^*	position of the ψ -distribution (Hasan-Boyce model)
a^*	standard deviation of the ψ -distribution (Hasan-Boyce model)
S	locally-stored transformation strain energy (Hasan-Boyce model)
$\Delta\upsilon$	shear activation volume (Hasan-Boyce model)
λ_1	linear coefficient of the shear activation volume (Hasan-Boyce model)
$\dot{\gamma}_1^p$, $\dot{\gamma}_2^p$	functions defined in the Hasan-Boyce model
$\dot{\gamma}_0$	pre-exponential factor (Hasan-Boyce model)
ζ_0	material constant (Hasan-Boyce model)
β_i	material constants (Hasan-Boyce model)
$f(\bar{\gamma}^p)$	function defined in the Hasan Boyce model

$\beta(\bar{\gamma}^p)$ function defined in the Hasan-Boyce model

σ_y yield stress (flow stress)

$\sigma_{y,0}$ initial yield stress (flow stress)

KH Knoop hardness

H linear strain-hardening coefficient

r^2 square of the linear correlation coefficient

Z stress amplitude of a disturbance (Markov process)

ϑ fluctuation in the distance covered by a disturbance (Markov process)

Combustion Theory

$W(T)$ reaction rate

$k(T)$ rate constant

k_0 pre-exponential factor

C_A concentration of reactant A

M molecular weight

v_i stoichiometric coefficient

m overall order of a chemical reaction

G activation energy for chemical reaction

R universal gas constant

Q heat of reaction

ξ dimensionless spatial coordinate

θ dimensionless temperature field

τ dimensionless time

r characteristic spatial dimension

T_* characteristic temperature in the neighborhood of reacting conditions

u_* parameter in Frank-Kamenetskii's method of expanding the exponent

t_{rxn} characteristic time for complete reaction

t_{ad} characteristic time of the adiabatic temperature rise

δ the Frank-Kamenetskii delta

δ_{cr} critical value of the Frank-Kamenetskii delta

T_c^{max}	maximum combustion temperature
θ_c^{max}	maximum value of the dimensionless temperature field during combustion
T_c	combustion temperature
r_h	radius of a hot spot
x	spatial coordinate located at the center of a hot spot
T_h	initial temperature of the hot spot
T_e	volume-fraction-weighted temperature of an element
T_{core}	core temperature of a hot spot
T_{surr}	temperature of the hot spot surroundings
B	model parameter (Merzhanov criterion)
n	hot spot symmetry factor (Merzhanov criterion)
A_m	constant that depend on the geometry of the hot spot (Merzhanov criterion)
m	constant that depend on the geometry of the hot spot (Merzhanov criterion)
A_n	coefficients of a polynomial fit of the activation energy
κ_{eff}	effective thermal conductivity
A_h	area of a hot spot
A_{surr}	surrounding area
r_{cr}	minimum critical radius
ζ	micro-initiation parameter
ζ_a	number of activated micro-initiation sites
ζ_p	number of partially-activated micro-initiation sites

SUMMARY

The shock compression of Reactive Particle Metal Mixtures (RPMMs) is studied at the microscale by direct numerical simulation. Mixture microstructures are rendered explicitly, providing spatial resolution of the coupled thermal, mechanical, and chemical responses at the particle level during shock compression. A polymer-bonded thermite system ($Al+Fe_2O_3$) is the focus of this work; however, the computational methods developed here may be extended to other reactive particle systems. Shock waves are propagated through the mixtures in finite element simulations, where Eulerian formulations are used to handle the highly-dynamic nature of particulate shock compression. Thermo-mechano-chemical responses are computed for a set of mixture classes (20% and 50% epoxy content by weight) subjected to a range of dynamic loading conditions (particle velocities ranging from 0.300–1.600 km-s^{-1}). Two critical sub-problems are addressed: (i) the calculation of Hugoniot data for variable mixture compositions and (ii) the prediction of sites that experience microscale reaction initiation. Hugoniot calculations are in excellent agreement with experimental data. Microscale reaction initiation sites are predicted in certain load cases for each mixture class, although such predictions cannot currently be validated by experimental methods.

CHAPTER 1
INTRODUCTION

This body of work is concerned with the thermo-mechano-chemical responses of Reactive Particle Metal Mixtures (RPMMs) during shock compression. RPMMs are highly-heterogeneous systems composed of micron- or nano-scale particles of reactive material. The particle mixtures are inert under ambient conditions, but exothermic chemical reactions are initiated by the thermal and mechanical states created by sufficiently-strong shock waves.

RPMMs are unique material systems in that they possess both energetic properties and structural load-bearing capabilities. The particulate phase provides structural reinforcement to the material system prior to energy release associated with chemical reactions. Such particle systems may be utilized in applications where it is desirable to replace part of a load-bearing structure by energetic material for purposes of enhancing overall specific energy release characteristics. Effective applications of RPMMs require a detailed understanding of the thermal, mechanical, and chemical processes that occur at the particle system level (i.e., the mesoscale).

The specific RPMM of interest in this work is a polymer-bonded Al+Fe_2O_3 thermite system. The thermite system is composed of micron-scale aluminum (Al) and iron oxide (Fe_2O_3) particles, which, in this case, are embedded in an epoxy matrix. This reactive system was selected due to the highly exothermic nature of the Al+Fe_2O_3 thermite reaction.

A broad goal of this research effort is to support the design of multifunctional energetic-structural materials by developing modeling techniques to observe and predict spatially-resolved thermo-mechano-chemical responses of discrete reactive particle systems during shock compression. Such responses are essential to our understanding of this class of materials. This research will also address two critical sub-problems: (i) the determination of mixture Hugoniot data, and (ii) the prediction of local reaction initiation sites at the microscale.

Spatially-resolved numerical models of the Al+Fe_2O_3 microstructure will elucidate particle-level responses that are not available from time-resolved experimental methods. Such responses include temperature fields, stress states, material melting, deformation behavior, and the evolution of reactant contact. Although not addressed specifically in this work, the prospect of designing RPMMs to sets of energetic and structural requirements is an exciting possibility.

The thermo-mechano-chemical responses of a range of particle systems could be investigated based on a set of parameters that characterize the morphological attributes of the mixture (e.g. particle size, particle shape, phase volume fractions, etc.) and the imposed loading conditions. In addition to exploring the performance ranges of different particle systems, the design studies would also provide insight to the effect of the stochastic nature of the microstructure on variability of the response of a particle system defined by a given set of nominal mixture parameters.

In this work, the shock compression of the polymer-bonded Al+Fe_2O_3 system is studied using a finite element code, Raven [1], developed at the University of California, San Diego. Model geometry is constructed by generating synthetic particle distributions that conform to stereological measures in actual microstructures. Eulerian formulations are used to simulate the dynamic responses of spatially-resolved particle systems subjected to shock loading, where the stress-strain response of each phase is modeled using distinct constitutive relations. Finite element simulations are augmented by algorithms that (i) calculate Hugoniot data, and (ii) apply microscale reaction initiation criteria to potential reaction sites. All aspects of the numerical models are automated so that a range of particle mixtures and loading conditions may be investigated efficiently. It should be noted that the aforementioned numerical techniques have been developed in a general manner, so that these analyses may be extended to other reactive systems. Finally, a set of simulations will be matched to experiments that have been performed to assess the validity of models.

CHAPTER 2
LITERATURE REVIEW

2.1 Shock consolidation of particle systems

Consolidation refers to a process by which a collection of loose particles is compacted into bulk form. During the consolidation process, interstitial pores are filled by inelastic material flow and particle surfaces are bonded, resulting in a compact that approaches the theoretical mixture density. Techniques available for consolidating particle systems can be classified broadly as static or dynamic. Static consolidation involves mechanical pressing of powders held at elevated temperatures for significant lengths of time. Dynamic consolidation involves the passage of shock waves, which are simply transient, high-amplitude stress pulses. Strain rates encountered in static consolidation are on the order of 1 s^{-1}; strain rates achieved during dynamic consolidation are on the order of 10^4–10^5 s^{-1}. Shock consolidation is of particular interest to this body of work because the dynamic impact loads experienced by RPMMs are equivalent to the shock consolidation of particle systems. Thus, an understanding of the shock consolidation process serves as a good starting point for a study of the dynamic behavior of RPMMs.

An extensive review of the shock consolidation process in particle systems has been published by Thadhani [2]. Shock waves induce high rates of energy deposition at particle surfaces, which are responsible for high levels of inelastic strain, the formation of strong temperature gradients, melting at particle surfaces, turbulent mixing (a term used qualitatively in this context), and the generation of high defect densities. The extent of compaction is influenced by the material properties of the constituents, the initial configuration of the particle system, and the magnitude of loading. The initial configuration defines the mixture morphology and relative phase content (including porosity). The magnitude of loading is described by a set of shock parameters (e.g., shock pressure). Insight to the thermal and mechanical interactions occurring at the particle level (mesoscale) enables the prescription of ideal shock parameters for efficient consolidation [3].

In comparison to conventional static techniques (e.g., sintering) used to consolidate metallic or ceramic powders, shock consolidation may be advantageous. Peak temperatures are usually confined to particle surfaces, effectively reducing the long-term exposure of particle interiors to elevated temperatures. Therefore, the degradation of temperature-sensitive material

properties is reduced by avoiding excessive exposure to elevated temperatures. Shock consolidation techniques are especially useful in ceramics and oxides, where processing by other means is difficult. Ceramics are typically brittle under quasistatic loads, exhibiting insignificant amounts of plastic deformation; however, the high levels of hydrostatic stress (in excess of the yield strength) produced by shock loading cause the material to behave more like a fluid. Additionally, ceramic grain sizes can be reduced by fracture and sub-grain structures can be achieved during shock loading [2].

The unique environments created by shock compaction (i.e., large inelastic strains, strong temperature gradients, configuration changes, mass mixing, and elevated defect densities) promote chemical reactivity in energetic systems. Chemical reactions that occur as a result of shock wave propagation aid the consolidation process by enhancing the melting and bonding of particle surfaces. The mechanical and thermal interactions at the particle level govern the initiation and propagation of chemical reactions. The intimate relation between thermomechanical behavior and chemical reactivity implies that reactions can be controlled, to an extent, by altering the initial configuration and loading conditions in a given material system.

2.2 Chemical reactions induced by shock waves

Chemical reactions caused by shock wave propagation may be classified as shock-induced or shock-assisted [4]. Shock-induced chemical reactions (SICRs) and shock-assisted chemical reactions (SACRs) are differentiated by their respective reaction initiation mechanisms. A SICR is initiated during the passage of a shock wave pulse on the (short) time scales of mechanical (pressure) equilibration. A SACR is initiated after release waves have allowed mechanical relaxation on the longer time scales of thermal equilibration.

The characterization of chemical reactions as shock-induced or shock-assisted is a difficult task. Post-shock recovery techniques [5] provide only the final morphological configuration of the microstructure. Large amounts of heat liberated during SICRs and SACRs leave little evidence of how reactions initiated or propagated. Micrographs of post-shock microstructures simply reveal the characteristics of the melted and re-solidified products and unreacted phases. Alternatively, time-resolved measurements [6, 7] provide temporal histories of macroscopic shock data. Time-resolved measurements are critical to our understanding of shock-induced and shock-assisted chemical reactions, as they provide detailed information

pertaining to reaction initiation and kinetics; however, such experimental techniques are challenging due to the short time scales of shock wave propagation and reaction initiation (SICRs can be initiated in nanoseconds) [4].

The mechanisms of shock-assisted reaction initiation include (i) the propagation of local instabilities activated (or assisted) by elevated bulk temperatures and (ii) solid-state diffusion processes that are enhanced by defect mobility. Mass transport rates are increased in reactive systems by the formation of new paths for vacancy (point defect) motion in grain boundaries. Such diffusion processes are enhanced by the increased bulk temperature attained in the mixture after thermal equilibration. SICRs must occur by other means because the time scales of shock wave propagation are too short for reactions to be initiated by elevated bulk temperatures or defect-enhanced solid-state diffusion [4]. A review of recent experimental studies of shock compaction will shed light on the mechanisms of shock-induced reaction initiation, culminating with the requirement of taking into account particle-level effects.

2.3 Experimental studies of shock compression

Experimental studies have been performed in a number of reactive particle systems to investigate mechanical, thermal, and chemical processes that lead to macroscale reaction initiation. A broad description of the experimental techniques utilized in the shock compression of particle systems will be given as a prelude to a chronological progression of the work performed. Additional details pertaining to experimental shock compression methods are available in the literature [2, 3, 8]. Shock waves are typically generated by either (i) impact of a flyer plate accelerated by compressed gas or explosives, or (ii) direct contact with detonated explosives. In the case of high-speed plate impact (e.g., Taylor tests), the amplitude of the shock wave depends on the impact speed of the projectile. The duration of the shock pulse is controlled by the thickness of the impacting plate. Smooth-bore light gas gun systems, as shown in Figure 2-1(a), can achieve impact velocities of 0.1–1.0 km-s^{-1}. Multi-stage gas gun assemblies can achieve impact velocities in the range of 0.5–2.5 km-s^{-1}. Gas gun experiments usually impact one simply contained specimen, as showing in Figure 2-1(b). Explosively-driven flyer plate arrangements, as shown in Figure 2-1(c), can attain impact speeds of 1.0–7.0 km-s^{-1}. Explosively-driven flyer plates typically impact target plates in which a set of specimens (6–12) are embedded (please refer to Figure 2-1(c)).

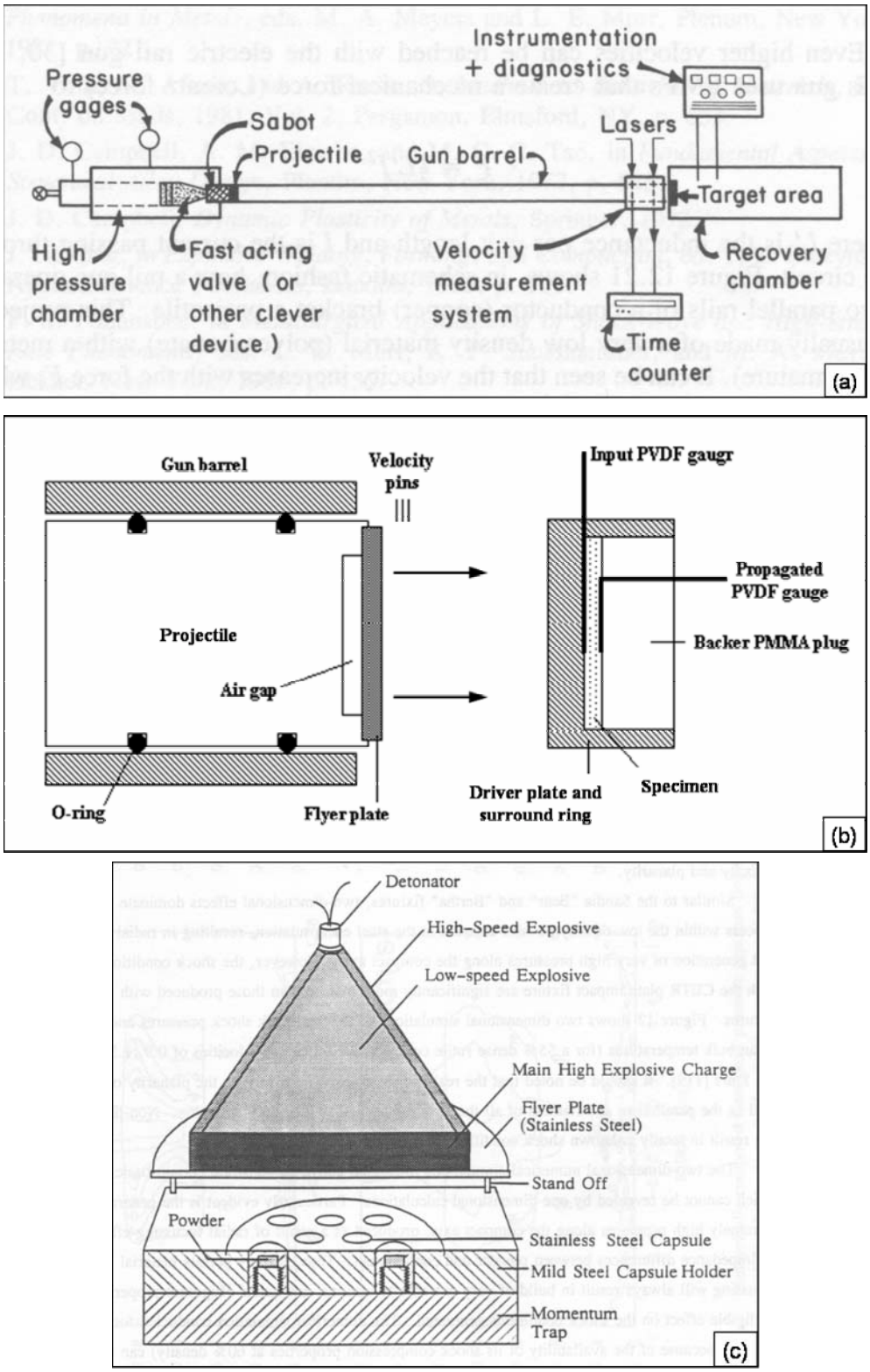

Figure 2-1. Schematics of techniques used in shock compression experiments; (a) a single-stage light gas gun (illustration taken from ref. [3]); (b) an enlarged view of a gas gun assembly prior to impact; (c) an explosively-driven flyer plate arrangement, i.e., the Sawaoka shock recovery fixture (illustration taken from ref. [2]).

In the case of direct contact with explosives, specimen containers are typically embedded in cylindrical explosive housings. Such configurations produce radial shock loading. In this case, shock parameters depend on the energy content of the explosives and the degree of confinement. As mentioned earlier, post-shock recovery techniques and time-resolved measurements are available for analysis.

The earliest reports of chemical reactions induced by shock wave propagation are commonly attributed to the work of Batsanov et al. [9, 10] in the 1960s. Extensive investigation of reactions in shock-loaded particle systems was carried out by Graham and co-workers [11-13] in the 1980s. A summary of recent experimental studies, starting with the work of Boslough [14] in the early 1990s, is presented next.

Boslough [14] conducted a series of planar impact experiments on 50% porous Al+Fe_2O_3 thermite systems (micron-scale Al and Fe_2O_3 particles). Here, temperatures were measured using time-resolved radiation pyrometry to assess reaction initiation. Elevated temperatures occurring in small, localized volumes of the microstructure (i.e., 'hot spots') were of particular interest. Temperature measurements indicated that partial reactions occurred almost immediately behind the shock front. These results are in agreement the observations of Hornig et al. [15], which showed that reactions are initiated on a sub-microsecond time scale (<100 ns) in the Al+Fe_2O_3 system. The observance that reactions did not go to completion after passage of the first shock wave suggested that reaction propagation kinetics were inhibited. Boslough attributed reaction inhibition to inadequate levels of local reactant mixing.

Krueger et al. [16] studied the shock compression of nickel silicides (Ni-Si) with planar impact techniques. Powders of similar size (20–45 μm) were tested. High-speed impact experiments showed that shock energy differences between conditions of no reaction and nearly full reaction were only on the order of 5%. Differential scanning calorimetry (DSC) was used to measure temperatures at which exothermic reactions occurred in statically-pressed powders. Sharp shock energy thresholds observed in experiments, which correlated with DSC results, formed a basis for the hypothesis that the mean bulk temperature of the mixture determined whether or not reactions initiated. This led to the proposal of a thermal energy threshold known as Krueger-Vreeland energy threshold, specific to each material system. Reaction initiation was predicted when the shock energy exceeded the thermal energy threshold. The macroscopic shock energy may be expressed from the Rankine-Hugoniot relations as

$$e_s = \frac{1}{2} P\left(\nu_{00} - \nu\right) \tag{2.1}$$

where e_s is the specific shock energy (per unit mass), P is the shock pressure, ν_{00} is the initial specific volume of the system (including porosity), and ν is the final compacted specific volume of the system. The specific thermal energy threshold measured in the Ni-Si system was approximately 384–396 kJ-kg^{-1}.

The extension of the Krueger-Vreeland energy threshold to other material systems is problematic. The prediction of reaction initiation from a macroscopic thermal energy threshold neglects the contributions of localized thermomechanical responses at the particle level. Krueger argued against particle-level reaction thresholds in the Ni-Si system because the existence of such a threshold excludes the possibility that the same local conditions may be found in traversing the threshold. For example, a local condition may be mass mixing due to local differences in particle velocities. Little evidence of mass mixing was observed outside melt pools and isolated surface layers just before the onset of reaction initiation, and Krueger argued that it was unlikely that increasing the shock energy as little as 5% would drastically enhance mass mixing. However, it was reported that reaction kinetics in the Ni-Si system were slower than the time scales of thermal equilibration. It is possible that local temperature gradients at the particle surfaces had sufficient time to equilibrate (raising the bulk temperature of the mixture), but particle-level effects were overlooked due to a lack of spatial and temporal resolution. Alternatively, the particle-level behavior may be specific to the particle morphology tested. In light of these points, it should be inferred that reaction initiation thresholds and mechanisms are specific to material systems and phase morphologies.

Shock consolidation techniques were used by Vecchio et al. [17] to synthesize niobium silicides (Nb-Si) and molybdenum silicides (Mo-Si). Shock waves were generated by planar impact of explosively-accelerated flyer plates. Post-shock microscopy analyses revealed regions that were unreacted, partially reacted, or fully reacted. It was found that reactions were initiated along the solid–molten interface of the reactants. Reaction product ($NbSi_2$ or $MoSi_2$) generated at the interface was continually ejected into the molten Si phase. This ejection mechanism precluded the formation of an interfacial product layer, so reaction kinetics were not limited by diffusion barriers. The major finding of this study was that reaction initiation required the melting of the Si phase. The complementary work of Meyers et al. [18] proposed a reaction

threshold based on the critical pool size of molten Si. Energy contours computed in 2-D numerical simulations performed by Norwood and Graham [19] were compared to reacted regions observed in post-shock recovered samples collected by Vecchio et al. [17]. The above correlation facilitated the identification of an energy threshold (600–800 kJ-kg^{-1}) for reaction initiation. The threshold shock energy was distributed among the constituent phases in order to calculate a critical melt fraction of Si (0.2–0.5). The requirement of a critical melt fraction of Si was rationalized by considering thermal activity at local hot spots; heat generated by reactions must exceed heat losses to the surroundings. A heat conduction analysis enabled the prediction of a critical pool size of molten Si (3–4 μm) for reaction initiation. The reaction threshold proposed by Meyers et al. progressed our understanding of reaction initiation because thermal processes at the particle level were taken into account. However, it suffers from the same inadequacy of the Kruger-Vreeland threshold, in that the macroscopic shock energy is ascribed to the microscopic phenomena of melt pool formation. Furthermore, this analysis is unable to pinpoint the exact onset of reactions, as recovered samples only show the final configuration of the microstructure after reactions have propagated.

The early work of Dremin and Breusov [20] indicated that the rates of chemical reactions and phase transformations increase in the presence of combined states of pressure and shear. In an extension of earlier work [18], Meyers et al. [21] considered the effects of plastic shear deformation in regard to SICRs. Direct-contact explosive shock loading was used to generate asymmetric shock loads in the Nb-Si and Mo-Si systems. The asymmetric loads created regions of shear localization. Recovered samples displayed reaction sites within shear bands at particle interfaces. The initiation of reactions was attributed to local temperature rises due to plastic deformation and frictional dissipation. The major finding of this study was that plastic deformation influenced the initiation of reactions. In a related work, Nesterenko et al. [22] showed that reactions in the Nb-Si system still initiated in controlled shear experiments at lower loading rates. The results of this study confirmed the finding of Meyers et al. [21] regarding the role of plastic deformation in SICRs. In order to take into account the effect of plastic deformation in the Krueger-Vreeland threshold, Yu et al. [23] adjoined an additional term to the shock energy, $e_{th} \leq e_s + e_d$, where e_{th} is the specific thermal energy threshold, e_s is the specific shock energy (cf. Eq. (2.1)), and e_d is the specific plastic deformation energy.

The experimental work performed in reactive silicide powders was extended by Thadhani et al. [6] to include time-resolved measurements. In these experiments, the titanium silicide system (Ti-Si) was studied over a range of shock-loading conditions and particle morphologies. The major finding of this work was that mechanical interactions at the particle level must be accounted for in the quantification of reaction initiation. Models that are purely thermochemical cannot be used exclusively to describe reaction initiation. Critical thermomechanical processes included relative plastic flow, thermal activation, configuration changes (e.g. melting and fracture), mixing, defect generation, cleansing of reactant surfaces, and the opening of fresh reactant surfaces. The effects of powder morphology were studied to shed light on the different mechanisms that induce chemical reactions. Particle morphology affects the amount of interparticle contact, which in turn influences local stress states. These local stress states control the extent of plastic deformation and mixing between reactants. The Ti-Si particle morphologies investigated were classified as fine powders (Ti: 1–3 μm, Si: <10 μm), medium powders (Ti: 10–44 μm, Si: <45 μm), and coarse powders (Ti: 105–149 μm, Si: 45–149 μm). Scanning Electron Microscopy (SEM) images of the initial configurations of these particle morphologies are shown in Figure 2-2. The medium-sized particles exhibited coordinated plastic deformation; this led to high degrees of intimate contact between reactants, as shown in Figure 2-3(a). The fine Ti particles exhibited agglomeration, while the coarse Si particles experienced extensive fragmentation and entrapment within the plastically-deformed Ti particles, as shown in Figure 2-3(b). These processes decreased the likelihood of reaction initiation because the amount of intimate mixing is limited. Time-resolved measurements showed a higher frequency of reaction initiation in the medium morphology powder. Here, increased levels of mixing effectively lowered reaction thresholds. Additionally, it was projected that plastic deformation at particle interfaces resulted in high rates of defect generation, which enhanced solid-state reactivity. Variations in the thermomechanical behavior of different particle morphologies support the notion that the underlying reaction mechanisms depend on a number of processes operating at the particle level.

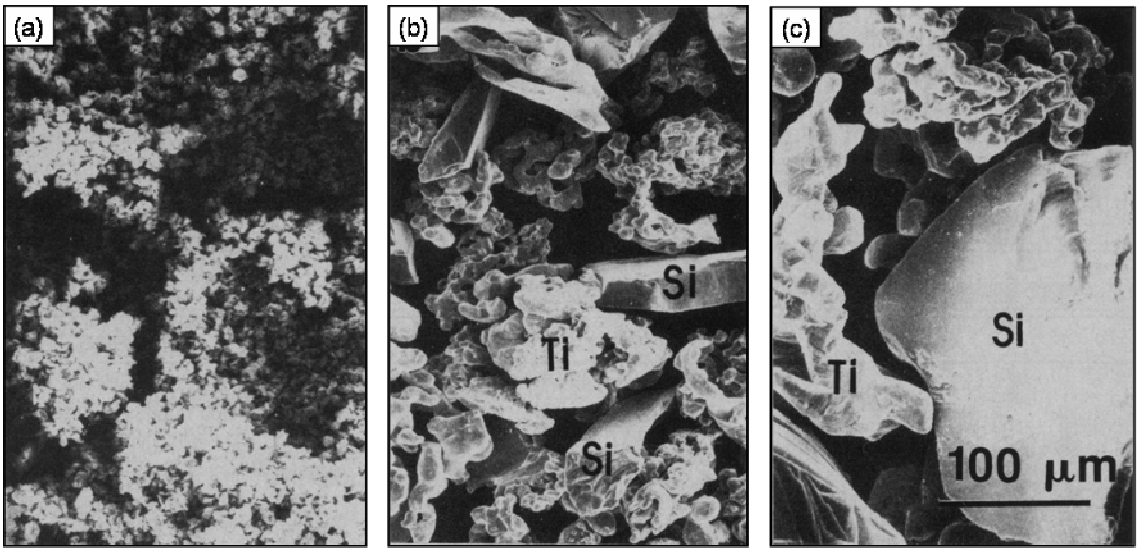

Figure 2-2. SEM images of the initial configurations of a set of different Ti-Si particle morphologies; (a) fine powders; (b) medium powders; (c) coarse powders (micrographs taken from ref. [6]).

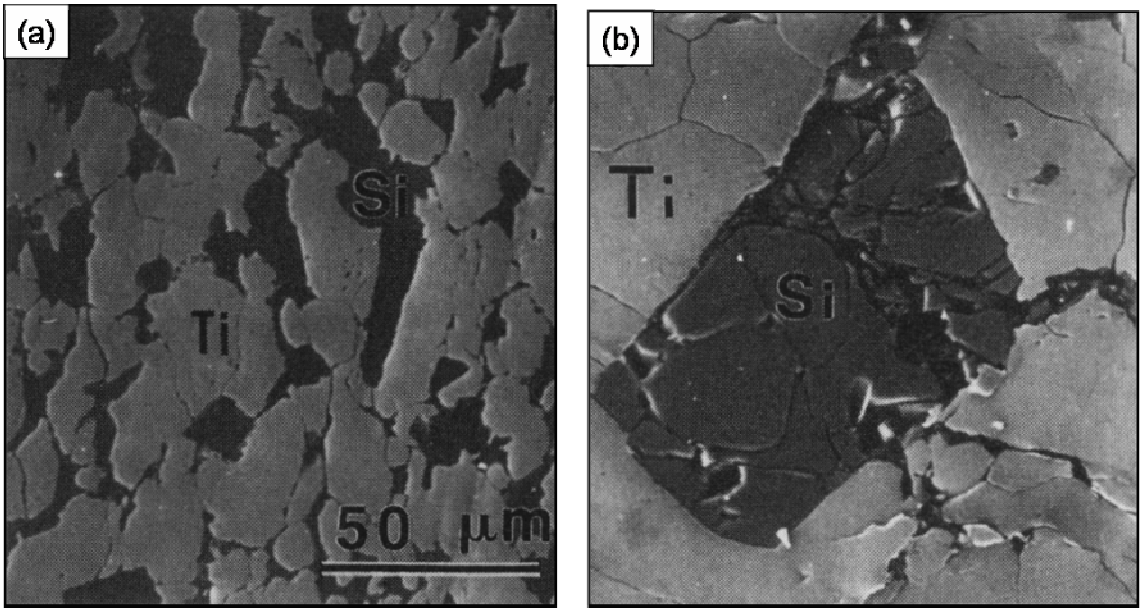

Figure 2-3. SEM images of the post-shock configurations in the Ti-Si system for (a) a medium morphology powder, and (b) a coarse morphology powder (micrographs taken from ref. [6]).

Dunbar et al. [24] conducted similar morphology studies in the nickel-aluminum system (Ni-Al). The initial configurations of the Ni-Al particle morphologies are shown in Figure 2-4.

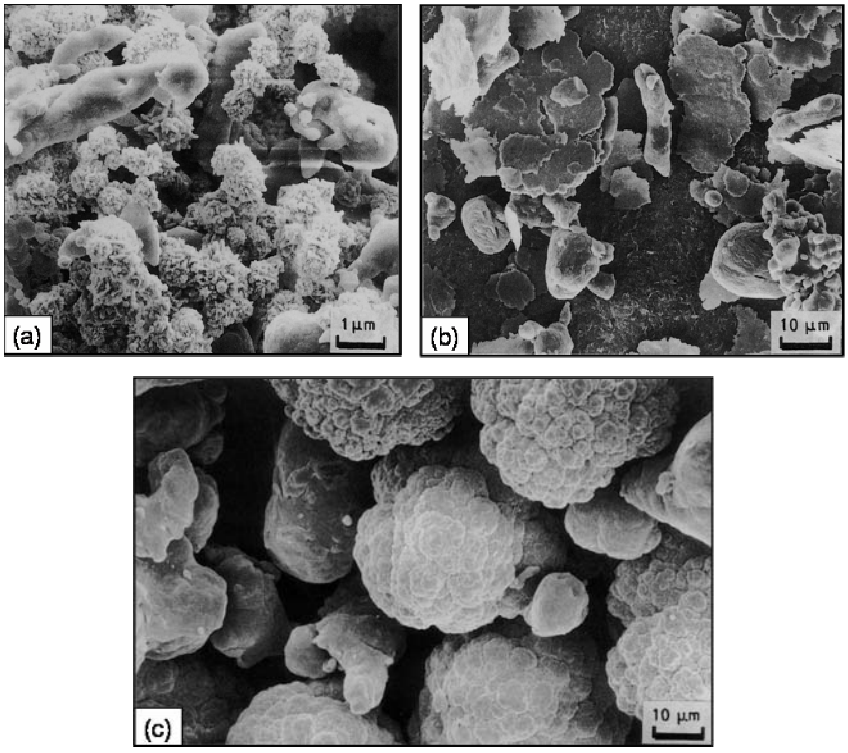

Figure 2-4. SEM images of the initial configurations of a set of different Ni-Al particle morphologies; (a) fine powders; (b) flaky powders; (c) coarse powders (micrographs taken from ref. [24]).

Post-shock micrographs of the microstructures, shown in Figure 2-5, were analyzed to assess the extent of reactions for each of the powder morphologies. Here, reacted and unreacted regions of the compact are discerned based on contrast and the presence of pores. In unreacted regions of the microstructure, the bright contrast of the Ni particles and the dark contrast of the Al particles are clearly visible (e.g., Figure 2-5(a)). In reacted regions of the microstructure, the product phase displays a uniform contrast, and dark pores (generated by melting and re-solidification processes) are present (e.g., Figure 2-5(d)). In Figure 2-5(a), coarse, spherical particle mixtures (Ni: 45–70 μm, Al: 45–150 μm) showed little evidence of chemical reaction; notice the marked contrast between the Ni and Al phases. In Figure 2-5(b), fine, spherical particle mixtures

(Ni: 3–7 μm, Al: 10–20 μm) experienced partial reactions; here, isolated regions of the mixture react due, in part, to increased surface contact of the reactants. In Figure 2-5(c), irregular, flaky-shaped Ni particles (44 μm) mixed with fine, spherical Al particles reacted almost completely; notice the decreased contrast between the Ni and Al phases at particle interfaces, and the presence of pores. The enhanced reactivity in the flaky morphology powder was caused by increased levels of mixing and reactant contact area.

The morphological findings of the studies conducted by Thadhani et al. [6] and Dunbar et al. [24] should not be generalized blindly to other energetic particle systems. Particle-level responses, and their influence on chemical reactivity, are specific to the particular reactive system of interest.

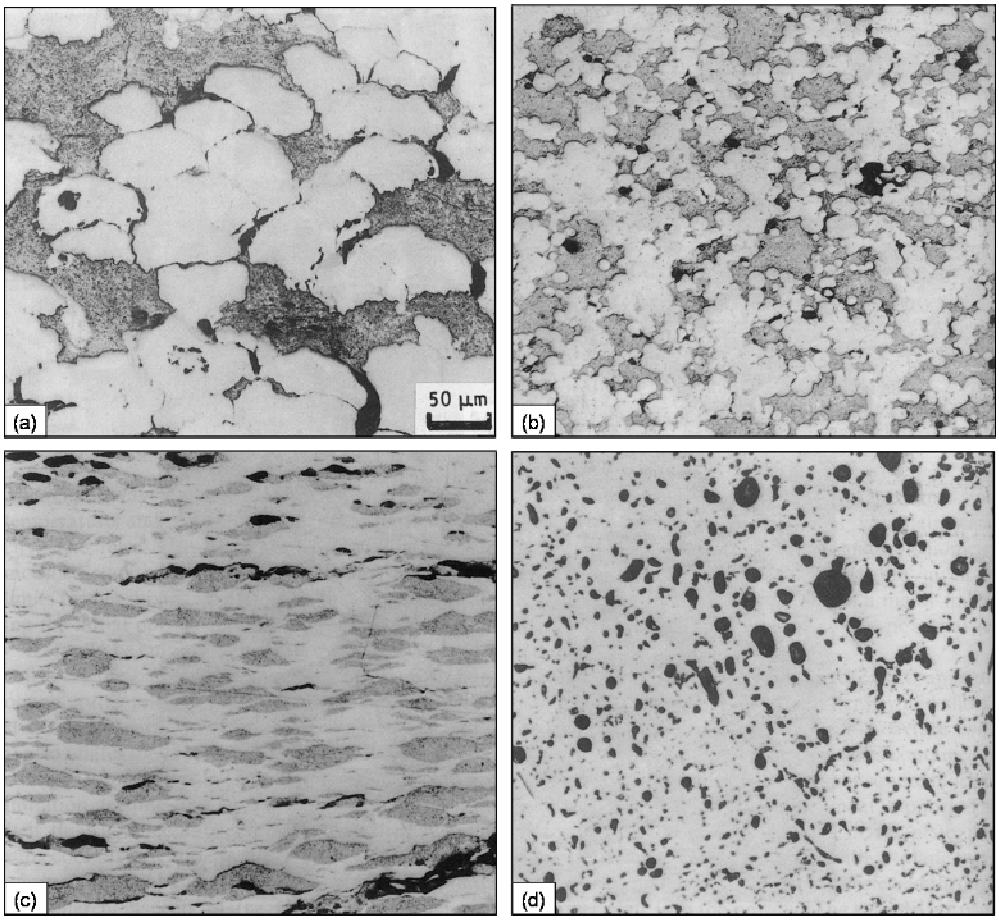

Figure 2-5. Optical images of powder compacts in the Ni-Al system, showing unreacted regions in (a) a coarse morphology powder, (b) a fine morphology powder, and (c) a flaky morphology powder; a fully reacted region is depicted in (d) (micrographs taken from ref. [24]).

In the recent work of Vandersall and Thadhani [7], macroscale reaction initiation in the Mo-Si system was investigated with time-resolved shock compression measurements. The interesting result of this experimental work was the observation that melting of the Si phase inhibited reaction initiation. This observance is in sharp contrast to the conclusions drawn earlier by Meyers et al. [18]. Vandersall and Thadhani observed that melting of the Si phase induced capillary flow around Mo particles. This resulted in reduced plastic deformation in the Mo phase due to a reduction in deviatoric stresses. Consequently, mixing between the reactants was limited. The inhibition of reaction initiation due to melting of the Si phase is in agreement with the theoretical studies of Tamura and Horie [25], where reactions were predicted within the adiabatic shear bands of the Nb-Si system. Reaction sites were formed in areas experiencing high shear strain rates, which led to increased thinning of reactants and higher levels of mixing. The likelihood of reaction initiation decreased when one reactant phase melted, despite increases in the shear rate. One may recall that the reaction initiation mechanism proposed by Meyers et al. [18] was based on the melting of Si in the Nb-Si and Mo-Si systems. Critical melt fractions of Si were predicted from experimentally-correlated shock energies. However, if the shock energy is an indicator of reaction initiation for all powder morphologies, then the coarse powders studied by Vandersall and Thadhani should have experienced reaction initiation at lower pressure thresholds due to their increased porosity. This behavior was not observed in time-resolved measurements. Perhaps the recovered samples analyzed by Meyers et al. underwent SACRs instead of SICRs, where the applicability of macroscopic energy thresholds is perhaps more appropriate.

2.4 Experimental studies specific to the aluminum–iron oxide thermite system

The reactive particle system considered in this body of work is the polymer-bonded $Al+Fe_2O_3$ thermite system. The model thermite system is composed of micron-scale particles of aluminum and iron oxide embedded in a polymer binder. Experimental work has been performed in both loose-particle and polymer-bonded thermite systems [14, 26, 27], but it is safe to say that shock compression data are sparse. A brief review of the chemical behavior in the $Al+Fe_2O_3$ thermite system at ambient pressure will be given next, followed by experimental studies of shock compression.

The $Al+Fe_2O_3$ thermite reaction is a gasless oxidation-reduction process. Thermite reactions can be initiated locally and may become self-sustaining due to the large heat of reaction (–420 kJ per mol Al) [28]. Additionally, combustion rates are increased by elevated states of pressure [28]. Mei et al. [29] used differential thermal analysis (DTA) to study the reaction sequence in non-shocked, particulate thermite systems. Particle mixtures were heated from ambient pressure conditions to determine threshold temperatures for reaction initiation. It is important to note that the reaction sequence is executed through a series of transition states. The first reaction occurred at 1233 K ($9Fe_2O_3+2\ Al \rightarrow 6\ Fe_3O_4+Al_2O_3 - Q_a$); the next sequence of reactions occurred at 1333 K ($Fe_2O_3+2\ Al \rightarrow Al_2O_3+2\ Fe - Q_b$; $3\ Fe_2O_3+2\ Al \rightarrow 5\ FeO+FeAl_2O_4 - Q_c$), where Q_a, Q_b, and Q_c represent the respective heats of reaction. It should be noted that these reaction temperatures are high enough to melt the Al phase. Pressed specimen reacted at lower temperatures, which may be attributed to the increased amount of reactant contact.

Boslough [14] collected a limited amount of shock compression data (hot spot temperatures) in loose-particle $Al+Fe_2O_3$ thermite systems mentioned earlier. Holman et al. [26] obtained high-pressure shock data in loose-particle $Al+Fe_2O_3$ thermite powder mixtures. Thadhani et al. [27] extended the work of Holman by performing shock compression experiments in loose-particle $Al+Fe_2O_3$ thermite systems over a range of volumetric distributions. Here, time-resolved techniques were used to measure shock wave velocities and shock pressures in 50% porous powder samples (Al and Fe_2O_3 particles were approximately 15 μm in diameter). Ferranti and Thadhani [30] recently conducted a set of Taylor anvil tests on polymer-bonded $Al+Fe_2O_3$ thermite systems. Here, shock pressures and shock wave velocities were measured with time-resolved techniques for particle velocities ranging from 0.3–0.6 km-s^{-1}. The experimental results of Ferranti and Thadhani will serve as an evaluative reference for the models developed in this body of work.

2.5 Conceptual models of reaction initiation

Attempts to rationalize the mechanisms of reaction initiation and propagation have led to the formulation of a set of conceptual models. Models referenced in the shock compression literature include the VIR model [31], the ROLLER model [20], and the CONMAH model [32].

A brief description and assessment of each will be provided; the interested reader should consult the literature for further details.

The VIR model, developed by Hwang [33] and Horie and Sawaoka [31], is a set of constitutive relations that describes the mechanical and energetic states of reactive mixtures by assuming macroscopic mass-fraction-weighted interactions in a thermodynamically-closed system of voids, inert species, and reactive species. The constitutive relations evolve based on assumed reaction kinetics, with no consideration of initiation mechanisms. Subsystems (voids, inert species, and reactive species) are assumed to be equilibrated mechanically, but not thermally. The effects of porosity, specific volume evolution (due to the formation of reaction products), and energy transport between reactive systems are taken into account. Bennett et al. [34] extended the model by (i) including time-delayed reactions initiated independent of temperature, and (ii) introducing a volumetric compatibility equation to guarantee that the calculated specific volumes match those from the hydrodynamic flow equations. The VIR model is useful in predicting states of the mixture after reactions are known to occur; however, it cannot be used to predict reaction initiation.

The ROLLER model was introduced by Dremin and Breusov [20] to describe reaction propagation mechanisms in shock-compacted mixtures. According to the model, when two reactant layers are displaced relative to one another, the product phase that nucleates between them may be regarded as a mechanical roller. The roller grows in size as products from, which promotes mixing between the reactant phases. Reactant mass is brought directly to nucleation sites by inelastic flow. This proposition differs from the usual diffusional growth mechanism, where nucleating crystals grow by 'random walks' of vibrating atoms assisted by thermal energy (cf. ref. [2]). Calculations by Dremin and Breusov showed that the rollers can be composed of approximately 30,000 atoms, reaching approximately 3 μm in size. Although the ROLLER model describes a possible reaction mechanism in well-mixed systems, it does not describe the processes that lead to reaction initiation.

In response to the need for a coupled thermo-mechano-chemical model that can describe the mechanisms that lead to reaction initiation, Graham [32] proposed the CONMAH model. The qualitative framework implemented here takes into account configuration changes (e.g., void closure), mass mixing, shock activation (i.e., enhancement of solid-state reactivity), and heating at sites of intimate reactant contact. The shortcoming of this model is an absence of numerical

schemes for calculating reaction initiation thresholds; however, it is fairly complete in terms of accounting for the mechanisms leading to reaction initiation. The key contributors to reaction initiation include: (1) large degrees of fluid-like plastic flow, (2) turbulent mixing, (3) defect generation, (4) cleansing of existing reacting surfaces, as well as the formation of new reactant surfaces, and (5) elevated surface temperatures.

The aforementioned conceptual frameworks are useful in describing reaction propagation mechanisms and general trends in experiments. However, resolution is needed at the mesoscale to predict reaction initiation based on quantifiable behavior. The time and length scales of shock wave propagation are too small to extract spatially-resolved data at the mesoscale with experimental methods; thus, numerical methods must be introduced.

2.6 The emergence of numerical resolution at the mesoscale

Analytical models of the shock compaction process have been developed by Gourdin [35] and Schwarz et al. [36] for spherical particles. These groups calculated the minimum shock energy and pulse duration necessary to melt particle interfaces. These models assumed that uniform amounts of energy were deposited by shock waves at particle surfaces. In each study, temperature profiles in a model particle were calculated via thermal equilibrium. A major limitation of these continuum models is their inability to describe the highly non-uniform thermomechanical interactions at the mesoscale (e.g. particle contact, mixing, relative plastic flow, void collapse, localized pressure and temperature spikes, melting, fracture, and bonding). The development of numerical models that take into account particle-level effects is imperative to our understanding of reaction initiation, as evidenced by the experimental work of Thadhani [4, 6] and Vandersall [7].

Williamson [37] is credited with the earliest numerical simulation of spatially-resolved shock compaction of particle systems. Williamson studied thermal and mechanical responses of a unit cell containing a small set of stainless-steel particles arranged in a highly-ordered, close-packed configuration (please refer to Figure 2-6(a)). Here, the particle systems contain a single phase, i.e., the particles are not embedded in a matrix phase. The dynamic nature of shock compaction induces extreme thermomechanical responses at the particle level. High levels of pressure, severe plastic strains, material jetting, and melting are quite common during shock wave propagation. Such extreme deformations render traditional Lagrangian finite element

methods inadequate. Consequently, Williamson used a 2-D Eulerian finite difference code, CSQII [38], in analyses. Shock waves were generated by impacting projectiles (impact velocities ranged from 0.5–2.0 km-s^{-1}). The plane strain condition was invoked, effectively extending 2-D circular particle cross sections to cylinders in 3D. Material strength was approximated by an elastic, perfectly plastic stress-strain constitutive relation (no work hardening). Frictional effects were ignored due to the fluid-like behavior of materials (especially at particle contacts) [37]. As expected, higher impact velocities led to elevated temperatures at particle surfaces. Williamson also investigated the effects of a bimodal size distribution of particles (please refer to Figure 2-6(b)), and the effects of increased porosity. A larger number of temperature spikes were observed in the bimodal distributions because there were a larger number of interstitial sites; however, the magnitudes of the peak temperatures were lower than that of a monosized particle mixture because the interstitial sites were smaller. This is in agreement with experimental results of Wright et al. [39], which showed that the largest monosized steel powders tested exhibited the highest amount of melting and bonding due to the size of their interstitial sites. Porosity effects were investigated by considering inclusions located at the centroids of the particles. The addition of porosity increased in the internal energy content of the particles during shock loading, which led to the formation of temperature spikes near void-collapsed regions. Despite the fact that strong temperature gradients exist, a heat conduction analysis in a model particle revealed that the heat transfer time constants were much larger than the time scales of shock compression. Therefore, the effects of conduction are insignificant in regions relatively close to the shock front [37].

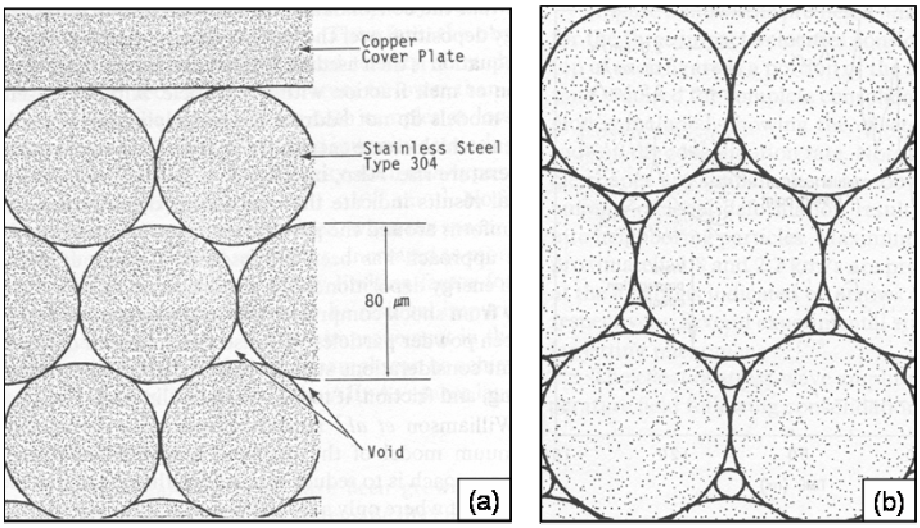

Figure 2-6. The initial configurations of the (a) monosized and (b) bimodal stainless-steel particle distributions simulated by Williamson (illustrations taken from ref. [37]).

Highly-structured materials, which display significant levels of periodicity, can be represented by repeated sets of unit cells. However, actual particle distributions do not display such high levels of periodicity. The heterogeneous nature of many particle systems requires the use of statistical volume elements (SVEs), which reflect the random spacing and size variations found in actual particle distributions. Additionally, the representation of porosity by inclusions within particles is quite a deviation from the true geometry of the microstructure. While the numerical simulations of Williamson have advanced our understanding of shock compaction at the mesoscale, more depth is needed for realistic particle distributions.

2.7 Numerical simulation of realistic particle systems

In response to the need for a robust numerical solution technique to handle the severe deformations associated with particulate shock compression, Benson developed a 2-D multi-material Eulerian hydrocode, Raven [1]. All finite element simulations described in this section were performed using Raven.

Benson [40] extended the study of Williamson by considering larger domains of randomly-distributed, micron-scale copper (Cu) particles (again, the particles are not embedded in a matrix phase). Williamson included 10–20 particles in his numerical simulations; Benson

included approximately 100 particles, as shown in Figure 2-7. A Monte Carlo algorithm was used to generate sets of particle sizes in agreement with experimental distributions [41]. A 'pseudo-gravity' technique [41] was used to locate particle centroids. Again, the geometry of the model was restricted to two dimensions in light of the computational expense of fully 3-D calculations. The plane strain condition was applied in numerical simulations. The initial boundary value problem approximated the passage of a single shock wave by compressing powders in a 'piston/cylinder' configuration using a velocity boundary condition (i.e., the particle velocity U_P). The accuracy of the calculations was validated by comparing (i) post-shock particle configurations to experimental texture micrographs, and (ii) calculated shock wave velocity–particle velocity relations to experimental data. The effects of particle morphology were assessed through temperature profiles of cylindrical and rectangular prismatic particles. The initial configurations of the cylindrical and rectangular prismatic particle distributions are depicted in Figure 2-7. Powder morphology studies showed that rectangular particles exhibited substantially lower levels of turbulent flow in comparison to cylindrical particles. Plastic flow was concentrated in a few channels that spanned the domain. Rectangular faces perpendicular to the wave direction experienced lower amounts of deformation and heating, which led to the prediction of anisotropic mechanical properties in the resulting compacts. The surface deformation and heating of the cylindrical particles, although highly non-uniform, did not exhibit any preferred orientations. Thus, predictions of the resulting mechanical properties were isotropic.

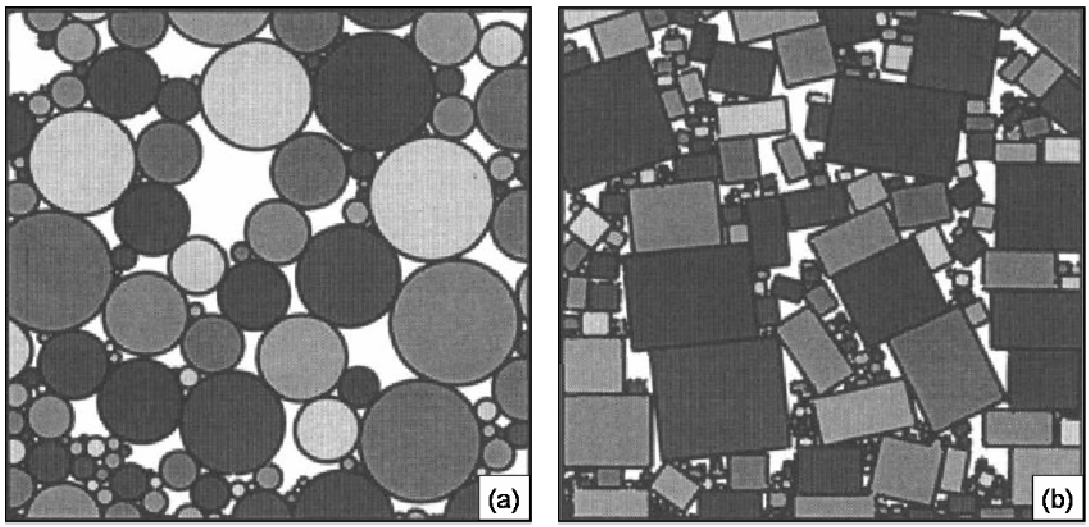

Figure 2-7. The initial configurations of the (a) cylindrical (19% porosity) and (b) rectangular prismatic (16% porosity) Cu particle distributions simulated by Benson (illustrations taken from ref. [40]).

Benson [41] characterized the Hugoniot response of the Cu particle system by calculating shock wave velocity–particle velocity relations in finite element simulations. The position of the shock front was tracked over time with averaging techniques, as shock fronts do not remain precisely planar in heterogeneous media. The shock wave velocity was calculated by applying a linear regression to the time history of the shock front position. The shock wave velocity displayed a strong linear dependence on the particle velocity, which is a common characteristic of many metals. The largest deviations from experimental results were observed for low particle velocities (U_P=0.25 km-s^{-1}). Low particle velocities led to the formation of diffuse wave fronts, which are difficult to track with averaging techniques. The agreement between simulation results and experimental measurements of the shock wave velocity provide confidence in using Eulerian formulations to predict other shock consolidation behavior at the mesoscale.

Previous modeling techniques established in the Cu powder system were applied by Benson [42] in numerical simulations of shock wave propagation in reactive titanium-silicon carbide (Ti-SiC) particle mixtures. These mixtures were composed of spherical Ti particles (~100 μm) surrounded by smaller, rectangular SiC particles (~12 μm). The same distribution generation techniques described above [41] were used. Pure Ti mixtures were analyzed first. The expected thermomechanical responses were confirmed: (i) highly heterogeneous

distributions of pressure, temperature, and plastic strain rate were found within the wave front, and (ii) hot spots formed in areas of extreme plastic deformation (e.g. void-collapsed regions). Mixtures of Ti and SiC particles (~10% volume fraction of SiC) were considered next. The addition of SiC particles had insignificant effects on consolidation time, shock front width, and the overall deformation behavior of the mixture. The SiC particles reduced the amount plastic flow in the Ti phase by occupying sites in between Ti particles. The reduction in plastic flow attenuated peak temperatures at particle junctions (similar to the behavior observed in the bimodal particle distributions of Williamson [37]). The similarity of the pure Ti mixture and the Ti-SiC mixtures suggested that the consolidation of the powder was dominated by the viscoplastic deformation of the particulate Ti phase. Additional simulations were conducted in pure Ti powders with increased particle sizes (up to four times the original size) to assess simple morphological effects. The shock front width and rise time scaled proportionately with particle size. The latter suggested that particle inertia influenced shock consolidation of the Ti powder. Spatial distributions and time histories of temperature proved to be valuable in estimating the initiation of reactions between Ti and SiC particles. Local hot spots at particle junctions provided the elevated temperatures necessary to promote reaction initiation and growth of interfacial reaction layers.

Benson et al. [43] studied the thermomechanical behavior of granular materials (two Ni-based alloys and a stainless steel system) with finite element simulations at the mesoscale. The intention of this study was to characterize transitions from the quasistatic deformation regime to the dynamic regime. In the context of this study, the transition to the dynamic regime is marked by the following behavior at particle interfaces: (1) severe amounts of plastic deformation, (2) turbulent mixing, and (3) melting. The aforementioned criteria are well characterized by a quantity known as the microkinetic energy. A definition of the microkinetic energy is elucidated by a decomposition of the total plastic deformation. Local pressure spikes observed in the vicinity of pores demonstrate that the geometrically-necessary plastic deformation associated with void collapse cannot fully dissipate the energy supplied by shock waves. Thus, the total plastic deformation can be separated into two components: (1) a geometrically-necessary component, and (2) a redundant component. The redundant energy serves as the work input for local material jetting and vortex formation. Nesterenko [44] introduced the microkinetic energy to quantify the redundant energy term. The microkinetic energy may be expressed as

$$T_{\mu} = \frac{1}{2}\rho\left(\dot{\boldsymbol{u}} \cdot \dot{\boldsymbol{u}} - U_P^2\right) \tag{2.2}$$

where ρ is the mass density, $\dot{\boldsymbol{u}}$ is the velocity vector, and U_P is the particle velocity. The microkinetic energy was useful in categorizing the dynamic nature of powder responses in the study of Benson et al. [43]; a critical threshold value of the microkinetic energy separated quasistatic and dynamic regimes of deformation. It will be seen later that the microkinetic energy is also useful in predicting reaction initiation and propagation, as chemical reactivity is dependent on mass mixing. The results of this study showed that increased pressure and higher levels of initial porosity promoted transitions to the dynamic regime. It is interesting to note that the solid density of constituent powders did not affect the dynamic behavior transition.

Benson and Conley [45] studied the thermomechanical responses of shock-compacted HMX in a set of numerical simulations (HMX is the high melting explosive cyclotetramethylene-tetranitramine; its chemical composition is $C_4H_8N_8O_8$). Up to this point, numerical simulations assumed simplified microstructures (i.e., particles were modeled as spheres or cylinders). However, it is known that many particulate phases, especially ceramics, are poorly represented by simple geometries. This is an important consideration, as the underlying geometry of the constituent phases has a strong influence on failure mechanisms and thermomechanical responses at the mesoscale. Benson and Conley explored the effects of not making these geometric simplifications. Finite element simulations were performed on highly-resolved, digitally-imported micrographs of mixture microstructures, as shown in Figure 2-8. This ensured that the starting microstructure morphology was an accurate representation of the actual 2-D geometry.

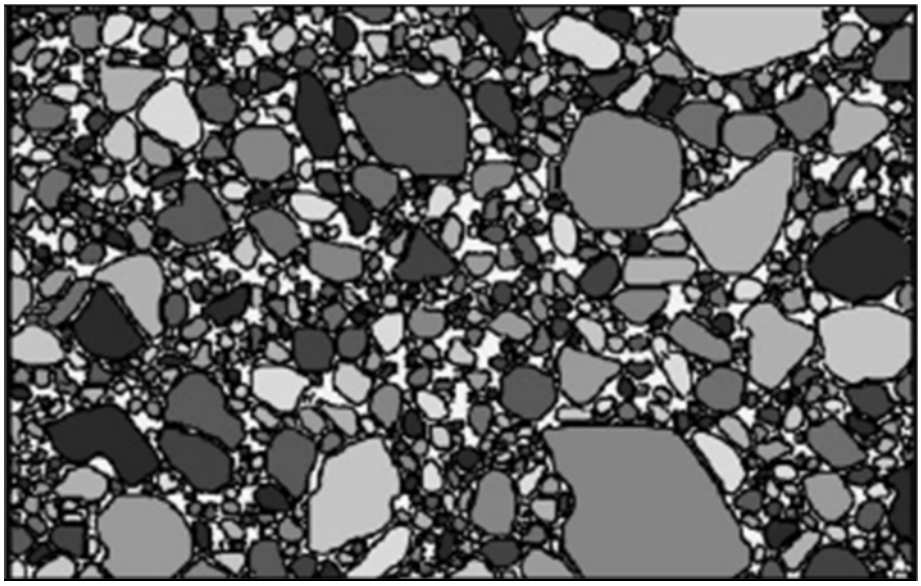

Figure 2-8. The initial configuration of a digitally-imported HMX microstructure (illustration taken from ref. [45]).

In these simulations, the polymer binder was removed so that only the powder was subjected to the shock wave (i.e., the binder was replaced by voids). At the time of this study, accurate material properties and constitutive laws were not available for HMX. Approximate material properties and assumed stress-strain relations were implemented. Again, peak temperatures were observed near particle boundaries; however, it is interesting to note that the depth of elevated temperatures is independent of particle size. Heat conduction near void-collapsed regions was insignificant due to the short time scales involved in these calculations. In this study, the Merzhanov criterion [46] was used to predict microscale reaction initiation. This criterion is based on the local time rate of change of the thermal energy. It was projected that sustained reactions will initiate at local hot spots when heat generation from chemical reactions outpaces conductive losses to the surroundings. Some of the hot spots observed in this study were of sufficient size and temperature to initiate chemical reactions. The effects of including a viscous stress term in the total stress tensor were evaluated. As expected, levels of inelastic deformation and jetting were considerably higher for the inviscid case because the material was more prone to flow (please refer to Figure 2-9). This led to substantial temperature increases at particle

junctions in the inviscid case. Consequently, inviscid calculations are more likely to satisfy the reaction initiation criterion.

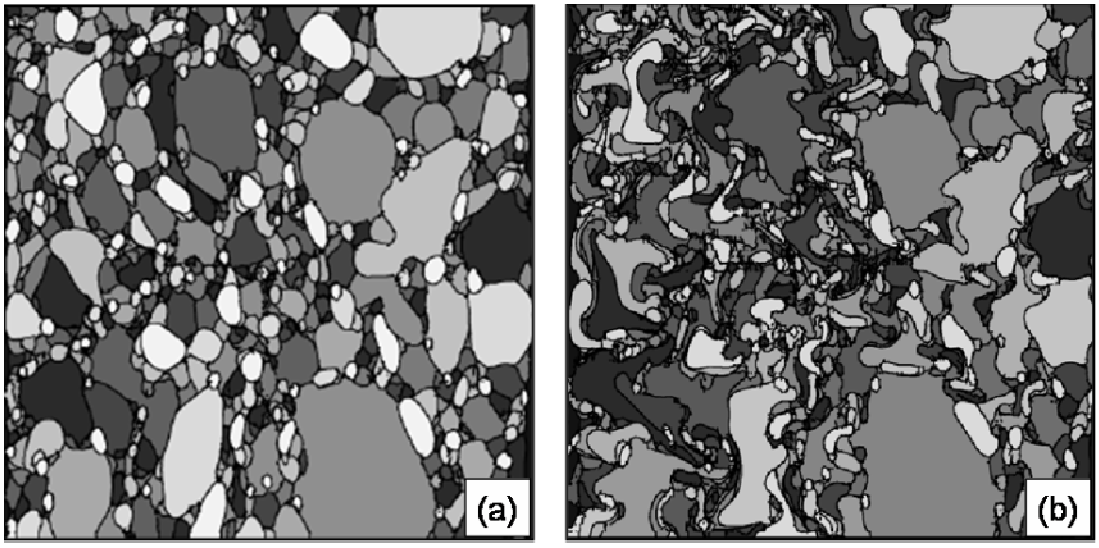

Figure 2-9. Post-shock microstructure morphologies in the HMX system for (a) the viscous case and (b) the inviscid case; shock waves were generated by applying a particle velocity (U_P =1.0 km-s^{-1}) to the left boundary of the microstructure (illustrations taken from ref. [45]).

2.8 The sensitivity of reaction initiation to hot spots

Various methods have been proposed for the quantification of reaction thresholds. However, no unique parameter has been found to describe 'universal' reaction initiation thresholds at the macroscale. The initiation of reactions is highly dependent on the material system. Batsanov et al. [47] and Iyer et al. [48] observed pressure thresholds in the Sn-S and Ni-Al systems, respectively. One may recall that Krueger et al. [16] proposed a thermal energy threshold for the Ni-Si system, and Meyers et al. [18] proposed a threshold based on configuration changes (melting) in the Nb-Si system. Current experimental evidence from Thadhani and co-workers [6, 7] supports the notion that reaction initiation is closely tied to coupled thermal and mechanical responses at the particle level. This claim is further substantiated by tracing reaction sources to hot spots formed in void-collapsed regions of

polymer-boned explosives (PBX) [49]. Void collapse serves as a potent source of heat generation in porous materials. The severe plastic deformation encountered during void collapse induces nearly-adiabatic temperature rises in the surrounding materials. These temperatures can be high enough to overcome reaction initiation energy barriers. Thus, mixture porosity should be analyzed carefully in regard to its contribution to reaction initiation.

Reaction criteria should consider thermal energy localization and dissipation in regions of intimate reactant contact. The Merzhanov criterion is attractive in this regard, as it takes into account the competing effects of heat generation due to chemical reaction and heat losses due to conduction.

Two approaches are available for modeling reaction initiation: thresholds may be assumed *a priori* or calculated *a posteriori*. If reaction thresholds are assumed *a priori*, reaction kinetics are not included after initiation; simulations are conducted to see if the reaction criteria are satisfied. Alternatively, thresholds may be calculated in simulations *a posteriori*; in this approach, reaction kinetics are coupled with the thermal and mechanical interactions after initiation. Reaction thresholds are calculated by tracking changes of pressure and temperature, among other parameters.

2.9 The inclusion of reaction kinetics in numerical simulation

Do and Benson [50, 51] presented a methodology for modeling spatially-resolved SICRs in the Nb-Si system with reaction kinetics after initiation. The Eulerian finite element methods, established by Benson in previous studies, were extended to model chemical reactions of the type: $A + B \rightleftharpoons C$. Here, the mechanical, thermal, and chemical processes were fully coupled. The thermal conductivity of the constituents was modeled with Fourier's law. Reaction kinetics were modeled with a modified Arrhenius equation (augmented temperature and pressure dependencies). Chemical reactions were modeled independently in each element, where product phases formed between reactants. This approach introduced a fundamental restriction to the simulations: once all of the reactants are used up in an element, the reaction is 'numerically quenched'. Reaction quenching was avoided by introducing a mass diffusion mechanism through the reaction product layer. Typically, the diffusion rate is a function of the gradient of material species content. However, experimental observations in the Nb-Si system indicated that the extent of the reaction was not limited by a transport mechanism, and the transport rate was

much higher than those predicted by traditional diffusion mechanisms (recall the 'ejection' reaction mechanisms from Meyers et al. [18]). The transport algorithm implemented here represented an infinite transport rate, which is to say unconsumed reactants are transported through the product layer instantaneously.

The initiation and propagation of reactions were tracked by monitoring a set of state variables (i.e., particle velocity, temperature, pressure) and the microkinetic energy. Inert mixtures displayed fairly constant profiles of the state variables. Reactive mixtures exhibited increases in the state variables as the calculation proceeded. Increasing spikes in the microkinetic energy were observed directly behind the shock front, which indicated higher levels of turbulent mixing due to chemical activity. Calculations showed that the reaction front followed the shock front closely, inferring that reactions were shock-induced rather than shock-assisted; however, this may be an artifact due to the use of an instantaneous transport mechanism rather than the true underlying reaction propagation kinetics of the system. The threshold energy (~500 kJ-kg^{-1}) for reaction initiation in the Nb-Si system was calculated, as in Eq.(2.1), for saturated product mass fractions. This threshold was lower than that predicted by Meyers et al. [18] because the effects of plastic deformation, viscous dissipation, and fracture were not taken into account.

CHAPTER 3
SYNTHETIC MICROSTRUCTURE GENERATION

An objective of this research is to observe and predict the local thermo-mechano-chemical responses of RPMMs based on mixture parameters that may be varied (e.g. particle size, phase content). Therefore, it is necessary to implement algorithms that synthetically generate realistic microstructures (particle distributions) based on a set of prescribed mixture parameters. An ability to generate such microstructures will allow material designers to explore performance ranges intermediate to and perhaps beyond those considered experimentally.

It is highly desirable that techniques used to generate synthetic microstructures are automated. Automated techniques facilitate the efficient exploration of (i) a wide range of mixture morphologies, and (ii) the variability in responses of systems that are generated randomly with identical mixture parameters. The manual execution of such tasks would be burdensome.

In order to simulate particulate shock compression as accurately as possible, it is essential that the geometry and statistical measures pertaining to the actual microstructures are respected during microstructure reconstruction. The sections that follow discuss the morphological features and stereological measures that are used to quantify the microstructures, and the techniques used to reconstruct synthetic microstructures.

3.1 Actual microstructures

The constitutent solid phases of the polymer-bonded Al+Fe_2O_3 thermite system are aluminum particles (Al-1100), agglomerates of iron oxide particles (Fe_2O_3), and the epoxy matrix (Epon 828). Pores are interspersed throughout the microstructure.

Particle mixtures will be identified by the weight percent (wt%) of epoxy contained in the microstructure. For example, a particle mixture that contains 50% epoxy by weight will be referred to as a 50 wt% mixture. Unless stated otherwise, it is assumed that the volume fractions of reactants in the actual and synthetic microstructures are in stoichiometric proportions (assuming complete reaction).

Micrographs of non-planar fracture surfaces from a 50 wt% mixture and a 20 wt% mixture are shown in Figure 3-1 and Figure 3-2, respectively. The smooth, large entities are

aluminum particles. The smaller, granular entities are iron oxide agglomerates. The dark regions are epoxy. Voids (pores) are present, but are difficult to differentiate from the epoxy phase. It should be noted that the iron oxide agglomerates are comprised of approximately 3–5 subparticles.

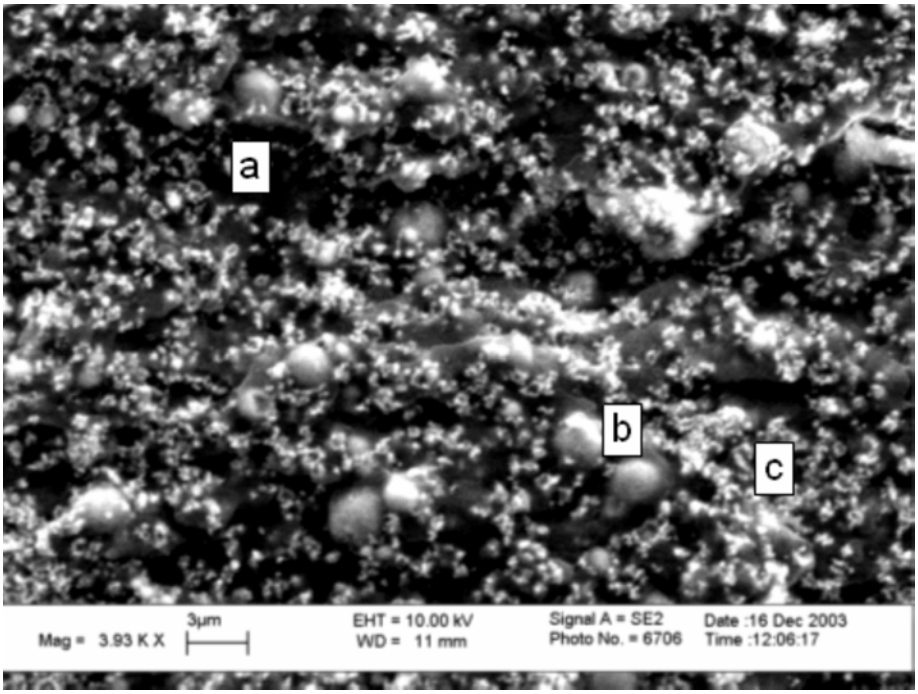

Figure 3-1. SEM micrograph of a 50 wt% mixture. Markers indicate: (a) epoxy, (b) aluminum particles, and (c) iron oxide agglomerates.

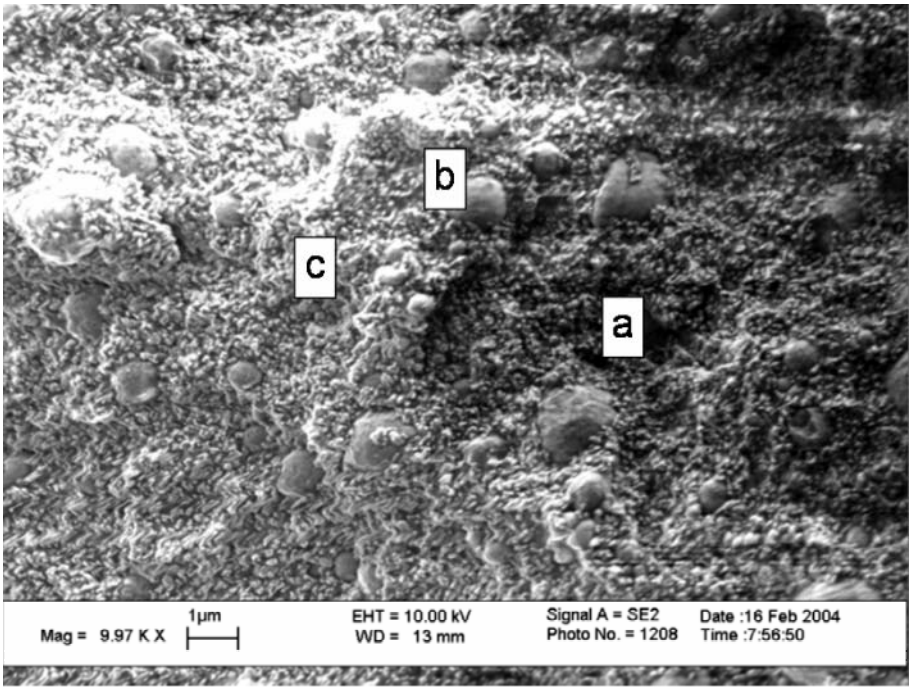

Figure 3-2. SEM micrograph of a 20 wt% mixture. Markers indicate: (a) epoxy, (b) aluminum particles, and (c) iron oxide agglomerates.

3.2 Stereological measures

Stereological measures are used to quantify the morphology of a microstructure [52]. In this work, the measures used to characterize actual and synthetic microstructures are size distributions and nearest-neighbor distributions.

Size distributions are fairly straight forward; such distributions define the probability of finding a particle of a given size (diameter). Nearest-neighbor distributions are 2-point correlations that provide statistics pertianing to the proximity of two entities. For example, the first nearest-neighbor (NN1) distribution defines the probability of finding a given entity's closest neighboring entity over a range of distances.

Stereological measures are useful for matching the synthetic microstructures created in models to the actual microstructures tested in experiments for model validation. However, such stereological measures can only be used as guidelines in exploration of the design space. Variations in mixture morphology will obviously cause shifts in the location and shape of the particle size distributions. Nearest-neighbor distributions will also be affected, as the relative spacing between particles is dependent on particle size. Thus, the general shape of the size distributions and nearest-neighbor distributions may be inferred from experimental microscopy and applied to mixture variations without a great loss of generality.

3.3 Microstructure reconstruction

The techniques pertaining to the methods used to generate synthetic microstructures are presented in the sections that follow.

3.3.1 Mixture parameters

In this work, the morphology of a particle distribution is characterized by a set of specified mixture parameters. Mixture parameters include:

1. The planar dimensions ($\mathbb{X}$, $\mathbb{Y}$) of the statistical volume element (SVE).
2. Volume fractions (V_f) of each phase.
3. The location (m) and shape (s) parameters of the lognormal particle size distributions, which are related to the expected values and vaiances of the particle radii.

Variations in the above parameters enable the simulation of a wide range of particle mixtures.

3.3.2 Approximation of the mixture geometry

The geometry of the actual microstructure is quite complex. The individual iron oxide subparticles exhibit a block-like rectangular shape, as shown in Figure 3-3; however, the shapes of the iron oxide agglomerates formed by these subparticles are difficult to quantify. The exact pore geometry is unknown, as this phase is difficult to differentiate from the epoxy binder in micrographs. Fortunately, it is known that the Al particles are essentially spherical.

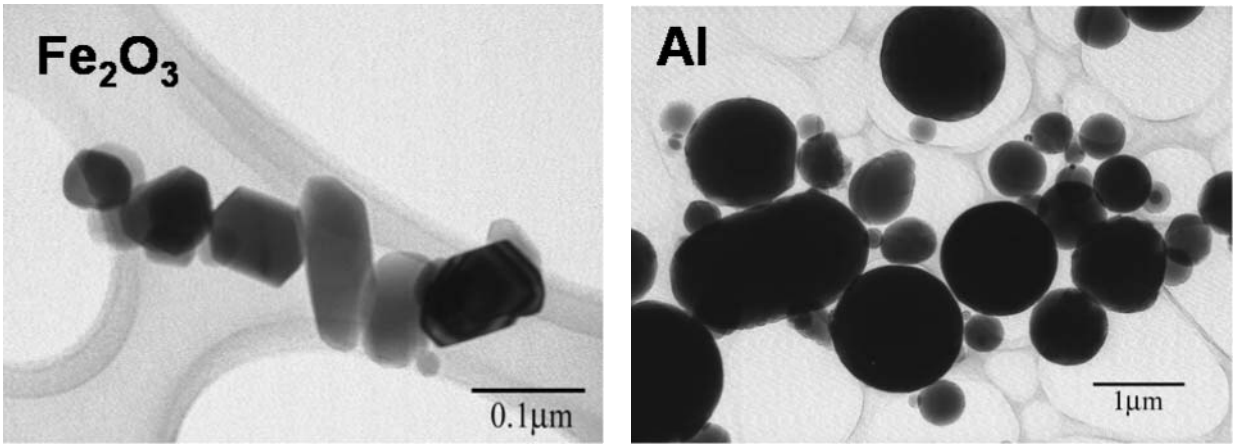

Figure 3-3. Optical micrographs of individual aluminum (Al) and iron oxide (Fe_2O_3) particles.

The complexity of the actual microstructure is simplified in the finite element models. It is assumed that the cross sections of all inclusions (e.g., particles and voids) are circular. This is a valid assumption for the Al particles, however, it is less justified for the iron oxide agglomerates. It is difficult to assess the validity of this assumption for the pores (voids). In the absence of contact with other particles, the pores should be spherical, as they are simply gas trapped in the epoxy binder, but in these microstructures, this need not be the case.

The geometry of the microstructure is further simplified by assuming a 2-D distribution of inclusions. Inclusions in the 2-D cross section are considered as cylinders in 3D, i.e., extended into the plane. This assumption is somewhat of a necessity in explicit hydrocode

calculations, as the time steps are very small. The computational expense of fully 3-D calculations is simply too large.

Volume fractions of the acual and synthetic microstructures are matched, rather than area fractions, resulting in a 2-D microstructure with an areal density of inclusions that is less than that observed in 2-D micrographs. Measurements from micrographs on arbitrary 2-D cross sections show that area fractions of Al range from 0.26–0.66 and area fractions of Fe_2O_3 range from 0.24–0.38. Generated area fractions are significantly less than those measured because particles are represented by cylinders rather than spheres in 3D. Matching area fractions is not a viable solution for two reasons:

1. Matching area fractions would drastically increase the mass density of the synthetic microstructures, which would not be an accurate representation of the mixture.
2. Area fractions that are measured in experimental micrographs are taken from a random 2-D cross-section of the microstructure. As exhibited above, area fractions of each phase display considerable amount of variability. Therefore, it is not always clear what volume fractions to include in the synthetic microstructures if this route is pursued.

3.3.3 Particle generation

Particle systems that are composed of micron-scale particles typically exhibit size distributions that are lognormal [53]. Thus, it is desirable to develop algorithms that are capable of generating particle distributions that conform to lognormal size distributions. We shall begin our discussion by introducing methods that may be used to generate large sets of 'particles' (Al particles, Fe_2O_3 agglomerates, and voids) that conform to lognormal size distributions. Many thousands of particles are contained in such distributions; in fact, the dimensions of such mixtures approach those necessary to construct a representative volume element (RVE). Our methods will be concerned with the realm of the statistical volume element (SVE), which contains substantially fewer particles than the RVE.

In constructing a particle distribution, particle sizes may be generated by taking random samples from specific lognormal distributions. This is achieved by transforming random deviates taken from a normal distribution to random deviates of a lognormal distribution.

A random variable X is said to be lognormally distributed with parameters m and s if $Y = \ln(X)$ is normally distributed with mean μ and standard deviation σ. Thus, lognormal deviates X_i are generated by transforming normal deviates Y_i via

$$X_i = \exp\{Y_i\} \tag{3.1}$$

Taking the particle radius R as the random variable ($X = \mathrm{R}$), random lognormal deviates R_i are generated as

$$\mathrm{R}_i = \exp\{\mathrm{m} + v_i \mathrm{s}\} \tag{3.2}$$

The parameters m and s are calculated as follows,

$$\mathrm{m} = \ln\left[E(\mathrm{R})\right] - \frac{1}{2}\mathrm{s}^2 \tag{3.3}$$

$$\mathrm{s} = \sqrt{\ln\left(\frac{var(\mathrm{R})}{E(\mathrm{R})^2} + 1\right)} \tag{3.4}$$

where $E(\mathrm{R})$ and $var(\mathrm{R})$ are the expected value and variance of the particle radius, respectively. The expected value and variance may be approximated from the desired data set as

$$E(\mathrm{R}) \approx \frac{1}{N}\sum_{i=1}^{N} \mathrm{R}_i \tag{3.5}$$

$$var(\mathrm{R}) \approx \frac{1}{(N-1)}\sum_{i=1}^{N} \left(\mathrm{R}_i - E(\mathrm{R})\right)^2 \tag{3.6}$$

where N is the total number of particles in a given phase.

The aforementioned method was used to generate a large 20 wt% mixture. The planar dimensions of the sample mixture were 200 $\mu\mathrm{m} \times 100$ $\mu\mathrm{m}$, and it contained approximately 50,000 particles. The range of particle sizes for a given phase was discretized into a set of bins, or classes, with a finite width. Histograms were constructed for each phase by counting the number of particle radii that fell in each bin; the results are plotted in Figure 3-4. From this example distribution, we gather that a 20 wt% mixture containing approximately 50,000 particles displays well-behaved lognormal size distributions.

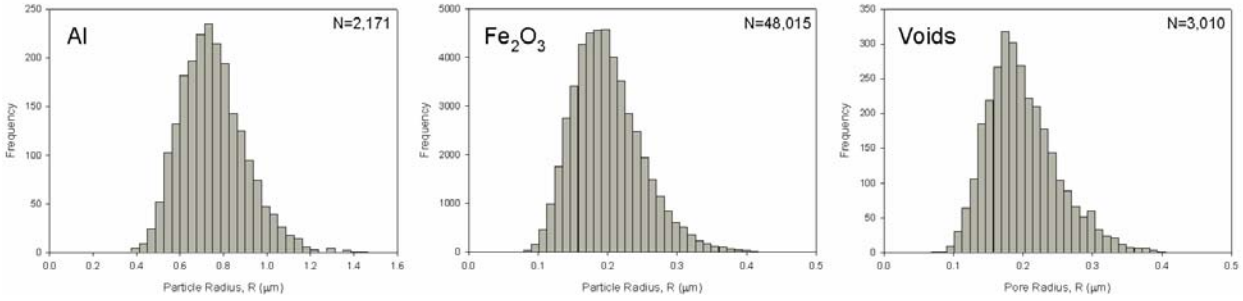

Figure 3-4. Histograms for each phase in a large 20 wt% mixture.

The simulations of shock compression are directed towards the observation of thermal, mechanical, and chemical responses that occur in random, heterogeneous media on length scales that are much smaller than the RVE (e.g., particle-level deformation, shock front propagation, and chemical activity at reactant interfaces). The dimensions of the spatial domain simulated numerically must be much smaller than the RVE, as computational resources limit the number of particles that may be included in simulations. Therefore, our analyses must be performed in SVEs, which are a fraction of the size of the RVE. The use of SVEs as an approach to modeling thermomechanical phenomena occurring at the mesoscale has been investigated by Ostoja-Starzewski [54]. The results obtained from the SVE will converge to those of the RVE as the size of the spatial domain approaches that of the RVE. For SVEs much smaller than the RVE size, a number of distinct realizations of the same microstructure are necessary to develop the statistics of the response function(s) [55].

The techniques that are used to generate the particles to be included in the SVE are identical to those used to generate large particle distributions. The only difference is that the total number of particles generated in each phase is much smaller in the SVE. The number of particles generated in the SVE is controlled by the volume fractions of the respective phases. The SVEs considered in this work will contain approximately 400–500 particles in total. The size distribution for each phase in the SVE will not appear lognormal; there simply are not enough particles included in the SVE to form any sort of relevent statictical measure. However, in the limit as the size of the SVE approaches that of the RVE, the size distributions will approach the desired lognormal distributions. In other words, if many small volume samples are taken from an RVE, none of them will display well-behaved lognormal size distributions;

however, the collection of a sufficiently large number of volume samples will display a well-behaved lognormal size distribution. The influence that the boundaries of the SVE have on the placement of particle will be discussed in section 3.3.5.

3.3.4 Definition of the placement sequence

The sequence in which the phases are placed in the SVE is an important consideration. The placement sequence affects both the likelihood of realizing a desired particle distribution and the accuracy of known spatial correlations. Two factors are used to determine the order in which the phases are placed: (1) the existence of defined spatial correlations, and (2) the expected particle radius. Phases with defined spatial correlations (e.g., nearest-neighbor distributions) are assigned top priority. These phases are placed first in order to create particle distributions that conform to the spatial correlations in actual microstructures. Computationally, it is easiest to construct such particle configurations in the absence of other phases. The remaining phases are placed in the SVE in decreasing order of the expected particle radius. The phases are placed in decreasing order of size so that the maximum volume fractions of each phase may be obtained, if desired. When the largest paritcles are located first, it is probable that adequate inter-particle space remains to accommodate the placement of the smaller particles. However, if the smaller particles are placed first, particularly in a diffuse manner, it may become extremely difficult (if not impossible) to locate the larger particles in the space that remains.

Spatial correlations are extremely difficult to measure with microscopy techniques in the polymer-bonded Al+Fe_2O_3 thermite system due to a lack of contrast between the different phases. Estimates of the first nearest-neighbor (NN1) distribution are available from the experimental mixtures for the Al phase. Unfortunately, nearest-neighbor distributions are not available for any of the other phases. According to the priorities defined above, the Al particles are always placed in the SVE first. The remaining phases are placed in decreasing order of size.

3.3.5 Techniques used to locate particle centroids

Now that the sequence of phase placement is known, we may discuss the techniques that are used to locate the centroids of the particles. The particles that were generated from the specified lognormal size distributions are added to the domain sequentially with a constrained Poisson process. A conventional constrained Poisson process involves randomly generating the

coordinates of all particle centroids, such that none of the particles overlap (this technique is also known as a random sequential addition process, cf. [56]). The constrained Poisson process used in our algorithm allows very small amounts of overlap, so that particle contact is permitted in the initial configuration. Intimate particle contact would not be permitted in the initial configuration if small amounts of overlap are not allowed, as the probability of randomly placing two circular entities in a plane that intersect at a single point is zero.

Once a particle is placed in the initial configuration of the SVE, its position is fixed for the purposes of microstructure synthesis. The Al particles are the exception to this rule, as a spatial correlation has been defined for this phase. Recall that the intial positions of the Al particles are located first. Before the particles of the other phases are located, the positions of the Al particles are shifted iteratively, using a simulated annealing technique, until spatial correlations for the Al phase in the synthetic microstructure match those estimated from experiments. The simulated annealing techniques will be discussed in section 3.4 so that the continuity of this section is maintained.

The constrained Poisson process begins with the placement of the current particle in the Cartesian plane. The coordinates of the current particle (x, y) are randomly generated from a uniform distribution,

$$(x, y) = (u_i \mathbb{X}, u_{i+1} \mathbb{Y}) \tag{3.7}$$

Here, $\mathbb{X}$ and $\mathbb{Y}$ are the planar dimensions of the SVE, and u_i is a random uniform deviate on the interval [0,1]. Since $u_i \in [0,1]$, particle centroids always fall within the bounds of the SVE.

The current particle must satisfy a set of conditions before it is located successfully, i.e.,

1. Excessive particle overlap must be avoided.
2. Adequate spacing must be maintained around the perimeter of non-contacting particles.

The position of the current particle is checked against all previously-located particles to ensure that these conditions are satisfied. The implementation of these conditions is discussed next.

In our discussion of the required geometric conditions, it will be easiest to consider the restricted cases, i.e., those in which the candidate particle centeroid must be rejected. In regard to the first condition, the amount of particle overlap must be limited to a small value. Stated mathematically, if the following condition holds,

$$d_{ij} < \mathrm{R}_i + \mathrm{R}_j - \hat{\delta} \tag{3.8}$$

the current particle centeroid is rejected. Here, R_i and R_j are the radii of particles i and j, respectively. The value of $\hat{\delta}$ is calculated as

$$\hat{\delta} = \min\left(\hat{\delta}_G, \alpha \mathrm{R}_{\min}\right) \tag{3.9}$$

where $\hat{\delta}_G$ is the global value of the parameter $\hat{\delta}$, α is a specified parameter ($0 < \alpha < 1$), and $\mathrm{R}_{\min} = \min\left(\mathrm{R}_i, \mathrm{R}_j\right)$. The maximum value of $\hat{\delta}$ is limited to a fraction of the minimum radius of the contacting particles, to avoid large amounts of overlap when dealing with the smallest of particles.

In regard to the second condition, the space between the surfaces of two non-contacting particles must be greater than a specified distance. Stated mathematically, if the following condition holds,

$$0 < d_{ij} - \left(\mathrm{R}_i + \mathrm{R}_j\right) < \beta \hat{\delta}_G \tag{3.10}$$

the current particle centeroid is rejected. Here, β is a specified parameter $0 < \beta < 1$. The lower bound in Eq. (3.10) is necessary so that contacting particles that satisfy the first condition are not rejected. The second condition is imposed so that thin layers of epoxy are not trapped in-between particles; not only would this be physically unrealistic (due to the viscosity of the epoxy before it cures), it would also create numerical instabilities during shock loading, as large strains would develop in the relatively compliant epoxy phase as it is compressed between two substantially stiffer phases.

An illustration of the geometric conditions is provided in Figure 3-5. Here, a set of four different particle configurations is depicted. The scales of the particle geometry have been exaggerated for clarity.

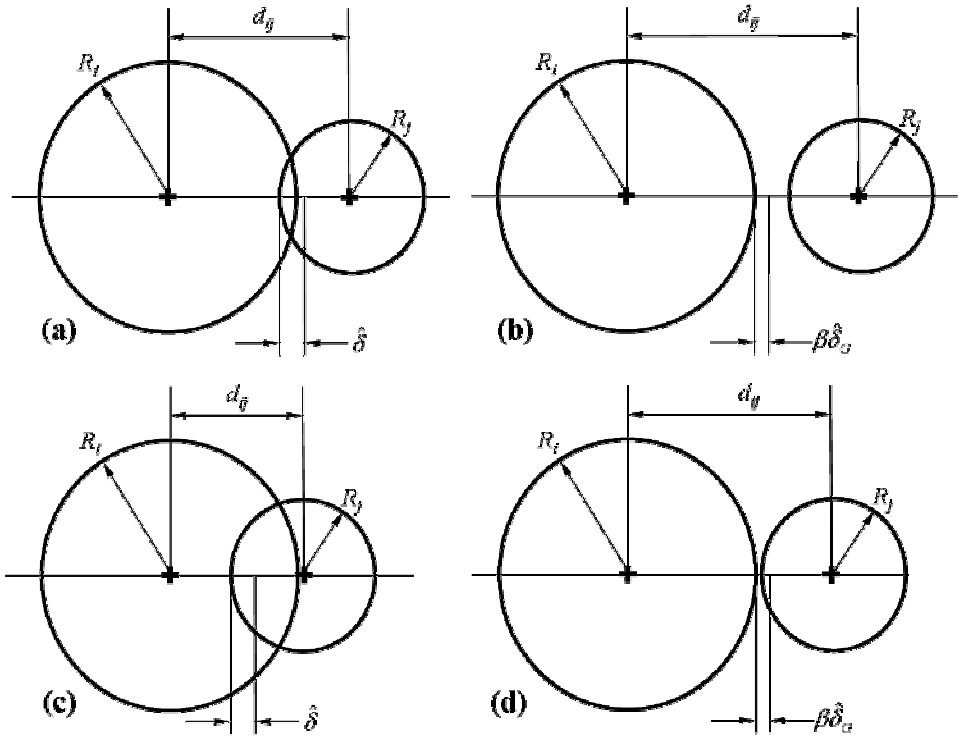

Figure 3-5. Permissible geometries are depicted in (a) and (b); restricted geometries are depicted in (c) and (d). The following conditions are illustrated: (a) $d_{ij} > \mathrm{R}_i + \mathrm{R}_j - \hat{\delta}$ **; (b)** $d_{ij} > \mathrm{R}_i + \mathrm{R}_j + \beta\hat{\delta}_G$ **; (c)** $d_{ij} < \mathrm{R}_i + \mathrm{R}_j - \hat{\delta}$ **; (d)** $d_{ij} < \mathrm{R}_i + \mathrm{R}_j + \beta\hat{\delta}_G$ **.**

The values of the parameters used to control particle contact in the synthetic microstructures are provided in Table 3-1. The values of the parameters were selected to allow relatively small amounts of particle overlap and to maintain a relatively small spacing between non-contacting particles. The maximum permissible amount of overlap associated with the largest particles was selected to be approximately 5% of the particle diameter; this provides a first approximation of the value of $\hat{\delta}_G$. The value of α was selected to limit the maximum permissible amount of overlap associated with the smaller particles to 10% of the particle diameter (20% of the particle radius). The value of β sets the spacing between non-contacting particle surfaces to a fraction of the permissible overlap associated with the largest particles. The values of the parameters were tuned to obtain particle distributions that seemed physically reasonable.

Table 3-1. Particle contact parameters

Parameters	Units	
$\hat{\delta}_G$	μm	0.09
α		0.20
β		0.80

It is now necessary to consider the treatment of particles that intersect the boundaries of the SVE. The boundaries of the SVE are, in effect, modeled as planes of symmetry. Thus, the volume of a particle that intersects a boundary of the SVE is reflected across the associated plane of symmetry. This introduces an artifact to the reconstruction process: the geometry of a particle reflected across a plane of symmetry is distorted, i.e., its cross section is no longer circular. A small amount of error is introduced into the calculations of the volume fractions of the SVE, as corrections are not applied for the increased particle volumes reflected about the boundaries. It should be noted that the conditions of particle contact outlined above also apply to particles that intersect the SVE boundaries. The use of periodic boundary conditions about the periphery of the SVE would, perhaps, be more appropriate; however, the algorithms required to create particle distributions amenable to the use of periodic boundary conditions are somewhat more complicated than those considered here.

3.3.6 Material definition in the spatial domain

The primary geometric features of the particle distribution have now been defined: the sizes of all particles are known, and the locations of all particle centroids have been determined. However, the mixture created thus far has not been defined uniquely (recall the allowance of particle overlap). The exact geometry of the particle distribution must now be defined in the spatial domain.

Particle geometry is defined in two steps: (1) any material occupying the area of the current particle is removed, and (2) the material of the current particle is assigned to the spatial domain. Therefore, the current particle will form an indent in any contacting neighbors that have already been defined. Future algorithms reconstruct the interface between contacting particles with a set of straight lines; therefore, contacting particles form mulit-faceted surfaces, which is a reasonable assumption. A schematic of intimate particle conact is provided in Figure 3-6.

The sequence in which the phases are defined in the spatial domain is an issue that warrants consideration. The void phase is always defined first; if this were not the case, the voids would form indents at the surfaces of any contacting particles defined beforehand. After the voids have been defined, the remaining particulate phases are defined in increasing order of size. This is done so that small particles do not form sharp indents in the larger particles (i.e., indents with a small radius of curvature). After all particles have been defined, the epoxy phase is assigned to areas not occupied by particles.

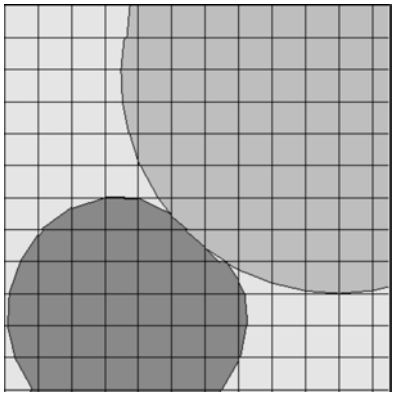

Figure 3-6. The geometry of particle contact.

3.4 Simulated annealing

This section is a supplement to the previous section (3.3.5) on techniques used to locate particle centroids.

Simulated annealing [57] is a computational technique that can be used to find the global minimum (minima) in a general combinatorial problem. In regard to this work, the global minimum that is sought is the difference between the first nearest-neighbor (NN1) distribution for the Al phase in the actual and synthetic microstructures. Simulated annealing can be used for other spatial correlations (e.g., second nearest-neighbor distributions) if the appropriate experimental data are available.

3.4.1 A thermodynamic analogy

The foundations of the simulated annealing technique are based on an analogy to thermodynamics, specifically the process by which molten metals at high temperatures are cooled down to a solid state. If the cooling process is slow, the atoms align themselves in a perfect crystal, which is the minimum energy state of the system. If the cooling process is rapid, a polycrystalline or amorphous structure is formed, which resides at a higher energy state. The polycrystalline structure may be considered the local energy minimum of the system; the perfect crystal may be considered the global energy minimum.

The Boltzmann probability distribution conveys the idea that the possible energy states E of a system at thermal equilibrium is distributed continuously according to

$$P(E) \simeq \exp\{-E/kT\} \tag{3.11}$$

where k is the Boltzmann constant, and T is the equilibrated temperature of the system. Metropolis et al. [58] postulated that a thermodynamic system, offered a new configuration with energy E', would accept the new configuration with probability $P = \exp\{-(E' - E)/kT\}$. If $E' \leq E$, then $P \geq 1$, so the updated configuration is always accepted. If $E' > E$, the updated configuration is accepted conditionally. This process corresponds to always accepting configuration changes that decrease the energy, and sometimes accepting configuration changes that increases the energy, based on the current temperature of the system. Configuration perturbations that increase the energy of the system are permitted conditionally so that the system does not become trapped in a local minimum; this allows the global minimum of the system to be found.

To extend the simualted annealing technique to a general system (e.g., a distribution of particles), the following information must be provided:

1. A description of the system configuration.
2. A generator of random changes to the system configuration.
3. An objective function for which a global minimum is sought (analagous to the energy).
4. A control parameter (analagous to the temperature).
5. An annealing schedule that describes how the control parameter is lowered from high values to low values.

We seek to evolve the NN1 distribution for the Al phase in the initial configuration of the synthetic microstructure to the distribution observed in actual microstructures. In the context of simulated annealing, the system configuration is described by the centroid locations of the Al particles. Incremental shifts in the locations of the centroids will serve as the random changes to the system configuration. The objective function will be defined as a measure of the deviation of the NN1 distribution in a synthetic microstructure from the NN1 distribution in an actual microstructure. The control and implementation of this process will be discussed next.

3.4.2 The nearest-neighbor distribution in actual microstructures

The stereological measures that are to be annealed must be specified based on experimental data. At this time, only estimates of the NN1 distribution are available from experiments [30] due to difficulties in resolving the different mixture phases using optical microscopy. It is estimated that the NN1 distributions in the actual microstructures are normally distributed with mean $\mu \sim 3.5$ μm and standard deviation $\sigma \sim 0.5$ μm. A continous normal probability distribution was constructed based on the aforementioned paramters. However, a discrete probability distribution is needed to compare the model calculations of the NN1 distribution to the experimental distribution. A discrete probability distribution was constructed by discretizing the domain of the NN1 distribution and evaluating the normal curve at a set of evenly-spaced points. The normal discrete probability distribution is given as

$$P\left[d_i \,\middle|\, (d_i - \Delta d/2) < d_i \le (d_i + \Delta d/2)\right] = a_{NN} \exp\left\{-\frac{1}{2}\left(\frac{d_i - \mu}{\sigma}\right)^2\right\}, \quad i = 1 \ldots N_d \tag{3.12}$$

Here, d is the distance from a given Al particle centroid to the centroid of its closest neighboring Al particle, N_d is the number of bins selected for the discretization of the NN1 distribution, Δd is the width of the bins used in the discretization, and a_{NN} is a scaling parameter selected so that the probabilities associated with each value of d sum to unity. A graphical representation of the estimated discrete probability distribution is depicted in Figure 3-7. The shaded bars in Figure 3-7 represent the probability that a given Al particle's closest neighbor (also an aluminum particle) is within that distance interval.

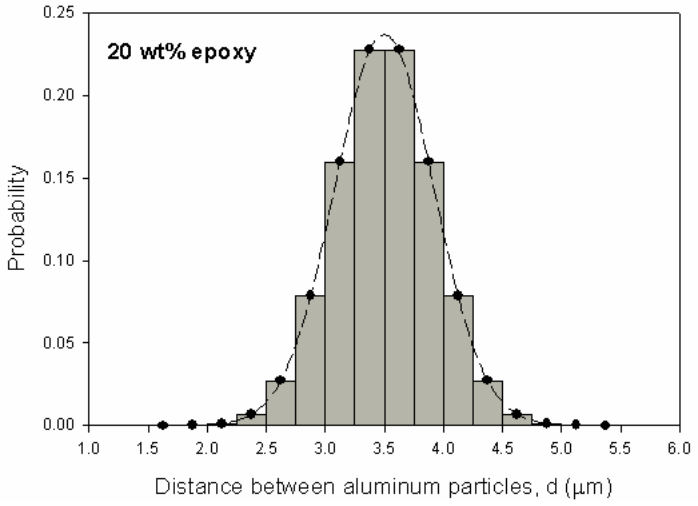

Figure 3-7. First nearest-neighbor (NN1) distribution estimated from experiments for the Al phase.

3.4.3 The nearest-neighbor distribution in synthetic microstructures

The intial positions of the Al particles were determined using the constrained Poisson processs described in section 3.3.5. The NN1 distribution in the synthetic micostructure is constructed in a series of steps:

1. The domain of the NN1 distribution is dicretized into a set of bins of finite width Δd .
2. The shortest centroid-to-centroid distance d between a given Al particle and its closest neighboring Al particle is calculated for all Al particles.
3. The particles are placed in the appropriate bin based on their value of d .
4. The number of Al particles in each bin is divided by the total number of Al particles in the full distribution to yield the probability associated with each bin.

Initial calculations of the NN1 distribution in models do not agree with normally-distributed experimental estimates, as shown in Figure 3-8. We must now quantify the differences between the spatial correlations in the synthetic and actual microstructures.

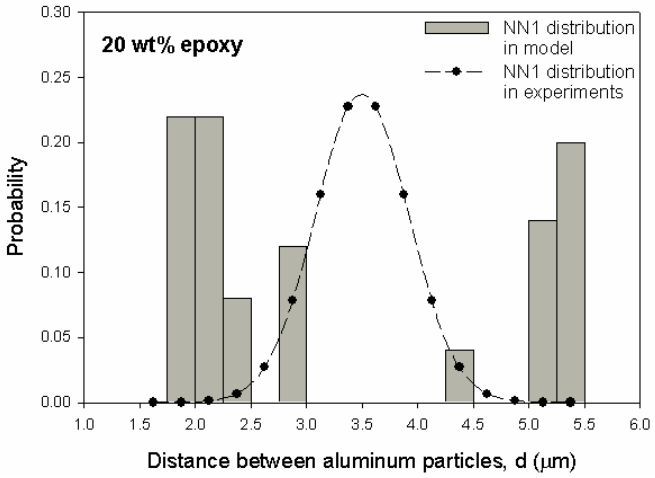

Figure 3-8. Initial calculation of the first nearest-neighbor (NN1) distribution in a synthetic microstructure.

3.4.4 Definition of the objective function

An objective function that is to be minimized must be constructed for use in the simulated annealing technique. In the case of the particle distributions, we seek to minimize the deviation of the NN1 distribution in the synthetic microstructure from that of the actual microstructure. Therfore, a measure of the aforementioned deviation must be defined. A cumulative measure of the deviation e_{NN} is defined as

$$e_{NN} = \sqrt{\sum_{i=1}^{N_d} \left(P(d_i)\big|_{syn} - P(d_i)\big|_{act} \right)^2} \tag{3.13}$$

where $P(d_i)\big|_{syn}$ and $P(d_i)\big|_{act}$ are the probability values of the NN1 distribution in the synthetic and actual microstructures, respectively. Calculations of e_{NN} in the initial configuration of the 20 wt% mixtures yield relatively large values (e_{NN} ~0.60–0.70). The goal of the simulated annealing technique is to adjust the configuration of the Al particles, in a random manner, until the objective function reaches a global minimum. Ideally, e_{NN} would approach zero.

3.4.5 Adjustment of particle centroids

It is now necessary to define the algorithms that are used to randomly adjust the spatial locations of the Al particles. The following steps are involved:

1. A subset of particles is selected for adjustment.
2. The centroid locations of the subset of particles are shifted.
3. The objective function is re-calculated for the new configuration.
4. The adjustment is accepted or rejected based on the new value of the objective function.
5. The configuration is updated as appropriate, and the process is repeated.

The number of particles included in the subset is 15% of the total number of Al particles contained in the particle distribution (this was calibrated through trial-and-error). The particles included in the subset are selected randomly (without replacement).

The centroid locations of the particles included in the subset are shifted randomly in the Cartesian plane. The maximum distance that a particle may be shifted in a single step is limited to half of the particle radius. Thus, the coordinates of a the shifted particle centroid (x', y') are calculated as

$$\begin{aligned} x' &= x + (R/2)\tilde{u}_i \\ y' &= y + (R/2)\tilde{u}_{i+1} \end{aligned} \tag{3.14}$$

Here, $\tilde{u}_i$ is a random uniform deviate on the interval [-1,1], which is generated as follows

$$\tilde{u}_i = 2u_i - 1 \tag{3.15}$$

The set of constraints that were utilized in the process of locating particle centroids (cf. section 3.3.5) apply here. Any shift that violates these constraints is disregarded (meaning the particle maintains is original position).

The objective function is now re-calculated based on the shifted particle configuration. The change in the objective function de_{NN} is calculated as

$$de_{NN} = e'_{NN} - e_{NN} \tag{3.16}$$

where e_{NN} and e'_{NN} are the values of the objective function before and after the centroid shift, respectively. If $de_{NN} \leq 0$, the shifted particle configuration is accepted, as it represents a successful step toward the minimization of the objective function. If $de_{NN} > 0$, the shifted particle configuration is not rejected immediately; the shifted particle configuration is accepted with a probability

$$P = \exp\{-de_{NN}/T_v\} \tag{3.17}$$

where T_v is the virtual temperature (i.e., the control parameter). At high values of T_v, the argument of the exponential is a small negative number, so it is not uncommon to accept shifts that increase the value of the objective function. As the value of T_v is lowered, the argument of the exponential grows to large negative numbers, and it becomes nearly impossible to accept shifts that increase the value of objective function. The decision whether or not to accept a shift for which $de_{NN} > 0$ is unbiased. A random uniform deviate u_i is generated on the interval [0,1]; if $u_i \le \exp\{-de_{NN}/T_v\}$, the shifted particle configuration is accepted. As mentioned earlier, shifts that cause increases in the objective function are accepted conditionally so that the algorithm does not become trapped in a local minimum.

If the shifted particle configuration is accepted, it becomes the current particle configuration, and the process repeats itself in search of a lower value of the objective function. If the shifted particle configuration is rejected, the particle configuration remains the same, and another shift is attempted.

3.4.6 The annealing schedule

The lowering of the control parameter is a key aspect of the simulated annealing algorithm. The initial value of the control paramter, i.e., the virtual temerature, is $T_v = T_{v,0}$. The virtual temperature is decremented when the number of successful configuration shifts exceeds a specified value (N_{succ}); this corresponds to conditions where it is easy to generate particle configurations that are accepted. The decremented virtual temperature T_v' is calculated by scaling back the reference value of the virtual temperature, i.e.,

$$T_v' = \beta_T T_v \tag{3.18}$$

Here, β_T is a specified scaling parameter.

The simulated annealing process is terminated after one of two conditions is satisfied:

1. At a given value of T_v, no successful shifts to the particle configuration are achieved for the maximum permissible number of attempts (N_{att}).
2. The number of temperature decrements exceeds a specified value (N_{dec}).

The values of the simulated annealing parameters are provided in Table 3-2. The values of the parameters were calibrated through a trial-and-error process to obtain particle distributions with the lowest values of the objective function.

Table 3-2. Simulated annealing parameters

Parameters	Units	
$T_{v,0}$	–	100
N_{succ}	–	100
β_T	–	0.95
N_{att}	–	10^5
N_{dec}	–	300

The final value of e_{NN} for the NN1 distributions in the annealed 20 wt% mixture (e_{NN} ~0.10) is considerably smaller than its initial value. Small distributions of Al particles induce larger deviations; thus, it is desirbale to have at least 12–15 Al particles included in a given SVE. The NN1 distributions of the Al phase before and after simulated annealing are depicted in Figure 3-9.

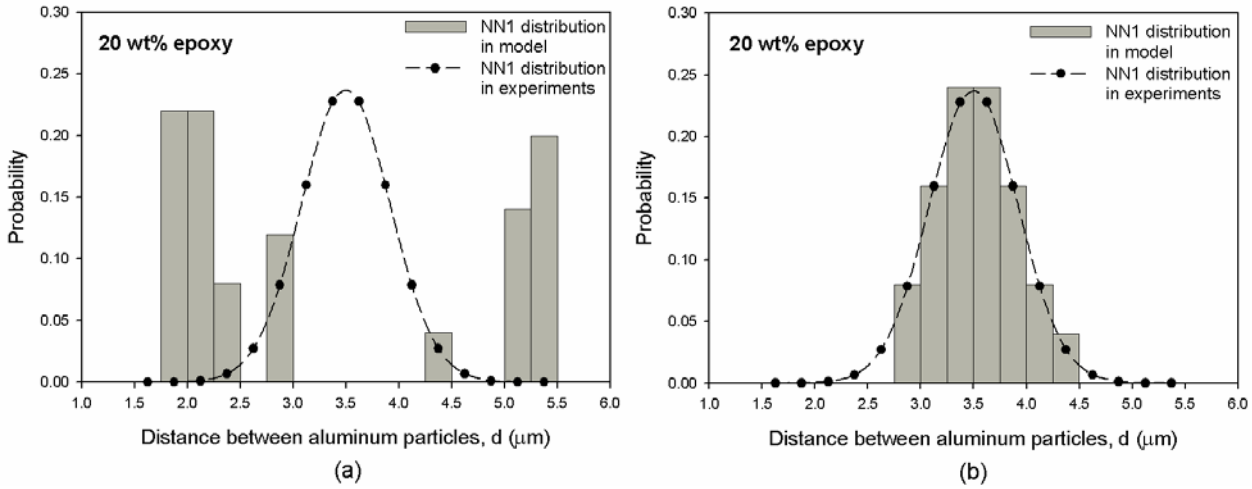

Figure 3-9. First nearest-neighbor (NN1) distributions calculated in a synthetic microstructure (a) before and (b) after simulated annealing.

3.5 The final synthetic microstructures

Two mixture classes were selected for this study. The first class corresponds to RPMMs that have been tested experimentally with 50% epoxy by weight. The second class corresponds to RPMMs that will be fabricated and tested in future experiments with 20% epoxy by weight.

The mixture parameters used to generate microstructures for simulation are given in Table 3-3. The volume fractions of reactants are in stoichiometric proportions for the mixtures defined below. Even though each weight class is simulated with the same mixture parameters, every simulation will be unique due to the random techniques used to generate the microstructures. In other words, our analyses address the stochasticity of the microstructure.

Table 3-3. Mixture parameters for simulated microstructures

wt% epoxy	Material	Expected Particle Radius, $E(R)$ (μm)	Variance in Particle Radius, $var(R)$ (μm)	Volume Fraction
20	Al	0.75	22.5×10^{-3}	0.21
	Fe_2O_3	0.20	2.5×10^{-3}	0.31
	Voids	0.20	2.5×10^{-3}	0.02
50	Al	0.75	22.5×10^{-3}	0.09
	Fe_2O_3	0.15	0.9×10^{-3}	0.13
	Voids	0.15	0.9×10^{-3}	0.02

3.5.1 Class I: 20 wt% epoxy

The components of the final SVE for a model 20 wt% mixture are shown in Figure 3-10.

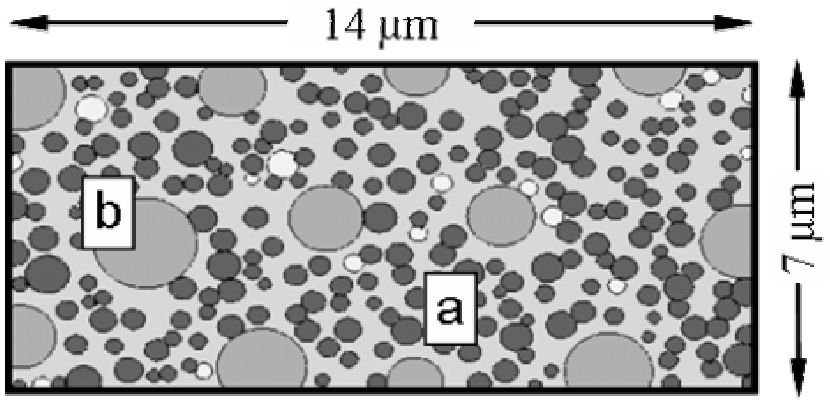

Figure 3-10. A typical 20 wt% synthetic microstructure. Markers indicate: (a) Fe_2O_3 agglomerates and (b) Al particles; the white circular entities are voids.

3.5.2 Class II: 50 wt% epoxy

The components of the final SVE for a model 50 wt% mixture are shown in Figure 3-11.

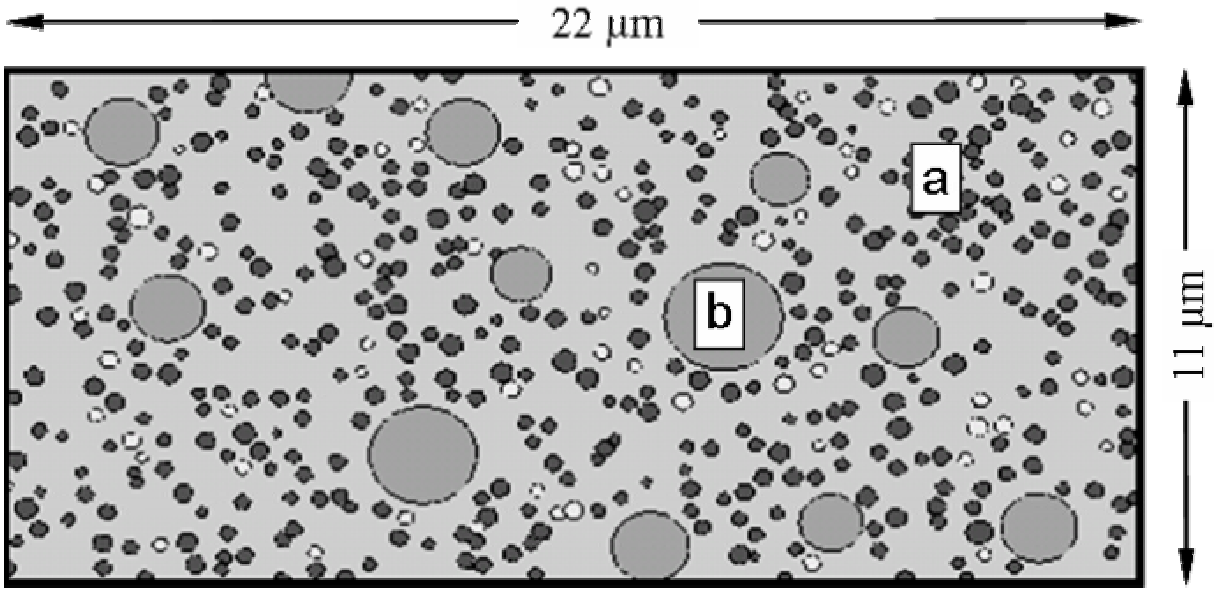

Figure 3-11. A typical 50 wt% synthetic microstructure. Markers indicate: (a) Fe_2O_3 agglomerates and (b) Al particles; the white circular entities are voids.

CHAPTER 4
THE EULERIAN FINITE ELEMENT METHOD

The finite element simulations are performed in the 2-D multi-material Eulerian hydrocode, Raven [1], developed by Benson. Eulerian formulations are particulaly useful in solving large deformation, finite strain problems occuring on a short time scale because they are immune to the severe element distortions that render traditional Lagrangian formulations inadequate. A concise description of the numerical techniques implemented in this work will be presented next. The primary reference of this chapter is a comprehensive review article by Benson [59] on the computational methods utilized in Lagrangian and Eulerian hydrocodes. This reference is cited at the outset, so that the flow of this discussion is not interupted by continual citation. Additional references appear in the text as necessary.

4.1 An overview of the computational sequence

Eulerian formulations are governed by the conservation of mass, momentum, and energy. The conservation equations may be cast as general transport equations, which are decoupled and solved sequentially through operator splitting. The operator split decomposes the solution into a Lagrangian step and an Eulerian step. The traditional displacement-based Lagrangian finite element method is used (with a few modifications) to advance the solution in time during the Lagrangian step. The Lagrangian mesh remains attached to the material as it deforms over the time increment. The calculations are explicit, so the detrmination of a sufficiently small time step is necessary for integration purposes. During the Lagrangian step, nuances arise from two sources: (i) the calculations are multi-material, which is to say more than one material is permitted in an element, and (ii) discontinuities associated with shock wave propagation are spatially resolved. The multi-material nature of the calculations is handled through the introduction of a mixture theory and algorithms that track material interfaces. An artifical viscosity is introduced to resolve the shock discontinuity (i.e., the shock wave front) and to yield a smooth shock profile behind the shock front. At the end of a time step, the solution is contained within the deformed Lagrangian mesh. The solution described by the Lagrangian mesh is remapped to the spatially-fixed Eulerian mesh during the Eulerian step (while time remains constant). Solution variables and material volumes are transported between the

elements, effectively reconciling the Lagrangian and Eulerian meshes. The advantage gained here is the avoidance of severe element distortions; thus, arbitrarily large deformations can be handled. The development of special techniques is obviously needed to advect solution quantities and reconstruct material interfaces during the Eulerian step.

4.2 Conventions

The derivations in this chapter make use of two systems of notation: indicial and direct. Indicial notation is used for clarity in developing the basics of the finite element method; here, generalized vectors are denoted by subscripted indices, partial differentiation is indicated by the subscripted comma notation, and the summation convention is implied unless stated otherwise. Direct notation is used in later sections for convenience, where generalized vectors are written in bold.

All derivations are constructed in the Cartesian coordinate system. The position of a point in the current configuration is denoted $\boldsymbol{x}$. The position of a point in the reference configuration is denoted $\boldsymbol{X}$. The current time is t, and the current time step is denoted Δt. Material time derivatives are indicated by a dot above the symbol. Mixed notation will sometimes be used to avoid confusion; for example, the displacement field in the current configuration is denoted $u_i(\boldsymbol{x})$. Thus, the velocity field is $\dot{u}_i(\boldsymbol{x})$ and the acceleration field is $\ddot{u}_i(\boldsymbol{x})$. Finally, quantities that are evaluated at a node or element are indicated by a subscript containing the logical coordinates of the mesh (e.g., a general solution quantity evaluted at node (j,k) is denoted $\phi_{(j,k)}$).

4.3 Governing equations

The conservation of mass (4.1), momentum (4.2), and energy (4.3) serve as the governing equations in the Eulerian finite element method, i.e.,

$$\frac{\partial \rho}{\partial t} + \nabla \cdot \left(\rho \dot{\boldsymbol{u}} \right) = 0 \tag{4.1}$$

$$\frac{\partial \rho \dot{\boldsymbol{u}}}{\partial t} + \nabla \cdot \left(\rho \dot{\boldsymbol{u}} \otimes \dot{\boldsymbol{u}} \right) = \nabla \cdot \boldsymbol{\sigma} + \rho \boldsymbol{b} \tag{4.2}$$

$$\frac{\partial \rho e}{\partial t} + \nabla \cdot \left(\rho e \dot{\boldsymbol{u}} \right) = \boldsymbol{\sigma} : \dot{\boldsymbol{\varepsilon}} \tag{4.3}$$

Here, ρ is the mass density, $\boldsymbol{\sigma}$ is the Cauchy stress tensor, $\boldsymbol{b}$ is the specific body force vector (per unit mass), e is the specific internal energy (per unit mass), and $\dot{\boldsymbol{\varepsilon}}$ is the strain rate tensor (rate of deformation tensor).

4.4 Operator splitting

The governing equations may be expressed in a generalized transport form

$$\frac{\partial}{\partial t}\phi + \dot{\boldsymbol{u}} \cdot \nabla \phi = \Phi \tag{4.4}$$

where the quantity ϕ represents a generalized solution variable and Φ is a source term. Operator splitting is a method of decoupling the material transport from the governing equations. The generalized transport equation is decomposed into the following terms

$$\frac{\partial}{\partial t}\phi = \Phi \tag{4.5}$$

$$\frac{\partial}{\partial t}\phi + \dot{\boldsymbol{u}} \cdot \nabla \phi = 0 \tag{4.6}$$

Thus, the governing differential equations are replaced by sets of equations that can be solved sequentially. This solution technique involves two steps: a Lagrangian step, defined by Eq. (4.5), and an Eulerian step, defined by Eq. (4.6). The Lagrangian step, which is performed first, advances the solution in time. The Eulerian step, which is performed afterwards, accounts for material transport.

4.5 The Lagrangian step

The use of operator splitting requires the spatial domain to be discretized by two computational meshes (Lagrangian and Eulerian) that are coincident at the beginning of a time step. During the Lagrangian step, the Lagrangian mesh remains attached to the material as it deforms. In a continuum framework, where the generalized solution variable ϕ is replaced by $\rho\dot{\boldsymbol{u}}$ and the source term Φ is replaced by $\nabla \cdot \boldsymbol{\sigma} + \rho \boldsymbol{b}$, Eq. (4.5) may be solved using a traditional Lagrangian formulation based on the principle of virtual work. Indicial notation is used in the sections that follow.

4.5.1 The principle of virtual work

The finite element method is based on the weak form of the momentum equation. The weak form is constructed by starting with the strong form of the equilibrium equation,

$$\sigma_{ij,j} + \rho b_i = \rho \ddot{u}_i \tag{4.7}$$

and a set of boundary conditions. The boundary conditions considered in this derivation are specified displacement fields or surface tractions, i.e.,

$$\begin{aligned} u_i(\boldsymbol{X},t) &= g_i(\boldsymbol{X},t) \quad on\ \Gamma_u \\ t_i &= \sigma_{ij} n_j \qquad\quad on\ \Gamma_t \end{aligned} \tag{4.8}$$

Here, g_i is the specified displacement field that is applied to the Γ_u-boundary, t_i is the surface traction applied to the Γ_t-boundary, and n_j is the surface normal. Contact inequality constraints are not considered because they will not be used in future calculations. Concentrated point forces are omitted as well; realistically, such forces should be resolved as surface tractions. The equilibrium equation and boundary conditions may be rearranged and combined as follows

$$\int_V \left(\rho \ddot{u}_i - \sigma_{ij,j} - \rho b_i\right) dV + \int_{\partial V} \left(\sigma_{ij} n_j - t_i\right) d\Gamma = 0 \tag{4.9}$$

where V represents the integration volume, and ∂V represents the bounding surface of V. An arbitrary displacement δu_i, subject to the constraint that $u_i + \delta u_i$ satisfies the boundary conditions (i.e., $\delta u_i = 0$ at the boundary), is referred to as an admissible virtual displacement. A solution for the displacement field that satisfies the equilibrium equation and the boundary conditions will also satisfy

$$\int_V \left(\rho \ddot{u}_i - \sigma_{ij,j} - \rho b_i\right) \delta u_i \, dV + \int_{\partial V} \left(\sigma_{ij} n_j - t_i\right) \delta u_i \, d\Gamma = 0 \tag{4.10}$$

for any admissible virtual displacement. The product differentiation rule and the divergence theorem are specialized in this case, to construct the following equations

$$\sigma_{ij,j}\, \delta u_i = \left(\sigma_{ij}\, \delta u_i\right)_{,j} - \sigma_{ij}\, \delta u_{i,j} \tag{4.11}$$

$$\int_V \left(\sigma_{ij}\, \delta u_i\right)_{,j} dV = \int_{\partial V} \left(\sigma_{ij}\, \delta u_i\right) n_j \, d\Gamma \tag{4.12}$$

Equations (4.11) and (4.12) may be substituted into Eq. (4.10) to yield the principle of virtual work, i.e.,

$$\delta W = \int_V \rho \ddot{u}_i\, \delta u_i \, dV - \int_V \rho b_i\, \delta u_i \, dV + \int_V \sigma_{ij}\, \delta u_{i,j} \, dV - \int_{\partial V} t_i\, \delta u_i \, d\Gamma = 0 \tag{4.13}$$

Here, $\delta u_{i,j} = \delta \varepsilon_{ij}$ is the virtual strain variation. It should be noted that the stress and strain measures in (4.13) must be work conjugates [40].

4.5.2 The central difference method

The central difference method is used during the Lagrangian step to advance the solution in time. The central difference method is derived from a Taylor series expansion about the center of a time step. A general function, f, may be expressed as

$$\begin{aligned} f^n &= f^{n+1/2} - f_{,t}^{n+1/2}\left(\frac{1}{2}\Delta t\right) + \frac{1}{2} f_{,tt}^{n+1/2}\left(\frac{1}{2}\Delta t\right)^2 + \cdots \\ f^{n+1} &= f^{n+1/2} + f_{,t}^{n+1/2}\left(\frac{1}{2}\Delta t\right) + \frac{1}{2} f_{,tt}^{n+1/2}\left(\frac{1}{2}\Delta t\right)^2 + \cdots \end{aligned} \tag{4.14}$$

Here, and in the remained of this chapter, the superscript n refers to the initial time, $n+1/2$ refers to the midpoint of the time step, and $n+1$ refers to the end of the time step. Subtraction of the first equation from the second in the above equation set yields an explicit second-order accurate integration rule, i.e.,

$$f^{n+1} = f^n + f_{,t}^{n+1/2}\Delta t + O\left(\left(\Delta t\right)^3\right) \tag{4.15}$$

If the displacement is substituted for the general function f, the following relation may be used to update the position based on the velocity

$$x_i^{n+1} = x_i^n + \dot{u}_i^{n+1/2}\Delta t \tag{4.16}$$

It should be clear that the velocity must be centered in time. Applying Eq.(4.15) again, the integration rule for the velocity is obtained

$$\dot{u}_i^{n+1/2} = \dot{u}_i^{n-1/2} + \ddot{u}_i^n \Delta t \tag{4.17}$$

A discussion of the mesh is now warranted, as the spatial domain must be discretized to apply the finite element method.

4.5.3 Mesh definition

The mesh is a discrete description of the continuous spatial domain. Traditional displacement-based Lagrangian formulations utilize an unstructured mesh to minimize the number of elements and to optimize their shape. In this particular multi-material Eulerian formulation, a logically-regular mesh is used to simplify the data structure and the transport

alogrithms. As shown in Figure 4-1, a set of quadrilateral elements are formed by two sets of orthogonal, intersecting lines. The nodes are located at the intersections of the lines, which are labeled by an ordered pair (j,k). Regions bounded by the nodes are known as cells, or elements; they are identified by an average of the logical coordinates of the nodes, e.g., $(j+1/2,k+1/2)$.

Kinematic quantities (accelerations, velocities, and displacements) are calculated at the nodes. Accelerations and displacements are evaluated at the nodes; velocities, however, are interpolated to the midpoints of cell edges. Edge-centered velocities are utilized because of their ability to resolve shear flow in two elements, which is to say adjacent elements can move in opposite directions; calculations utilizing nodal velocities require more than two elements to resolve shear flow. It should be noted that only the component of velocity normal to the edge of a cell is included in calculations. The use of edge-centered velocities requires that mesh lines remain orthogonal. Consequently, only one Lagrangian step may be performed before a solution remapping is required. The remaining solution quantities (e.g., stress, density, and internal energy) are evaluated at the centroid of a cell. A discussion of the specific elements that populate the mesh is presented in the next section.

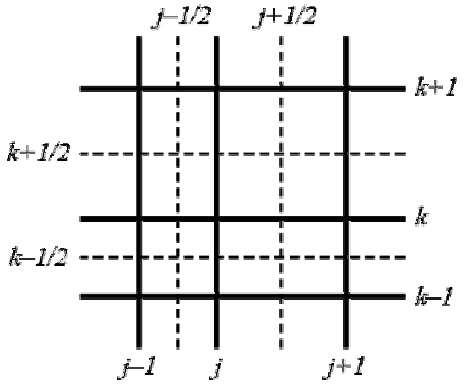

Figure 4-1. A portion of the computational mesh that depicts the logical coordinate system.

4.5.4 Element Derivations

The computational domain is discretized by 2-D solid plane strain quadrilateral elements that contain a single integration point. This particular element is frequently used in hydrocode

calculations because it is computationally efficient and sufficiently robust. The computational expense of an element is a real concern in explicit calculations, as the time step is required to be extremely small. Higher order elements require complicated interpolation functions and smaller stable time steps, making them computationally impractical.

The nodes of the quadrilateral element are defined by the intersections of the orthogonal mesh lines. A set of local curvilinear coordinates, ξ^i, is introduced to simplify the interpolation functions. As shown in Figure 4-2, the origin of the local coordinate system is located at the element centeroid, and the coordinates range from –1 to +1. These local coordinates are referred to as isoparametric coordinates.

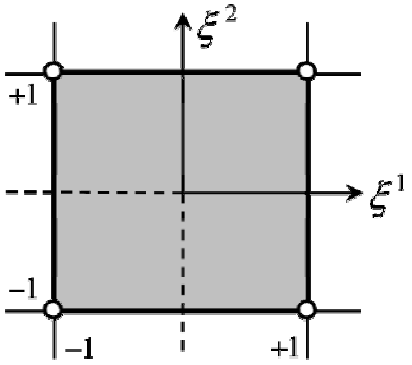

Figure 4-2. The isoparametric coordinate system for the plane strain quadrilateral element.

The interpolation function of node α expressed in terms of the isoparametric coordinates is denoted $N_\alpha(\xi^i)$. The interpolation functions of the element must satisfy three requirements: (i) they must be continuous within an element, (ii) they must sum to unity at any interior point of the element, and (iii) the value of $N_\alpha(\xi^i)$ at node β must be equal to $\delta_{\alpha\beta}$ (the Kronecker delta). A set of bilinear interpolation functions that satisfy these requirements is expressed as

$$N_\alpha(\xi^i) = \frac{1}{4}\left(1+\xi_\alpha^1\xi^1\right)\left(1+\xi_\alpha^2\xi^2\right) \tag{4.18}$$

where ξ_α^i refers to the value of ξ^i at node α.

The spatial gradient of a field within an element is calculated using the chain rule. For example, the spatial gradient of the interpolation function (a quantity that is required in future derivations) is given as

$$\frac{\partial N_\alpha(\boldsymbol{x})}{\partial x_j} = \frac{\partial N_\alpha(\xi^1,\xi^2)}{\partial \xi^1}\frac{\partial \xi^1}{\partial x_j} + \frac{\partial N_\alpha(\xi^1,\xi^2)}{\partial \xi^2}\frac{\partial \xi^2}{\partial x_j} \tag{4.19}$$

where the derivatives $\partial \xi^i / \partial x_j$ are evaluated by inverting the Jacobian matrix $[J] = \partial x_i / \partial \xi^j$. The spatial gradient will be needed to calculate both the velocity gradient tensor and the divergence of the stress tensor.

Solution quantities (e.g., stress) are integrated numerically over an element with Gaussian quadrature. A single integration point is used at the centeroid of the element; hence, the elements are known as reduced-integration elements. The use of a single integration point leads to the calculation of a spatially-constant stress in an element.

A consequence of using reduced integration elements is the development of zero energy modes in the Lagrangian mesh. The zero energy modes are not resisted by elemental stresses, and they can grow without bound. These modes are known as hourglass modes (due to their shape). Hourglass modes arise due to an excess of unconstrained degrees of freedom. A single 2-D quadrilateral element has eight degrees of freedom (two at each node). The three rigid body modes (two translational, one rotational) should not be resisted. This leaves five degrees of freedom, but in 2D, there are only three stresses that can resist them. Thus, two unrestrained degrees of freedom remain, as depicted in Figure 4-3. Lines that pass through the integration point remain unstretched in these configurations; therefore, elements exposed to these modes experience no strain and develop no resisting stresses.

The usual approach to controlling the hourglass modes is to introduce a small viscosity or stiffness to the momentum calculations. It has been shown that the addition of a stiffness term is better suited for small-strain problems, and a viscous term is better suited for finite strain problems. Therefore, viscous hourglass control will be used in these calculations. The Eulerian mesh is immune to hourglass modes because it is fixed in space, however the hourglass viscosity is still included to filter out discontinuities (diamond patterns) that arise in the contours of the velocity field.

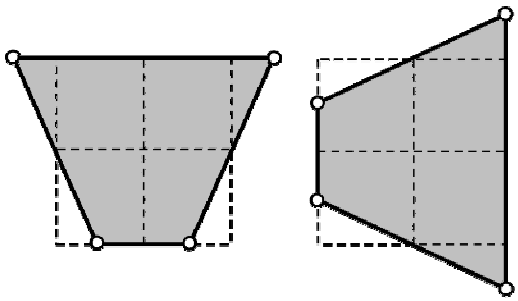

Figure 4-3. Hourglass modes associated with the 2-D solid plane strain element.

4.5.5 Shock viscosity

The physics across a shock discontinuity are governed by the Rankine-Hugoniot equations. The Rankine-Hugoniot equations relate the mass density (ρ), pressure (P), and specific internal energy (e) behind the shock front to these same quantities ahead of the shock front in terms of the particle velocity (U_P), and shock wave velocity (U_S). These equations are derived directly from the conservation of mass, momentum, and energy across a shock front, as in ref. [60]. Assuming a steady-state shock profile, where the material ahead of the shock front is stationary, the Rankine-Hugoniot relations are expressed as

$$\rho\left(U_S - U_P\right) = \rho_0 U_S \tag{4.20}$$

$$P - P_0 = \rho_0 U_S U_P \tag{4.21}$$

$$PU_P = \frac{1}{2}\left(\rho_0 U_S\right)U_P^2 + \left(e - e_0\right)\left(\rho_0 U_S\right) \tag{4.22}$$

Here, quantities ahead of the shock front (the initial state) are indicated by a subscript zero. Equations (4.20) and (4.21) may be combined and substituted into Eq. (4.22) to eliminate both U_S and U_P. Hence, the Rankine-Hugoniot relation pertaining to the conservation of energy may be expressed conveniently as

$$e - e_0 = \frac{1}{2}\left(P + P_0\right)\left(\nu_0 - \nu\right) \tag{4.23}$$

where ν is the specific volume.

Special computational methods are necessary to handle the jump discontinuities associated with shock waves. This is addressed by introducing a viscous term, known as the artificial shock viscosity q, which smears the shock front over a transition region that is sharp

but continuous. In solids, the shock viscosity introduces the proper amount of irreversibility (damping) to prevent oscillations in the solution variables in the vicinity of the shock front. Thus, the Rankine-Hugoniot relations are satisfied across the shock front, and the effects of the shock viscosity on the solution behind the shock front are negligible. Shock waves are typically resolved over 3–5 elements with the shock viscosity.

The numerical form of the shock viscosity is motivated by Rankine-Hugoniot relation for the pressure behind a shock front, as expressed in Eq. (4.21). Here, the particle velocity is approximated by the elemental velocity jump $\Delta\dot{u} = \dot{u}_{(j)} - \dot{u}_{(j+1)}$ in the 1-D case. The shock wave velocity is approximated by the empirical relation $U_S = C + S_1 U_P$, which holds for many materials (here, C is the acoustic wave speed of a material, and S_1 is the slope of the linear $U_S - U_P$ relation). Hence, the shock viscosity may be equated to the pressure jump in an element as

$$q = \Delta P = \rho_0 \Delta\dot{u}\left(c_\ell \bar{C} + c_q \left|\Delta\dot{u}\right|\right) \tag{4.24}$$

where $\bar{C}$ is the mean acoustic wave speed in an element (as more than one material may be contained in a single element), and c_ℓ and c_q are the linear and quadratic artificial shock viscosity coefficients, respectively. The viscosity coefficients are not material parameters; they are coefficient that are adjusted to yield a smooth shock wave profile. Typical values of the shock viscosity coefficients are c_ℓ=0.06, and c_q=1.5 [1]. The shock viscosity in Eq. (4.24) may be interpreted as a pressure jump across a shock front for a velocity jump equal to $\Delta\dot{u}$. Therefore, the hydrostatic contributions of the shock viscosity must be considered in the calculation of nodal forces and the integration of the energy equation. Furthermore, it may be seen in Eq. (4.24) that the shock viscosity is positive for compressive shocks and negative for rarefactions. One question still remains in regard to the shock viscosity calculations: how is the mean acoustic wave speed calculated in a mixed element?

A mixture theory must be used to account for individual material contributions to mean quantities in a mixed element. For the sake of clarity, a complete discussion of the mixture theory is withheld until a future section. This will not inhibit the progression of this section because the mean quantities are defined in a rather simple manner. The definition of the mean acoustic wave speed in an element, $\bar{C}$, is an obvious extension from the acoustic wave speed in a single material, C, i.e.,

$$C = \sqrt{\frac{(4/3)\mu + \tilde{K}}{\rho_0}}, \qquad \bar{C} = \sqrt{\frac{(4/3)\bar{\mu} + \bar{\tilde{K}}}{\bar{\rho}_0}} \tag{4.25}$$

Here, μ is the shear modulus of a single material, ρ_0 is the initial mass density of a single material, and $\tilde{K}$ is the corrected bulk modulus of a single material. The corrected bulk modulus is calculated from the equation of state (EOS) $P(\rho, E)$ as follows

$$\tilde{K} = \rho_0 \frac{\partial P(\rho, E)}{\partial \rho} + \frac{P}{\rho^2} \frac{\partial P(\rho, E)}{\partial E} \tag{4.26}$$

The first term in the above equation is the normal representation of the bulk modulus, K; the second term is appended to account for a stiffening effect due to an increase in the internal energy at high levels of compression [61]. The mean values of the shear modulus, initial mass density, and corrected bulk modulus are computed according to

$$\bar{\mu} = \sum_{m=1}^{M} \mu_m V_m^f, \qquad \bar{\rho}_0 = \sum_{m=1}^{M} \rho_{0m} V_m^f, \qquad \bar{\tilde{K}} = \left(\sum_{m=1}^{M} \frac{1}{\tilde{K}_m V_m^f} \right)^{-1} \tag{4.27}$$

where $\bar{\mu}$ and $\bar{\rho}_0$ are simply volume-fraction-weighted sums of the individual quantities (here, a solution quantity for a given material is denoted by a subscript 'm', and the total number of materials in a mixed element is denoted M). The corrected bulk modulus $\bar{\tilde{K}}$ is calculated by assuming that the individual material pressures are equilibrated (a detailed discussion of the pressure equilibration mixture theory will be provided in section 4.5.11).

4.5.6 Determination of the explicit time step

Quantities that are integrated in time (e.g., stress and strain) are done so with explicit techniques, i.e., forward-Euler integration. Therefore, it is essential that the time step is small enough to respect the dynamic behavior of the material. The calculation of a stable time step is dependent on the geometry of the mesh and the materials that populate it. Here, the time step is determined by the Courant stability criterion, which limits the time step to the minimum time necessary for an acoustic wave to traverse the shortest edge of an element [61]. The explicit time step for each element Δt_e is calculated as

$$\Delta t_e = \frac{\ell}{Q + \sqrt{Q^2 + \left(\bar{C} + |\Delta \dot{u}| \right)^2}} \tag{4.28}$$

where ℓ is the shortest edge of the element, and Q is a term that is related to the shock viscosity ($Q = c_\ell \overline{C} + c_q \left|\Delta \dot{u}\right|$ for elements in compression). The time step used to advance the solution is taken as the minimum time step calculated for all elements, i.e., $\Delta t = \min\left(\Delta t_e\right)$ for $e = 1 \ldots N$, where N represents the number of elements in the mesh. The time step is further reduced by a scaling factor, to be conservative. This completes the necessary preliminaries of the multi-material Eulerian finite element method; the sequence of calculations performed during the Lagrangian step is examined next.

4.5.7 The computational sequence of the Lagrangian step

The Lagrangian calculations performed here adhere broadly to the framework used in many traditional Lagrangian formulations. There is, however, a complicating factor: the allowance of more than one material in a single element. The calculations are adapted to handle this behavior through the introduction of a mixture theory. The flow of calculations performed in a Lagrangian step is summarized as follows:

1. The forces at the nodes are calculated from the stress state an applied forces at t^n.
2. Nodal accelerations are calculated from the nodal forces at t^n.
3. The acceleration is integrated to obtain the velocity at $t^{n+1/2}$.
4. The velocity is integrated to obtain the displacement at t^{n+1}.
5. The density is calculated from the deformation gradient at t^{n+1}.
6. The total strain rate at $t^{n+1/2}$ is calculated from the velocity gradient.
7. The total strain rate is partitioned among the materials in a mixed element according to a mixture theory.
8. The deviatoric stress in each material is updated using an objective stress rate, where the stress increment from the constitutive model is added at the midpoint of the time step.
9. The mean deviatoric stress tensor in an element is calculated according to a mixture theory.
10. The updated artificial shock viscosity and hourglass viscosity are calculated from the time-centered velocity.
11. The internal energy is updated based on the work done during the time step.

12. The pressure is calculated from the equation of state (EOS) based on the internal energy and density at t^{n+1}.
13. The updated total stress tensor is calculated now that all components are known at t^{n+1}.
14. A new time step Δt^{n+1} is calculated based on the Courant stability criterion.

4.5.8 Nodal force calculations

The force calculations at the nodes are derived from the weak form of the momentum equation. The nodal displacements $u_{\alpha i}$ are known at the current time t^n (here, α denotes the node number, and i denotes the direction). It is assumed that the displacement at any interior point of the element may be interpolated from the nodal values, i.e., $u_i(\boldsymbol{x}) = N_\alpha(\boldsymbol{x}) u_{\alpha i}$, where $N_\alpha(\boldsymbol{x})$ is the interpolation function of node α evaluated at $\boldsymbol{x}$. In a similar manner, the virtual displacement may be interpolated as $\delta u_i(\boldsymbol{x}) = N_\alpha(\boldsymbol{x}) \delta u_{\alpha i}$. The gradient of the virtual displacement is obtained by differentiating the interpolation function, i.e.,

$$\delta u_{i,j}(\boldsymbol{x}) = \frac{\partial N_\alpha(\boldsymbol{x})}{\partial x_j} \delta u_{\alpha i} \tag{4.29}$$

Substituting the expressions for $u_i(\boldsymbol{x})$, $\delta u_i(\boldsymbol{x})$, and $\delta u_{i,j}(\boldsymbol{x})$ into Eq. (4.13) yields the discrete form of the principle of virtual work, i.e.,

$$\left[\int_\Omega \rho N_\alpha(\boldsymbol{x}) N_\beta(\boldsymbol{x}) \ddot{u}_{\beta i} \, d\Omega - \int_\Omega \rho b_i N_\alpha(\boldsymbol{x}) \, d\Omega + \int_\Omega \sigma_{ij} \frac{\partial N_\alpha(\boldsymbol{x})}{\partial x_j} \, d\Omega - \int_{\partial\Omega} t_i N_\alpha(\boldsymbol{x}) \, d\Gamma \right] \delta u_{\alpha i} = 0 \tag{4.30}$$

Here, quantities are integrated over the generalized domain Ω and its bounding contour $\partial\Omega$. The bracketed term in Eq. (4.30) must be identically zero since the individual virtual displacements at the nodes $\delta u_{\alpha i}$ are arbitrary (recall that $\delta u_{\alpha i} = 0$ is required only at the essential boundary conditions). Therefore,

$$\left[\int_\Omega \rho N_\alpha(\boldsymbol{x}) N_\beta(\boldsymbol{x}) \, d\Omega \right] \ddot{u}_{\beta i} = - \int_\Omega \sigma_{ij} \frac{\partial N_\alpha(\boldsymbol{x})}{\partial x_j} \, d\Omega + \int_\Omega \rho b_i N_\alpha(\boldsymbol{x}) \, d\Omega + \int_{\partial\Omega} t_i N_\alpha(\boldsymbol{x}) \, d\Gamma \tag{4.31}$$

where the bracketed term is the consistent mass matrix $M^c_{\alpha i \beta j}$ (here, the subscripts αi and βj indicate the ith component at node α, and the jth component at node β, respectively). These

equations are coupled because the consistent mass matrix is not diagonal. It is not desirable to use the consistent mass matrix to solve for the nodal accelerations due to (i) the discontinuous nature of shock waves, and (ii) the high computational cost of solving coupled equations. In consideration of the first point, formulations that use the consistent mass matrix will calculate negative accelerations ahead of the shock front due to the inertial coupling between the nodes. This is contrary to the physics of the problem, as the only nodes accelerated should be those behind the shock wave front. This anomaly is avoided by using the diagonal lumped mass matrix $M_{\alpha i \beta j}$, which is defined as

$$M_{\alpha i \beta j} = \left(\frac{1}{N} \sum_{\gamma=1}^{N} M_{\gamma} \right) \delta_{\alpha\beta} \delta_{ij} \tag{4.32}$$

where M_{γ} denotes the mass at a node γ and N denotes the number of nodes contained in the element. Thus, the mass of the element is uniformly distributed over the nodes.

It is now convenient to specialize the nodal force calculations to the element of interest. The nodal forces due to the stress state in a constant stress quadrilateral element are approximated as

$$F_{\alpha i}^{\sigma} = \int_{\Omega} \sigma_{ij} \frac{\partial N_{\alpha}(\boldsymbol{x})}{\partial x_j} \, d\Omega \approx \sigma_{ij} \frac{\partial N_{\alpha}(\boldsymbol{x}^{\boldsymbol{0}})}{\partial x_j} A \tag{4.33}$$

where $\boldsymbol{x}^0$ indicates the position of the centroid of the element, and A is the area enclosed by the element. The force calculations due to the stress state are greatly simplified through the introduction of the discrete gradient operator $B_{ij\alpha k}$, which may be derived for any element. The discrete gradient operator transforms the stress state into a vector of forces, i.e.,

$$F_{\alpha k}^{\sigma} = \sigma_{ij} B_{ij\alpha k} A \tag{4.34}$$

The derivation of the discrete gradient operator for the 4-node reduced-integration quadrilateral element may be found in ref. [59]. The body force terms are evaluated by assuming that the body force is constant in an element, i.e.,

$$F_{\alpha i}^{b} = \int_{\Omega} \rho b_i \, N_{\alpha}(\boldsymbol{x}) \, d\Omega \approx \left(\frac{1}{4} \sum_{\beta=1}^{4} M_{\beta} \right) b_i(\boldsymbol{x}^{\boldsymbol{0}}) \tag{4.35}$$

Boundary tractions are assumed to vary linearly between two nodes, α and β, which are separated by a distance L_e. The force terms due to boundary tractions are distributed between the two nodes of an element edge, i.e.,

$$F_{\alpha i}^{t} = F_{\beta i}^{t} = \frac{1}{2}\left(t_{\alpha i} + t_{\beta i}\right) L_e \tag{4.36}$$

Finally, the summation of external and internal forces at a node is expressed as

$$F_{\alpha i}^{ext} - F_{\alpha i}^{int} = F_{\alpha i}^{b} + F_{\alpha i}^{t} - F_{\alpha i}^{\sigma} \tag{4.37}$$

Now that the nodal forces are known at t^n, the nodal accelerations may be calculated from an equilibrium force balance, i.e.,

$$\ddot{u}_{\alpha i} = M_{\alpha i \beta j}^{-1}\left(F_{\beta j}^{ext} - F_{\beta j}^{int}\right) \tag{4.38}$$

The implementation of this calculation for a 4-node quadrilateral element may be easier to visualize with matrix notation, as shown in the equation set below. The column vector $\ddot{\boldsymbol{u}}$ is constructed such that the entries are sequential sets of the acceleration components at each node; the force vector is constructed in the same manner.

$$\boldsymbol{M} = \begin{bmatrix} M_{1111} & & & 0 \\ & M_{1212} & & \\ & & \ddots & \\ & & & M_{4242} \end{bmatrix}, \quad \ddot{\boldsymbol{u}} = \begin{Bmatrix} u_{11} \\ u_{12} \\ \vdots \\ u_{41} \\ u_{42} \end{Bmatrix}, \quad \boldsymbol{F}^{ext} - \boldsymbol{F}^{int} = \begin{Bmatrix} F_{11} \\ F_{12} \\ \vdots \\ F_{41} \\ F_{42} \end{Bmatrix} \tag{4.39}$$

The nodal accelerations are solved according to $\ddot{\boldsymbol{u}} = \boldsymbol{M}^{-1}\left\{\boldsymbol{F}^{ext} - \boldsymbol{F}^{int}\right\}$, where the calculation of $\boldsymbol{M}^{-1}$ is trivial.

The central difference method may now be used to calculate the motion of the Lagrangian mesh. The edge-centered velocity field is integrated from the nodal accelerations, as in Eq. (4.17), and the nodal positions are integrated from velocity field, as in Eq. (4.16).

4.5.9 The density update

The deformation gradient F_{ij} is calculated from the updated nodal positions, i.e.,

$$F_{ij} = \frac{\partial x_i}{\partial X_j} \tag{4.40}$$

The density is updated according to $\rho^{n+1} = J^{-1}\rho^{n}$, where $J = \det\left(F_{ij}\right)$.

4.5.10 Strain rate calculations

The velocity gradient L_{ij} is calculated from the motion of the mesh. The velocity gradient may be expressed as

$$L_{ij} = \frac{\partial \dot{u}_i}{\partial x_j} = \frac{\partial N_a(\boldsymbol{x})}{\partial x_j} \dot{u}_{\alpha i} \tag{4.41}$$

where the velocity of an interior point of an element is interpolated from the nodes. Again, the discrete gradient operator simplifies the calculation, i.e., $L_{ij} = B_{ij\alpha k} \dot{u}_{\alpha k}$. The velocity gradient is now decomposed into symmetric and anti-symmetric terms in the normal manner,

$$L_{ij} = D_{ij} + W_{ij} \tag{4.42}$$

$$D_{ij} = \frac{1}{2}\left(L_{ij} + L_{ji}\right), \quad W_{ij} = \frac{1}{2}\left(L_{ij} - L_{ji}\right) \tag{4.43}$$

Here, D_{ij} is the rate of deformation tensor, and W_{ij} is the spin (vorticity) tensor. It should be noted that both D_{ij} and W_{ij} are evaluated at $t^{n+1/2}$ since the velocity field is centered in time. The strain rate applied to the material within an element is equivalent to the rate of deformation, i.e., $\dot{\varepsilon}_{ij}^{n+1/2} = D_{ij}^{n+1/2}$. The stress increment may now be calculated from the appropriate constitutive model, as the time-centered strain rate $\dot{\varepsilon}_{ij}^{n+1/2}$ is known; but first, the evaluation of quantities in an element containing more than one material must be considered. Direct notation is used in the sections that follow.

4.5.11 The mixture theory

The evaluation of stress and strain in an element containing more than one material requires the definition of a mixture theory [61]. Sub-element thermodynamics are handled by the mixture theory, which is used in two essential calculations at this stage. First, the mixture theory defines how the total strain rate in an element is partitioned among the constituent materials. Second, the mixture theory defines how the mean stress in an element is computed after the stress in each material has been updated; a discussion of this procedure is reserved for section 4.5.12.

It is now useful to consider the usual decomposition of the strain rate tensor into volumetric and deviatoric components, i.e., $\dot{\boldsymbol{\varepsilon}} = \dot{\boldsymbol{\varepsilon}}' + \left(\dot{\varepsilon}^v\right)\boldsymbol{I}$, where the volumetric strain rate is

$\dot{\varepsilon}^v = tr(\dot{\boldsymbol{\varepsilon}})$. The deviatoric strain rate in each material is equal to the total deviatoric strain rate in an element, i.e., $\dot{\boldsymbol{\varepsilon}}'_m = \dot{\boldsymbol{\varepsilon}}'$ (here, and in the remainder of this section, a solution quantity for a given material is denoted by a subscript 'm'). This is a necessary condition because slip is not permitted at material interfaces, which is to say the materials within an element are perfectly bonded. This may seem overly restrictive, but the overall flow is probably not highly sensitive to this assumption since the maximum shear stress that can be sustained in typical hydrodynamic calculations is a small fraction of the hydrostatic stress in each material. Consequently, the effects of friction are not considered in mixture theories pertaining to these calculations.

At this pont, the volumetric strain rates in each material ($\dot{\varepsilon}^v_m$), and the volume fractions of each material (V^f_m) in an element are unknowns at $t^{n+1/2}$. A mixture theory must be selected to define these quantities. Two possible mixture theories are (i) the mean strain rate mixture theory, and (ii) the single-iteration pressure-equilibration mixture theory. The mixture theory must be selected carefully, as it can have a profound effect on the modeling of local temperature spikes, or hot spots. Hot spots in porous systems typically arise from the collapse of voids, which is simply the thermomechanical interaction between a void and the surrounding material.

The mean strain rate mixture theory assigns the total strain rate to each material within an element, i.e., $\dot{\varepsilon}^v_m = tr(\dot{\boldsymbol{\varepsilon}})$. This theory is inadequate in mixed elements for which there is a large difference between the compressibility of the constituent materials. For example, if a mixed element contained a metal and a gas, both materials would be subjected to the same strain rates; this is obviously contrary to the physics of the situation, as the stiffer material should carry a larger portion of the load. This difficulty may by avoided by including algorithms that compress out any 'void' material before imposing the total element strain rate on each of the constituents.

The single-iteration pressure-equilibration mixture theory calculates the volumetric strain rates in each material by allowing the pressure in each material to approach an equilibrium state. This theory yields better results in cases of the substantially different compressibility of constituent materials. Artificial void collapse algorithms are not necessary (as in the mean strain rate theory) because the voids will be compressed out naturally by material expansion.

The single-iteration pressure-equilibration mixture theory is used in these calculations. A detailed discussion of this mixture theory is presented next.

The single-iteration pressure-equilibration mixture theory assumes that materials in a mixed element approach mechanical equilibrium by the end of a time step (thermal equilibration is not imposed). This is a reasonable thermodynaimc assumption when the time step is short in comparison to the time scale of the complete calculation and the spatial discretization of the domain is sufficiently fine. Full mechanical equilibrium is not imposed because a shock wave would traverse an element multiple times before the pressure equilibrated completely.

A fully equilibrated pressure state within a mixed element at time t^{n+1} is expressed as

$$P_m^{n+1} - P_{m+1}^{n+1} = 0 \quad \text{for } m = 1,\ldots,M-1 \tag{4.44}$$

where M represents the number of materials in a mixed element. However, the pressures at t^{n+1} are still unknown (and they cannot be calculated from the EOS because the internal energy has not been updated). To simplify the implementation of this mixture theory, the pressure change in each material is linearized for the current time step, i.e.,

$$P_m^{n+1} = P_m^n - \rho_m C_m^2 \, \dot{\varepsilon}_m^v \, \Delta t \tag{4.45}$$

Here, the bulk modulus of each material is well-approximated by the relation $K_m = \rho_m C_m^2$. The actual pressure at t^{n+1} will be calculated according to the EOS after the internal energy is updated; this linearization is performed only for the simplification of the mixture theory. The substitution of Eq. (4.45) into Eq. (4.44) defines a set of $M-1$ equations expressed in terms of $\dot{\varepsilon}_m^v$. An additional condition that must be satisfied is the sum of the volume-fraction-weighted volumetric strain rates in each material must be equal to the total volumetric strain rate in an element, i.e.,

$$\sum_{m=1}^{M} \dot{\varepsilon}_m^v V_m^f = \dot{\varepsilon}^v \tag{4.46}$$

Since the volumetric strain rates are time-centered, the volume fractions should be evaluated at $t^{n+1/2}$ to maintain second-order accuracy. Volume changes are linearized to calculate the time-centered volume fractions as

$$V_m^{f,n+1/2} = \left(1 + \frac{1}{2}\dot{\varepsilon}_m^v \, \Delta t\right) V_m^{f,n} \tag{4.47}$$

The substitution of Eq. (4.47) into Eq. (4.46) completes the set of equation necessary to solve for the M unknown volumetric strain rates $\dot{\varepsilon}_m^v$. However, a constraint must be placed on the solution to these equations, i.e., the absolute value of the volume fractions must sum to unity

$$\sum_{m=1}^{M} \left| V_m^f \right| = 1 \tag{4.48}$$

Otherwise, the equations could be satisfied with negative volume fractions. It should be noted that this set of equations is nonlinear due to the time-centering of the volume fractions. The Newton-Raphson method is used to solve this nonlinear system of equations. A single iteration is used so that the pressures approach equilibrium, rather than enforcing equilibrium exactly. The error incurred by linearizing the pressure and volume changes during a time step are on the same order of the approximations introduced by the thermodynamic assumptions in the single-iteration pressure-equilibration mixture theory.

The mixture theory must also be used to compute the mean stress in a mixed element. However, a discussion of this topic is saved for the next section, after the stress has been updated

4.5.12 The stress update

It is now convenient to introduce the usual decomposition of the Cauchy stress tensor. The stress tensor may be separated into hydrostatic and deviatoric contributions, i.e., $\boldsymbol{\sigma} = \boldsymbol{\sigma}' - (P+q)\boldsymbol{I}$, where $\boldsymbol{\sigma}'$ is the deviatoric stress tensor, P is the pressure, q is the artificial shock viscosity, and $\boldsymbol{I}$ is the second-order identity tensor.

The stress is integrated over a time step (using an appropriate stress rate) now that the time-centered strain rate is known for each material in an element. The material time derivative of stress is not objective, which is to say it does not transform properly as a tensor when subjected to rigid body rotations. This may be rationalized by considering the incremental motion of the mesh during a time step. The strain calculated in an element is composed of two components: material deformation (stretch), and rigid body rotation (spin). The rigid body rotation must be removed, as it cannot enter into calculations of the stress state. This is handled by using an objective stress rate.

The Jaumann stress rate is an objective stress rate that is commonly used in hydrocode calculations. Other objective stress rates are available (e.g., the Truesdell rate, or the Grenn-Naghdi rate), but the Jaumann stress rate was chosen for these calculations because of its ability to handle large deformations with second-order accuracy (although oscillatory shear stresses are predicted for shears strains that exceed unity) and its relatively low computational cost. The Jaumann stress rate $\overset{\nabla}{\dot{\boldsymbol{\sigma}}}$ is expressed as

$$\overset{\nabla}{\boldsymbol{\sigma}} = \dot{\boldsymbol{\sigma}} + \boldsymbol{\sigma}\boldsymbol{W} - \boldsymbol{W}\boldsymbol{\sigma} \tag{4.49}$$

where $\boldsymbol{W}$ is the spin tensor (i.e., the skew-symmetric part of the velocity gradient).

The numerical implementation of the Jaumann stress rate is relatively straight-forward. Here, the stress update for the total stress tensor is presented; however, the hydrocode calculations only update the deviatoric part of the stress tensor $\boldsymbol{\sigma}'$. The stress update is performed in two half-steps because the stress increment calculated from the constitutive model is dependent on the current stress. The time-centered stress $\boldsymbol{\sigma}^{n+1/2}$ is calculated as

$$\boldsymbol{\sigma}^{n+1/2} = \boldsymbol{\sigma}^{n} + \left(\boldsymbol{\sigma}^{n}\boldsymbol{W}^{n+1/2} - \boldsymbol{W}^{n+1/2}\boldsymbol{\sigma}^{n}\right)\frac{1}{2}\Delta t \tag{4.50}$$

Both the spin tensor and the rate of deformation tensor are evaluated at t^n because the velocity gradient is centered with respect to time. The stress increment $\dot{\boldsymbol{\sigma}}\Delta t$ is calculated from the appropriate constitutive model and added to the time-centered stress

$$\boldsymbol{\sigma}^{*} = \boldsymbol{\sigma}^{n+1/2} + \dot{\boldsymbol{\sigma}}(\boldsymbol{\sigma}, \boldsymbol{D}, \boldsymbol{h})\Delta t \tag{4.51}$$

where $\boldsymbol{h}$ is a vector of internal state variables. The time-centered stress is updated to the end of the time step by performing the remaining rotation, i.e.,

$$\boldsymbol{\sigma}^{n+1} = \boldsymbol{\sigma}^{*} + \left(\boldsymbol{\sigma}^{*}\boldsymbol{W}^{n+1/2} - \boldsymbol{W}^{n+1/2}\boldsymbol{\sigma}^{*}\right)\frac{1}{2}\Delta t \tag{4.52}$$

One drawback of this method of time-centering is that the stress may fall slightly outside the yield surface after the second half-step rotation. This problem is handled by scaling back the stress with a radial return algorithm if necessary.

The mean stress in an element can now be computed using the mixture theory. Again, the total stress tensor is used in this development, whereas only the deviatoric part is used in the hydrocode calculations. The mean stress in an element $\bar{\boldsymbol{\sigma}}$ is calculated simply as the volume-fraction-weighted sum of the individual material stresses, i.e.,

$$\bar{\boldsymbol{\sigma}}^{n+1} = \sum_{m=1}^{M} \boldsymbol{\sigma}_m^{n+1} V_m^{f,n+1} \tag{4.53}$$

Here, $\boldsymbol{\sigma}_m^{n+1}$ denotes the spatially-constant stress in a material at t^{n+1}.

4.5.13 The internal energy update

The incremental change in the internal energy is calculated as the pressure-volume work performed during a time step. The total updated internal energy may be expressed as

$$E^{n+1}V^{n+1} = E^{n}V^{n+1} - \frac{1}{2}\left[P^{n} + P(\rho^{n+1}, E^{n+1})\right]\Delta V \tag{4.54}$$

Here, E is the specific internal energy (per unit volume). The internal energy is updated from the current mass density ρ^{n+1}, the change in material volume ΔV, and the average value of the pressure over a time step. However, the updated pressure and the updated internal energy are implicitly related. Fortunately, this problem is solvable because most equations of state are constructed with linear contributions of internal energy, e.g.,

$$P(\rho^{n+1}, E^{n+1}) = A(\rho^{n+1}) + B(\rho^{n+1})\,E^{n+1} \tag{4.55}$$

where A and B are general functions. Thus, the updated specific internal energy may be expressed as follows

$$E^{n+1} = \frac{E^{n}V^{n+1} - \frac{1}{2}\left[P^{n} + A(\rho^{n+1})\right]\Delta V}{V^{n+1} + \frac{1}{2}B(\rho^{n+1})\Delta V} \tag{4.56}$$

4.5.14 Pressure calculations

Now that both the updated mass density and internal energy are known, the updated pressure is calculated from the EOS, i.e. $P^{n+1} = P\left(\rho^{n+1}, E^{n+1}\right)$. This concludes the calculations involved in the Lagrangian step. The Eulerian step is performed next.

4.6 The Eulerian step

The deformed state of the material (i.e., all solution variables and material coordinates) is described completely by the Lagrangian mesh at the end of a time increment. It is now necessary to perform the Eulerian step. During the Eulerian step, the material description contained in the Lagrangian mesh is remapped to the spatially-fixed Eulerian mesh while time remains constant. The transport of material (and the associated solution variables) between the elements is handled with advection algorithms.

It is easiest to visualize the remapping process by considering a domain that is discretized by two meshes (Lagrangian and Eulerian) that are coincident at the beginning of a time step, as in Figure 4-4. Here, the thin mesh lines that span the domain represent the Eulerian mesh, and a portion of the Lagrangian mesh is depicted by the bold mesh lines (both meshes are logically

regular). The Lagrangian mesh remains attached to the material as the solution is advanced in time. At the end of a time step, the deformed state (described by the Lagrangian mesh) is projected onto the Eulerian mesh while time remains constant. The meshes are effectively reconciled. The Lagrangian mesh at the beginning of the next time step is defined by the Eulerian mesh at the end of the current time step, thus avoiding the formation of severe element distortions. The Arbitrary Lagrangian-Eulerian (ALE) formulation is an extension of the aforementioned technique, in which the motion of the Eulerian mesh is pre-defined. For example, the Eulerian mesh may translate, rotate, or contract, independent of the motion of the system, so that the area of interest is discretized efficiently.

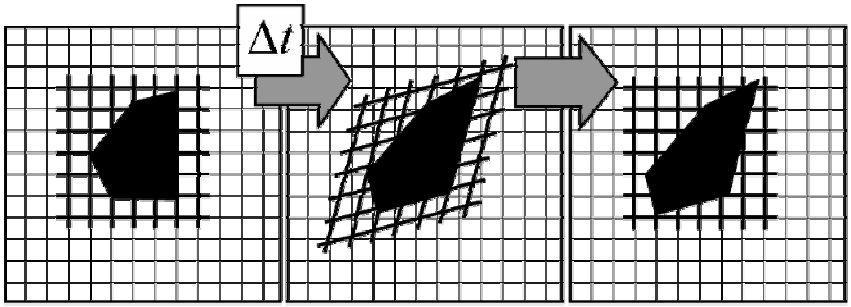

Figure 4-4. Operator splitting is achieved by a Lagrangian step followed by an Eulerian step (illustration taken from ref. [59]).

It is now necessary to recall the numbering scheme that is used for a logically-regular computational mesh, as this notation will be used extensively in the sections that follow. The nodes of the Eulerian mesh are identified by integer row and column indices (j,k) and the elements are referenced by the node-centered coordinates $(j+1/2,\, k+1/2)$, as shown in Figure 4-1.

4.6.1 The computational sequence of the Eulerian step

The remapping of the solution described by the Lagrangian mesh to the Eulerian mesh involves the following procedures:

1. The volume transported between elements is calculated.

2. The mean values of the solution variables associated with the transported volume are calculated and advected.
3. The material interfaces within a mixed element are reconstructed.
4. The computational meshes are reconciled and the calculation proceeds to the next Lagrangian step.

The work of Benson [1, 41, 42, 45] provides exceptional insight to these procedures.

4.6.2 Transport volume calculations

The transport volume is calculated by considering the displacement of the Lagrangian mesh relative to the Eulerian. The volume transported between two adjacent elements (in the Eulerian mesh) is the volume that is swept out by their common edge during a time step (which is described by the Lagrangian mesh). Hence, the transport volume calculation is purely geometric. It should be noted that the relative mesh motion is less than the smallest characteristic element dimension due to the Courant stability criterion.

The transport volume calculation is relatively simple in an element that contains a single material. In mixed elements, 'interface trackers' must be used to resolve material interfaces. The interface trackers calculate the volumes of each material transported between elements. Once the transport volume of each material has been determined, transport algorithms update the solution variables in each element based on the transport volumes that are advected.

4.6.3 Transport algorithms

The advection of solution variables will be discussed in cases of increasing complexity so that the most complicated algorithms are developed from a few basic principles. The simplest 1-D case will provide insight to the mechanisms at the core of the transport algorithms; subsequent cases are extensions of the 1-D case. First, the advection of element-centered solution quantities in a 1-D mesh of elements that contain a single material will be discussed. Next, the 1-D case will be extended to 2D with the allowance of more than one material in an element. Finally, the advection of solution quantities that are not located at the centroid of an element (e.g., momentum) are discussed. This section is closed by assessing the performance of the transport algorithms.

Element-centered solution quantities (e.g., mass density, internal energy, and stress) are advected using the MUSCL (Monotone Upwind Scheme for Conservation Laws) transport algorithm developed by Van Leer [62]. The MUSCL transport algorithm may be described by considering a 1-D mesh of elements containing a single material. Let the 1-D mesh be comprised of a set of nodes that are numbered sequentially from left to right, where a solution quantity in an element defined by nodes (j) and $(j+1)$ is indicated with a subscript $(j+1/2)$. Since time remains constant during the Eulerian step, the values of the solution quantities before and after the transport calculation are indicated with a superscript $-$ and $+$, respectively. The 1-D mesh is swept from left to right, element-by-element, updating the solution variables in each element. The value of a generalized solution variable ϕ in an element after the transport calculation is expressed as

$$\phi^{+}_{(j+1/2)} = \frac{1}{V^{+}_{(j+1/2)}}\left[V^{-}_{(j+1/2)}\phi^{-}_{(j+1/2)} + \Delta V_{(j)}\phi_{(j)} - \Delta V_{(j+1)}\phi_{(j+1)}\right] \tag{4.57}$$

where the volume transported from element $(j-1/2)$ to element $(j+1/2)$ through node (j) is denoted $\Delta V_{(j)}$. The volume in an element after transport is calculated as $V^{+}_{(j+1/2)} = V^{-}_{(j+1/2)} + \Delta V_{(j)} - \Delta V_{(j+1)}$. The mean value of a generalized solution variable associated with the transported volume is denoted $\phi_{(j)}$. The $\phi_{(j)}$ terms are calculated by linear interpolation about an element centeroid for second-order accuracy, i.e.,

$$\phi_{(j)} = \phi^{-}_{(j-1/2)} + \frac{1}{2}s_{(j-1/2)}\left[V^{-}_{(j-1/2)} - \Delta V_{(j)}\right] \tag{4.58}$$

where $s_{(j-1/2)}$ represents the slope of the piece-wise linear approximation of a solution variable within an element. The slope is limited according to a range defined by the minimum and maximum values of ϕ in elements $(j-1/2)$, $(j+1/2)$, and $(j+3/2)$ so that new minima or maxima are not introduced during the solution remap; this avoids the development of spurious oscillations in solution variables. It should be noted that advection algorithms alter the stress state in an element; therefore, the stress state must be scaled back, should it happen to fall outside the yield surface.

The transport mechanism is extended to 2D by spatial operator splitting, which is also known as the alternating direction method. The solution variables in each element are updated by performing two orthogonal, 1-D sweeps along the rows (j-direction) and columns

(k -direction) of the Eulerian mesh, where solution quantities are advected using the same procedures outlined for the 1-D MUSCL algorithm. The direction of the first sweep is alternated each time step to prevent aliasing errors, as shown in Figure 4-5. To obtain formal second-order accuracy, each Eulerian step would require four sweeps (the sequence of sweep directions would be j, k, k, j, where each sweep accounts for half the transport in that direction). However, it has been found that alternating series of two sweeps for each time step is adequate in practice (i.e., j, k, time step, k, j, time step). The transport volume of each material (ΔV_m) is calculated, and solution quantities are updated using the MUSCL algorithm, where the contributions of each material are summed.

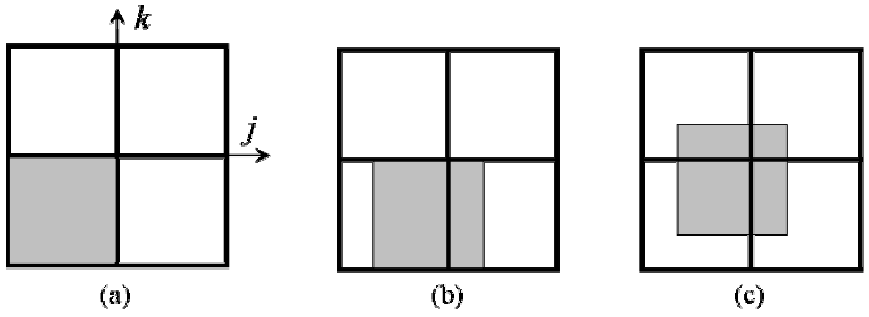

Figure 4-5. Alternating sweeps of the mesh during the transport step; (a) the original configuration, (b) the material transported after the j-sweep, and (c) the material transported after the k-sweep (illustration taken from ref. [42].

Special techniques are needed to advect momentum due to the differing locations of the mass density and the velocity. Recall that the mass density is located at the centroid of an element, whereas the velocity is located at the centers of the element edges. Therefore, the element-centered MUSCL transport algorithm must be modified to advect momentum. This is accomplished by using a staggered-mesh algorithm [63], which dynamically constructs a dual mesh with nodes placed at the centroids of the original elements. The MUSCL algorithm is now applied to the newly-constructed dual mesh, with the volume terms replaced by mass terms in Eq. (4.57).

The performance of the transport algorithm is assessed by considering the amount of error introduced to the solution by the remap step. Ideal advection techniques are (1) conservative, (2) second-order accurate, (3) isotropic, and (4) monotonic. Other transport algorithms are available (e.g., the donor cell algorithm and the half index shift algorithm); the MUSCL algorithm was selected for its performance in the aforementioned categories and its computational efficiency.

The transport calculation for a given solution variable is said to be conservative if the volume integrals of the solution variable are equal before and after the transport step. It is essential that mass density, momentum, and internal energy are conserved during the transport calculation since they are governed by conservation laws. The conservation of other quantities, not explicitly governed by conservation laws (e.g., stress and history variables), is desirable. In accordance with the conservation laws, the MUSCL algorithm conserves mass density, momentum, and internal energy exactly. The conservation of the total energy of the system is desirable, but elusive. This is because the conservation laws for momentum and total energy both include velocity-dependent terms. The transport algorithms conserve momentum by construction, which causes kinetic energy losses. To understand why the kinetic energy is dissipated, consider a 1-D mesh of uniform element length, and assume that only one node has a non-zero velocity. To conserve both the kinetic energy and the momentum, the velocity must be transported in such a manner that some nodal velocities would be imposed in the opposite direction of the non-zero nodal velocity (i.e., noise would be introduced to the solution). The physics of this scenario are clearly not realistic. As a consequence, the total energy decreases when the momentum and internal energy are transported in a conservative manner. However, kinetic energy loses are not critical to the calculations performed in this body of work.

Second-order accuracy ($O(\Delta t)^3$) is required in transport algorithms so that solution variables are not excessively smeared across the computational mesh. The time step in explicit calculations is extremely small, therefore, many time steps are required in typical simulations (on the order of 10^4–10^5). Thus, second-order accuracy is a practical necessity. The MUSCL algorithm is second-order accurate in smooth regions of the solution; some error is introduced in the discontinuous regions of the spatial domain (i.e., the shock front), which is to be expected.

The isotropy of a transport technique is a measure of the mesh aliasing errors introduced by advection. Aliasing errors arise from corner coupling, which is the transport of material

through elements that share a node but not an edge (i.e., diagonal elements). The isotropic nature of the 2-D MUSCL algorithm is preserved by reversing the orthogonal sweep direction priorities each time step.

A transport algorithm is said to be monotonic if it does not introduce any new minima or maxima to the solution during the remap step. The monotonic nature of the transport algorithm is of particular importance for the advection of mass density and internal energy at the shock front, where negative values would lead to unrealistic solutions. One may recall that the MUSCL algorithm is constructed in such a way that the interpolation of solution variables within an element is limited by the pre-existing minima and maxima of an element and its neighbors; therefore, the MUSCL algorithm is completely monotonic.

4.6.4 Interface reconstruction

Now that the appropriate volumes and solution variables have been transported, the material interfaces must be reconstructed. A nine-point finite difference stencil is used to reconstruct material interfaces in an algorithm developed by Youngs [64]. Here, a material interface within an element is represented by a straight line. The orientation (angle) of a material interface is determined by considering the volume fractions of the materials in the current element, as well as the volume fractions of the materials in the eight neighboring elements. The position of an interface in an element is adjusted so that the proper volume fractions are obtained.

Individual materials within a mixed element are distinguished by material identification numbers. This is a subtle aspect of the interface reconstruction algorithm that must be taken into consideration when constructing discrete particle models. If two separate entities that of the same material identification number come into contact, they will effectively coalesce (similar to a fluid). Consequently, an adequate number of materials must be defined (with the same constitutive models and material parameters, if necessary) to keep track of distinct contacting entities.

Special techniques are required to reconstruct material interfaces in elements that contain more than two materials. In this work, a priority list is used to determine the ordering of materials, based on the coordinates of the material centroids within an element. A full development of this algorithms is available in ref. [65].

4.7 Temperature calculations

The absolute temperature T is calculated from the thermal energy content of a material. Now that the internal energy has been updated and advected as appropriate, the absolute temperature may be calculated as

$$T = \frac{E - E_C\left(\rho/\rho_0\right)}{\rho C_P} \tag{4.59}$$

where E is the total specific internal energy (per unit volume), E_C is the cold compression energy (which is a function of the relative density), and C_P is the specific heat at constant pressure. Element-centered temperatures are interpolated to the nodes and averaged.

CHAPTER 5
CONSTITUTIVE MODELS

Stress-strain responses are separated into hydrostatic and deviatoric components, which are calculated explicitly from the constitutive models for each phase. The constitutive models implemented in this body of work will be presented in the sections that follow; but first, the general thermal and mechanical properties used in the finite element calculations will be discussed.

5.1 General material properties

Material properties used in the finite element calculations are given in Table 5-1. Material properties are well defined for the Al phase; properties listed may be found in most metal handbooks, e.g. ref. [66]. This cannot be said of the remaining phases. Therefore, certain approximations have been made. The density and specific heat of Fe_2O_3 are given in ref. [34]; here, the specific heat at constant volume C_V is substituted for the specific heat at constant pressure C_P, which is a reasonable assumption. The shear modulus of Fe_2O_3 is approximated from its relation to the elastic wave speed [67] and the bulk modulus [34], i.e., $\rho_0^2 C = \sqrt{(4/3)\mu + K}$. The thermal conductivity of Fe_2O_3 is estimated from a survey of oxides (e.g., TiO_2, ZrO_2, Al_2O_3, NiO) in ref. [68]; the melting temperature of Fe_2O_3 is given in ref. [68]. The latent heat of melting for the iron oxide phase is not included in the calculations due to an absence of data in the open literature. This assumption is not overly restrictive, as only small volume fractions of Fe_2O_3 melt for the most severe loading conditions. The density and shear modulus of Epon 828 were reported from experiments performed by Ferranti and Thadhani [30] at the Georgia Institute of Technology. The specific heat and thermal conductivity of epoxy resins, such as Epon 828, is provided in ref. [69]. Thermoset polymers, such as Epon 828, do not melt at a distinct temperature; instead, polymeric chains dissociate at the decomposition temperature. The decomposition temperature of Epon 828 is given in ref. [70]. Any additional energy pertaining to a phase change in the epoxy phase is neglected since Epon 828 is noncrystalline [71]. The initial mass density of the pores is approximated by that of air; other material properties are not necessary for the pores.

Table 5-1. Material properties for the Al+Fe_2O_3 thermite system

Properties	Units	Al-1100	Fe_2O_3	Epon 828	Pores
Initial mass density, ρ_0	g-cm^{-3}	2.71	5.27	1.20	1.0×10^{-3}
Shear modulus, μ	GPa	26.8*	225	1.393	—
Specific heat, C_P	kJ-kg^{-1}-K^{-1}	0.904	0.607	2.1	—
Conductivity, κ	W-m^{-1}-K^{-1}	222	5	0.2	—
Melting temperature, T_m	K	926	1780	533	—
Latent heat, E_H	kJ-kg^{-1}	390	—	—	—

* reported at room temperature (cf. ref. [72]).

5.2 Hydrostatic stress models

An equation of state (EOS) describes the relationship between the pressure, mass density, and internal energy of a material, e.g., $P = P(\rho, e)$. In regimes of low pressure, the hydrostatic response is well-approximated by the simple linear elastic relation $P = K\varepsilon_{kk}$, where $\varepsilon_{kk} = (\rho_0/\rho) - 1$. However, hydrostatic responses deviate from linearity above the Hugoniot elastic limit (HEL). The pressures achieved during shock compression are well above the HEL. Therefore, an appropriate EOS must be used to describe the hydrostatic response of a material

The Gruneisen EOS is used extensively in hydrodynamic calculations, as it is derived from the conservation equations. A wealth of high-pressure shock data [67] has been compiled over the years for many different materials, which can be used to obtain the necessary parameters for the Gruneisen EOS. The Gruneisen EOS is used to calculate pressure-volume responses for the Al and epoxy phases. The lack of shock data pertaining to the Fe_2O_3 phase restricts the availability of hydrostatic models. Forunately, material constants for Fe_2O_3 have been determined for the Murnaghan EOS, a model less ubiquitous than the Gruneisen EOS.

5.2.1 The Gruneisen equation of state

The following basic derivation is taken from refs. [60] and [73]. The interested reader is encouraged to consult the aforementioned references for extensions of the Gruneisen EOS to a

range of conditions. The Gruneisen EOS is derived from the Rankine-Hugoniot equations, which are re-stated here, i.e.,

$$\rho\left(U_S - U_P\right) = \rho_0 U_S \tag{5.1}$$

$$P - P_0 = \rho_0 U_S U_P \tag{5.2}$$

$$e - e_0 = \frac{1}{2}\left(P + P_0\right)\left(\nu_0 - \nu\right) \tag{5.3}$$

As mentioned earlier, the Hugoniot of many materials can be adequately represented by a linear relationship between the particle velocity and the shock wave velocity, i.e.,

$$U_S = C + S_1 U_P \tag{5.4}$$

where C is the acoustic wave speed, and S_1 is the slope of the linear $U_S - U_P$ (deviations from linearity are usually due to high levels of porosity or phase transformation). It is now convenient to introduce a quantity known as the compression, i.e., $\eta = 1 - \left(\rho_0/\rho\right)$. The combination of η with the expression of mass conservation, Eq. (4.20), yields $\eta = U_P/U_S$. Eq. (5.4) may now be rearranged to express the particle velocity and shock velocity in terms of the compression, i.e.,

$$U_P = C\eta/\left(1 - S_1\eta\right) \tag{5.5}$$

$$U_S = C/\left(1 - S_1\eta\right) \tag{5.6}$$

The above equations are substituted into the expression of momentum conservation, Eq. (4.21), to yield the following pressure-compression relation (assuming $P_0 = 0$)

$$P_H = \frac{\rho_0 C^2 \eta}{\left(1 - S_1\eta\right)^2} \tag{5.7}$$

where the subscripted H refers to a point on the Hugoniot curve. The conservation of energy may also be expressed in terms of the compression (assuming $e_0 = 0$), i.e.,

$$e_H = \frac{1}{2} P_H \left(\frac{\eta}{\rho_0}\right) \tag{5.8}$$

Many applications require the calculation of states that do not fall exactly on the Hugoniot curve; at this point, the Gruneisen approximation is introduced. A thermodynamic state that deviates from the Hugoniot curve is calculated as

$$P - P_H = \frac{\Gamma}{\nu}\left(e - e_H\right) \tag{5.9}$$

where the Gruneisen parameter Γ is defined as

$$\Gamma = \nu \left(\frac{\partial P}{\partial e} \right)_{\nu} \tag{5.10}$$

Upon substitution of Eqs. (5.7) and (5.8) into Eq. (5.9), the pressure (in compression) is expressed as

$$P = \frac{\rho_0 C^2 \eta \left[1 - (\Gamma/2)\left(\eta/(1-\eta)\right) \right]}{\left(1 - S_1 \eta\right)^2} + \Gamma \rho e \tag{5.11}$$

Equation (5.11) is the basic form of the Gruneisen EOS. It should be noted that the Gruneisen EOS is singular for certain values of the compression η, namely $\eta = 1/S_1$.

Model parameters for Al-1100 [67] and Epon 828 [67] are given in Table 5-2. The parameter S_1 is obtained through a linear regression of the $U_S - U_P$ data. For simplicity, the Gruneisen parameter is assumed constant; it is estimated using the common approximation $\Gamma = 2S_1 - 1$, as in ref. [3]. Sample Hugoniot curves for Al-1100 and Epon 828 are shown in Figure 5-1.

Table 5-2. Gruneisen EOS parameters for Al-1100 and Epon 828

Parameters	**Units**	**Al-1100**	**Epon 828**
C	km-s^{-1}	5.38	2.60
S	—	1.34	1.59
Γ	—	1.68	2.18

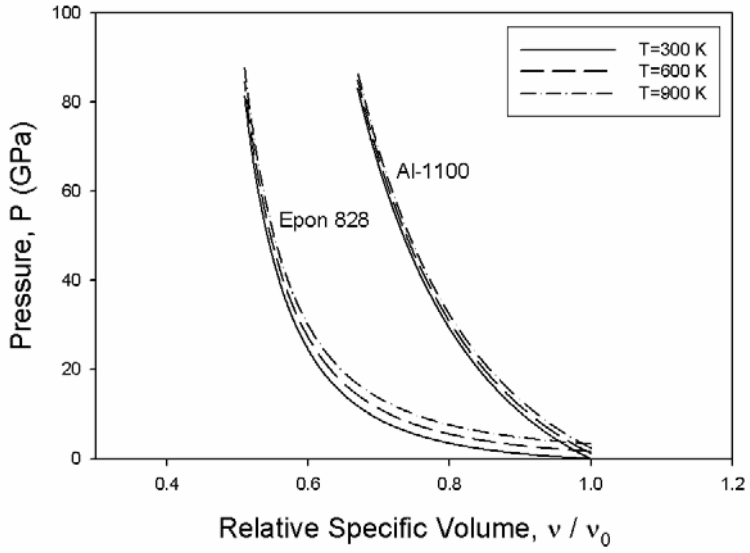

Figure 5-1. Hugoniot curves (pressure–relative specific volume) predicted by the Gruneisen EOS for Al-1100 and Epon 828 over a range of temperatures.

5.2.2 The Murnaghan equation of state

The Murnaghan EOS [74] is derived from the variation of the bulk modulus with respect to pressure. The bulk modulus K, and its pressure derivative K', may be represented as

$$K = -V\left(\frac{\partial P}{\partial V}\right)_T \tag{5.12}$$

$$K' = \left(\frac{\partial K}{\partial P}\right)_T \tag{5.13}$$

where the quantities in parentheses with a subscript T represent incremental processes that occur at constant temperature. Experimental observations in many materials show that the bulk modulus varies linearly with pressure. Therefore, it may be assumed that K' is constant. This provides an alternate expression for the bulk modulus as

$$K = K_0 + K_0'\left(P - P_0\right), \tag{5.14}$$

where K_0 and K_0' are quantities at the reference pressure P_0 (here, $P_0 = 0$). Equations (5.12) and (5.14) may now be combined, assuming a constant temperature, to yield

$$\frac{dV}{V} = \frac{-dP}{K_0 + K_0'P} \tag{5.15}$$

The above equation is integrated to obtain the pressure-volume relation

$$P = \frac{K_0}{K_0'}\left[\left(\frac{V}{V_0}\right)^{-K_0'} - 1\right] \tag{5.16}$$

Equation (5.16) is the basic form of the Murnaghan EOS. The basic form may be augmented by an additional term to account for the thermal energy content of the material, i.e.,

$$P = \frac{K_0}{K_0'}\left[\left(\frac{\rho_0}{\rho}\right)^{-K_0'} - 1\right] + \Gamma^M \rho_0 C_V \left(T - T_0\right) \tag{5.17}$$

Here, the volumes have been replaced by mass densities, C_V is the specific heat at constant volume, Γ^M is a material constant, and T_0 is the reference temperature. Model parameters for Fe_2O_3 [34] are given in Table 5-3. Sample pressure plots over a range of temperatures are shown in Figure 5-2.

Table 5-3. Murnaghan EOS parameters for Fe_2O_3

Parameters	**Units**	**Fe_2O_3**
K_0	GPa	20.27
K_0'	—	4.35
Γ^M	—	1.99
C_V	kJ-kg^{-1}-K^{-1}	0.607

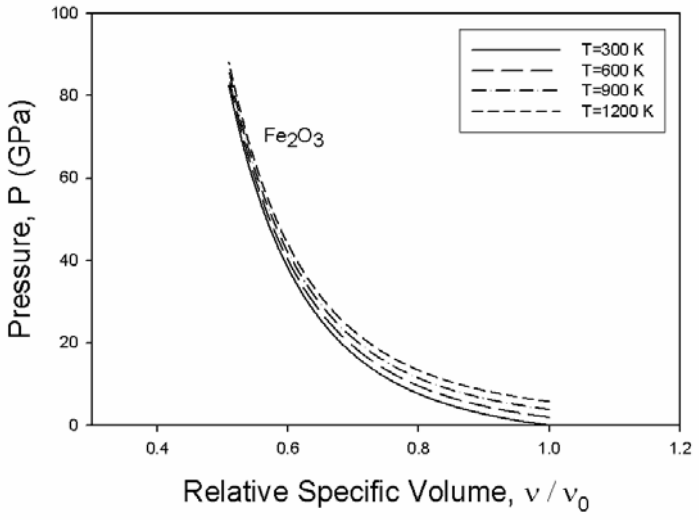

Figure 5-2. Hugoniot curves (pressure–relative specific volume) predicted by the Murnaghan EOS for Fe_2O_3 over a range of temperatures.

5.3 Deviatoric strength models

Shock compression processes induce high local strain rates and elevated temperatures throughout the microstructure. Therefore, it is desirable to use deviatoric strength models that are sensitive to a wide range of strain rates and temperatures. Furthermore, physically-based models are preferred, rather than empirical models, for their ability to accurately describe material behavior without an excess of fitting parameters.

Physically-based constituive models for polycrystalline fcc metals, such as Al, are well-defined over a range of strain rates and temperatures. The Klepaczko model is used to model the deviatoric strength behavior of the fcc Al phase. Physically-based constitutive models for glassy polymers, such as epoxy, are sparse at high strain rates and temperatures. Fortunately, one such model, the Hasan-Boyce model, is available; it is used to model the deviatoric stress-strain response of the epoxy phase. No model whatsoever (physically-based or empirical) is currently available in the open literature for the iron oxide phase; consequently, approximations are made. Concise descriptions of the deviatoric strength models are provided in the sections that follow.

5.3.1 The Klepaczko model

In modeling the stress-strain response of high purity fcc metals, it has become apparent that the evolution of the microstructure must be taken into account. Accordingly, Klepaczko [72] has proposed a constitutive model for high-purity fcc Al. Here, thermally-activated mechanisms are used to model the kinetics of dislocation glide and the rate-sensitive generation of dislocations is taken into account. Thus, the model is sensitive to variations in temperature and strain rate. The current state of the microstructure is tracked through the dislocation density, which serves as a single, physically-based internal state variable. The evolution of the dislocation density is based on the competing processes of dislocation generation and annihilation.

Klepaczko's model is effective at shear strain rates up to $\dot{\gamma}=10^4$ s^{-1} (please note that references to γ indicate the total (engineering) shear strain, which is related to the tensorial shear strain by $\gamma_{ij}=2\varepsilon_{ij}$ for $i\neq j$). Experimental stress-strain curves [75] indicate that strain rates above 10^4 s^{-1} engender marked strain hardening due to viscous drag effects that impede dislocation motion; such effects are not taken into account in Klepaczko's model.

The remainder of this section is devoted to the derivation of the Klepaczko model. The derivation presented here is rather compact; an extensive review of the role and modeling of thermal activation in the inelastic flow of polycrystalline metals has been provided by Kocks, Argon, and Ashby in ref. [76].

It is assumed that the flow stress in shear τ, may be decomposed as

$$\tau=\tau_u+\tau^* \tag{5.18}$$

where τ_u is the internal (athermal) stress, and τ^* is the effective (thermally-activated) stress. The decomposition of the flow stress assumes the existence of different barriers that impede the motion of dislocations. The internal stress is associated with long-range obstacles that are athermal in character (e.g., grain walls, cell walls, and cell dislocations). The internal stress may be expressed as

$$\tau_u=\alpha_i\mu(T)b\sqrt{\hat{\rho}} \tag{5.19}$$

where α_i is the dislocation/obstacle interaction coefficient, $\mu(T)$ is the temperature-dependent shear modulus, b is the Burgers vector, and $\hat{\rho}$ is the history-dependent dislocation density. The internal stress is proportional to the shear modulus because the strength of long-range obstacles

is controlled by the elasticity of the lattice. The temperature-dependent shear modulus is defined as

$$\mu(T) = \mu_0 \left[1 - \frac{T}{T_m} \exp\left\{ \theta_* \left(1 - \frac{T_m}{T} \right) \right\} \right] \tag{5.20}$$

where, μ_0 is the shear modulus at 0 K, T_m is the melting temperature, and θ_* is a material constant. The effective stress is associated with weaker obstacles (e.g., forest dislocations and Peierls barriers) that may be overcome by thermal fluctuations of the lattice. The effective stress is cast in a generalized Arrhenius form, i.e.,

$$\tau^* = \tau_0^*(\hat{\rho}) \left[1 - \left\{ \frac{kT}{\Delta G_0} \ln\left(\frac{\nu_0(\hat{\rho})}{\dot{\bar{\gamma}}^p} \right) \right\}^{1/q} \right]^{1/p}, \tag{5.21}$$

where $\dot{\bar{\gamma}}^p$ is the effective plastic shear strain rate, $\tau_0^*(\hat{\rho})$ is the thermally-activated part of the threshold stress (i.e., the strength barrier associated with short range obstacles at 0 K) , $\nu_0(\hat{\rho})$ is the attempt frequency factor at 0 K, ΔG_0 is the activation energy at 0 K (i.e., the activation enthalpy), k is Boltzmann's constant, and p and q are constants that describe the shape of the energy barrier. In this case, the thermally-activated part of the threshold stress is based on the interaction of mobile dislocations with immobile dislocation forests, i.e.,

$$\tau_0^*(\hat{\rho}) = \frac{\Delta G_0 \sqrt{\hat{\rho}}}{b\, a}, \tag{5.22}$$

where a is the activation distance covered by a dislocation overcoming an energy barrier. Hence, the area swept out while overcoming an energy barrier is given by $a\lambda$, where the statistically-averaged mean free path is given as $\lambda = 1/\sqrt{\hat{\rho}}$. The activation distance is assumed to be equal to the Burgers vector for a simple 'box-shaped' energy barrier. The frequency factor is expressed as

$$\nu_0(\rho) = f \hat{\rho} \nu_D b^2 \tag{5.23}$$

where f is the fraction of mobile dislocations, and ν_D is the Debye frequency.

The dislocation density is updated to account for the evolution of the microstructure during a general loading history. The dislocation density evolves with respect to the effective plastic shear strain according to

$$\frac{\partial \hat{\rho}}{\partial \bar{\gamma}^p} = M_{II}(\dot{\bar{\gamma}}^p) - k_a(\dot{\bar{\gamma}}^p, T)[\hat{\rho} - \hat{\rho}_0] \tag{5.24}$$

Here, $M_{II}(\dot{\bar{\gamma}}^p)$ is the rate-dependent dislocation generation term, $k_a(\dot{\bar{\gamma}}^p, T)$ is the dislocation annihilation factor, and $\hat{\rho}_0$ is the initial dislocation density. In the case of high-purity Al, a reasonable phenomenological expression for the dislocation generation is given as

$$M_{II} = M_0 \left[\mathrm{B} + \mathrm{C} \tanh \left\{ \mathrm{A} \ \log \left(\frac{\dot{\bar{\gamma}}^p}{\dot{\gamma}_m} \right) \right\} \right] \tag{5.25}$$

where M_0 is the dislocation generation at a reference strain rate $\dot{\gamma}_m$, and A, B, and C are material constants. The dislocation annihilation factor is defined as

$$k_a = k_0 \left(\frac{\dot{\bar{\gamma}}^p}{\dot{\gamma}_0} \right)^{-2 m_0 T} \tag{5.26}$$

where k_0 is the dislocation annihilation factor at 0 K, m_0 is the strain-hardening rate-sensitivity constant, and $\dot{\gamma}_0$ is the threshold strain rate, which may be expressed as $\dot{\gamma}_0 = f \hat{\rho} \nu_D b^2$.

The material constants for 5N polycrystalline Al are presented in Table 5-4 with the necessary physical constants. 5N polycrystalline Al and polycrystalline Al-1100 are nearly identical in composition, so the material parameters provided are justifiably extended to Al-1100. Numerical simulations utilizing the Klepaczko's model compare well with experimental data [77, 78] for shear strain rates up to 10^4 s^{-1}. Plots of the flow stress over a range of strain rates and temperatures are given in Figure 5-3.

Table 5-4. Klepaczko model parameters for 5N polycrystalline Al

Parameters	Units		Parameters	Units	
ΔG_0	J	4.58×10^{-20}	θ_*	–	0.553
p	–	1	k_0	–	3.83
q	–	1	m_0	K^{-1}	6.78×10^{-5}
b	mm	2.86×10^{-7}	M_0	$(mm)^{-2}$	4.73×10^{8}
ν_D	$(\mu s)^{-1}$	10^7	A	–	0.212
ρ_0	$(mm)^{-2}$	5.0×10^6	B	–	2.887
f	–	2.0×10^{-3}	C	–	1.924
a	mm	$2.86 \times$ x 10^{-7}	$\dot{\gamma}_m$	$(\mu s)^{-1}$	1.0
α_i	–	0.52	k	$J\text{-}K^{-1}$	1.38×10^{-23}
μ_0	GPa	30			

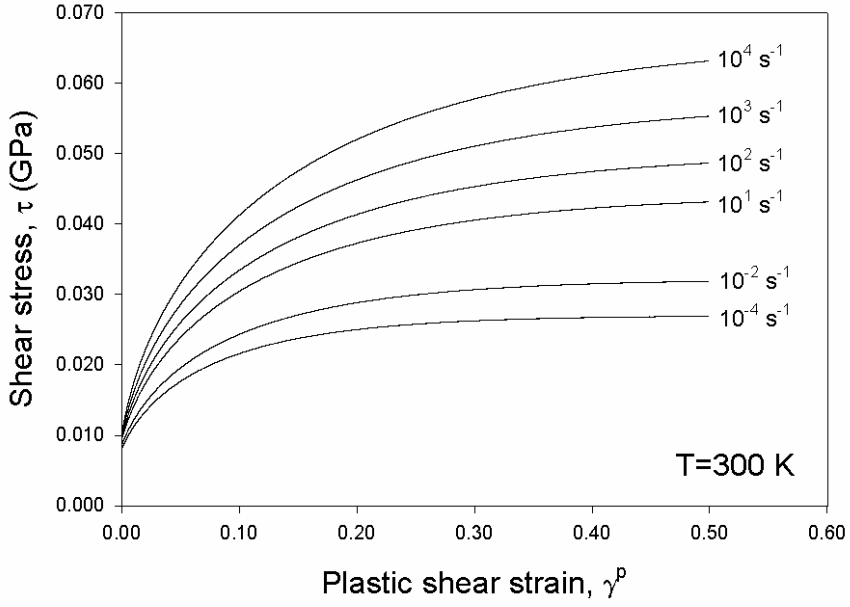

(a)

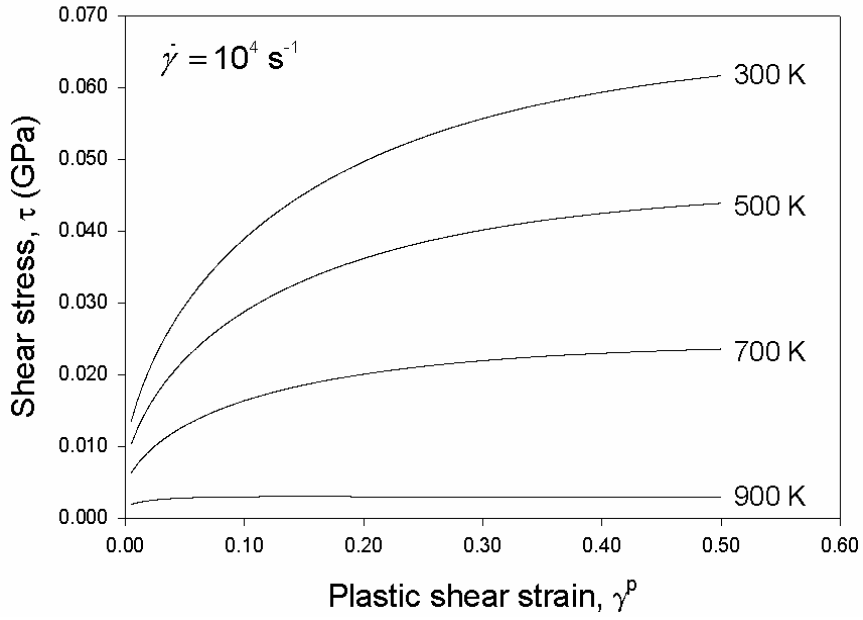

(b)

Figure 5-3. Flow stress predicted by the Klepaczko model for 5N polycrystalline Al; (a) a range of shear strain rates for T=300 K; (b) a range of temperatures for $\dot{\gamma}=10^4$ s^{-1}.

5.3.2 The Hasan-Boyce model

The Hasan-Boyce model is used to model the deviatoric stress-strain response of the epoxy phase. A brief description of the deformation behavior observed in experiments performed on Epon 828 will be given as a prelude to the model. Data from quasi-static and dynamic uniaxial compression tests, performed by Chen and Zhou [79], show that the stress-strain response of Epon 828 is characterized by five stages: (i) linear elasticity, followed by (ii) nonlinear elasticity, (iii) yielding, (iv) strain softening, and (v) eventual nearly perfect plastic flow. Chen and Zhou [79] proposed an empirical model for Epon 828, but it only agreed with experimental results at low strain levels (less than 0.10). The physically-based viscoelastic-viscoplastic model of Hasan and Boyce [80], constructed earlier for polymethyl methacrylate (PMMA), may be calibrated for use in the Epon system.

The deformation of an amorphous glassy polymer is controlled by the energetically-distributed nature of its microstructure and its thermally-activated evolution with time. The distributed nature of the microstructure is characterized by activation energy barriers. Plastic deformation occurs when local energy barriers are overcome. Here, plastic deformation is achieved by local shear transformations (i.e., molecular re-arrangements)

Local rearrangements in glassy polymers are thermoreversible. Therefore, mechanisms for both forward transformations and reverse transformations (strain recovery) must be included. Drawing on the mechanisms of thermal activation [76], the transformation rate ω may be expressed as a product of the attempt frequency ω_0 and the net probability of success according to a Boltzmann distribution, i.e.,

$$\omega = \omega_0 \left| \exp\left\{\frac{-\Delta G_f}{kT}\right\} - \exp\left\{\frac{-\Delta G_b}{kT}\right\} \right| \tag{5.27}$$

Here, ΔG_f and ΔG_b represent the activation energies for forward and backward (reverse) transformations. Again, k is Boltzmann's constant, and T is the temperature.

The thermoreversible re-arrangements of generalized quantities may be constructed as

$$\dot{\Psi} = -\Psi\omega \tag{5.28}$$

where Ψ represents the fraction of material available for such re-arrangements. However, Eq. (5.28) is only valid for microstructures that have spatially-uniform distributions of activation energies. In order to capture the energetically-distributed nature of a polymeric microstructure,

Ψ must be distributed continuously over the activation energy space; therefore, we introduce the quantity

$$\dot{\psi} = -\psi(\Delta G_f, \Delta G_b)\,\omega \tag{5.29}$$

where $\psi(\Delta G_f, \Delta G_b)$ is a probability density function (PDF) in a mathematical sense, subject to the normalization

$$\int_0^\infty \int_0^\infty \psi(\Delta G_f, \Delta G_b)\, d\Delta G_f\, d\Delta G_b = 1 \tag{5.30}$$

If a forward transformation is associated with a positive increment of inelastic strain $\Delta\gamma^p$, and a reverse transformation is associated with a negative increment of inelastic strain, the macroscopic inelastic strain rate $\dot{\gamma}^p$ is given by

$$\dot{\gamma}^p = \dot{\gamma}_0 \int_0^\infty \int_0^\infty \psi(\Delta G_f, \Delta G_b) \left[\exp\left\{\frac{-\Delta G_f}{kT}\right\} - \exp\left\{\frac{-\Delta G_b}{kT}\right\} \right] d\Delta G_f\, d\Delta G_b \tag{5.31}$$

Furthermore, if an Eyring form is assumed for the stress dependence of the activation energy (i.e., simple box-shaped energy barriers), then

$$\Delta G_f = \Delta G - \tau\,\Delta\upsilon(T) \tag{5.32}$$

$$\Delta G_b = \Delta G + \tau\,\Delta\upsilon(T) - S \tag{5.33}$$

Here, τ is the applied shear stress, $\Delta\upsilon(T)$ is the temperature-dependent shear activation volume, and S is the locally-stored transformation strain energy. It can be seen in Eq. (5.32) that the work done by the applied stress lowers the energy barrier of forward transformations. Alternatively, it can be seen in Eq. (5.33) that the reverse transformations are resisted by the applied stress, but aided by the local strain energy. Hence, the macroscopic inelastic strain rate may be re-written as

$$\begin{aligned} \dot{\gamma}^p = \dot{\gamma}_0 \int_0^\infty \psi(\Delta G) \Bigg[& \exp\left\{\frac{-\left(\Delta G - \tau\,\Delta\upsilon(T)\right)}{kT}\right\} \\ & - \exp\left\{\frac{-\left(\Delta G + \tau\,\Delta\upsilon(T) - S\right)}{kT}\right\} \Bigg] d\Delta G_f\, d\Delta G_b \end{aligned} \tag{5.34}$$

It is now necessary to choose the form of the PDF for $\psi(\Delta G)$. A pseudo-Gaussian distribution was selected in the work of Hasan and Boyce. This distribution differs from the traditional Gaussian distribution in that it has a finite bandwidth, meaning the distribution goes to zero outside a set of specified bounds. Here, the distribution is characterized by two parameters a^*

and α^{-1}, which denote the position and standard deviation of the distribution. Normalized expressions of $\psi(\Delta G)$, which become somewhat lengthy, are available in ref. [80]. When all terms in Eq. (5.34) are defined, the expression may be integrated over the range of activation energies, which yields

$$\dot{\bar{\gamma}}^p = \left(\dot{\gamma}_1^p(a^*) + \dot{\gamma}_2^p(a^*, \alpha^{-1})\right)\left[\exp\left\{\frac{\bar{\tau}\,\Delta\upsilon(T)}{kT}\right\} - \exp\left\{\frac{-\bar{\tau}\,\Delta\upsilon(T) + S}{kT}\right\}\right] \tag{5.35}$$

Here, the effective plastic shear strain rate $\dot{\bar{\gamma}}^p$ and the effective shear stress $\bar{\tau}$ are used to account for a general stress state. The terms $\dot{\gamma}_1^p(a^*)$ and $\dot{\gamma}_2^p(a^*, \alpha^{-1})$ are derived from the previous definition of the PDF, i.e.,

$$\dot{\gamma}_1^p = \dot{\gamma}_0 e^{-a^*\varpi}\frac{\sqrt{2} + (2-\varpi)e^{3\pi(1-\varpi)/4}}{\left[1+(1-\varpi)^2\right]\left(\sqrt{2}+2e^{3\pi/4}\right)} \tag{5.36}$$

$$\dot{\gamma}_2^p = \dot{\gamma}_0 e^{-\left(a^* + \pi\alpha^{-1}/2\right)\varpi}\frac{\sqrt{2}e^{\pi(1/4-\varpi)} + (2+\varpi)e^{\pi(1-\varpi/4)}}{\left[1+(1+\varpi)^2\right]\left(\sqrt{2}e^{\pi/4}+2e^{\pi}\right)} \tag{5.37}$$

where $\varpi = (kT)^{-1}$, and $\dot{\gamma}_0$ is a pre-exponential factor. The local shear activation volume is assumed to be a linear function of temperature, i.e., $\Delta\upsilon(T) = \Delta\upsilon(T_0) + \lambda_1(T - T_0)$.

The evolution of the microstructure is handled through the internal state variables a^*, α^{-1}, and S. Here, a^* and α^{-1} characterize the distribution of energy barriers, and S tracks the locally-stored transformation strain energy. The evolution of α^{-1} reflects the fact that the standard deviation of the PDF is increased, or broadened, due to the depletion of sites available for transformation with higher free volume (lower activation energy) up to the macroscopic yield point. The evolution of a^* reflects the fact that the position of PDF is shifted to the left, resulting in a lower mean activation energy, due to the creation of soft sites (higher free volumes). These soft sites are created by free volume re-distribution in the vicinity of recently-transformed sites. The evolution of the local strain energy S is the result of two competing processes: increases due to work storage and decreases due to strain recovery phenomena. Thus, the evolution of the internal state variables may be constructed[1] as

$$\dot{a}^* = -(a^* - a_{eq}^*) f(\dot{\bar{\gamma}}^p)\omega(\dot{\bar{\gamma}}^p) \tag{5.38}$$

[1] The expression for $\dot{a}^*$ reported by Hasan and Boyce differs by a negative sign. It is assumed that this was a typographical error in their publication, as the appropriate behavior of this internal state variable is described by the expression provided here.

$$\dot{\alpha}^{-1} = -(\alpha^{-1} - \alpha_{eq}^{-1})\omega(\dot{\bar{\gamma}}^p) \tag{5.39}$$

$$\dot{S} = \beta(\bar{\gamma}^p)\bar{\tau}\,\dot{\bar{\gamma}}^p - S\omega(\dot{\bar{\gamma}}^p) \tag{5.40}$$

where supplemental relations are chosen accordingly,

$$f(\bar{\gamma}^p) = \exp\left[-\zeta_0 \exp\left(-\zeta_0 \bar{\gamma}^p\right)\right] \tag{5.41}$$

$$\beta(\bar{\gamma}^p) = \beta_1\left[1 + \beta_2 \exp\left(-\beta_3 \bar{\gamma}^p\right)\right] \tag{5.42}$$

Here, a_{eq}^* and α_{eq}^{-1} are the steady-state values of the respective internal state variables, $\omega(\dot{\bar{\gamma}}^p)$ is the effective frequency of local shear transformations, and ζ_0 and β_i $(i = 1,2,3)$ are adjustable material constants. The effective frequency of inelastic shear transformations is expressed as $\omega(\dot{\bar{\gamma}}^p) = \left(\omega_0 / \dot{\gamma}_0\right)\dot{\bar{\gamma}}^p$, where ω_0 is the fundamental frequency of transformation attempts. The function $f(\bar{\gamma}^p)$ is chosen to reflect the fact that the creation of soft sites, due to volume re-distribution, occurs at a negligible rate until the effective plastic strain is sufficiently large; therefore $f(\bar{\gamma}^p)$ is near zero in the linear stage, and increases rapidly to unity in the vicinity of yield phenomena. The function $\beta(\bar{\gamma}^p)$ accounts for a decrease in the storage rate of strain energy with increasing plastic strain.

Model parameters were calibrated to experimental data [79] for Epon 828 by Lu et al. [81]; parameters and initial values of the internal state variables (a_0^*, α_0^{-1}, and S_0) are given in Table 5-5. It should be noted that the reported values of the parameters β_2 and β_3 are shifted slightly in these calculations for reasons of numerical stability; the effect of these shifts on the overall stress response of the material is insignificant.

Table 5-5. Hasan-Boyce model parameters for Epon 828

Parameters	Units		Parameters	Units	
ω_0	$(\mu s)^{-1}$	7.5×10^{5}	a_0^*	J	1.405×10^{-19}
$\dot{\gamma}_0$	$(\mu s)^{-1}$	4.0×10^{4}	a_{eq}^*	J	1.282×10^{-19}
ζ_0	–	80	S_0	J	0
λ_1	$(mm)^3$-K^{-1}	2×10^{-21}	β_1	$(mm)^3$	9.0×10^{-18}
$\Delta\upsilon(T_0)$	$(mm)^3$	1090×10^{-21}	β_2		4.0×10^{4} (a)
α_0^{-1}	J	1.602×10^{-19}	β_3		15.0×10^{4} (b)
α_{eq}^{-1}	J	2.676×10^{-19}	k	J-K^{-1}	1.38×10^{-23}

(a) $\beta_2 = 5.0\times10^{4}$ was reported in ref [81].
(b) $\beta_3 = 11.0\times10^{4}$ was reported in ref [81].

Numerical simulations exhibit reasonable agreement with the experimental results over a range of shear strain rates. Plots of the flow stress over a range of strain rates and temperatures are given in Figure 5-4. The predicted flow stress is accurate at the highest and lowest shear strain rates (9.0×10^{3} s^{-1} and 1.9×10^{-4} s^{-1}); however, the flow stress is overestimated by about 15% for intermediate shear strain rates. It should be noted that uniaxial compression data from experiments were converted to a stress state of pure shear ($\bar{\tau} = \bar{\sigma}/\sqrt{3}$, $\bar{\gamma} = \bar{\varepsilon}\sqrt{3}$). Since the Hasan-Boyce model is used for the deviatoric stresses in the epoxy phase, the incompressibility of the model in the plastic regime is not considered here.

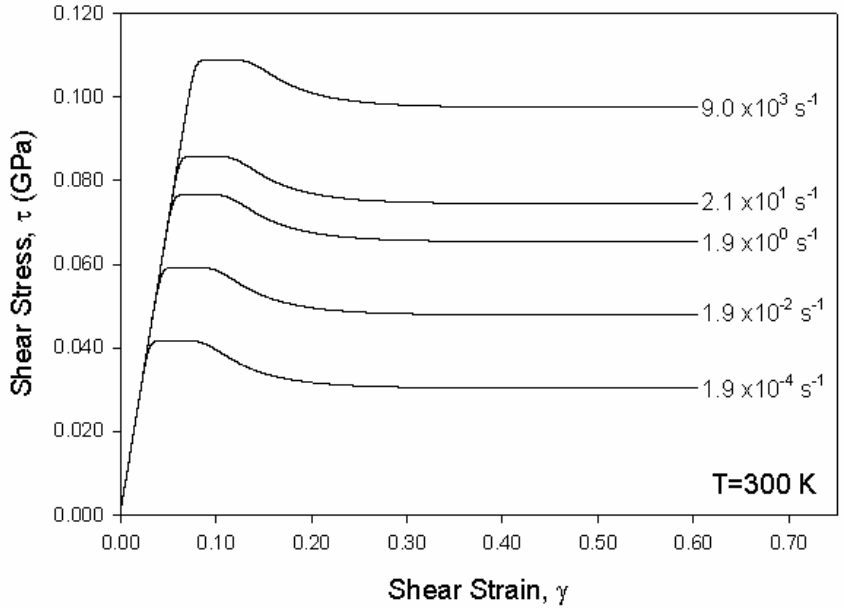

(a)

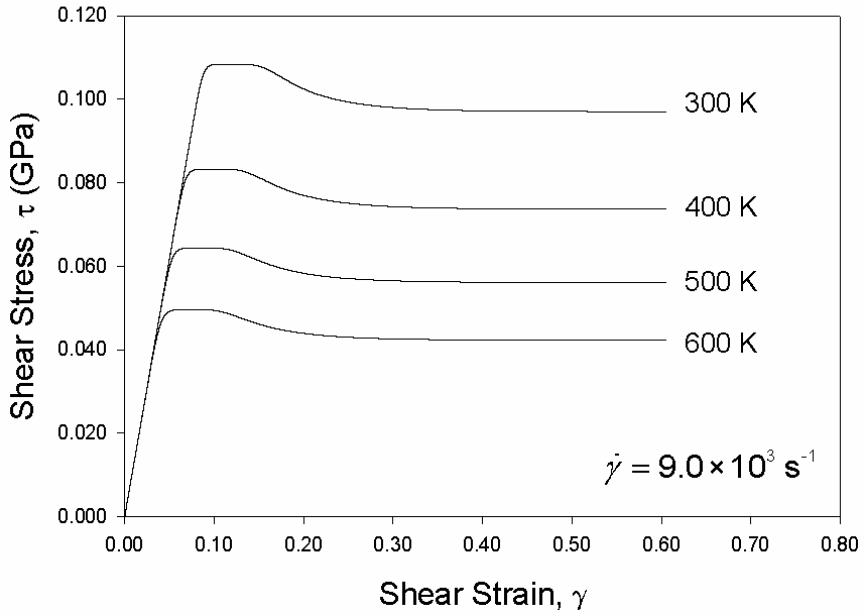

(b)

Figure 5-4. Flow stress predicted by the Hasan-Boyce model for Epon 828; (a) a range of shear strain rates for T =300K; (b) a range of temperatures for $\dot{\gamma}$ =9.0 × 10^3 s^{-1}.

5.3.3 An approximate model for the iron oxide phase

Experimental stress-strain data for iron oxide are extremely sparse at any strain rate. Consequently, a constitutive model for iron oxide was not available for this study. A simple elastic-plastic model has, therefore, been adopted, consisting of an initial linear-elastic response followed by linear, isotropic strain-hardening. The flow stress σ_y is given as

$$\sigma_y = \sigma_{y,0} + H\bar{\varepsilon}^p \tag{5.43}$$

where $\sigma_{y,0}$ is the initital yield stress, H is the linear strain-hardening coefficient, and $\bar{\varepsilon}^p$ is the effective plastic strain. One may recall that the the iron oxide phase is composed of agglomerates of smaller iron oxide subparticles. It is proposed that once the initial yield strength of the agglomerate is reached, the collection of particles will flow with a small degree of hardening. This seems to be a reasonable assumption, as the iron oxide phase is much stronger and stiffer than the aluminum and epoxy phases.

Parameters for the elastic-plastic model are given in Table 5-6. The initial yield stress of iron oxide is estimated from the Knoop hardness (KH) of a monolithoc/bulk sample as $\sigma_{y,0} \approx KH/3$; the Knoop hardness of iron oxide is reported as 545 kg-mm^2 (5.35 GPa) in ref. [82]. The initial yield stress is scaled back (~50%) to account for the strength decreases associated with agglomerates of subparticles. The strain-hardening coefficient is estimated as 0.2% of the elastic modulus. A plot of the flow stress is given in Figure 5-5; model predictions from the uniaxial stress case are again converted to a stress state of pure shear to be consistent with ealier sections.

It is recognized that the assumed constitutive relation is insensitive to variations in strain rate and temperature, which is certainly a shortcoming of the model. Future work should include an experimentally-validated phenomenological model for the iron oxide phase.

Table 5-6. Elastic-plastic model parameters for Fe_2O_3

Parameters	Units		Parameters	Units	
$\sigma_{y,0}$	GPa	0.800	H	GPa	0.200

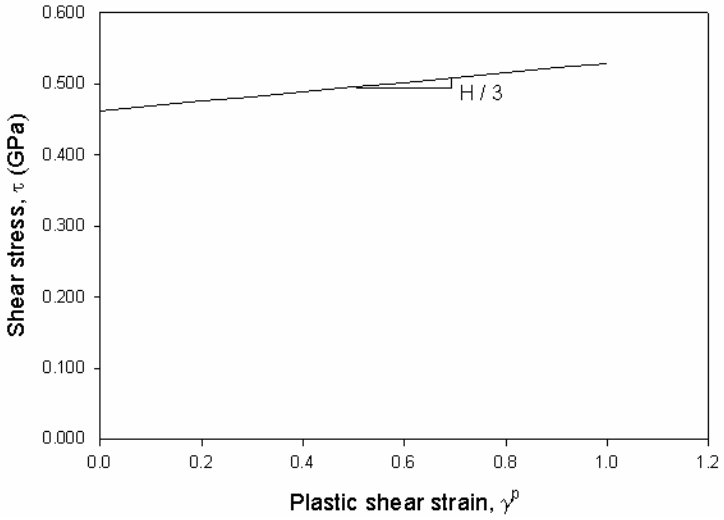

Figure 5-5. Flow stress predicted by the elastic-plastic model for Fe_2O_3.

5.4 Stress models for pores

In the Eulerian finite element method, all regions of the mesh must be filled with material. Therefore, it is assumed that the pores in the microstructure contain low-pressure air. The pressure in a pore is assumed constant, meaning pressure increases are not modeled during collapse. A small, arbitrary value was selected for the constant pressure in the pores. The deviatoric stresses in the pores are equal to zero.

5.5 Numerical implementation of the constitutive models

Methods used to update the pressure and deviatoric stress within the context of the Eulerian finite element method were provided in Chapter 4. A few supplemental details pertaining to the deviatoric strength models are presented in this section.

One may recall that the Eulerian calculations are explicit, and that forward-Euler integration is used with the time step determined from the Courant stability criterion. Here, deviatoric strength models are framed with respect to J_2-flow theory. The time-rate of change of the deviatoric stress tensor is defined simply as $\dot{\boldsymbol{\sigma}}' = 2\mu\left(\dot{\boldsymbol{\varepsilon}}' - \dot{\boldsymbol{\varepsilon}}'^{p}\right)$, where $\dot{\boldsymbol{\varepsilon}}'^{p}$ is the plastic (inelastic) part of the total deviatoric strain rate tensor $\dot{\boldsymbol{\varepsilon}}'$. The constitutive models are integrated with an elastic trial stress method, where a radial return algorithm [83] is used to return stress

states to the yield surface when necessary. The use of radial return algorithms is prevalent in Eulerian schemes because it is sufficiently accurate ($O(\Delta t)^2$), computationally efficient, and extremely robust.

The elevated temperatures that are achieved during simulation require provisions to reflect a loss of strength due to melting. In these calculations, deviatoric stresses are set equal to zero when local material temperatures reach the melting temperature (or the decomposition temperature in the case of epoxy). Hydrostatic stress components remain; therefore, melted materials flow easily, but still carry hydrostatic loads.

The effective plastic strain and the effective stress are defined in the usual manner, i.e.,

$$\bar{\varepsilon}^p = \sqrt{\frac{2}{3}\boldsymbol{\varepsilon}^p : \boldsymbol{\varepsilon}^p} \tag{5.44}$$

$$\bar{\sigma} = \sqrt{\frac{3}{2}\boldsymbol{\sigma} : \boldsymbol{\sigma}} \tag{5.45}$$

As noted earlier, the effective shear components of stress and strain are related to their respective normal counterparts through $\bar{\sigma} = \bar{\tau}\sqrt{3}$ and $\bar{\varepsilon} = \bar{\gamma}/\sqrt{3}$.

As a final aside, some provisions were necessary in the implementation of the Klepaczko and Hasan-Boyce models to avoid numerical instabilities. In the Klepaczko model, the temperature-dependent shear modulus $\mu(T)$ is set equal to zero for temperatures above the melting temperatures ($T > T_m$) to avoid negative values of the shear modulus. In the Hasan-Boyce model, the system of units implemented in calculations (Table 5-5) is different from the consistent set of units used in this modeling work (mm-μs-K). It was necessary to adopt a different set of units (Å-s-K) due to the precision of the computations.

CHAPTER 6

THE INITIAL BOUNDARY VALUE PROBLEM

The initial boundary value problem must reflect the loading conditions indicative of shock compression at the mesoscale. Such loading conditions are achieved by propagating shock waves through the SVE of the reactive particle mixtures.

As mentioned earlier, two mixture classes were selected for this study (cf. section 3.5): the 20 wt% and 50 wt% mixture classes. This chapter is devoted to the incorporation of the synthetic microstructures into the finite element code.

6.1 Boundary conditions

The shock compression process is idealized by the passage of a single 1-D shock wave. The initial boundary value problem, which aims to replicate idealized shock loading, is defined through a set of boundary conditions (BCs) applied to the models in the finite element simulations.

The Eulerian finite element method necessitates the application of BCs to both the Lagrangian and Eulerian meshes. The Lagrangian BCs impose a set of physical constraints on the material contained within the SVE. The Eulerian BCs impose a set of constraints on the motion of the Eulerian mesh. The BCs applied in these calculations are similar to those used in the prior modeling work of Benson et al. [40-42].

A compressive shock wave is propagated though the mixture by applying a Lagrangian velocity boundary condition to the left surface of the SVE. The shock wave is allowed to traverse 90–95% of the axial coordinate of the SVE before the simulation is terminated. The time at which the simulation is terminated is defined as the termination time t_{term}. The velocity boundary condition (i.e., the particle velocity U_P) is ramped up during the first stage of the simulation according to a quadratic function of time, i.e.,

$$\tilde{U}_P = \begin{cases} \left(t/t_{ramp}\right)^2 U_P & \text{for } t < t_{ramp} \\ U_P & \text{for } t \geq t_{ramp} \end{cases} \tag{6.1}$$

Here, $\tilde{U}_P$ is the blended time profile of the particle velocity, and t_{ramp} is the time period over which the velocity boundary condition is ramped up to its full value. An illustration of a typical particle velocity profile is provided in Figure 6-1. The ramp time is specified as 5% of the termination time. The velocity boundary condition is ramped up to avoid spurious oscillations in the solution associated with instantaneous loading.

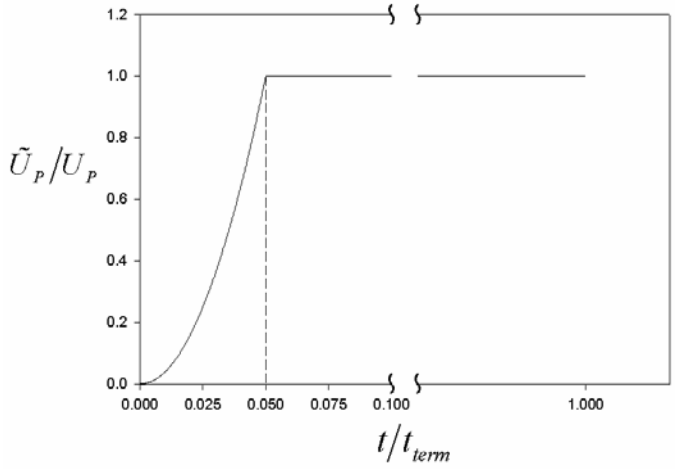

Figure 6-1. The particle velocity profile.

The ranges of particle velocities that will be simulated for each mixture class are provided in Table 6-1. The maximum particle velocity that can be achieved consistently in the 20 wt% mixture is 1.000 km-s^{-1}; numerical instabilities develop at higher particle velocities. Higher particle velocities can be achieved for the 50 wt% class. Issues pertaining to numerical instabilities will be discussed in section 6.4.

Table 6-1. Particle velocity ranges

Mixture Class	Units	Range of particle velocities, U_P
20 wt%	km-s^{-1}	0.500–1.000
50 wt%	km-s^{-1}	1.200–1.600

The remaining Lagrangian BCs restrain the motion of the SVE. Symmetry planes serve as the Lagrangian BCs for the top and bottom surfaces of the model (i.e., displacements in the normal direction are equal to zero, and surface tractions in the tangential direction are equal to zero). Thus, the geometry of the model is reflected about the top and bottom boundaries of the SVE. A fixed Lagrangian BC is imposed on the right surface of the model. Recall that the simulation is terminated before the shock front reaches the remote BC so that wave reflections are avoided. The complete set of Lagrangian BCs is depicted in Figure 6-2.

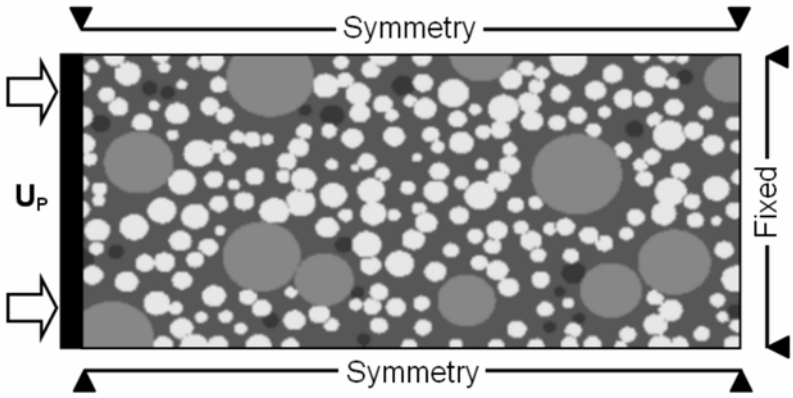

Figure 6-2. The Lagrangian boundary conditions.

The Eulerian BCs are applied in such a manner that the Eulerian mesh contracts in the direction of compression, so that the mesh is always filled by the domain. Eulerian BCs must be specified for the normal and tangential directions of each surface. The complete set of Eulerian BCs is depicted in Figure 6-3. Fixed BCs indicate that the size of the mesh remains constant in the specified direction. The 'Lagrangian' BC follows the motion of the Lagrangian mesh.

Propagating BCs allow the mesh to contract in the specified direction. Since the motion of the mesh is pre-defined, the calculations are considered Arbitrary Lagrangian-Eulerian (ALE).

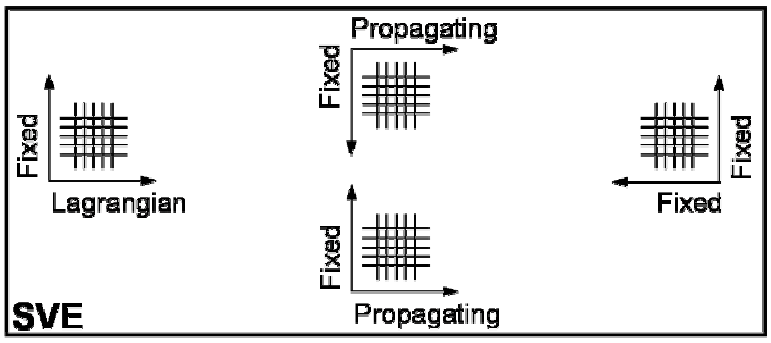

Figure 6-3. The Eulerian boundary conditions.

6.2 The plane strain assumption

The synthetic microstructures that are imported into the finite element code are 2D in nature. As mentioned earlier, the plane strain assumption is invoked to reduce the true 3-D nature of shock loading to a more tractable 2-D case (cf. section 3.3.2). The reader is reminded that the computational domain is discretized by 2-D solid quadrilateral elements that contain a single integration point and that an hourglass viscosity is used to control the modes that develop in reduced integration calculations (cf. section 4.5.4).

6.3 The explicit time step

The time step is used to integrate the constitutive models and to advance the solution in time. Forward-Euler integration is used in these calculations, so the explicit time step must be very small. As mentioned earlier, the explicit time step is controlled by the Courant stability criterion (cf. section 4.5.6), which limits the time step to the minimum time necessary for an elastic wave to propagate across the shortest edge of an element. The time step is further reduced by a factor of two to be conservative.

6.4 Numerical instabilities

Eulerian formulations are well-suited for deformation processes that involve high strain rates and extreme levels of material flow–however, multi-material Eulerian calculations are still susceptible to certain numerical instabilities. Small fragments of isolated materials contained in a mixed element are subjected to extremely high volumetric strain rates. Such strain rates may lead to the calculation of unrealistically-high mass densities or negative volumes, either of which will cause the calculations to terminate prematurely. Furthermore, some equations of state are singular at certain mass densities, e.g., the Gruneisen equation of state. It is not uncommon for a material subjected to high volumetric strain rates to reach the mass density at which the singularity occurs [45]. According to Benson [61], the best way to handle these numerical instabilities is to scale the material properties of the problematic constituents; however, this approach may significantly alter the physics of the problem.

In these calculations, the epoxy phase is usually responsible for introducing numerical instabilities, as it is the most compliant solid phase contained in the microstructure and it has a tendency to become trapped between two impinging particles of considerably higher stiffness. The numerical instabilities that may develop during the course of shock propagation limit the range of particle velocities that may be simulated for each mixture class. As shown in Table 6-1, the maximum particle velocity that can be achieved consistently for the 20 wt% mixture is U_P=1.000 km-s^{-1}. Higher particle velocities may be achieved for the 50 wt% mixtures (U_P=1.600 km-s^{-1}) because the number density of particles contained in the microstructures is substantially lower than that of the 20 wt% mixtures; thus, the entrapment of epoxy is less probable.

6.5 A study of the mesh density for the 20 wt% mixture class

The density of the Eulerian mesh is an important consideration. As with all finite element methods, the accuracy of the results increases as the mesh is refined. However, meshes that are extremely refined incur excessive computation costs. Therefore, a mesh density study is warranted to balance the accuracy and speed of the finite element calculations.

A mesh density study was conducted over a range of element sizes for a 20 wt% mixture. The density of the Eulerian mesh is defined by the number of elements that span the planar dimensions of the SVE, i.e. $N_{\mathbb{X}} \times N_{\mathbb{Y}}$ (recall the logical structure of the Eulerian mesh). The

results presented in this section are for a subset of the mesh densities investigated for an SVE measuring 14 μm × 7 μm; the subset of mesh densities is provided in Table 6-2. The number of elements per unit length that span the transverse dimension of the SVE ($N_{\mathbb{Y}} / \mathbb{Y}$) is slightly greater than that of the axial dimension ($N_{\mathbb{X}} / \mathbb{X}$). This is done because the Eulerian mesh contracts uniformly in the axial direction as the calculation proceeds; when the shock front has passed half-way through the SVE, the aspect ratio of the elements is approximately 1:1.

Table 6-2. Mesh densities

	Number of elements, $N_{\mathbb{X}} \times N_{\mathbb{Y}}$
Coarse	160×85
Intermediate	250×135
Fine	300×165

The following results were investigated to determine their respective sensitivity to refinements of the computational mesh:

1. Material deformation
2. Spatial distributions of pressure and temperature
3. Time histories of the number of reactant contact sites
4. Time histories of the number of sites that experience microscale reaction initiation

The strategy employed in this study was to refine the mesh until the changes observed in the results were insignificant. It should be noted that the results that follow were collected from the same 20 wt% mixture; the mesh density was the only characteristic that varied.

The post-shock microstructure morphology of a 20 wt% mixture subjected to a particle velocity U_P =1.000 km-s^{-1} was studied for the mesh densities of interest (coarse, intermediate, and fine). The full SVE is depicted in Figure 6-4. It can be seen in Figure 6-4, that the amount of material flow in the coarse mesh is less than that of the intermediate and fine meshes. Discrepancies between the coarse and intermediate meshes are boxed in the deformed configuration of the coarse mesh.

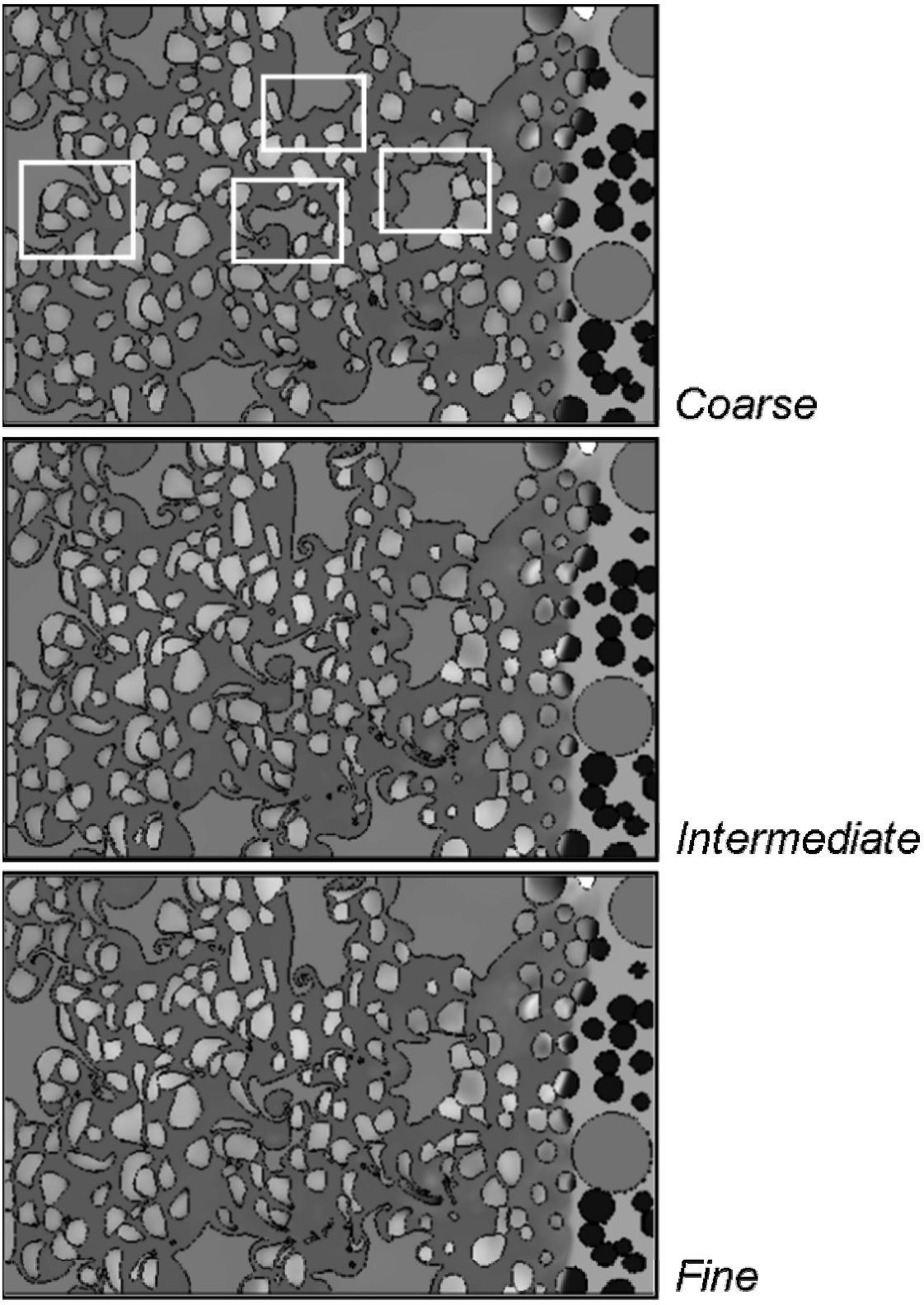

Figure 6-4. Deformation of a 20 wt% mixture for the mesh densities of interest (U_P=1.000 km-s^{-1}).

An enlarged region of the SVE, which corresponds to the boxed area furthest to the right in Figure 6-4, is depicted in Figure 6-5. Again, discrepancies between the coarse and intermediate meshes are boxed in the deformed configuration of the coarse mesh. It can be seen in Figure 6-5 that the coarse mesh fails to resolve the intricacies in material deformation at the particle surfaces, particularly in the Al phase. Additionally, iron oxide fragments that are present in the intermediate and fine meshes are lost in the coarse mesh. Differences between the material deformation of the intermediate and fine mesh are insignificant.

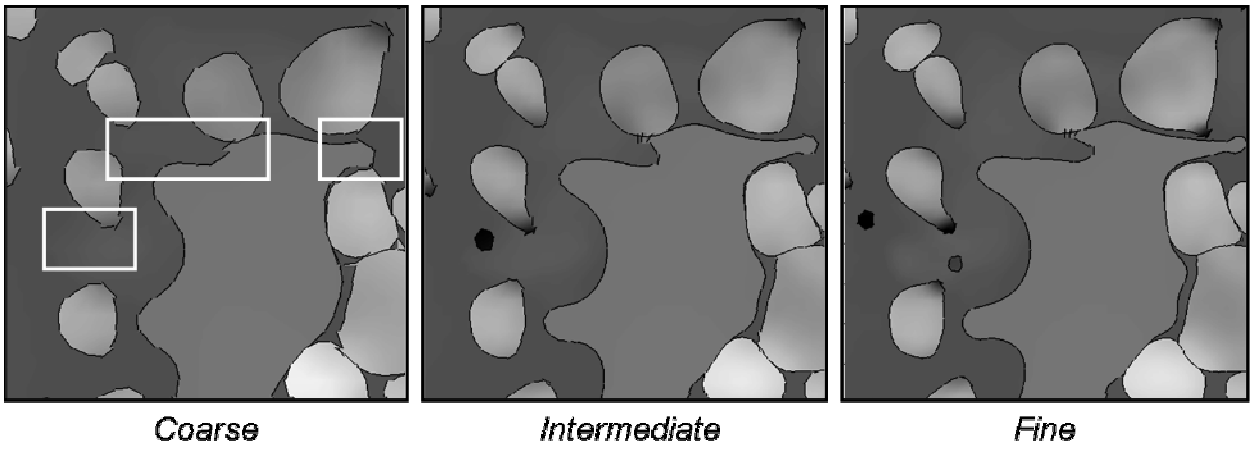

Figure 6-5. Deformation of an enlarged region of a 20 wt% mixture for the mesh densities of interest (U_P=1.000 km-s^{-1}).

Spatial profiles of pressure were obtained by recording the pressure at each node that falls on the horizontal centerline of the microstructure after the shock wave has traversed 90–95% of the SVE. Spatial profiles of temperature were constructed in the same manner. Centerline pressure and temperature profiles are plotted in Figure 6-6 and Figure 6-7, respectively, for a 20 wt% mixture discretized by the mesh densities of interest. It can be seen in Figure 6-6 that the pressure calculations of the coarse mesh exhibit moderate deviations from the pressures calculated with the intermediate and fine meshes. In particular, the pressure is overestimated by

the coarse mesh directly behind the shock front. The pressure profiles calculated by the intermediate and fine meshes are nearly identical.

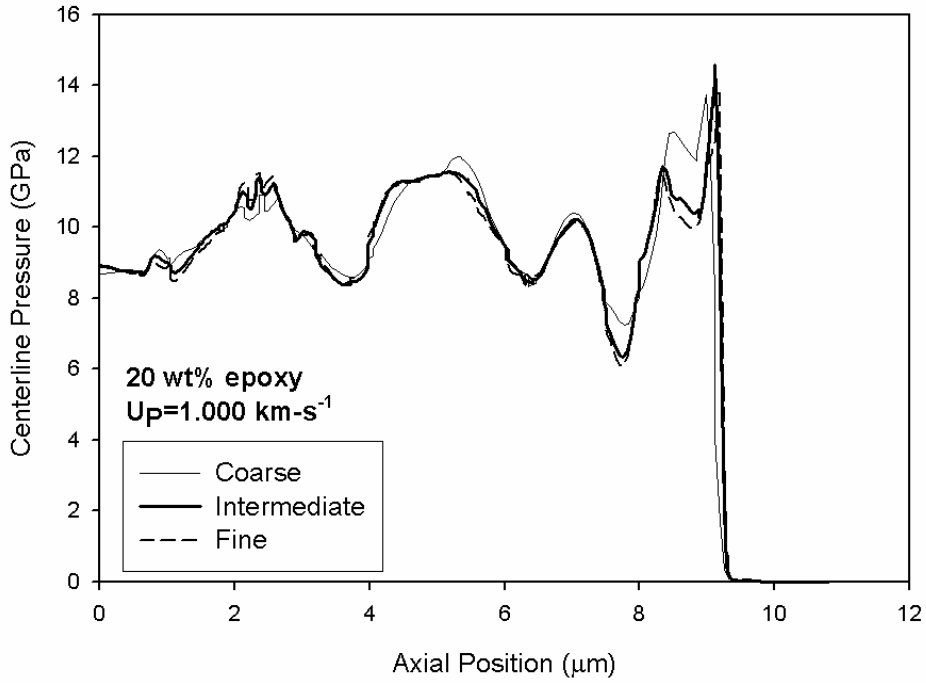

Figure 6-6. A profile of the pressure at the centerline of the SVE for the mesh densities of interest.

It can be seen in Figure 6-7 that the centerline temperatures calculated by the coarse mesh again exhibit moderate deviations from the temperatures calculated with the intermediate and fine meshes. Although it cannot be seen clearly in the Figure 6-7, the temperature spike (near an axial position of 1 μm) calculated by the coarse mesh is approximately 1000 K; the temperature spike calculated by the intermediate and fine meshes is approximately 1300 K. The differences in the temperature profiles calculated by the intermediate and fine meshes are insignificant.

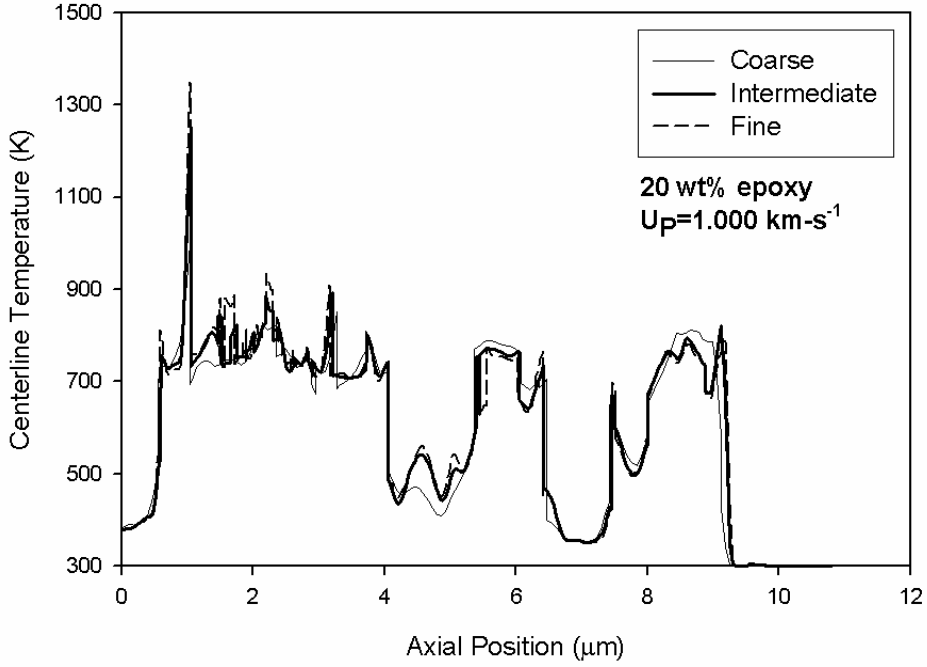

Figure 6-7. A profile of the temperature at the centerline of the SVE for the mesh densities of interest.

The evolution of the number of reactant contact sites present in the SVE is an important result of these calculations. Therefore, this quantity must be considered in the mesh density study. A reactant contact site is simply a small region of the SVE where the reactants (Al and Fe_2O_3) are in direct, intimate contact. This quantity evolves with time as the microstructure deforms. The evolution of the number of reactant contact sites N_c for a 20 wt% mixture discretized by the mesh densities of interest is depicted in Figure 6-8. It can be seen in Figure 6-8 that the coarse mesh underestimates the number of reactant contact sites in the later stages of the simulation, as compared to the calculations of the intermediate and fine meshes. The number of reactant contact sites calculated by the intermediate and fine meshes follows the same trend, despite the inherent variability of the measure.

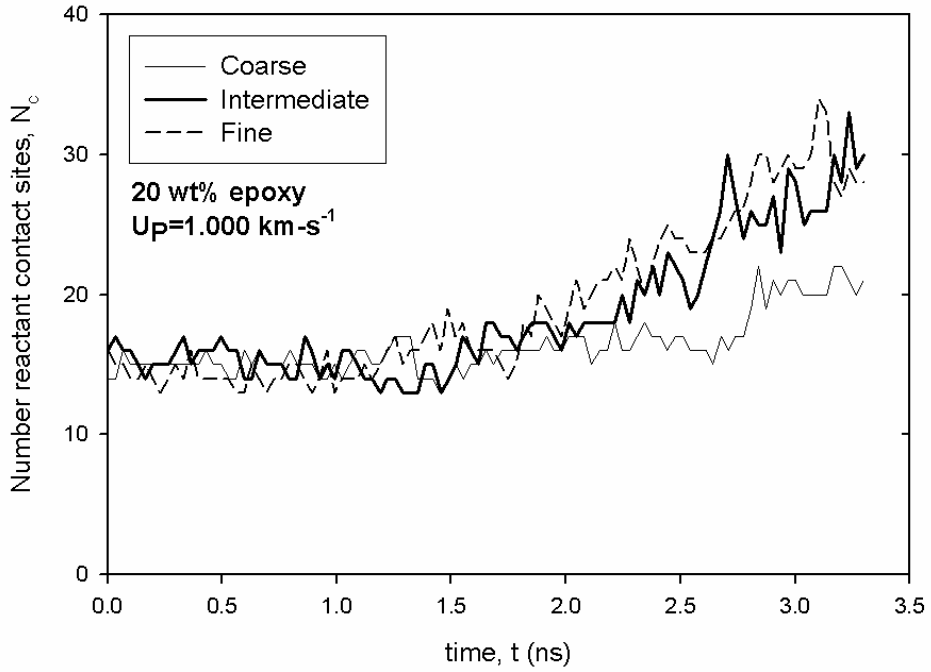

Figure 6-8. Evolution of the number of reactant contact sites for the mesh densities of interest.

The predictions of sites that experience microscale reaction initiation are key results of these analyses. However, at this point, the topic of microscale reaction initiation has not been approached nor has it been defined. Therefore, a discussion of the mesh convergence for such results is premature. In Chapter 9, it will be shown that the predictions of microscale reaction initiation are sensitive to the mesh density, and that the results converge for the intermediate mesh.

The results presented above lead to the conclusion the intermediate mesh (250×135 elements) is of sufficient density for analyses pertaining to the 20 wt% mixtures. The coarse mesh is inadequate, as significant discrepancies were observed in all results of interest. Alternatively, the results obtained with the fine mesh are nearly identical to those of the intermediate mesh. The small improvements in accuracy that are obtained with the fine mesh are not worth the added computational cost.

In the previous work of Benson [41], it was recommended that the smallest particles be spanned by 2–3 elements, at a minimum. The mesh density that has been selected for these

calculations spans the smallest particles (in the iron oxide phase) with 3–4 elements. It is noted that shock propagation is not highly resolved in the smallest of particles, but there are usually only a few of these particles in a typical particle distribution. The majority of iron oxide particles are spanned by 6–8 elements.

6.6 A study of the domain size for the 20 wt% mixture class

The size of the SVE is an issue that warrants consideration. The SVE must be large enough, and should contain enough particles, so that the results obtained are statistically relevant. Therefore, a study of the domain size was conducted to balance the speed and statistical relevance of the finite element calculations.

A range of domain sizes were investigated for a 20 wt% mixture in this study. The planar dimensions of the SVE that were considered are provided in Table 6-3. The range of domain sizes investigated may seem limited–however, the number of inclusions contained within the SVE ranges approximately from 190 (for the small domain) to 340 (for the large domain). The intermediate mesh density, which was selected for the SVE measuring 14 μm × 7 μm, was scaled appropriately to the smaller and larger domains. The axial dimension $\mathbb{X}$ is twice as large as the transverse dimension $\mathbb{Y}$ so that adequate sampling regions are available after the shock front is fully developed.

Table 6-3. Domain sizes

	SVE dimensions, $\mathbb{X} \times \mathbb{Y}$
Small	12 μm × 6 μm
Medium	14 μm × 7 μm
Large	16 μm × 8 μm

It is not useful to investigate the deformation behavior of the particles or the spatial profiles of pressure and temperature for the different domain sizes, as these results are not particularly sensitive to the domain size. Instead, we must consider the results that depend directly on the size of the SVE; such results include:

1. Time histories of the number of reactant contact sites
2. Time histories of the number of sites that experience microscale reaction initiation

The evolution of the areal density of reactant contact sites (N_c / A) for three different 20 wt% mixtures contained in the domain sizes of interest is depicted in Figure 6-9 (here, A is the area of the SVE). It can be seen in Figure 6-9 that all three domain sizes predict approximately the same levels of reactant contact density, i.e., there is no apparent monotonic trend associated with increases in domain size. Therefore, this measure is negligibly sensitive to the sizes of the domains considered here.

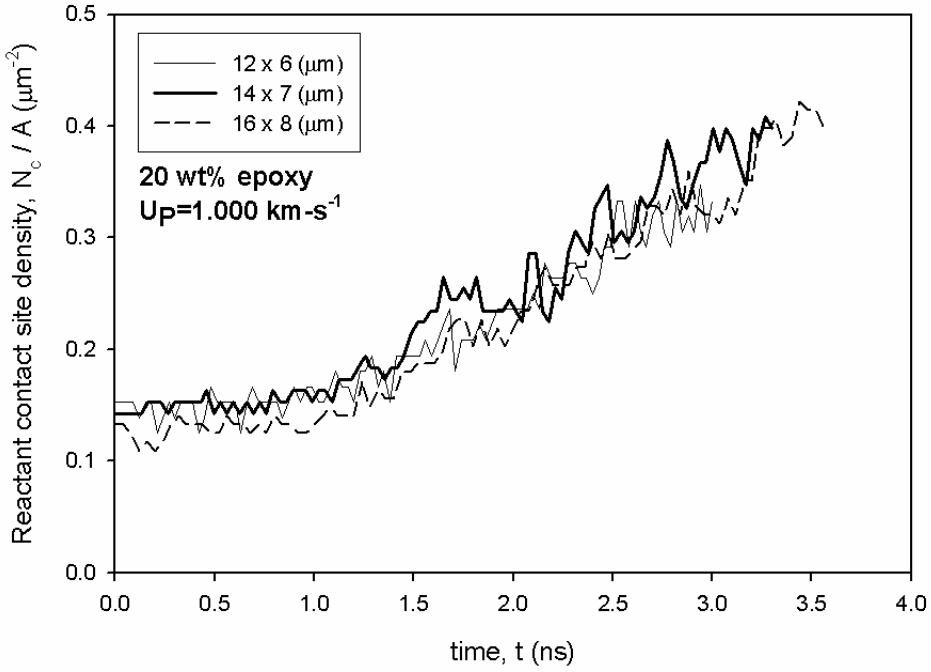

Figure 6-9. Evolution of the areal density of reactant contact sites for the domain sizes of interest.

The evolution of the areal density of sites that experience microscale reaction initiation must be considered in the selection of the domain size–but again, such results have not yet been defined. A discussion of the domain convergence is postponed until Chapter 9, where it will be shown that convergence is achieved for the medium-sized domain.

The cases presented above lead to the conclusion that the medium-sized domain (14 μm × 7 μm) is of sufficient size for analyses pertaining to the 20 wt% mixtures. The small

domain did not contain enough particles for convergence of the microscale reaction initiation results. Alternatively, the results obtained for the large domain were not noticeably different from those obtained with the medium-sized domain; therefore, the medium-sized domain is chosen in lieu of the increased computational cost of the large domain.

6.7 Selection of the mesh density and domain size for the 50 wt% mixture class

Studies of the mesh density and domain size were also conducted for the 50 wt% mixture class. The procedures used in the studies pertaining to the 50 wt% mixture class were identical to those outlined for the 20 wt% mixture class in sections 6.5–6.6. A derivation of the results is omitted for brevity.

The size of the SVE selected for the 50 wt% mixtures is $22\ \mu\text{m} \times 11\ \mu\text{m}$. The size of the SVE is increased from that of the 20 wt% mixtures so that an adequate number of Al particles are included in the distributions. The mesh density selected for this larger domain is $N_{\mathbb{X}} \times N_{\mathbb{Y}} = 380 \times 200$ elements.

CHAPTER 7

THERMOMECHANICAL RESPONSES AT THE PARTICLE LEVEL

A priority of this research is to simulate the thermal, mechanical, and chemical interactions that occur at the particle level during shock compression. The observation of these interactions provides insight to the conditions that lead to shock-induced reaction initiation (at the mesoscale) and reaction propagation (at the macroscale). The coupled thermal and mechanical responses of the shock-compacted particle mixtures will be explored in this chapter; chemical responses will be addressed in Chapter 9.

The finite element simulations resolve the microscale thermal and mechanical responses of the particle mixtures during shock compression. The thermomechanical responses studied in the polymer-bonded Al+Fe_2O_3 thermite system include:

1. Microstructure-scale deformation
2. Spatial distributions of pressure and temperature
3. Melting of the constituent phases
4. The evolution of intimate reactant contact

The results from the finite element simulations are presented for the 20 wt% and 50 wt% mixture classes in the sections that follow.

7.1 Post-shock microstructure morphologies

Microstructure morphologies in the deformed state are shown for a 20 wt% mixture in Figure 7-1. Here, the SVE was loaded with particle velocities of 0.500 km-s^{-1} and 1.000 km-s^{-1}. The same powder microstructure was subjected to different load cases to highlight the differences in particle deformation. It is clear that the 1.000 km-s^{-1} load case exhibits substantially greater amounts of plastic deformation than the 0.500 km-s^{-1} load case. Inelastic flow in the Al phase is particularly severe. The iron oxide phase exhibits a considerably stiffer response, as agglomerates remain fairly circular in the 0.500 km-s^{-1} load case; the classical 'parachute shape' is assumed in the 1.000 km-s^{-1} load case. Higher levels of 'turbulent flow' (a term used qualitatively in this context) are observed for the 1.000 km-s^{-1} load case.

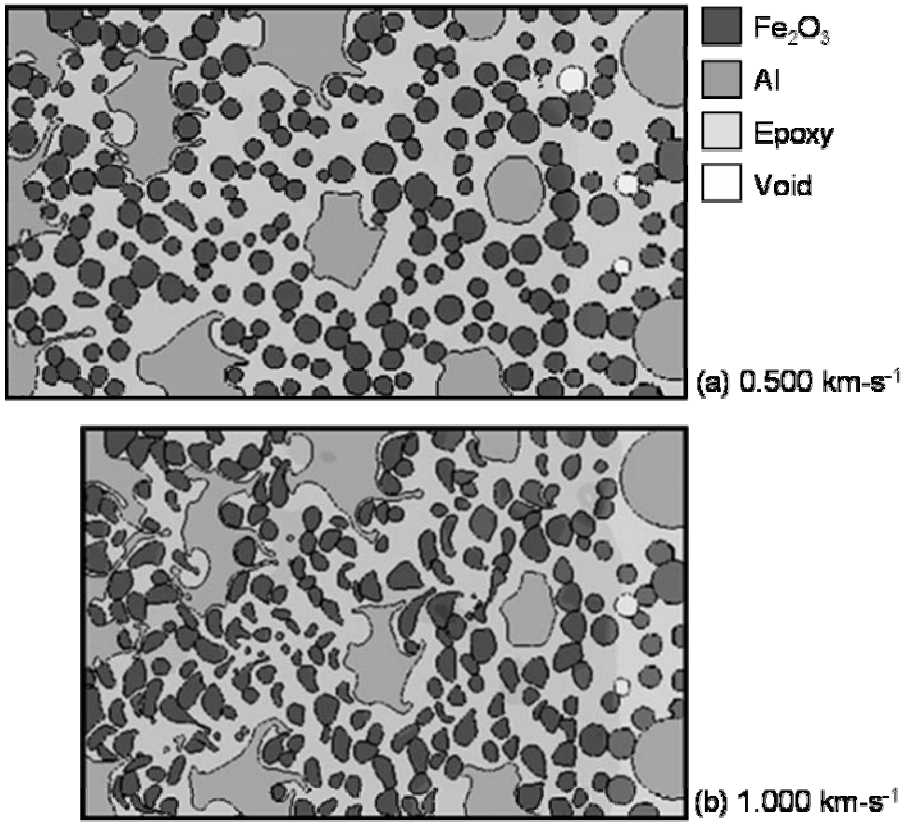

Figure 7-1. Post-shock microstructure morphologies for a 20 wt% mixture subjected to (a) the 0.500 km-s^{-1} load case and (b) the 1.000 km-s^{-1} load case.

The post-shock microstructure morphologies for a 50 wt% mixture are shown in Figure 7-2. Here, the SVE was subjected to particle velocities of 1.200 km-s^{-1} and 1.600 km-s^{-1}. Again, the same powder microstructure was subjected to different load cases to highlight the differences in particle deformation. The observations noted for the 20 wt% mixtures apply here as well. A few additional observations are noted: (i) the bowing of the iron oxide phase is heavily pronounced for the 1.600 km-s^{-1} load case and (ii) the fragmentation of the iron oxide phase is prevalent for the 1.600 km-s^{-1} load case. The latter observation is of particular interest, as this behavior is only slightly noticeable for the 20 wt% mixture subjected to the 1.000 km-s^{-1} load case and the 50 wt% mixture subjected to the 1.200 km-s^{-1} load case.

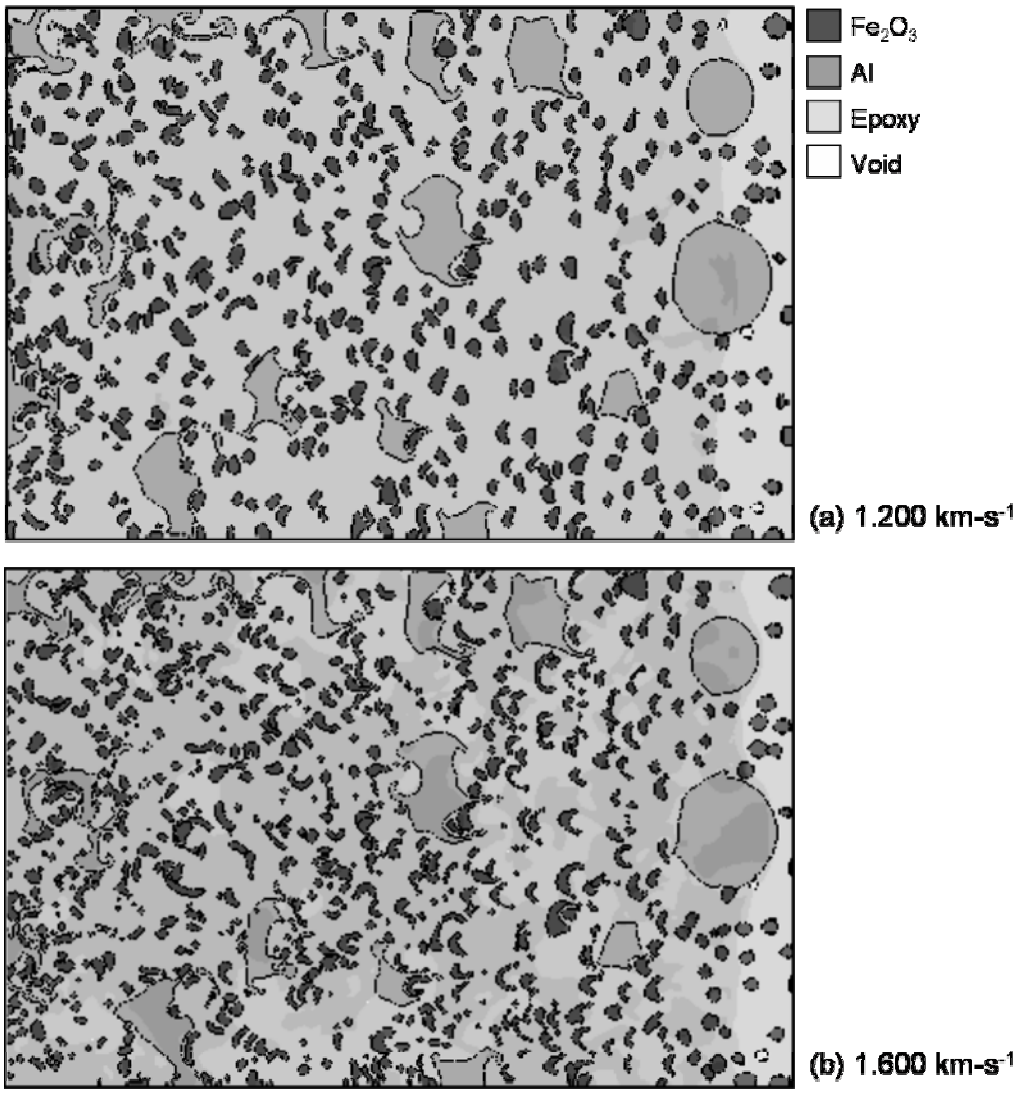

Figure 7-2. Post-shock microstructure morphologies for a 50 wt% mixture subjected to (a) the 1.200 km-s^{-1} load case and (b) the 1.600 km-s^{-1} load case.

In both mixture classes, the Al particles flow in-between and around the strong iron oxide obstacles. Damage criteria for material failure (fracture) have not been implemented for the Al phase, so the Al particles likely exhibit higher levels of ductility than would be considered normal. However, the temperatures of these particles approach their melting temperature, so increases in ductility might be expected. The inelastic flow of the Al particles could be an important consideration in the design of energetic powder mixtures; for example, if it is desirable to delay the onset of reaction initiation, the content and dispersion of Al particles could be manipulated to control (to an extent) the number density of reactant contact sites. The levels of fragmentation in the iron oxide phase could also be a design consideration; for example, the extreme fragmentation observed in the 50 wt% mixture subjected to the 1.600 km-s^{-1} load case would lead to considerably higher levels of reactant contact.

Spurious deformation artifacts tend to arise within 1 μm of the velocity boundary condition (i.e., the left surface of the SVE) for both mixture classes, as shown in Figure 7-1(b) and Figure 7-2(b). Particle deformation in this region is more severe than that found away from the left surface of the model. Temperature anomalies were also observed near the left surface of the SVE; this 'wall heating' phenomenon is caused by the addition of the shock viscosity [42]. Future sampling of results will omit consideration of this thin strip of the domain. Significant artifacts were not found near the planes of symmetry.

Unfortunately, post-shock micrographs of the microstructure are not available from experiments. The severe fragmentation experienced during impact precludes recovery of the samples. Therefore, our predictions of the deformed microstructure morphologies cannot be compared to experimental data.

7.2 Spatial distributions of pressure and temperature

Spatial profiles of pressure and temperature quantify the thermomechanical responses of the SVE. Such measures resolve particle-level interactions and highlight the heterogeneous nature of the microstructure during shock compression. Furthermore, the spatial profiles of pressure allow us to compare simulation results to experimental data.

Shock pressures are measured experimentally in a macroscopic sense. Stress gages on the free surfaces of a specimen record the impact stress and the propagated stress during an impact test. However, the spatial distributions of pressure calculated in the finite element

simulations are highly non-uniform due to the heterogeneity of powder microstructures. Therefore, averaging techniques must be used to convert the heterogeneous pressure distributions to measures that can be compared to experimental data.

In a method similar to that used by Benson [45], a slice of the microstructure has been taken at the horizontal centerline of the SVE, as shown in Figure 7-3. Here, the position of the shock wave front is clearly visible; it is the boundary between the material residing at ambient pressure (the white region) and the material experiencing elevated pressures (the dark gray regions). The values of pressure for the nodes that fall on the horizontal centerline are recorded. This construction yields a 1-D distribution of pressure along the axial direction (x), which shall be known as the centerline pressure P_c (averaging has not been performed here). If one imagines taking a horizontal slice of the microstructure at every nodal position in the transverse direction (y) and averaging the values, transversely-averaged 1-D profiles of pressure are obtained along the axial coordinate of the SVE as

$$\overline{P}_j = \frac{1}{n_{\mathbb{Y}}} \sum_{k=1}^{n_{\mathbb{Y}}} P_{j,k} \tag{7.1}$$

Here, $\overline{P}_j$ is the transversely-averaged pressure on the centerline at node j, $n_{\mathbb{Y}}$ is the number of nodes in the transverse direction, and $P_{j,k}$ is the pressure value at the node (j,k). The 1-D transversely-averaged pressure profiles are averaged along the axial position of the SVE (behind the shock front) to obtain the stationary pressure P_{st}, which may be compared to the propagated stress in experiments.

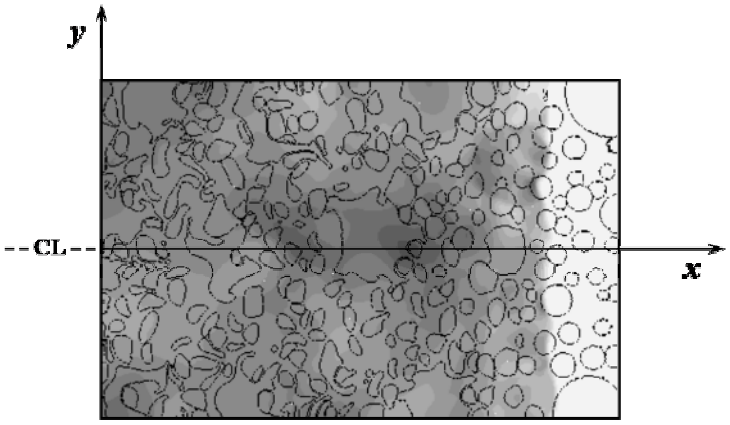

Figure 7-3. The coordinate system and centerline (CL) of the SVE.

The method outlined above is also used to construct centerline temperature profiles. However, it is not desirable to construct transversely-averaged profiles of temperature. Averaging schemes would smear out the temperature gradients present in the microstructure, which is undesirable because local temperature fields are of primary interest. Therefore, our interests shall reside in the centerline temperature profiles; if necessary, the average temperature of the SVE can be inferred from the centerline profiles.

Centerline pressure profiles and transversely-averaged pressure profiles for three different 20 wt% mixtures subjected to a range of particle velocities are provided in Figure 7-4 and Figure 7-5, respectively. Centerline temperature profiles for three different 20 wt% mixtures subjected to a range of particle velocities are provided in Figure 7-6.

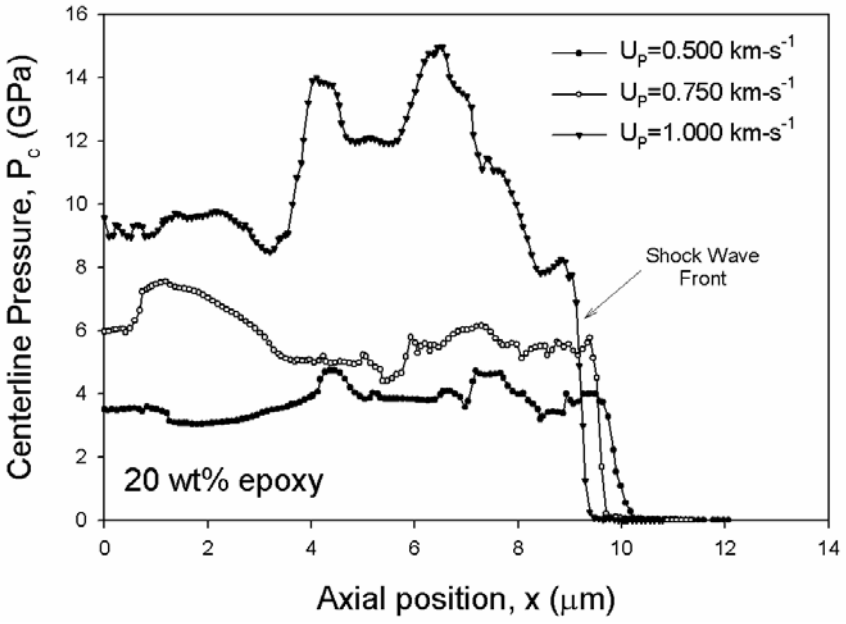

Figure 7-4. Centerline pressure profiles for the 20 wt% mixture class.

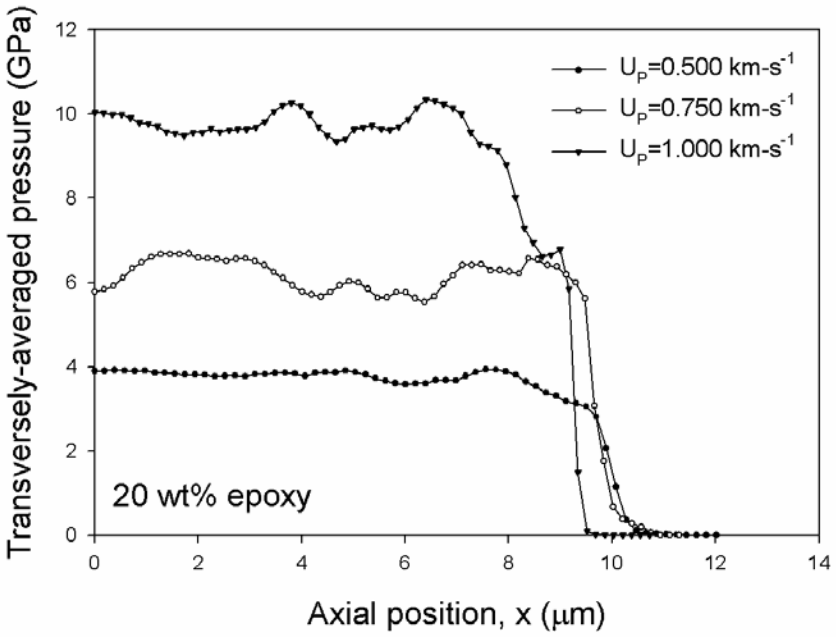

Figure 7-5. Transversely-averaged pressure profiles for the 20 wt% mixture class.

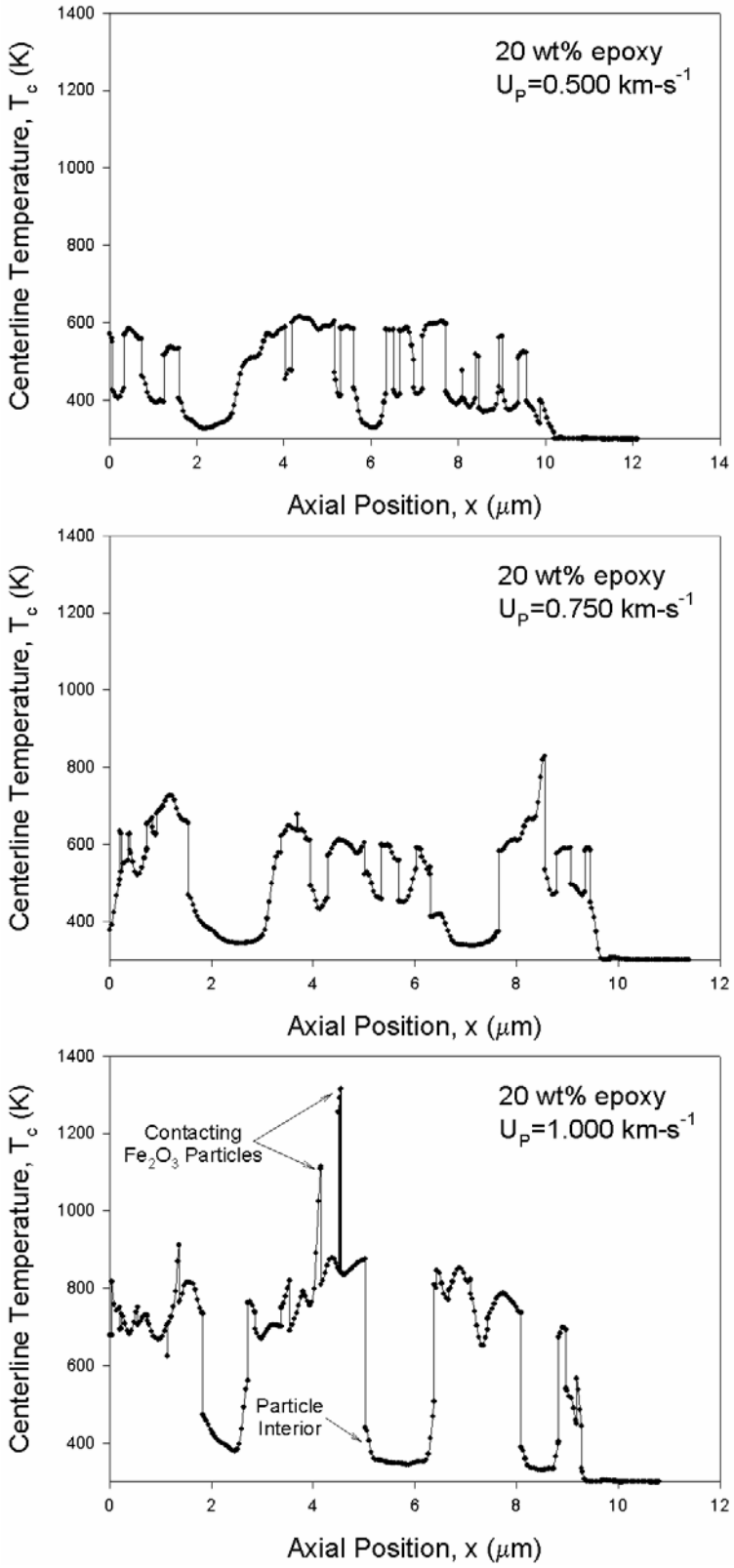

Figure 7-6. Centerline temperature profiles for the 20 wt% mixture class.

Centerline pressure profiles and transversely-averaged pressure profiles for three different 50 wt% mixtures subjected to a range of particle velocities are provided in Figure 7-7 and Figure 7-8, respectively. Centerline temperature profiles for three different 50 wt% mixtures subjected to a range of particle velocities are provided in Figure 7-9.

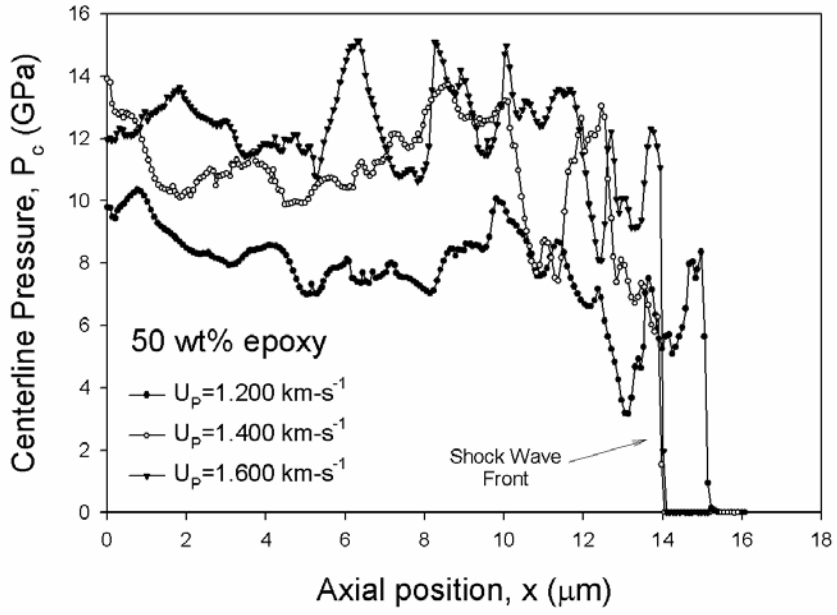

Figure 7-7. Centerline pressure profiles for the 50 wt% mixture class.

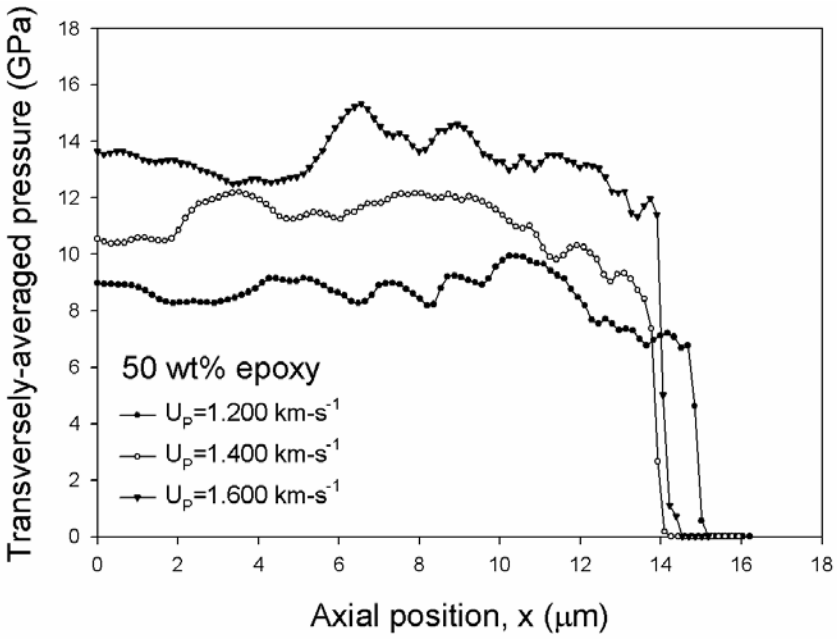

Figure 7-8. Transversely-averaged pressure profiles for the 50 wt% mixture class.

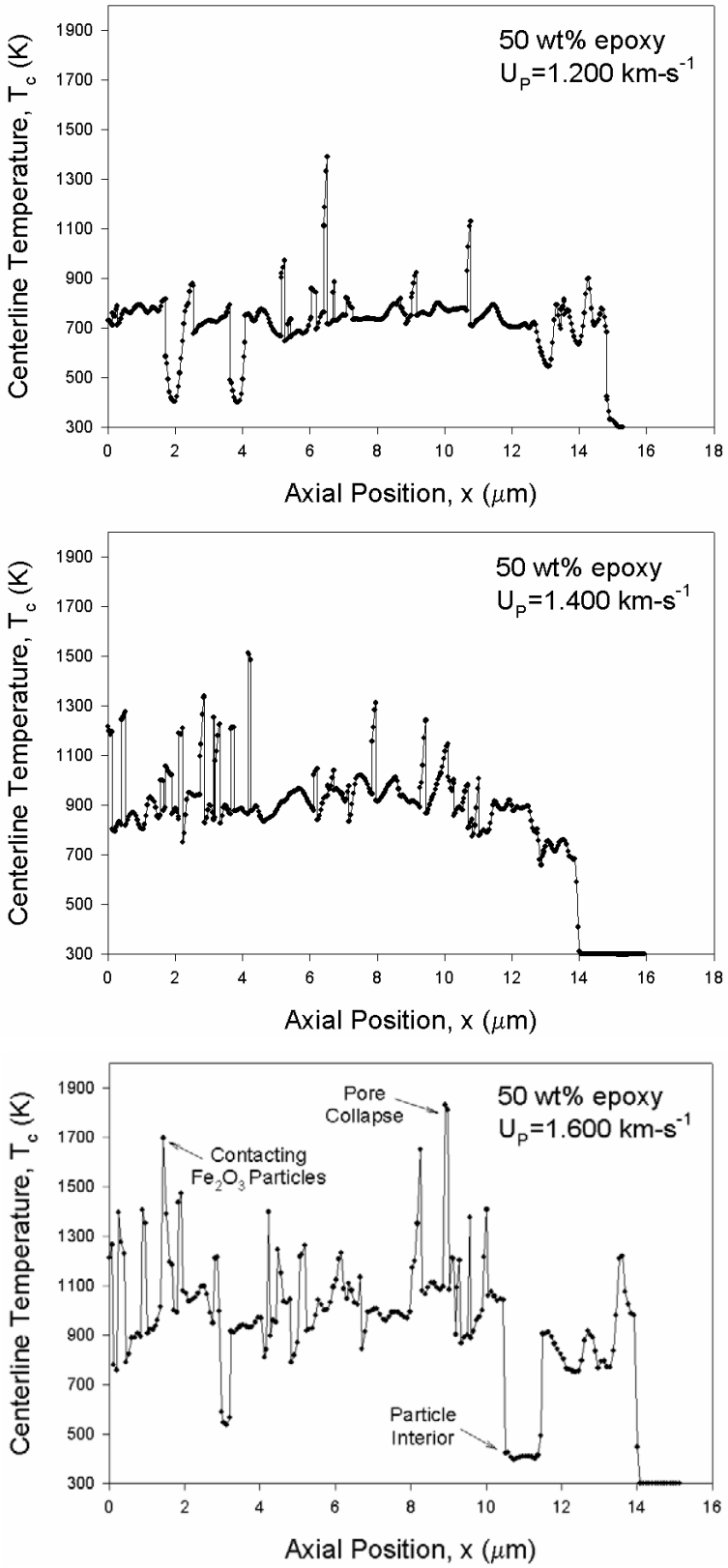

Figure 7-9. Centerline temperature profiles for the 50 wt% mixture class.

The sudden drop in pressure depicted in Figure 7-4 and Figure 7-7 represents the shock wave front (i.e., the boundary between virgin material and shocked material). The width of the shock front is dependent on the magnitude of the particle velocity; higher particle velocities generate shock waves with sharp, well-defined fronts. Here, the shock front is spread over 8–10 elements (~0.4 μm) for the particle velocities associated with the 20 wt% mixtures, and 3–6 elements (~0.3 μm) for the particle velocities associated with the 50 wt% mixtures.

As shown in Figure 7-4 and Figure 7-7, the relative magnitude of pressure peaks increases with particle velocity. Higher levels of variability are contained in the centerline pressure profiles as compared to the transversely-averaged pressure profiles due to the heterogeneity of the mixture (e.g., moderate pressure spikes occur at particle interfaces). As shown in Figure 7-5 and Figure 7-8, transversely-averaged pressure profiles are relatively flat due to the averaging scheme described above. As shown in Figure 7-6 and Figure 7-9, centerline profiles of temperature are extremely erratic due to temperature spikes found at contacting particle boundaries and in void-collapsed regions, and temperature minima at the Al particle interiors. An approximate mean temperature of the SVE may be inferred for the 50 wt% mixtures subjected to the 1.200 km-s^{-1} and 1.400 km-s^{-1} load cases, due to the high epoxy content of the microstructure; however, the centerline temperature profile for the 1.600 km-s^{-1} load case contains higher variability.

7.3 Melting behavior

The melting of each phase is important to the study of the thermomechanical responses at the particle level, as well as future studies of reaction initiation at sites of intimate reactant contact. The melting of the Al phase is an important consideration, as reactions in experiments (at ambient pressure) initiate near the melting temperature of Al (926 K). The decomposition of epoxy causes a loss of strength in the matrix phase, which will induce higher levels of mixing and turbulent flow. Any melting in the iron oxide phase will also lead to higher levels of flow due to a loss of strength.

Spatial distributions of melted materials in a 20 wt% mixture subjected to the 1.000 km-s^{-1} load case are depicted in Figure 7-10. The dark gray regions in Figure 7-10 indicate materials that have melted completely (including epoxy decomposition); white regions indicate no melting. The decomposition of the epoxy phase closely follows the shock front, as

temperatures reach 600 K directly behind the shock front; temperatures in regions of epoxy trapped in-between iron oxide particle exceed 1000 K.

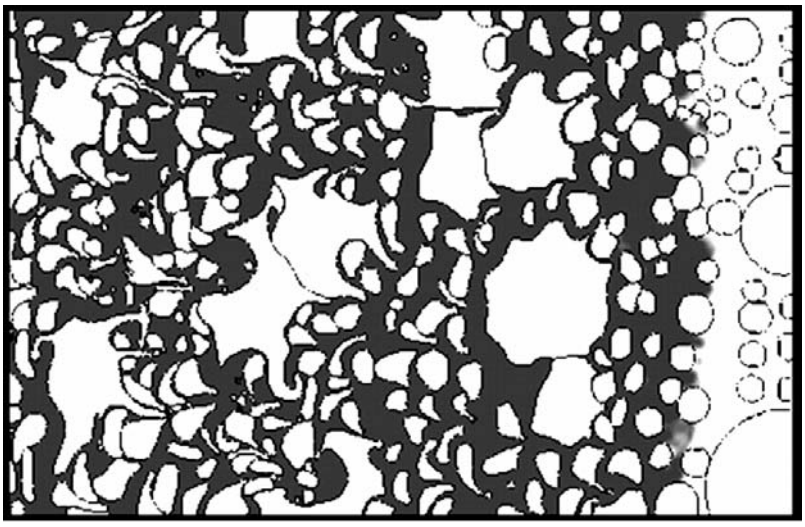

Figure 7-10. Spatial distributions of melted material in a 20 wt% mixture subjected to the 1.000 km-s^{-1} load case.

An enlarged region of a 20 wt% mixture subjected to the 1.000 km-s^{-1} load case is depicted in Figure 7-11. Again, dark gray regions indicate materials that have melted–however, the decomposition of the epoxy phase is omitted for clarity. A bold circle has been placed around two iron oxide particles that experience melting. The small iron oxide fragment experiences complete melting, whereas the neighboring iron oxide particle has begun to melt at the surface. This sort of melting behavior is scattered intermittently throughout the SVE for the 1.000 km-s^{-1} load case. Interestingly, the Al phase experiences no melting. Neither of the particulate phases melt for the 0.750 km-s^{-1} or 0.500 km-s^{-1} load cases.

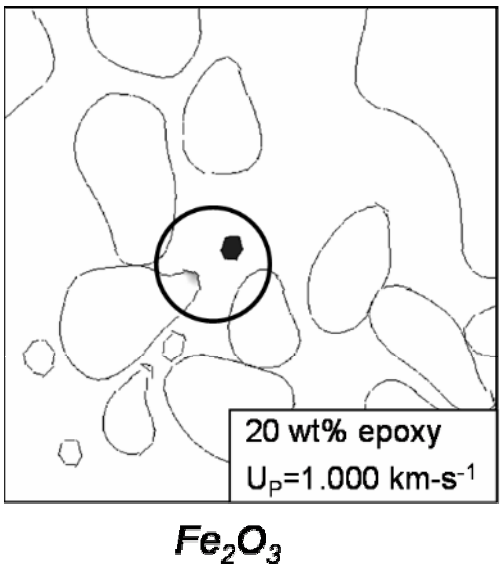

Figure 7-11. An enlarged view of the spatial distribution of melted Fe_2O_3 in a 20 wt% mixture subjected to the 1.000 km-s^{-1} load case.

The epoxy phase decomposes immediately behind the shock wave front in the 50 wt% mixtures for all particle velocities simulated, just as it did in the 20 wt% mixtures. For a 50 wt% mixture subjected to the 1.600 km-s^{-1} load case, temperatures in the epoxy matrix directly behind the shock front reach 1000 K, and volumes of epoxy compressed in-between iron oxide particles exceed 1400 K.

Enlarged regions of two 50 wt% mixtures subjected to the 1.200 km-s^{-1} and 1.600 km-s^{-1} load cases are depicted in Figure 7-12 and Figure 7-13, respectively. Again, the decomposition of the epoxy phase is omitted for clarity, and bold circles have been placed around particles that experience melting. As shown in Figure 7-12, small fragments of both Al and iron oxide experience melting sporadically throughout the SVE for the 1.200 km-s^{-1} load case. The melting behavior for the 1.600 km-s^{-1} load case is somewhat different. As shown in Figure 7-13, isolated fragments of Al still melt–but now, the melting of the fragments of iron oxide is widespread. The melting of the iron oxide particle surfaces is also more pronounced.

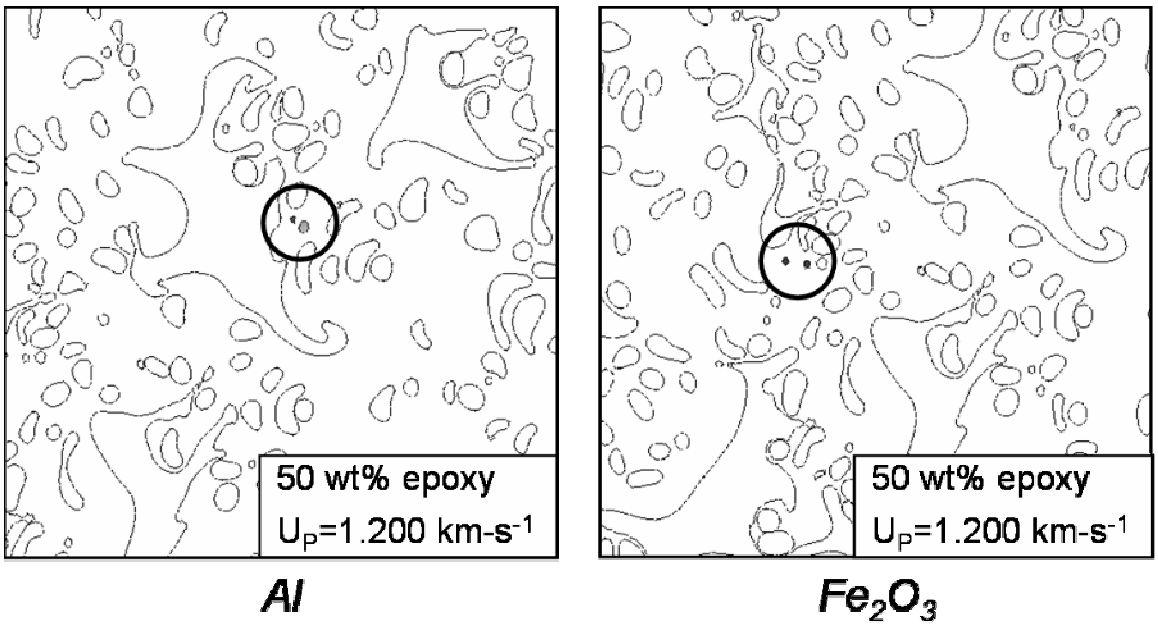

Figure 7-12. Enlarged views of the spatial distributions of melted Al and Fe_2O_3 in a 50 wt% mixture subjected to the 1.200 km-s^{-1} load case.

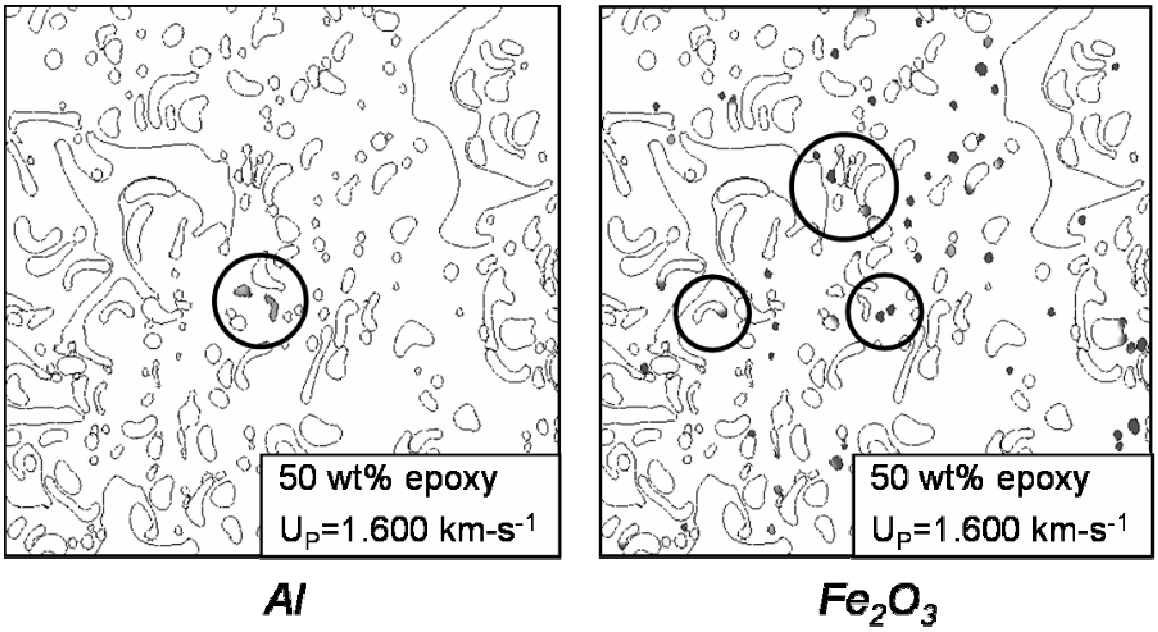

Figure 7-13. Enlarged views of the spatial distributions of melted Al and Fe_2O_3 in a 50 wt% mixture subjected to the 1.600 km-s^{-1} load case.

The Al phase exhibits very small amount of melting in both the 20 wt% and 50 wt% mixtures. With the exception of the 1.600 km-s^{-1} load case, the iron oxide phase also exhibits small amounts of melting. This should be expected for the iron oxide phase due to its high melting temperature, but it is interesting that the surfaces of the Al particles do not melt despite intense plastic deformation and elevated surrounding temperatures. The lack of melting, despite elevated surrounding temperatures, indicates that the time scales involved in these shock passage events are too small for the effects of heat conduction to be realized. The surfaces of the Al particles may melt in simulations performed at higher particle velocities.

7.4 Pore collapse

The collapse of pores is a potent source of heat generation in the particle mixtures. In fact, pore collapse is known to play a key role in the initiation of chemical reactions in polymer-bonded explosives, as evidenced by the experimental work of Bowden [49]. Pores contained in the microstructure are closed rapidly by the passage of a shock wave. Here, the collapse of a pore is caused by the inelastic deformation of the surrounding material. Such deformation processes cause nearly-adiabatic temperature rises in the vicinity of collapsed regions. Thus, small volumes of the microstructure experience localized temperature spikes. These small volumes, which reside at elevated temperatures, are known as hot spots. Hot spots are also caused by the rapid deformation processes occurring at the surfaces of contacting particles. Therefore, a shock wave propagating through a porous medium leaves behind a trail of hot spots in its wake. Hot spots occurring at, or near, reactant interfaces are responsible for microscale reaction initiation.

The magnitude of a temperature spike in a void-collapsed region is dependent, primarily, on the size of the pore and the magnitude of the particle velocity. In the 20 wt% mixtures, local temperature spikes of approximately 1200 K and 1800 K were found in void-collapsed regions for the 0.500 km-s^{-1} and 1.000 km-s^{-1} load cases, respectively. In the 50 wt% mixtures, local temperature spikes of ranging from 1000–1100 K and 1800–1900 K were found in void-collapsed regions for the 1.000 km-s^{-1} and 1.600 km-s^{-1} load cases, respectively. Similar to Benson's observations in HMX [45], hot spots remain intact after the shock front has moved past the void-collapsed region.

7.5 Evolution of reactant contact

A reactant contact site is simply a small region of the SVE where the reactants (Al and Fe_2O_3) are in direct, intimate contact. The number of reactant contact sites that are present in the SVE during shock wave passage is an important quantity to consider, as microscale reaction initiation is restricted to such sites. The ideal definition of a reactant contact site is simple; however, the implementation of such a measure in the finite element calculations is not trivial. Therefore, a brief discussion of the algorithmic definition of reactant contact is presented next.

The SVE must be searched systematically to determine the number of reactant contact sites contained in a particle mixture. However, certain restrictions are placed on the regions of the SVE from which our measurements are taken; namely, small regions near the top, bottom, and left boundary conditions are not sampled. This restriction is imposed to prevent sampling from the region of the SVE near the velocity boundary condition, where artifacts tend to arise. Although it may not be necessary, sampling is restricted near the top and bottom boundary conditions as a precautionary measure. For the SVEs associated with both the 20 wt% and 50 wt% mixture classes, regions that are less than 1 μm from the left boundary condition or 0.25 μm from the top or bottom boundary conditions are not sampled. A schematic of these restricted areas is shown for the 20 wt% mixture class in Figure 7-14; here, the blacked-out areas are those that are not sampled. Such provisions are not necessary for the right boundary condition because the simulation is stopped once the shock front traverses 90–95% of the SVE.

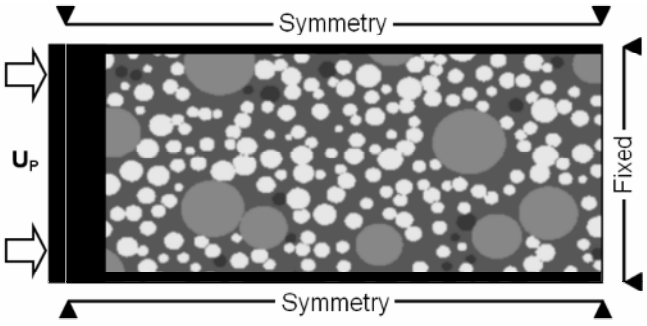

Figure 7-14. Restricted sampling areas near the boundary conditions.

At a given time step, the non-restricted portion of the Eulerian mesh is searched for sites of reactant contact. A reactant contact site is defined as an element that contains both reactants (Al and Fe_2O_3), with the additional constraint that the volume fraction of epoxy is less than 0.50. The constraint on the volume fraction of epoxy is imposed to avoid cases where a layer of epoxy separates the reactant surfaces. It is recognized that this constraint does not guarantee intimate contact in all cases, but there is no way to determine the orientation of materials in an element *a priori*. Fortunately, this technique works well in practice if the mesh is sufficiently fine. The sweeps of the mesh are performed element-by-element. Therefore, precautions must be taken to avoid repeated counting of reactant contact sites, as neighboring elements likely satisfy the requirements for reactant contact, but these elements are contained in the same contact site.

The evolution of the number of reactant contact sites N_c during wave propagation for three different 20 wt% mixtures is shown in Figure 7-15. Each of the three mixtures, labeled (i), (ii), and (iii), were subjected to particle velocities ranging from 0.500–1.000 km-s^{-1}. The evolution of the number of reactant contact sites for three different 50 wt% mixtures is shown in Figure 7-16. Each of the three mixtures, labeled (iv), (v), and (vi), were subjected to particle velocities ranging from 1.200–1.600 km-s^{-1}.

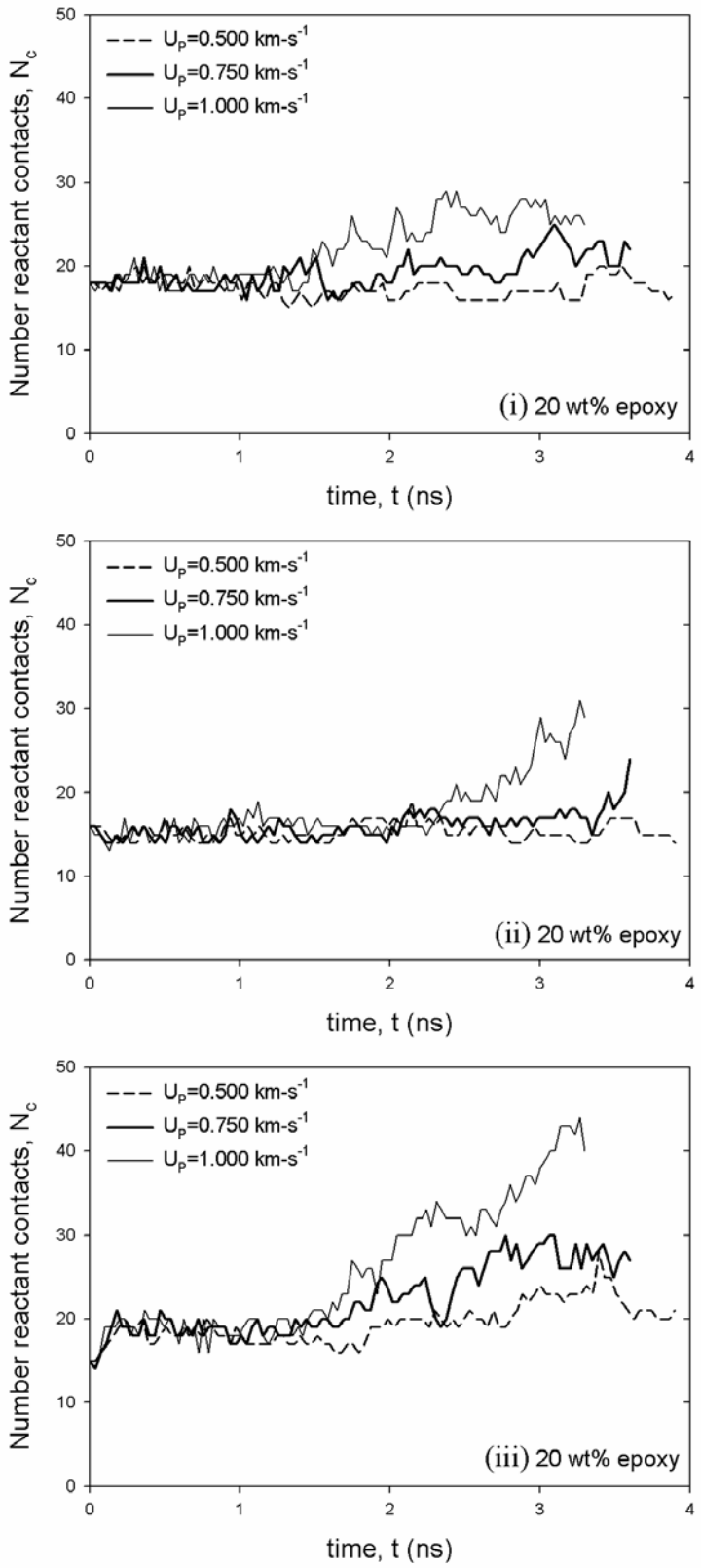

Figure 7-15. Evolution of reactant contact for three different 20 wt% mixtures subjected to particle velocities ranging from 0.500–1.000 km-s^{-1}.

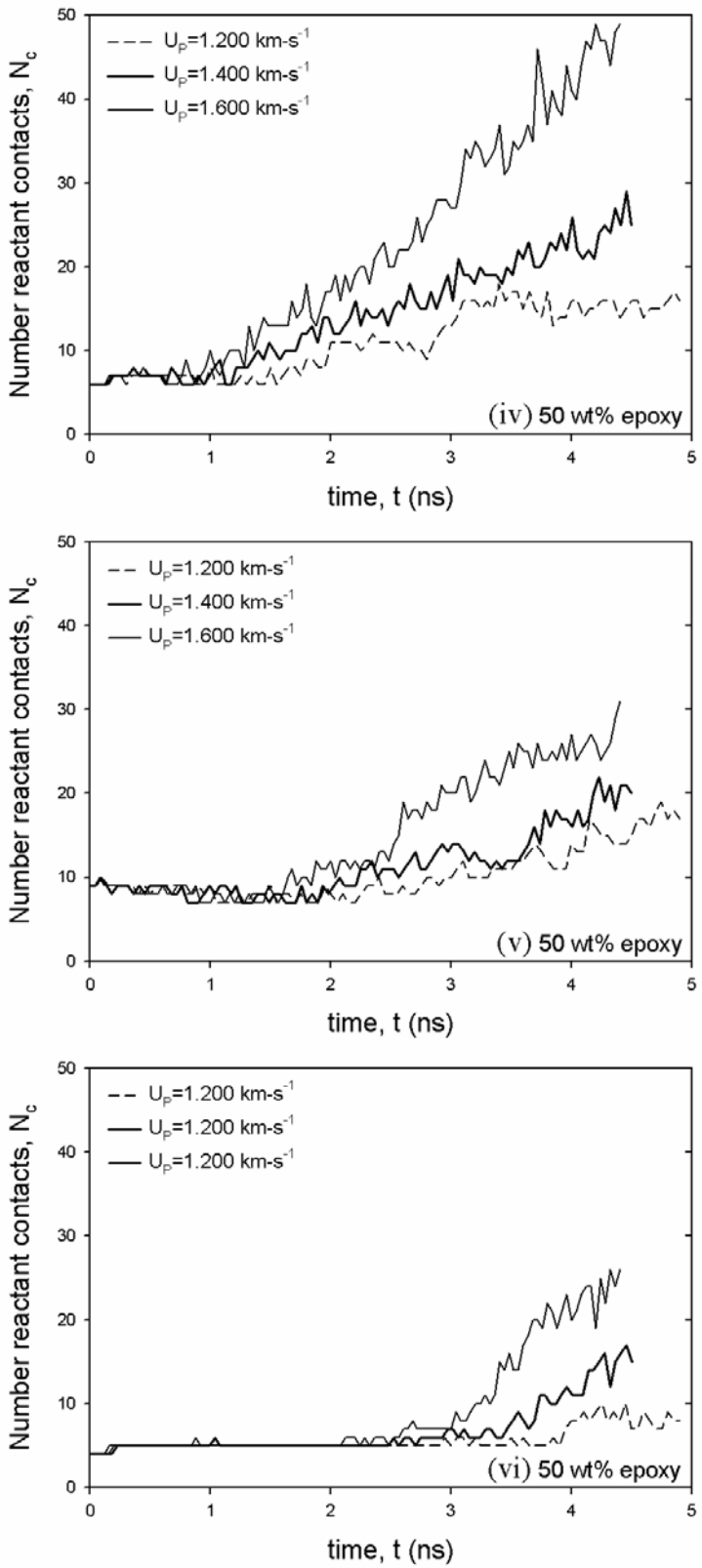

Figure 7-16. Evolution of reactant contact for three different 50 wt% mixtures subjected to particle velocities ranging from 1.200–1.600 km-s^{-1}.

The number of reactant contact sites in the initial configurations of the SVEs ranges from 15–20 for the 20 wt% mixtures and 5–10 for the 50 wt% mixtures. This corresponds to an areal density of reactant contact sites of 0.15–0.20 μm^{-2} for the 20 wt% mixtures and 0.02–0.04 μm^{-2} for the 50 wt% mixtures. Not surprisingly, the number of reactant contact sites increases for higher particle velocities in both mixture classes. As shown in Figure 7-15, N_c remains fairly constant for the 0.500 km-s^{-1} load case, especially for mixtures (i) and (ii). Substantial increases in N_c are realized in the 1.000 km-s^{-1} load case, especially for mixture (iii). A set of interesting cases are shown in Figure 7-16 for the 50 wt% mixture class. In mixture (iv), substantial increases in N_c are realized. In particular, the number of reactant contact sites has increased nearly 10-fold after shock wave passage for the 1.600 km-s^{-1} load case; this dramatic increase is due, in part, to the extreme levels of fragmentation in the iron oxide phase for the 1.600 km-s^{-1} load case. In mixture (v), a loss of reactant contact is reflected by a shallow dip in the plot at $t \sim 1$ ns. The slight decreases in N_c are attributed to the separation of reactant particles, that were once in contact, due to bulk material flow. In mixture (vi), the value of N_c is fairly constant up until $t \sim 2.5$ ns. This is due to an Al-deficient region in the SVE near velocity BC (i.e., the left-hand side of the SVE); relatively sharp increases in N_c ensue.

CHAPTER 8

HUGONIOT CHARACTERIZATION

The Hugoniot defines the thermodynamic state of a shock-compacted material. As mentioned earlier, an equation of state (EOS) is necessary to model hydrostatic responses of a material in the high-pressure regime. Hugoniot data are essential for the validation and calibration of EOS models.

The collection of Hugoniot data by experimental methods is time-consuming and expensive. Homogeneous materials require, at a minimum, 15–20 data points over a range of loading conditions to construct a set of Hugoniot curves; this establishes a lower bound on the number of experiments (e.g., Taylor impact tests) needed to characterize the high-pressure response of the material. Obtaining Hugoniot data for a range of particle mixtures (different phase contents and particle morphologies) would be prohibitively expensive. To address this problem, a method for predicting the Hugoniot for different particle mixtures has been implemented in the finite element calculations.

8.1 Calculation of the Hugoniot from the numerical models

The Hugoniot can be expressed in terms of five quantities (pressure, density, internal energy, particle velocity, and shock wave velocity). The Rankine-Hugoniot relations (cf. section 4.5.5) are used in combination with any two of the aforementioned quantities to uniquely define the Hugoniot. The particle velocity (U_P) is known in the shock compression simulations; it is simply the velocity boundary condition that is applied to the SVE. The shock wave velocity (U_S) and stationary pressure (P_{st}) are calculated in the simulations. This yields two definitions of the Hugoniot for each particle mixture.

The shock wave velocity is calculated by tracking the position of the shock front over time. An averaging scheme must be used to define the location of the shock front because shock waves do not remain planar when propagating through heterogeneous media. Materials with dissimilar acoustic wave speeds cause bowing of the wave front and mixtures that are densely packed with particles introduce percolation effects [3].

As an aside, the stochastic nature of shock wave propagation in random heterogeneous media has been studied extensively by Ostoja-Starzewski [84, 85]. Here, the dynamics of a disturbance (a single point of a stress pulse in the 1-D case) are governed by a Markov process $(Z,\vartheta)_t$, where Z is the stress amplitude of the disturbance, and ϑ is the fluctuation in the distance covered by the disturbance up to time t. This treatment permits the inclusion of microscale phenomena (e.g., variations in phase orientation, mass density, and stiffness) in an analysis of wave front behavior (e.g., decay, broadening, and randomly-distributed arrival times).

In this study, the position of the shock front (x_s) is determined by averaging the number of elements in each row of the Eulerian mesh that are above a small pressure threshold, as shown in Figure 8-1(a). It is important to note that the size of the elements must also be tracked because the Eulerian mesh contracts as the simulation proceeds. The shock wave velocity is obtained through a least-squares fit of the shock front position with respect to time, as shown in Figure 8-1(b).

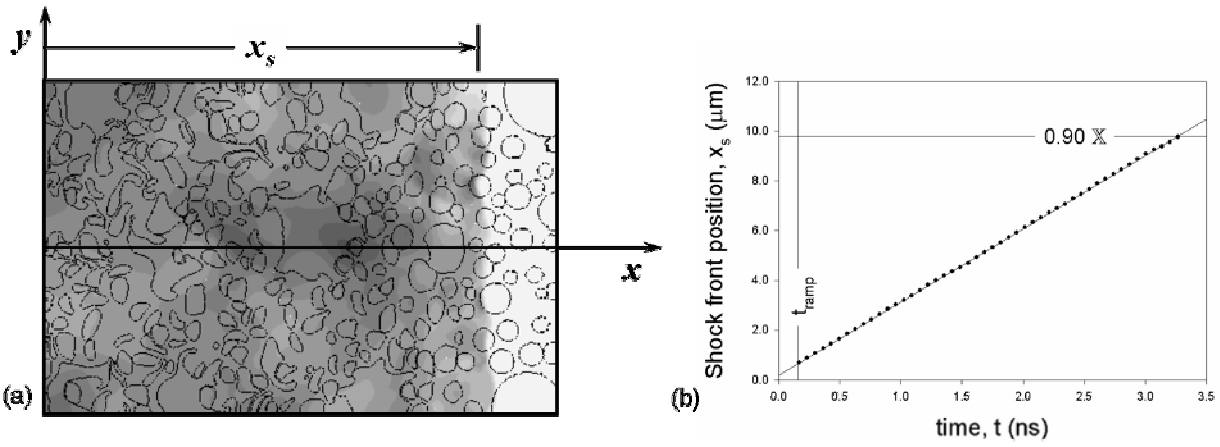

Figure 8-1. A schematic of the calculation of the shock wave velocity; (a) the position of the shock front; (b) a time history of the shock front position.

As mentioned earlier (cf. section 7.2), the stationary pressure is calculated by taking the average of the 1-D transversely-averaged pressure profile along the axial position of the SVE. Here, regions of the SVE that are less than 1 μm from the left boundary and less than 1 μm behind the shock front are not included in the calculation of the stationary pressure. Recall that

the deformation behavior close to the left boundary is not representative of the remainder of the SVE; regions directly behind the shock front are not taken into account because the amplitude of the pressure wave is not fully developed. An illustration of the stationary pressure calculation is depicted in Figure 8-2.

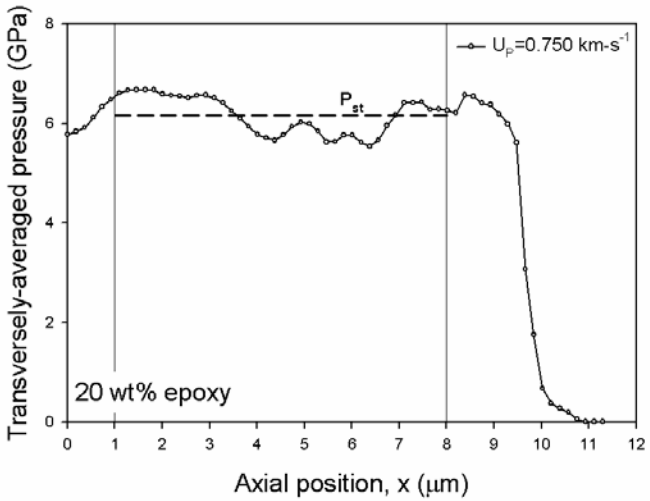

Figure 8-2. A schematic of the calculation of the stationary pressure (P_{st}).

8.2 Comparison of the numerical results to experimental data

The $U_S - U_P$ and $P - U_P$ relations for the 50 wt% epoxy mixture class are provided in Figure 8-3 (tabulated data is provided in Appendix A). Here, the simulation results are plotted alongside experimental data obtained by Ferranti and Thadhani [30] at the Georgia Institute of Technology and Jordan and co-workers [86] at Eglin Air Force Base. Three to four different particle mixtures were simulated for each particle velocity. The scatter in the numerical results for the 50 wt% mixtures simulated at the low-velocity case ($0.364 \le U_P \le 0.607$ km-s^{-1}) is extremely small (± 0.026 km-s^{-1} and ± 0.077 GPa for the $U_S - U_P$ and $P - U_P$ relations, respectively). The scatter in the numerical results for the 50 wt% mixtures simulated at the high-velocity case ($1.400 \le U_P \le 1.683$ km-s^{-1}) is somewhat larger (± 0.037 km-s^{-1} and ± 0.365 GPa for the $U_S - U_P$ and $P - U_P$ relations, respectively).

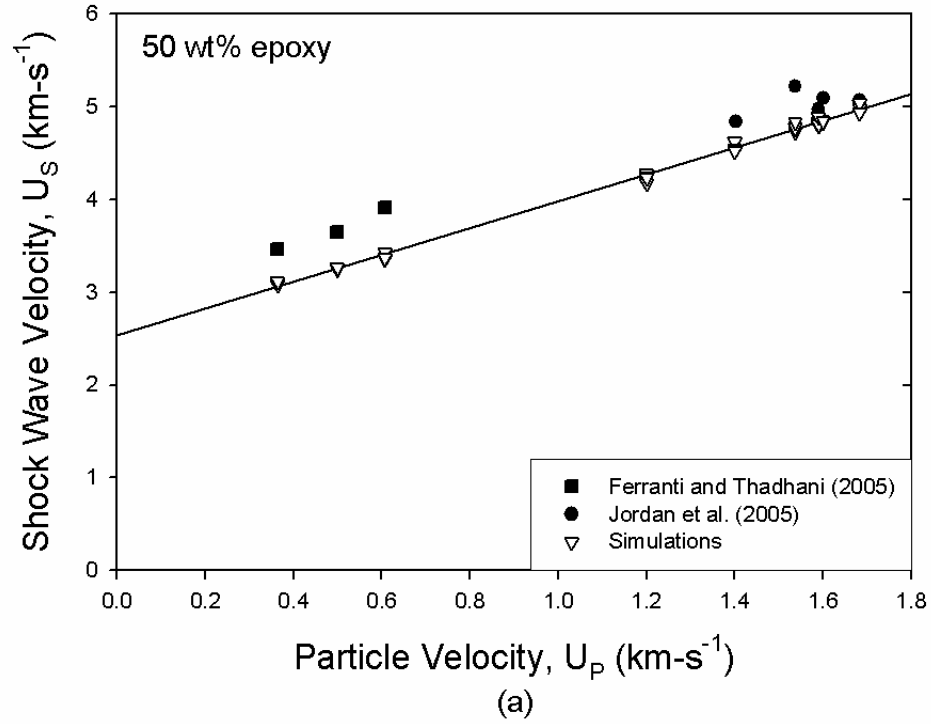

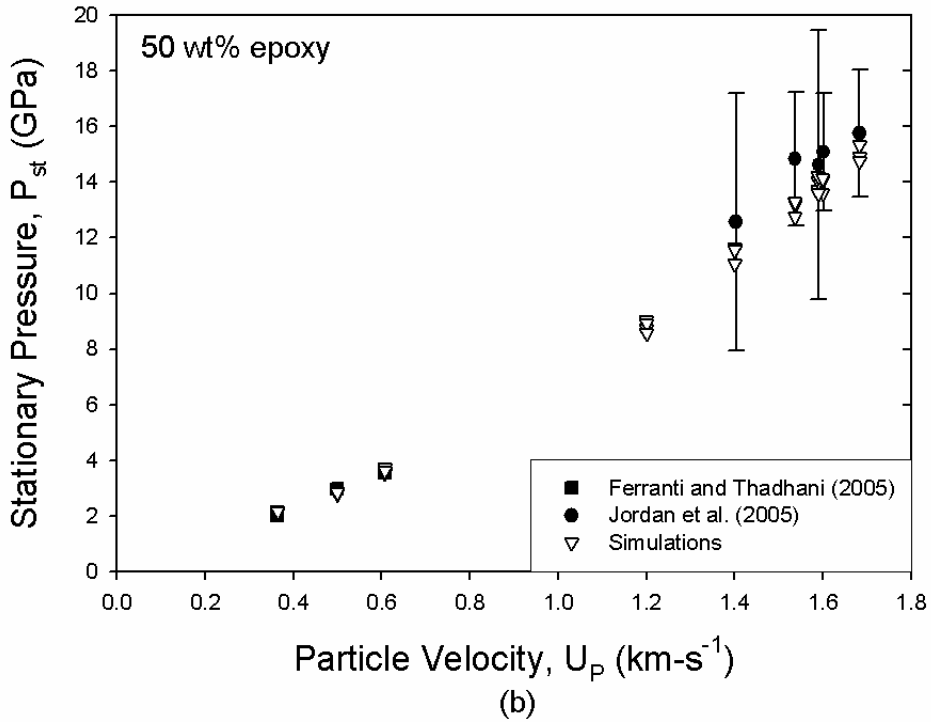

Figure 8-3. Hugoniot curves for the 50 wt% mixture class; (a) $U_S - U_P$ relations; (b) $P - U_P$ relations; tabulated data is provided in Appendix A.

The differences between the results obtained from the numerical models and experiments were calculated by averaging the numerical results at each particle velocity and comparing it against the experimental data point. As shown in Figure 8-3(a), the shock wave velocity calculations agree well with experimental data in the high-velocity case, as differences are less than 8%; in the low-velocity case, differences are somewhat larger (capped at 14 %). This trend is in line with the prior observations of Benson [41] for pure Cu powders, where larger deviations in the shock wave speed calculations were observed at lower particle velocities. As shown in Figure 8-3(b), the stationary pressure calculations show excellent agreement with experimental data in the low-velocity case, as differences are less than 7%; in the high-velocity case, differences are somewhat larger (capped at 12 %). However, all stationary pressure calculations in the numerical models for the high-velocity case fall within the uncertainty bars associated with each experimental data point (measures of uncertainty were not provided for experiments performed in the low-velocity case). The results presented here suggest that the Hugoniot of the 50 wt% mixture class is better characterized by the $P-U_P$ relation in the low-velocity regime (e.g., $0.200 \le U_P \le 0.800$ km-s^{-1}) and the U_S-U_P relation in the high-velocity regime (e.g., $1.200 \le U_P \le 1.800$ km-s^{-1}).

The U_S-U_P and $P-U_P$ relations for the 20 wt% mixture class subjected to particle velocities ranging from 0.500–1.000 km-s^{-1} are provided in Figure 8-4 (tabulated data is provided in Appendix A). Again, three to four different particle mixtures were simulated for each particle velocity. The scatter in the numerical results for the 20 wt% mixtures is comparable to that observed for the 50 wt% mixture class (± 0.024 km-s^{-1} and ± 0.150 GPa for the U_S-U_P and $P-U_P$ relations, respectively).

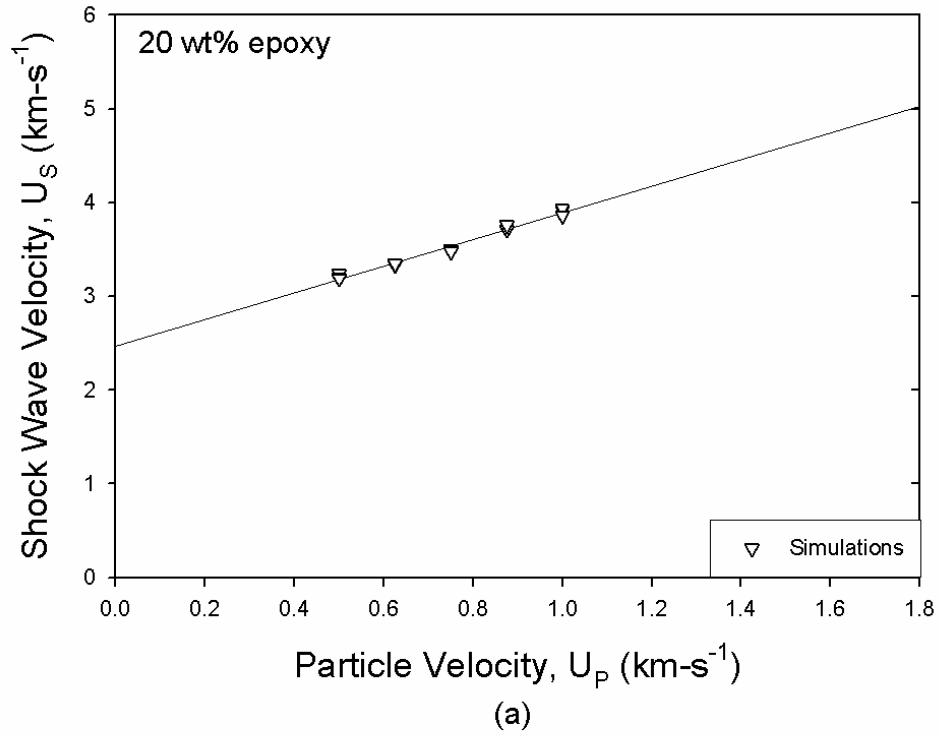

(a)

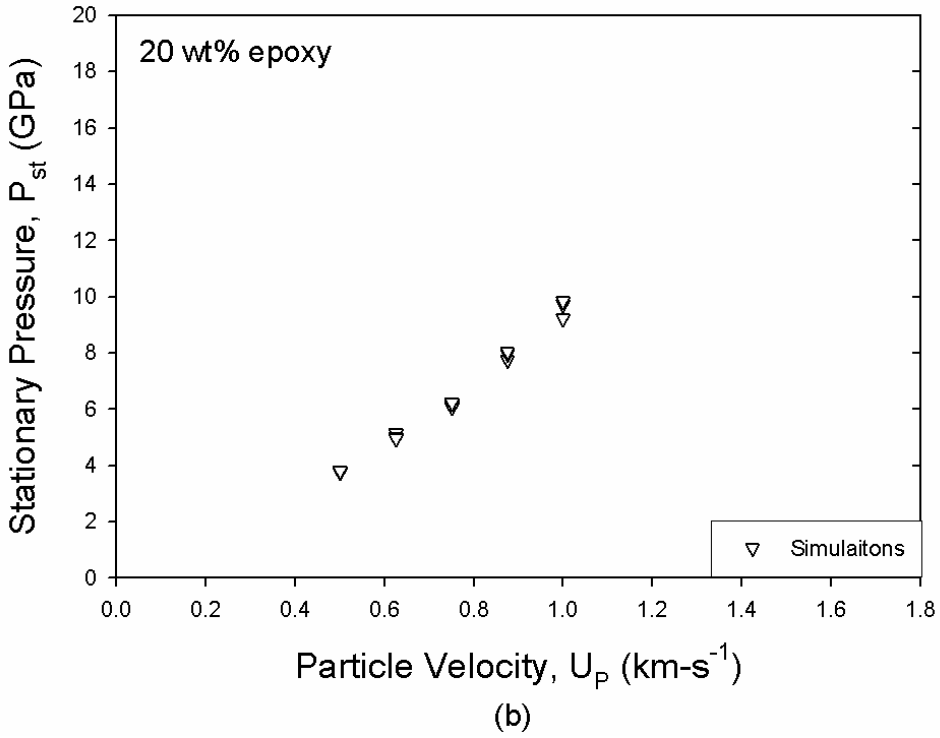

(b)

Figure 8-4. Hugoniot curves for the 20 wt% mixture class; (a) $U_S - U_P$ relations; (b) $P - U_P$ relations; tabulated data is provided in Appendix A.

The simulation results for the 20 wt% mixture class follow the same general trends as those from the 50 wt% mixture class. Unfortunately, experimental data are not available for a critical evaluation of the results for the 20 wt% mixture class; however, a goal of this research is to predict the Hugoniot of an arbitrary particle mixture with limited data from experiments.

Despite moderate discrepancies in the $U_S - U_P$ relation for the 50 wt% mixture class, it is encouraging to see a linear dependence between the shock wave speed and particle speed for both mixture classes, as such a relation holds for many materials. Recall that the $U_S - U_P$ relation is commonly framed as $U_S = C + S_1 U_P$, where C is the acoustic wave speed at ambient conditions and S_1 is the slope of the linear $U_S - U_P$ relation. As shown in Figure 8-3(a) and Figure 8-4(a), lines have been fit to the $U_S - U_P$ plots for the 50 wt% and 20 wt% mixture classes, respectively. The parameters for each fit are provided in Table 8-1 (here, r^2 is the square of the linear correlation coefficient).

Table 8-1. Fitting parameters for the $U_S - U_P$ relations

Parameters	Units	20 wt% mixture class	50 wt% mixture class
C_0	km-s^{-1}	2.473	2.538
S_1	–	1.421	1.444
r^2	–	0.982	0.997

It is interesting to note that the value of C for the 20 wt% mixture class is slightly lower than that of the 50 wt% mixture class, considering the acoustic wave speeds of the particulate phases (C_{Al} =5.38 km-s^{-1}, $C_{Fe_2O_3}$ =6.57 km-s^{-1}) are significantly higher than that of the epoxy phase (C_{Epon} =2.60 km-s^{-1}) [67]. One would suppose that a mixture densely-packed with metal/oxide particles would exhibit an acoustic wave speed that is substantially higher than that of a mixture containing high volume fractions of epoxy. However, the microstructures of the 20 wt% mixture are not fully percolated, meaning a continuous path cannot be traced from the left edge of the SVE to the right edge without encountering layers of epoxy–therefore, similar wave propagation behavior in the 20 wt% and 50 wt% mixture is reasonable. Furthermore, the

extrapolation of the $U_S - U_P$ relation to U_P=0 is not a rigorous method of calculating the acoustic wave speed, as $U_S - U_P$ relations normally deviate from linearity at low particle velocities.

8.3 The source of deviation in the Hugoniot curves

The differences between the shock wave speed calculations and the experimental data (cf. Figure 8-3(a)) can be explained by recalling how the microstructures were reconstructed. The use of cylindrical geometries in synthetic microstructures reduces the in-plane area fraction of particles, as compared to a random 2-D slice of the true microstructure. The reduced area fraction of particles is occupied by epoxy, which is responsible for decreasing the calculated shock wave speed. It is conceivable that a correction could be applied for this effect of particle rendering, but may not be necessary since the principal objective of this modeling effort is to support the design of energetic materials. Hence, predicting trends is somewhat more important than absolute values.

8.4 An application of the numerical results

The Hugoniot data calculated for different particle mixtures may be used to calibrate EOS models pertinent to higher length scales, as model parameters will certainly vary for different phase contents and morphologies of the constituents. For example, it would be desirable to calculate the EOS parameters for a bulk sample of a specific particle mixture to be included in macroscopic simulations. A hierarchy of models could be constructed, in which the results from the mesoscale calculations (e.g., the Gruneisen EOS parameters) are fed into the model definitions of the macroscale calculations. The framework established in this chapter would enable such an undertaking, as the Hugoniot of any particle mixture within the design space can be calculated directly and efficiently. The essential Gruneisen parameters (C and S_1) could be estimated from $U_S - U_P$ relation and the Gruneisen parameter may be approximated by the simple relation $\Gamma = 2S_1 - 1$ introduced earlier (cf. section 5.2.1).

CHAPTER 9

MICROSCALE REACTION INITIATION

The initiation of shock-induced and shock-assisted chemical reactions has been the subject of intense research efforts for many years. Analytical methods are plagued by the impossibility of finding closed-form solutions to the reaction initiation problem due, in part, to the spatial heterogeneity of the microstructure. Experimental methods are limited by a lack of simultaneous spatial and temporal resolution at the microstructural level. Fortunately, numerical methods are now a viable solution to the prediction of reaction initiation in reactive particle systems. The numerical methods pursued in this work achieve spatial and temporal resolution of the thermomechanical responses in reactive particle systems during shock wave propagation. Such computational tools have provided a foundation for developing predictive capabilities pertaining to the initiation and propagation of shock-induced and shock-assisted chemical reactions in RPMMs.

9.1 Motivation

Spatially-resolved shock compression simulations elucidate (i) the coupled thermal, mechanical, and chemical conditions that lead to microscale reaction initiation and (ii) the macroscopic behavior of the reactive system after reaction initiation, i.e., reaction propagation or extinction. From a materials design perspective, an ability to predict reaction initiation allows particle mixtures to be tailored to achieve the desired energetic behavior. The development of such predictive capabilities is a significant contribution to the fundamental body of knowledge pertaining to shock-induced or shock-assisted chemical reactions.

The processes that lead to the shock-induced (or shock-assisted) reaction propagation can be broken down into three general stages [46]:

1. The external energy brought to the system by a shock wave is dissipated, which leads to nearly-adiabatic temperature rises due to the heat liberated from inelastic deformation and frictional dissipation.

2. Small volumes of the system experience particularly intense heating (e.g., void-collapsed regions). Chemical reactions are initiated in these local regions when a set of critical conditions are reached.
3. A self-sustaining, propagating process is formed, resulting in a sustained macroscale energy release, which consumes all fuel in the article.

A theoretical treatment of macroscale reaction initiation and propagation contains many physical and mathematical complexities. As a starting point, we shall consider the phenomena of shock-induced reaction initiation foci (i.e., local hot spots at reactant interfaces); this corresponds to stage (2) above. It should be noted that such phenomena are distinctly different from the process of reaction initiation and propagation at the macroscale. The study of microscale shock-induced reaction initiation is relegated to the length scales of the SVE, typically on the order of tens to hundreds of microns. From this point forward, we shall refer to the onset of self-sustaining reaction propagation at the macroscale as *macroscopic reaction initiation*; the rapid growth of chemical reaction foci due to the localization of thermal energy at the microstructural level will be referred to as *micro-initiation*, and may or may not lead to chemical reaction propagation (macroscopic reaction initiation). In the literature, some experimentalists may refer to our definition of reaction propagation as reaction initiation, simply because they are taking measurements in high-velocity impact experiments and can only ascertain macroscopic propagation events, not quenched, distributed micro-initiation events.

Micro-initiation at a single hot spot (or a collection of dispersed micro-initiation events) does not guarantee the initiation of a self-sustaining reaction at the macroscale. An assessment of reaction initiation at the macroscale would require an investigation into the interaction between a set of spatially-distributed micro-initiation events over longer time scales. However, predictions of thermally-driven micro-initiation events at the mesoscale serve as a natural starting point for gaining a fundamental understanding of the complex processes involved in macroscopic reaction initiation. In this body of work, the numerical calculations at the mesoscale are well-suited for such investigations of micro-initiation due to the highly-resolved rendering of the microstructure. From a standpoint of materials design, an investigation into the different conditions that induce micro-initation would be a start to bridging the gaps between micro-initiation events and macroscopic reaction initiation of self-sustaining propagation reactions. Thus, the prediction of micro-initiation events at the mesoscale is critical to this work.

The approach taken here to the micro-initiation problem is to decouple the thermomechanical responses of the reactive particle system from the chemical kinetics. Consequently, the calculations performed are essentially a post-processing step to the finite element calculations. It is therefore imperative to develop mathematical models that link the thermomechanical and chemical responses of the reactive system at the particle level, as the finite element calculations do not take into account the heat generated due to chemical reactions, nor any other aspects of the chemical processes. The mathematical models developed will allow us to predict if and when regions of the mixture experience micro-initiation based on the thermomechanical states calculated during the shock simulations. Future work will address full coupling of the thermo-mechano-chemical responses of the reactive system by embedding algorithms in the finite element calculations that take into account the heat and mass transfer associated with chemical reactions.

In the sections that follow, the details pertaining to the development and application of the thermally-driven micro-initiation theory adopted in this work will be presented. We shall first provide a brief background on combustion phenomena. Next, we will develop the mathematical tools needed for our analyses, and address the underlying assumptions of the proposed micro-initation theory. Finally, the micro-initiation theory will be applied to the $Al + Fe_2O_3$ system.

9.2 A brief background on combustion phenomena

In a qualitative sense, combustion is a rapid reaction process that involves the generation of large amounts of heat. However, the aforementioned definition is not rigorous, as the characteristic features of the combustion process do not reside in the chemical nature of the reactants, but in the physiochemical circumstances of the reaction process. The salient feature of a combustion process is that the conditions necessary for a reaction to proceed are created by the reaction itself. Small changes in external conditions (e.g., an incremental temperature rise) cause a transition from the steady state (where the reaction kinetics are slow) to a state where the reaction rate increases rapidly. It is this self-accelerating process that defines combustion phenomena [87].

The reaction rate for homogenous reactions (i.e., those that occur in the bulk phase of a well-mixed system) is the amount of substance reacting per unit time per unit volume. In

general, the reaction rate $W(T)$ is a function of the temperature and the reactant concentrations, i.e.,

$$W(T) = k(T) C_A^{m_A} C_B^{m_B} \cdots \tag{9.1}$$

Here, $C_A, C_B \ldots$ are the molar concentrations of the constituent phases $A, B \ldots$ that participate in the reaction, and m_A, $m_B \ldots$ are the order of the reaction with respect to the individual phases. The overall order of the reaction m is given as the sum of the exponentials (i.e., $m = \sum m_i$). The temperature-dependent rate constant is commonly expressed in an Arrhenius form,

$$k(T) = k_0 \exp\{-G/RT\} \tag{9.2}$$

where k_0 is a pre-exponential factor related to the frequency of collisions between reactants, G is the activation energy for the reaction, and R is the universal gas constant.

The rise in temperature is the main cause of the acceleration to microscale reaction initiation, as the Arrhenius form of the reaction rate is highly sensitive to temperature. The effects of heating are more pronounced than those of mass transfer because the dependence of the reaction rate on the reactant concentration is only a power law relation; the temperature dependence is exponential.

Combustion phenomena occur at a set of critical conditions, for which a distinct change in the thermal behavior of the system is observed. The existence of critical conditions that separate stable states from unstable states is required for combustion processes; otherwise, self-accelerating conditions could never be achieved. The basic premise behind the formation of critical conditions was originally formulated by van t'Hoff [88]. It was proposed that the critical conditions reside in the impossibility of achieving thermal equilibrium between the reacting system and its surroundings. The development of this idea was carried out by a number of researchers, most notably Semenov [89]and Frank-Kamenetskii [90].

In the context of this work, the critical conditions that render thermal equilibration impossible describe the onset of *thermal explosion*. A thermal explosion is the unbounded temperature growth of a small volume of the mixture (i.e., a hot spot) due to the localization of heat from exothermic chemical reactions.

9.3 The governing equation

The mathematical analysis of combustion phenomena requires the solution of the transient heat transfer equation, which includes terms for the heat generated from exothermic reactions and conduction to the surroundings. For a stationary medium, the transient heat transfer equation is expressed as

$$\rho C_P \frac{\partial T}{\partial t} = QW(T) - \nabla \cdot \boldsymbol{q} \tag{9.3}$$

Here, T is the temperature field, Q is the heat of reaction, $W(T)$ is the reaction rate, and $\boldsymbol{q}$ is the heat flux vector. The conduction of heat is described by Fourier's law, i.e.,

$$\boldsymbol{q} = -\kappa \nabla T \tag{9.4}$$

where κ is the thermal conductivity. This continuum-level relation breaks down at the nanoscale, but it should be sufficient for our analyses at the mesoscale. It should be noted that Fourier's law of heat conduction is a good approximation for solids; however, it does not apply to convective heat transfer. This is an important point to consider, as some the constituents may melt during shock wave propagation. If the effects of reactant concentration are neglected, the reaction rate simplifies to $W(T) = k(T)$, according to Eq. (9.1). Upon substitution of the Arrhenius form of the reaction rate, Eq. (9.2), and the expression for the heat flux, Eq. (9.4), the transient heat transfer equation may be re-written as

$$\rho C_P \frac{\partial T}{\partial t} = Qk_0 \exp\{-G/RT\} + \kappa \nabla^2 T \tag{9.5}$$

where ∇^2 is the Laplacian operator. Here, the temperature field T, which is the unknown variable, enters into the differential equation in a nonlinear form, i.e., the Arrhenius reaction rate. The terms involving derivatives of the temperature, which are associated with heat conduction, are linear. Such equations are known as quasilinear equations. It should be noted that there must be a nonlinear dependence on the temperature in order to realize the self-accelerating process associated with combustion.

The equations derived above apply to a range of combustion phenomena. However, we are interested in the case of thermal explosion. The solution for the case of thermal explosion is found by solving the quasilinear partial differential equation (PDE) defined in Eq. (9.5) subject to a set of imposed boundary conditions. If thermal explosion does not occur, the solution to the governing equation will yield the stationary temperature distribution. However, at some

threshold temperature, the stationary temperature distribution becomes impossible and thermal explosion occurs; this threshold temperature is known as the inflammation temperature.

The exact solution to the governing PDE is difficult to obtain in a closed form. Therefore, numerical methods are required to investigate the behavior of the temperature field. This is not a serious drawback to our approach if one considers the information that we must obtain from the solution to the PDE. The exact solution to the PDE would provide a detailed description of the temperature field at each point in space over the specified time interval, which is more information than our needs require. We must determine whether or not the temperature distribution is stable (thermal equilibrium) or unstable (thermal explosion). Thus, a solution scheme incorporating numerical methods for integration of the governing PDE may be justified [87].

9.4 The method of expanding the exponent

The solution to the governing PDE, Eq. (9.5), is approached by introducing a technique that simplifies the mathematics involved. This technique, originally introduced by Frank-Kamenetskii [87], is known as the method of expanding the exponent. Using this method, a series expansion of the Arrhenius expression is obtained that preserves its exponential nature. It may be shown that the argument of the exponential in the Arrhenius form may be expressed as

$$\frac{G}{RT} = \frac{G}{R\left(T_* + \Delta T\right)} = \frac{G}{RT_*}\frac{1}{1+\left(\Delta T/T_*\right)} \approx \frac{G}{RT_*} - \frac{G}{RT_*^2}\Delta T \tag{9.6}$$

Here, T is the actual temperature of the mixture, T_* is the characteristic temperature in the neighborhood of reacting conditions, and ΔT is the characteristic temperature difference (i.e., $\Delta T = T - T_*$). In problems related to thermal explosion, T_* is the inflammation temperature. We may now define the dimensionless temperature field θ,

$$\theta = \frac{G}{RT_*^2}\left(T - T_*\right) \tag{9.7}$$

This allows us to re-write the Arrhenius exponential as

$$\exp\{-G/RT\} \approx \exp\{-G/RT_*\}\exp\{\theta\} \tag{9.8}$$

In the neighborhood of T_*, the expanded exponential form is a good approximation of the true Arrhenius form. This is advantageous, as the expanded form is much more conducive to mathematical manipulation.

The exact form of the exponential argument may be expressed as

$$\frac{G}{RT} = \frac{G}{RT_*} - \frac{\theta}{1+u_*\theta} \tag{9.9}$$

where the parameter u_* is defined as

$$u_* \equiv \frac{RT_*}{G} \tag{9.10}$$

In the limiting case $u_* \to 0$, Eqs. (9.6) and (9.9) are equivalent statements.

9.5 Key assumptions

A rigorous treatment of combustion phenomena is complicated by a number of difficulties that are both physical and mathematical in nature. Therefore, certain assumptions and approximations must be made to idealize the processes involved in thermal explosion. It is essential that such idealizations preserve the key features of the underlying physics. The remainder of this section deals with the assumptions made in the development of the thermal explosion theory. An assessment of the validity of these assumptions will be presented in section 9.8 for the Al+Fe_2O_3 system.

The parameter u_*, defined in Eq. (9.10), must be small to apply the method of expanding the exponent. Thus, the requirement $RT_* \ll G$ places a constraint on the applicability of the thermal explosion theory. The pre-explosion temperature rise is the temperature increment that induces the transition from a stable thermal state to the unbounded growth of a hot spot. It may be shown, as in ref. [87], that the condition $RT_* \ll G$ corresponds to a pre-explosion temperature rise that is small in comparison to the temperature of the immediate surroundings, i.e., $(\Delta T/T_*) \ll 1$.

In our treatment of the heat generated from exothermic chemical reactions, it is assumed that the reaction rate depends on the temperature only, i.e., $W(T) = k_0 \exp\{-G/RT\}$. This assumption neglects (i) the consumption of reactants, and (ii) any temperature dependence of the pre-exponential factor. We shall formulate a set of conditions for which these assumptions hold in section 9.8.

Finally, it is assumed the chemical reactions that occur in the medium are not accompanied by any phase transformations or other physiochemical processes. This should not

be a serious limitation to the solution method that will be developed for thermal explosion phenomena.

9.6 The stationary case of thermal explosion

The stationary form of the thermal explosion theory [87] refers to the steady state, i.e., all time derivatives are equal to zero ($\partial T/\partial t = 0$), and the consumption of reactants is neglected. Thus, the transient heat transfer equation reduces to

$$\nabla^2 T = -\frac{Q}{\kappa} k_0 \exp\{-G/RT\} \tag{9.11}$$

We seek the critical conditions for which a stationary temperature distribution becomes impossible.

The use of similitude theory serves as a starting point for determining the critical conditions necessary for thermal explosion. Similitude theory establishes the general form of the desired solution in terms of a set of dimensionless parameters through integration of the governing differential equation. The dimensionless parameters must be functions of the variables that characterize the physical properties of the medium and the nature of its behavior. The appropriate choice of dimensionless parameters is essential to the analysis of combustion phenomena, as they provide interpretations of the physics and mathematical simplifications [87]. The dimensionless quantities involved in our analyses are introduced next.

Let the dimensionless spatial coordinate ξ be defined as

$$\xi \equiv \frac{x}{r} \tag{9.12}$$

where r is the characteristic spatial dimension. The Laplacian operator in the dimensionless coordinate system is now $\nabla_\xi^2(\cdot) = r^2 \nabla^2(\cdot)$. Recall that the dimensionless temperature field θ was defined earlier, cf. Eq. (9.7), by the method of expanding the exponent. Therefore, we may re-write Eq. (9.11) in terms of the dimensionless quantities, ξ and θ, as

$$\nabla_\xi^2 \theta = -\frac{Q}{\kappa} \frac{G}{RT_*^2} r^2 k_0 \exp\{-G/RT_*\} \exp\{\theta\} \tag{9.13}$$

Here, the method of expanding the exponent has been used to approximate the Arrhenius form of the reaction rate near the inflammation temperature. We now define a dimensionless parameter δ (i.e., the Frank-Kamenetskii delta),

$$\delta \equiv \frac{Q}{\kappa}\frac{G}{RT_*^2} r^2 k_0 \exp\{-G/RT_*\} \tag{9.14}$$

The definition of δ contains all the information necessary for considering the thermal explosion, i.e., the kinetics of the chemical reaction (Q, G, and k_0), the relevant thermal properties (κ), the thermal state (T_*), and the characteristic geometry (r). Substitution of δ into Eq. (9.13) yields the transient heat transfer equation in terms of a set of dimensionless quantities, i.e.,

$$\nabla_{\xi}^2 \theta = -\delta \exp\{\theta\} \tag{9.15}$$

The solution to Eq. (9.15) that satisfies the desired boundary conditions provides a spatial description of the dimensionless temperature distribution. Assuming a set of homogeneous boundary conditions, the solution must take the following form,

$$\theta = f(\xi, \delta) \tag{9.16}$$

As mentioned earlier, the threshold conditions for which a stationary temperature field becomes impossible are the critical conditions for thermal explosion. Since neither the governing PDE nor the boundary conditions contain any parameters other than δ, the critical condition may be expressed explicitly in terms of δ, i.e., $\delta = \delta_{cr}$,. If $\delta < \delta_{cr}$, a stationary temperature distribution will develop, which is given as $\theta = f(\xi, \delta)$. If $\delta > \delta_{cr}$, thermal explosion occurs.

An illustration of the critical conditions leading to thermal explosion is contained in the so-called Semenov diagram, which is depicted in Figure 9-1. Here, the heat supply curve, which is labeled q_{rxn}, represents the heat that is generated in the mixture due to chemical reaction over a range of temperatures. The lines q_i $(i = 1,2,3)$ represent the heat losses due to conduction over a range of temperatures for cases of differing thermal conductivity. When the heat supply is greater than the heat loss for a given value of θ, heating takes place. Conversely, when the heat supply is less than the heat loss for a given value of θ, the mixture approaches a thermal equilibrium with its environment. The critical condition for thermal explosion is the case where the heat loss line is tangent to the heat supply curve. If the heat loss is always less than the heat supply, thermal explosion is predicted. In Figure 9-1, the heat loss q_1 corresponds to a state where the heat generation and conduction reach a thermal equilibrium (the intersection between q_{rxn} and q_1); the heat loss q_2 defines the threshold condition, which represents a stationary, but unstable, thermal state; the heat loss q_3 indicates that thermal explosion will occur.

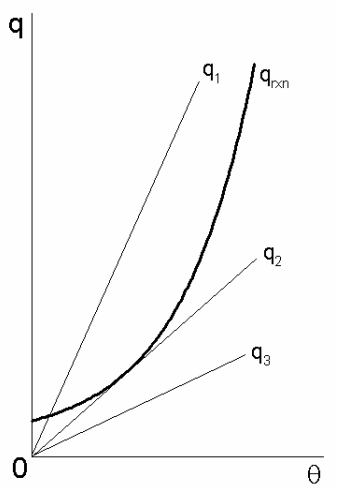

Figure 9-1. The Semenov diagram for an arbitrary reactive system (illustration taken from ref. [87].

9.7 Non-stationary conditions

We now consider the question: under what conditions is it permissible to neglect the consumption of reactants during thermal explosion? To address this question, we must consider the characteristic time period that leads to the formation of a local hot spot or reaction focus. This time interval is known as the induction period. After the critical conditions have been satisfied, the sharp temperature rise at the reaction focus occurs during the induction period.

Non-stationary conditions indicate that the time derivatives of kinetic quantities are not equal to zero. In particular, the time rates of change of the reactant concentrations are non-zero (i.e., reactants are consumed). For simple reaction kinetics, the consumption of reactant A is expressed as

$$\frac{dC_A}{dt} = -v_A k_0 \exp\{-G/RT\} \tag{9.17}$$

where C_A is the molar concentration of reactant A and v_A is the appropriate stoichiometric coefficient. It is now convenient to introduce the characteristic time for complete reaction t_{rxn}, so that Eq. (9.17) may be re-written as

$$\frac{dC_1}{dt} = -\frac{C_1}{t_{rxn}} \tag{9.18}$$

where C_1 denotes the molar concentration of the deficient reactant. Assuming $\nu_1 = 1$, the characteristic reaction time is

$$t_{rxn} = \frac{C_1}{k_0} \exp\{G/RT\} \tag{9.19}$$

If the conduction of heat can be neglected during the induction period, the process may be considered adiabatic. This is a reasonable assumption for reactions occurring on a short time scale. Under this condition, the induction period approaches the characteristic time of the adiabatic temperature rise t_{ad}. The characteristic time of the adiabatic temperature rise may be derived from Eq. (9.5) by setting the heat conduction term equal to zero, i.e.,

$$t_{ad} = \frac{\rho C_P}{Q k_0} \int_{T_0}^{T_c^{max}} \exp\{G/RT\}\, dT \tag{9.20}$$

Here, the limits of integration represent the temperature rise form the initial temperature T_0 to the maximum combustion temperature T_c^{max}. Using the method of expanding the exponent, and the relation $dT = \left(RT_*^2/G\right) d\theta$, Eq. (9.20) may be re-written as

$$t_{ad} = \frac{\rho C_P}{Q k_0} \frac{RT_*^2}{G} \exp\{G/RT_*\} \int_0^{\infty} \exp\{-\theta\}\, d\theta \tag{9.21}$$

In cases of thermal explosion, the dimensionless temperature increases without limit, as does the reaction rate, so the upper limit of integration is infinity. Integration of Eq. (9.21) yields

$$t_{ad} = \frac{\rho C_P}{Q k_0} \frac{RT_*^2}{G} \exp\{G/RT_*\} \tag{9.22}$$

It is now convenient to introduce the dimensionless time τ,

$$\tau \equiv \frac{t}{t_{ad}} \tag{9.23}$$

Here, the actual time is normalized by t_{ad}, as it is a characteristic time scale of thermal explosion phenomena. Thus, the dimensionless time is expressed as

$$\tau = t \frac{Q k_0}{\rho C_P} \frac{G}{RT_*^2} \exp\{-G/RT_*\} \tag{9.24}$$

We now define a parameter B as the ratio of the characteristic time for complete reaction t_{rxn} to the characteristic time of the adiabatic temperature rise t_{ad}, i.e.,

$$B \equiv \frac{t_{rxn}}{t_{ad}} = \frac{Q C_1^0}{\rho C_P} \frac{G}{RT_*^2} \tag{9.25}$$

where C_1^0 is the initial molar concentration of the deficient reacting component. The maximum combustion temperature that may be reached by an adiabatic temperature rise during the induction period is expressed as

$$T_c^{max} = T_0 + \frac{Q}{\rho C_P} C_1^0 \tag{9.26}$$

By solving for the initial molar concentration in Eq. (9.26) and substituting it into Eq. (9.25), and recalling the prior definition of the dimensionless temperature field θ from Eq. (9.7), the parameter B may be expressed as

$$B = \frac{G}{RT_0^2}\left(T_c^{max} - T_0\right) \tag{9.27}$$

Thus, $B = \theta_c^{max}$, where θ_c^{max} represents the maximum value of the dimensionless temperature field during combustion.

In cases where $B \gg 1$, the consumption of reactants during the induction period may be neglected, as the characteristic time necessary to exhaust the reactants is much greater than the characteristic time of the adiabatic temperature rise. When B assumes intermediate values (e.g., $1 \le B \le 4$), reactant consumption must be taken into account. In cases where $B < 1$, there cannot be a thermal explosion, as the reaction is completed before any adiabatic temperature rise.

9.8 An assessment of the key assumptions

A number of necessary conditions were established in section 9.5 pertaining to the applicability of the thermal explosion theory. We now investigate these conditions for the Al+Fe_2O_3 system. Data relevant to this analysis may be found in Table 9-1.

In order to use the method of expanding the exponent, the condition $u_* = RT_*/G \ll 1$ must be satisfied. Here, the characteristic temperature T_* is taken to be the combustion temperature T_c; thus, for the Al+Fe_2O_3 system, $u_* \sim 0.14$. This corresponds to a difference of 14% between the true value of the exponent and the approximated value, which is a reasonable approximation near the combustion temperature.

The consumption of reactants was neglected in our development of the stationary theory of thermal explosion. For this to be a reasonable assumption, it is necessary to satisfy the condition $B \gg 1$. Combining Eqs. (9.26) and (9.27), where the pre-explosion temperature is

taken as the combustion temperature ($T_0 = T_c$), an expression for B is obtained in terms of the initial molar concentration of the deficient reactant C_1^0, i.e.,

$$B = \frac{G}{RT_c^2}\frac{Q}{\rho C_P}C_1^0 \tag{9.28}$$

The parameters necessary to evaluate Eq. (9.28) for a well-mixed Al+Fe_2O_3 system (with no binder) are provided in Table 9-1 (here, ρ is calculated for a stoichiometric mixture of the reactants with a simple mixture rule). If the lower bound is defined as $B > 4$, then the consumption of reactants may be neglected during the induction period for $C_1^0 > 2.0 \times 10^{-3}$ mol-cm^{-3}. However, it is difficult to apply this criterion to the particle systems considered in this work because the concentration requirement was derived for a homogenous reactive system. The chemical reactions considered in the discrete particle models occur at the surfaces of reactant particles. Nevertheless, the molar concentration of a reactant in a mixture is calculated as $C = \rho V_f / M$, where M is the molecular weight of the reactant. In the polymer-bonded Al+Fe_2O_3 systems, the deficient reactant in the 20 wt% epoxy and 50 wt% epoxy mixtures is the Fe_2O_3 component ($C_{Fe_2O_3} = 10.0 \times 10^{-3}$ mol-cm^{-3} for the 20 wt% mixture class; $C_{Fe_2O_3} = 4.0 \times 10^{-3}$ mol-cm^{-3} for the 50 wt% mixture class). The concentrations of the deficient reactants in each mixture class satisfy the conditions necessary for neglected reactant consumption (for the homogeneous case) during the induction period.

Finally, it was assumed that the pre-exponential frequency factor k_0 is not a function of temperature. In our calculations, the pre-exponential frequency factor is approximated by the Debye frequency ν_D, which may be expressed as

$$\nu_D = \left(\frac{3N}{4\pi V}\right)^{1/3}\sqrt{\frac{\mu}{\rho}} \tag{9.29}$$

where N/V is the number density of atoms for a given material. The shear modulus may be a function of temperature; however, the overall sensitivity of the Debye frequency to temperature is relatively weak. Therefore, the assumption that the Debye frequency is independent of temperature is on the order of other approximations involved in this analysis.

In summary, the assumptions pertaining to the aforementioned treatment of combustion phenomena are justified for the Al+Fe_2O_3 system. Therefore, the thermal explosion theory

outlined in the preceding sections may be used in our predictions of microscale reaction initiation.

9.9 The Merzhanov criterion

In accordance with the theory developed thus far, a mathematical description of the thermal explosion of a hot spot (i.e., micro-initiation) is embodied in the governing heat equation, cf. Eq. (9.5). Merzhanov [46] performed a series of investigations pertaining to micro-initiation events in a number of different geometric configurations. In the general case, the governing heat transfer equation is expressed as

$$\rho C_P \frac{\partial T}{\partial t} = Q k_0 \exp\{-G/RT\} + \kappa\left(\frac{\partial^2 T}{\partial x^2} + \frac{n}{x}\frac{\partial T}{\partial x}\right) \tag{9.30}$$

where x is the spatial coordinate located at the center of a hot spot, and n is the hot spot symmetry factor. The value of n depends on the geometry of the hot spot, i.e.,

$n = 0$ for a planar hot spot

$n = 1$ for a cylindrical hot spot

$n = 2$ for a spherical hot spot

In our calculations, we shall consider the case of cylindrical hot spots within the context of the 2-D finite element calculations.

A schematic of an idealized representation of a reaction focus is depicted in Figure 9-2. The following set of initial conditions and boundary conditions are applied:

$T = T_h$ for $x < r_h$, $t = 0$

$T = T_{surr}$ for $x > r_h$, $t = 0$

$\dfrac{\partial T}{\partial x} = 0$ for $x = 0$, $t > 0$

$\dfrac{\partial T}{\partial x} = 0$ for $x = \infty$, $t > 0$

Here, r_h is the radius of the hot spot, T_h is the initial temperature of the hot spot, and T_{surr} is the temperature of the surroundings.

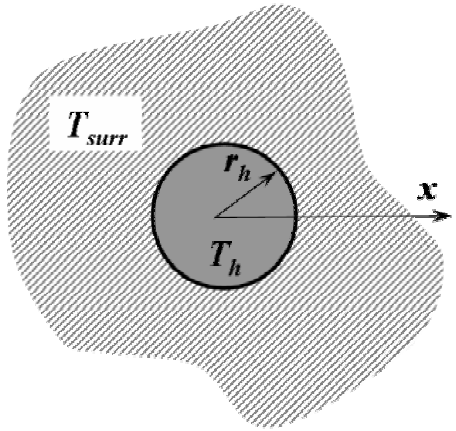

Figure 9-2. The geometry of an idealized reaction focus.

The exact solution to Eq. (9.30) cannot be obtained analytically for the desired boundary conditions. We shall deal with this problem by transforming the governing PDE to a dimensionless form and performing numerical integration.

Recall the dimensionless variables θ, ξ, and τ that were introduced earlier (cf. Eqs. (9.7), (9.12) and (9.24)). When applied to the case of thermal explosion, $r = r_h$, $T_* = T_h$, and $T_0 = T_{surr}$; therefore, the dimensionless quantities are expressed as

$$\xi = \frac{x}{r_h} \tag{9.31}$$

$$\theta = \frac{G}{RT_h^2}\left(T - T_h\right) \tag{9.32}$$

$$\tau = t\frac{Qk_0}{\rho C_P}\frac{G}{RT_h^2}\exp\left\{-G/RT_h\right\} \tag{9.33}$$

Now, recall that the Frank-Kamenetskii delta is defined as

$$\delta \equiv \frac{Q}{\kappa}\frac{G}{RT_h^2}r_h^2 k_0 \exp\left\{-G/RT_h\right\} \tag{9.34}$$

and the dimensionless temperature difference between the hot spot and its surroundings is expressed as

$$\theta_h = \frac{G}{RT_h^2}\left(T_h - T_{surr}\right) \tag{9.35}$$

It should be noted that the parameters δ and θ_h are expressed in terms of three key quantities: (i) the radius of the hot spot r_h, (ii) the initial temperature of the hot spot T_h, and (iii) the temperature of the surroundings T_{surr}.

The governing equation may now be expressed in terms of the dimensionless quantities defined above. In cylindrical coordinates,

$$\frac{\partial\theta}{\partial\tau} = \exp\{\theta\} + \frac{1}{\delta}\left(\frac{\partial^2\theta}{\partial\xi^2} + \frac{1}{\xi}\frac{\partial\theta}{\partial\xi}\right) \tag{9.36}$$

The above equation is identical to Eq. (9.15) for the stationary condition (i.e., $\partial\theta/\partial\tau = 0$). The transformed initial conditions and boundary conditions are now

$$\theta = 0 \quad \text{for } \xi < 1,\ \tau = 0,\ \theta_h > 0$$
$$\theta = -\theta_h \quad \text{for } \xi > 1,\ \tau = 0,\ \theta_h > 0$$
$$\frac{\partial\theta}{\partial\xi} = 0 \quad \text{for } \xi = 0,\ \tau > 0$$
$$\frac{\partial\theta}{\partial\xi} = 0 \quad \text{for } \xi = \infty,\ \tau > 0$$

A detailed analysis of Eq. (9.36) was performed for a range of values of the parameter δ and the temperature boundary condition θ_h. The transient thermal behavior of the system was investigated using numerical integration [91], i.e., the dimensionless temperature field θ was obtained by numerically integrating Eq. (9.36) for given values of δ and θ_h. Here, Eq. (9.36) is reduced to a set of coupled first-order differential equations, which are integrated numerically using an Adams method. The Adams method is a multi-step predictor-corrector scheme that advances the solution in time based on a cubic interpolating function that is fit to the functional values that span four consecutive points. Therefore, it is necessary to start the algorithm with single-step scheme (e.g., a Runge-Kutta method). The Adams method is fourth order accurate, i.e., $O(\Delta\tau)^5$.

If the numerical integration of Eq. (9.36) yields a stable temperature field, the selected value of δ is less than the critical value, i.e., $\delta < \delta_{cr}$. If the temperature field increases without bound, micro-initiation has occurred, i.e., $\delta \geq \delta_{cr}$. Iterative techniques may be used to locate precise values of δ_{cr} for given values of θ_h. Thus, the solution is reduced to finding a functional relation between δ and θ_m. Merzhanov constructed the functional relation

$$\delta_{cr} = A_m \left(\ln \theta_h \right)^m \tag{9.37}$$

Here, A_m and m are constants that depend on the geometry of the hot spot (planar, cylindrical, or spherical). The values of A_m and m were calibrated over the range $4 < \theta_h < 25$; for cylindrical hot spots, $A_m = 7.39$ and $m = 0.83$. Stated simply, the Merzhanov criterion for microscale reaction initiation is satisfied for $\delta > \delta_{cr}$.

9.10 Numerical implementation of the micro-initiation criterion

Now that a criterion has been defined for micro-initiation, it must be implemented in the spatially-resolved numerical simulations. The Merzhanov criterion must be evaluated at a number of points during the passage of a shock wave (through the SVE) in the finite element simulations. Such evaluations will provide time histories of micro-initiation events during shock wave propagation.

The hydrocode simulations take into account the heat generated due to plastic deformation and the conduction of heat through the spatial domain. However, the simulations do not consider the heat generated by exothermic chemical reactions; in other words, the thermomechanical and chemical behavior of the system are not coupled. Thus, it is necessary to assess the Merzhanov criterion as a post-processing step.

9.10.1 Energetic properties of the aluminum–iron oxide thermite system

Properties pertaining to the chemical behavior of the Al+Fe_2O_3 system are given in Table 9-1. The temperature-dependent activation energy $G(T)$ was fit to experimental data by X. Lu at the Georgia Institute of Technology,

$$G(T) = A_4 T^4 - A_3 T^2 + A_2 T^2 - A_1 T + A_0 \tag{9.38}$$

Here, A_n $(n = 0,1\ldots4)$ are the coefficients of the polynomial fit. The heat of reaction is calculated from the heats of formation of the reactants and products ($\Delta H_{f,Al_2O_3} = -1670$ kJ-mol^{-1}, $\Delta H_{f,Fe_2O_3} = -822$ kJ-mol^{-1}). The pre-exponential frequency factor is approximated by an intermediate value of the Debye frequencies of Al and Fe_2O_3. The Debye frequencies of Al and Fe_2O_3 are calculated as $\nu_{D,Al} = 7.5 \times 10^6$ μs^{-1} and $\nu_{D,Fe_2O_3} = 11 \times 10^6$ (μs)$^{-1}$ according to Eq. (9.29). Thus, the pre-exponential frequency factor is approximated as 10×10^6 (μs)$^{-1}$. The combustion

temperature and specific heat of the Al+Fe_2O_3 thermite system are provided in ref. [92]. The specific heat of the mixture was calculated using a simple mixture rule. An accurate approximation of the effective thermal conductivity of the polymer-bound Al+Fe_2O_3 thermite system is a difficult task. One might approximate the effective thermal conductivity with an effective medium theory for particulate systems, cf. ref. [93]; however, the dimensions of the hot spots are too small to implement such an approximation. Alternatively, the effective thermal conductivity could be approximated from a series configuration of Al and Fe_2O_3, where the thermal resistivities of the reactants would be summed; however, the location of the heat source is not known, so the preceding approximation is not justified in all cases. We must base our approximation on our knowledge that each Al particle is typically surrounded completely by Fe_2O_3 particles and epoxy. Small pockets of Al in the mixture provide regions of high thermal conductivity (κ_{Al} =222 W-m^{-1}-K^{-1}), but the overall heat conduction is limited by the iron oxide and epoxy phases ($\kappa_{Fe_2O_3}$ =5 W-m^{-1}-K^{-1}, κ_{Epon} =0.2 W-m^{-1}-K^{-1}). Therefore, the effective thermal conductivity of the Al+Fe_2O_3 system is taken as that of Fe_2O_3.

Table 9-1. Energetic properties of the Al+Fe_2O_3 thermite system

Properties	**Units**	
Activation energy, G	kJ-mol^{-1}	120 [(a)]
Heat of reaction, Q	kJ-mol^{-1}	848
Pre-exponential frequency factor, k_0	(μs)$^{-1}$	10×10^6
Combustion temperature, T_c	K	2070 [(b)]
Specific heat of the mixture, C_P	kJ-kg^{-1}-K^{-1}	0.42 [(b)]
Effective thermal conductivity, κ_{eff}	W-m^{-1}-K^{-1}	5
Universal gas constant, R	kJ-mol^{-1}-K^{-1}	8.314×10^{-3}
Coefficients		
A_4	kJ-mol^{-1}-K^{-4}	3.00×10^{-13}
A_3	kJ-mol^{-1}-K^{-3}	6.00×10^{-9}
A_2	kJ-mol^{-1}-K^{-2}	3.10×10^{-5}
A_1	kJ-mol^{-1}-K^{-1}	6.13×10^{-2}
A_0	kJ-mol^{-1}	1.62×10^{2}

[(a)] Reported at $T = T_c$.
[(b)] 22 wt% Al_2O_3

9.10.2 Quantities necessary for the evaluation of the Merzhanov criterion

It is necessary to determine three quantities from the simulations to evaluate the Merzhanov criterion: (1) the temperature of the hot spot T_h, (2) the temperature of the hot spot surroundings T_{surr}, and (3) the radius of the hot spot r_h. Recall that the parameter θ_h is a function of T_h and T_{surr}, cf. Eq. (9.35), and that the critical value of δ is expressed in terms of θ_h, cf. Eq. (9.37). Therefore, a knowledge of T_h and T_{surr} allow us to determine the critical value of δ. Recall that δ is a function of the radius of the hot spot r_h, from Eq. (9.34). When $\delta = \delta_{cr}$, the radius of the hot spot becomes the minimum critical radius of the hot spot necessary for micro-initiation, i.e. $r_h = r_{cr}$. Therefore, Eq. (9.34) may be rearranged to yield the minimum critical radius of a hot spot necessary for micro-initiation, i.e.,

$$r_{cr} = \left[\frac{\kappa}{Qk_0} \frac{RT_h^2}{G} \delta_{cr} \exp\{G/RT_h\} \right]^{1/2} \tag{9.39}$$

It may be helpful to consider an example: if the core temperature of a hot spot (at a reactant interface) is 1000 K and the surrounding temperature is 600 K, then the hot spot must have a radius greater than 0.35 μm for a micro-initiation event to occur in the Al+Fe_2O_3 system. The techniques used to determine the quantities needed to evaluate the Merzhanov criterion in the finite element simulations are discussed next.

Reaction foci can only occur in regions where there is intimate contact between the reactants; otherwise, there would be no heat input to the hot spot from chemical reactions. Thus, we must determine the aforementioned quantities at sites of intimate reactant contact. A schematic of the geometry of a hot spot at a site of intimate reactant contact is depicted in Figure 9-3.

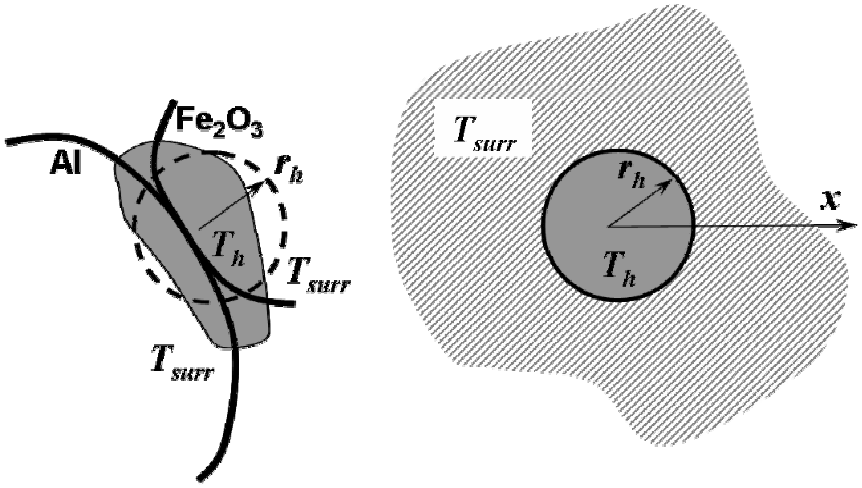

Figure 9-3. Transformation of the actual hot spot geometry to the idealized hot spot geometry.

The arbitrarily-shaped hot spot may be approximated by a circular area with radius r_h. The temperature of the hot spot T_h is taken as the average temperature associated with the hot spot area. The temperature of the hot spot surroundings T_{surr} is taken as the average temperature of the immediate surrounding area of the hot spot. It should be noted that the temperature of the hot spot surroundings is assumed constant in the Merzhanov criterion. In actuality, the temperature of the surroundings will change with time due to plastic work and heat conduction, which makes T_{surr} a moving target. However, the time scales of micro-initiation are extremely short for

elevated temperatures, as shown in Figure 9-4. The duration of shock wave passage through the SVE is on the order of 3–5 ns in the finite element simulations. In the Al+Fe_2O_3 system, the characteristic time for the explosion of a hot spot with temperature T_h=1200 K is t_{ad} ~0.2 ns. Therefore, it is reasonable to assume that the surrounding temperature is constant.

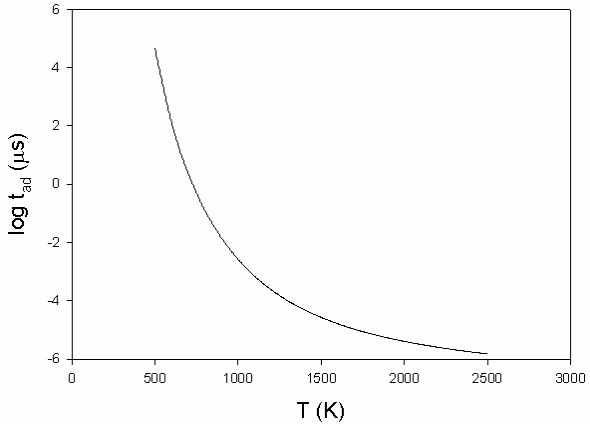

Figure 9-4. The characteristic time of the adiabatic temperature rise in the Al+Fe_2O_3 thermite system.

9.10.3 Calculation of the quantities necessary for evaluation of the Merzhanov criterion

It would be extremely tedious to manually determine the quantities required to evaluate the Merzhanov criterion during the shock wave simulations. Therefore, it is necessary to embed algorithms in the finite element calculations that determine the necessary quantities (T_h, T_{surr}, and r_h) at a specified number of evenly-spaced time steps. Such algorithms will the reactive behavior of the particle mixture to be studied over a range of morphologies. The techniques for determining these quantities are discussed next.

The SVE must be searched systematically to determine the number of micro-initiation sites. Here, regions near the boundaries of the SVE must be excluded, as the deformation processes in these regions may not be representative of the remainder of the microstructure. Recall the spatial restrictions that were imposed in the calculations of the number of reactant

contact sites (cf. section 7.5); the same restrictions are imposed in the calculations of the number of micro-initiation sites.

At a given time step, the non-restricted portion of the Eulerian mesh is searched for sites of intimate reactant contact (the algorithmic definition of a reactant contact site was provided in section 7.5). The volume-fraction-weighted temperature of an element T_e that contains intimate reactant contact is calculated as

$$T_e = \sum_{m=1}^{M} V_m^f T_m \tag{9.40}$$

where V_m^f and T_m are the volume fraction and temperature of material m, respectively, in an element containing M materials. If T_e is greater than a specified threshold temperature (900 K), the element is marked as a potential hot spot core and T_e is stored as the core temperature T_{core}. The area of the core is calculated from the dimensions of the element (recall the logical structure of the Eulerian mesh). However, it is necessary to take into account the contraction of the elements in the direction of shock wave propagation, as the entire mesh contracts over the course of the simulation. At this point, the area of the hot spot A_h is taken as the area of the core.

The thermal environment of the area surrounding the marked element is now investigated. This is accomplished using a step-out algorithm, which is illustrated in Figure 9-5. The volume-fraction-weighted temperatures T_e are calculated and stored for the first layer of elements that surround the core. If $T_e \geq T_{core}$ for any of the elements in the first layer, the area of the element is added to the hot spot area A_h. If $T_e < T_{core}$, the area of the element is added to the surrounding area A_{surr} It should be noted that intimate reactant contact is not required in elements other than the core. This process is repeated for the second layer, and so on. The step-out algorithm is terminated when no further area is added to the hot spot area (i.e., the areas of all elements in the current layer are added to the surrounding area).

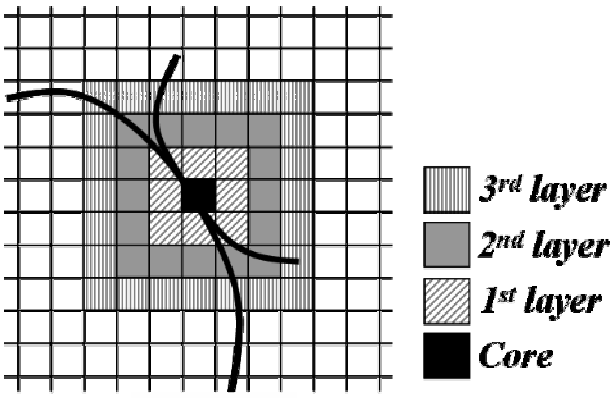

Figure 9-5. A schematic of the step-out algorithm at a site of reactant contact.

The stored temperatures associated with the hot spot area A_h are averaged over the number of elements contained in the hot spot area; this is the hot spot temperature T_h. The stored temperatures associated with the surrounding area A_{surr} are averaged over the number of elements contained in the surrounding area; this is the surrounding temperature T_{surr}. It is assumed that the hot spot area may be approximated as a circular region; therefore, the radius of the hot spot is calculated as $r_h = \sqrt{A_h / \pi}$. The quantities required to evaluate the Merzhanov criterion are now known.

9.10.4 An example hot spot calculation

At this point, it may be useful to consider an example to illustrate the techniques used to determine the quantities necessary to evaluate the Merzhanov criterion. Consider an arbitrarily-shaped hot spot at a reactant interface, as show in Figure 9-6. Starting with the hot spot core, which is labeled 'c', the step-out algorithm calculates the areas of the hot spot A_h and the surroundings A_{surr}. The temperature of the hot spot T_h and the surroundings T_{surr} are calculated by averaging the volume-fraction-weighted temperatures (T_e) of the elements contained in A_h and A_{surr}, respectively. Since the step-out algorithm terminates when no more area is added to the hot spot, at least one layer of elements beyond the hot spot is used in the calculation of A_{surr} and T_{surr}. The area of the hot spot is now transformed to a circular area with radius r_h.

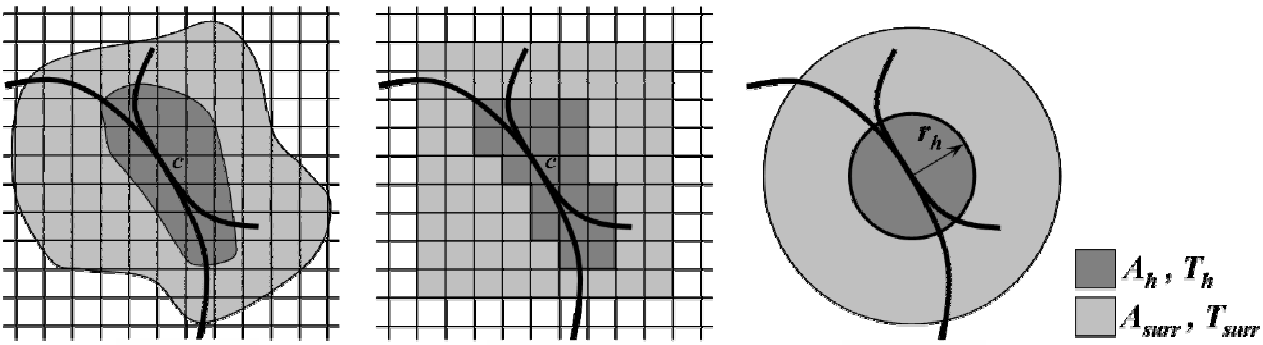

Figure 9-6. A schematic of the approximation of the hot spot temperature field and radius.

9.10.5 Evaluation of the Merzhanov criterion

The number of micro-initiation events are tracked as the shock wave passes through the SVE. This is accomplished by evaluating the Merzhanov criterion for all hot spots at reactant interfaces at a specified number of time steps throughout the simulation. The Merzhanov criterion ($\delta \geq \delta_{cr}$) provides the minimum critical radius r_{cr} of a hot spot needed for micro-initiation based on the values of T_h and T_{surr}. If $r_h \geq r_{cr}$, a micro-initiation event is recorded.

Precautions must be taken to avoid repeated counting of micro-initiation events, as it is possible for more than one site of intimate reactant contact to be contained in a hot spot. For example, consider the hot spot shown in Figure 9-6; there are three sites of intimate reactant contained in the area of this hot spot. The algorithms described in the preceding sections will record three distinct micro-initiation events, when, in fact, there is only one micro-initiation event. Therefore, the proper steps must be taken to avoid repeated counting. This is accomplished by checking the immediate neighboring elements of a hot spot core during the mesh sweeps. If a neighboring element contains a micro-initiated hot spot core, the current hot spot core is considered part of the neighboring micro-initiation event.

It is now convenient to define a parameter related to the number of micro-initiation events present in the SVE at a given time step, as well as some terminology unique to these analyses. An activated site is simply one that satisfies the Merzhanov criterion (i.e., a micro-initiation site). A partially-activated site is defined as a hot spot that is not large enough to satisfy the Merzhanov criterion. Therefore, cases for which $r_h / r_{cr} \geq 1$ are activated sites, while

cases for which $r_h/r_{cr} < 1$ are partially-activated sites. The value of the micro-initiation parameter ζ is defined as the number of activated sites plus the largest value of the ratio r_h/r_{cr} for all partially-activated sites, i.e.,

$$\zeta \equiv \zeta_a + \zeta_p \tag{9.41}$$

Here, ζ_a is the number of activated sites, and ζ_p is calculated as

$$\zeta_p = \max\left(r_h/r_{cr}\right)_i \text{ for } i = 1 \ldots N_c \tag{9.42}$$

where N_c is the total number of reactant contact sites in the SVE. The micro-initiation parameter is constructed in this manner to provide enhanced discernment of the reactive behavior of the particle system. The value of ζ_p provides an estimate of how close a partially-activated site is to micro-initiation; this construction is most useful when $\zeta_a = 0$.

The results to be collected are time histories of the micro-initiation parameter ζ. This will provide a detailed description of the number of micro-initiation events in the SVE during shock compression.

9.10.6 Convergence of the mesh density and domain size

As stated earlier, calculations of the number of micro-initiation sites must converge for the mesh density and domain size that are selected (cf. sections 6.5 and 6.6). Now that the concept of micro-initiation has been defined, these topics may be discussed. Time histories of the micro-initiation parameter ζ for the same 20 wt% mixture discretized by the mesh densities of interest (cf. Table 6-2) are provided in Figure 9-7. Despite the erratic nature of ζ, it should be fairly clear that the coarse mesh underestimates the value of ζ; the calculations performed with the intermediate and fine meshes display reasonable convergence. Therefore, it is confirmed that the intermediate mesh is of sufficient density for these calculations.

Time histories of the areal density of the micro-initiation parameter (ζ / A) for three distinct 20 wt% mixtures contained in the domain sizes of interest (cf. Table 6-3) are provided in Figure 9-8 (here, areal densities are calculated based on the area of the SVE). Again, despite the erratic nature of ζ, it should be clear that the areal density of the micro-initiation parameter is underestimated for the 12 μm × 6 μm domain. The 14 μm × 7 μm and 16 μm × 8 μm domains predict approximately the same levels of micro-initiation density; the value of ζ / A fluctuates

about 0.025 once the shock wave is fully developed. Therefore, it is confirmed that a domain size of 14 μm × 7 μm is of sufficient size for the 20 wt% mixture class in these calculations. As an aside, it appears that the onset of micro-initiation activity is shifted in time for each decrement in domain size. However, this effect is not a direct consequence of the domain size. The 14 μm × 7 μm and 12 μm × 6 μm domains happened to contain Al-deficient regions near the left boundary condition (actually, Al particles were present, but they were fully contained within the 1-μm strip of the domain that is excluded from calculations), which delayed the onset of micro-initiation activity.

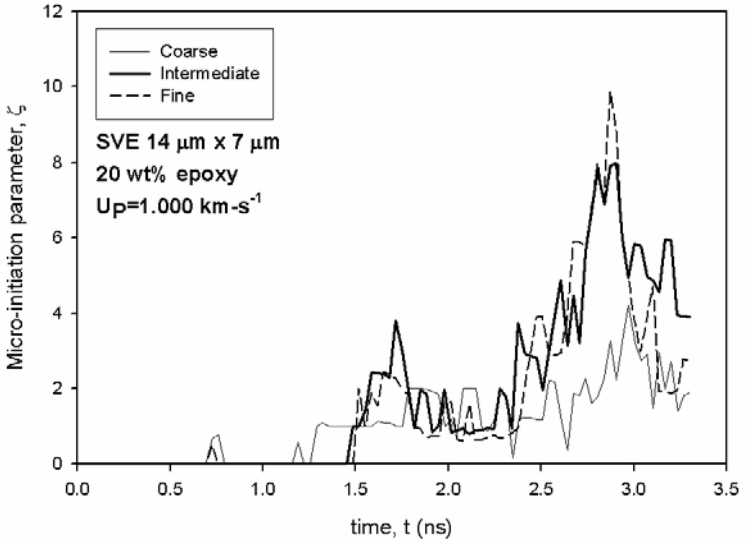

Figure 9-7. Evolution of the micro-initiation parameter for the mesh densities of interest.

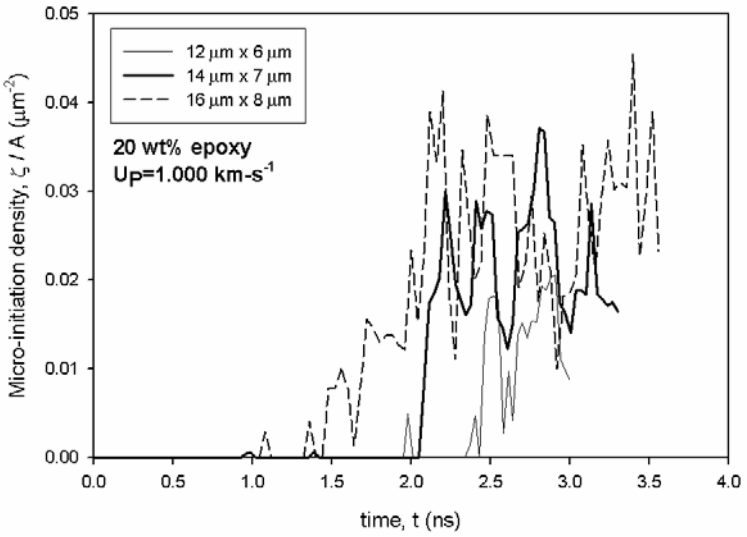

Figure 9-8. Evolution of the micro-initiation density for the domain sizes of interest; areal densities are based on the area of the SVE.

9.11 Predictions of numerical models

The evolution of the micro-initiation parameter ζ during wave propagation (across the SVE) for three distinct 20 wt% mixtures is shown in Figure 9-9. Here, mixtures (i), (ii), and (iii) are three realizations of the same microstructure. The mixture parameters used to generate each microstructure were identical; however, the pseudo-random techniques used in microstructure reconstruction render each mixture distinct. Each of the mixtures was subjected to particle velocities ranging from 0.500–1.000 km-s^{-1}. A reference line ($\zeta = 1$) is plotted to distinguish load cases that achieve at least one activated site. Results are not plotted for loading conditions for which there is no micro-initiation activity (i.e., $\zeta = 0$ for all t).

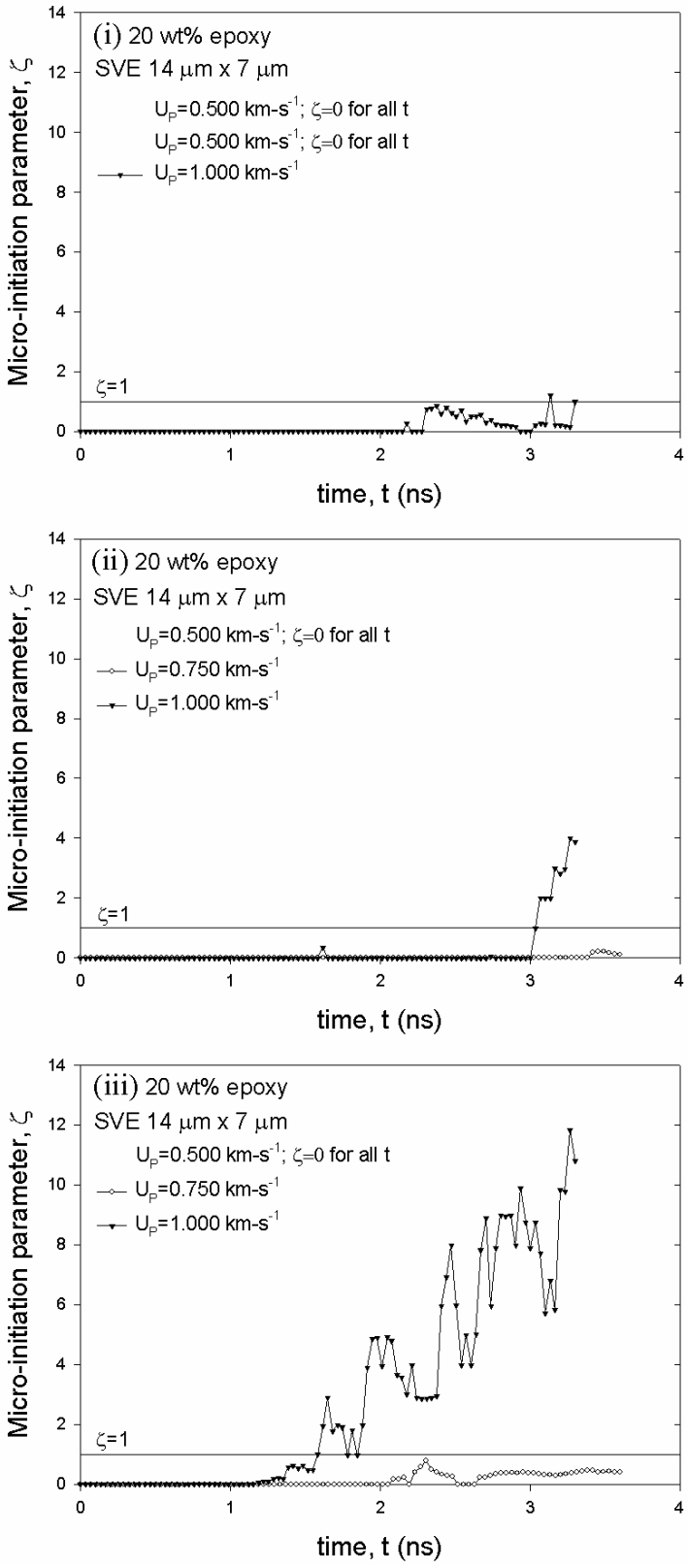

Figure 9-9. Evolution of the micro-initiation parameter for three distinct 20 wt% mixtures, (i), (ii) and (iii), subjected to particle velocities ranging from 0.500–1.000 km-s^{-1}.

It can be seen in Figure 9-9 that mixture (i) exhibits no micro-initiation activity for U_P<1.000 km-s^{-1} and ζ is rarely greater than unity for U_P=1.000 km-s^{-1}. In mixture (ii), there is a marked increase in ζ for the 1.000 km-s^{-1} load case near t=3 ns; slight micro-initiation activity is also observed in this mixture for U_P=0.750 km-s^{-1}, in the form of partially-activated sites. Substantial increases in ζ are observed in mixture (iii). In the 1.000 km-s^{-1} load case, ζ exceeds unity relatively early during wave propagation (t~1.6 ns). In the 0.750 km-s^{-1} load case, ζ never exceeds unity, but there are marked increases in the strength of partially-activated sites.

The micro-initiation responses of 20 wt% mixtures constructed with identical mixture parameters and subjected to identical loading conditions exhibit substantial variability. In Figure 9-9, mixtures (i), (ii), and (iii) exhibit micro-initiation responses that are extremely different for the 1.000 km-s^{-1} load case. The major contributing factor to these differences is the amount of reactant contact associated with each of the mixtures. Recall the evolution of the number of contact sites (cf. Figure 7-15) for these corresponding 20 wt% mixtures. In Figure 7-15, the number of reactant contact sites in mixture (i) remains fairly low and constant (N_c~25) for U_P=1.000 km-s^{-1}; this leads to small amounts of micro-initiation activity. In mixture (ii), moderate increases in the number of reactant contact sites ($N_c \rightarrow 30$) are observed for U_P=1.000 km-s^{-1} at t~3 ns; increases of ζ are also observed at t~3 ns. Substantial increases in N_c are realized in mixture (iii) for the 1.000 km-s^{-1} load case, as $N_c \rightarrow 45$ by the end of the simulation; this leads to elevated values of ζ during wave propagation. The correlation between the reactant contact behavior and the evolution of the micro-initiation events is quite apparent.

A full statistical analysis of the stochastic nature of the micro-initiation parameter is beyond the scope of this work. Meaningful statistical analyses would require many realizations of the microstructure to quantify the statistical nature of the micro-initiation behavior of different particle systems. Collaborative efforts are underway with research groups at the Georgia Institute of Technology that specialize in the quantification of variability in materials design.

The evolution of the micro-initiation parameter ζ during wave propagation (across the SVE) for three distinct 50 wt% mixtures is shown in Figure 9-10. Again, mixtures (iv), (v), and (vi) are three realizations of the same microstructure. Each of the three mixtures was subjected to particle velocities ranging from 1.200–1.600 km-s^{-1}. Again, a reference line (ζ=1) indicates the threshold above which there is at least a single activated site.

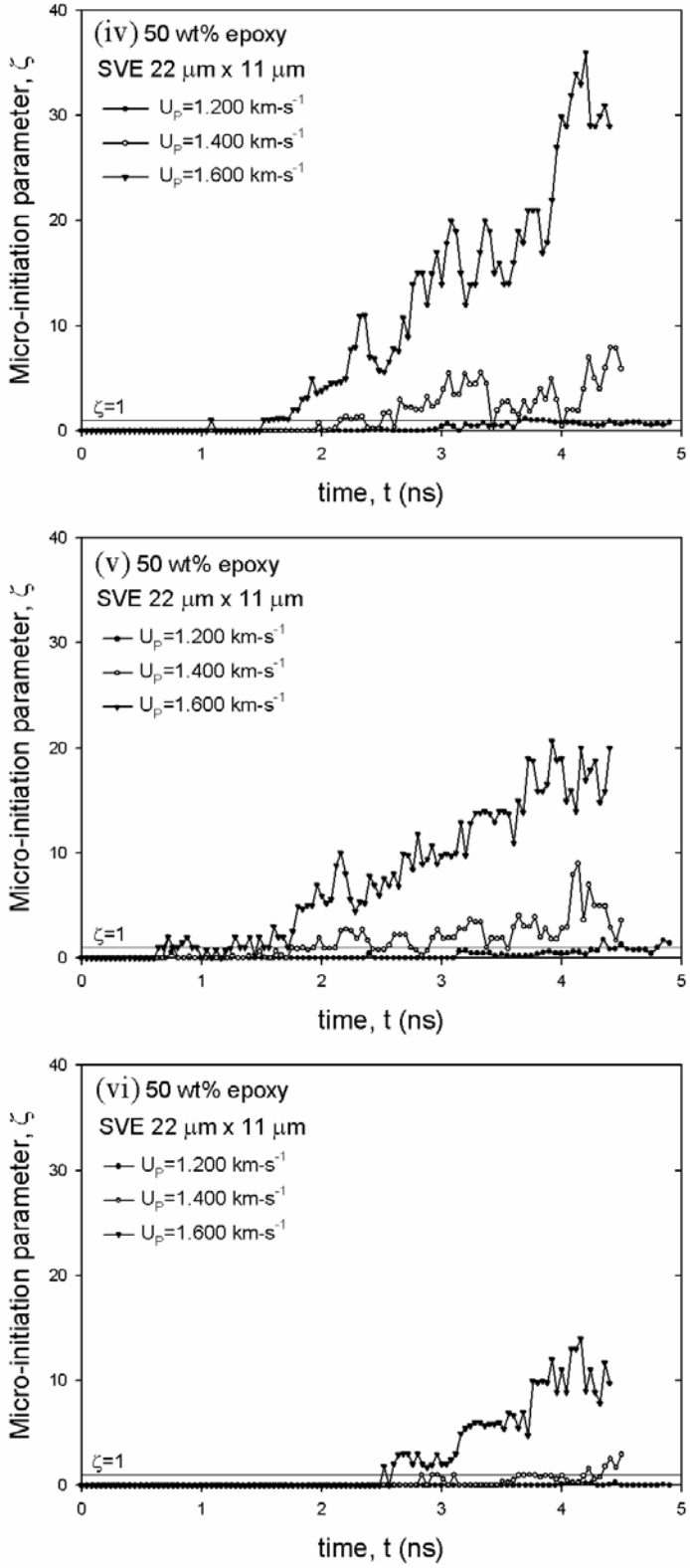

Figure 9-10. Evolution of the micro-initiation parameter for three distinct 50 wt% mixtures, (iv), (v), and (vi), subjected to particle velocities ranging from 1.200–1.600 km-s^{-1}.

It can be seen in Figure 9-10 that mixture (iv) exhibits substantial micro-initiation activity for the 1.600 and 1.400 km-s^{-1} load cases; ζ exceeds unity intermittently for the 1.200 km-s^{-1} load case. Mixture (v) exhibits the same micro-initiation trends as mixture (iv). In mixtures (iv) and (v), it is clear that micro-initiation activity commences earlier for higher particle velocities. In mixture (vi), the value of ζ is equal to zero for t<2.5 ns and the magnitude of ζ is depressed for all loading conditions thereafter. In fact, ζ is less than unity for all t for U_P=1.200 km-s^{-1}. As shown in Figure 9-10, the value of the micro-initiation parameter increases in a nearly step-wise manner for the 50 wt% mixtures. The step-wise nature of ζ suggests that once a micro-initiation site is formed, it remains intact for the duration of SVE wave propagation. This result is to be expected because the short time scales of SVE wave propagation preclude significant amounts of heat conduction away from local hot spots.

The micro-initiation responses of 50 wt% mixtures also display substantial variability. In Figure 9-10, mixtures (iv), (v), and (vi) exhibit micro-initiation responses that are noticeably different for the 1.600 km-s^{-1} load case. The value of ζ for the 1.600 km-s^{-1} load case increases monotonically with time (despite fluctuations about the general trend), whereas the value of ζ for the 1.400 and 1.200 km-s^{-1} load cases seems to reach a saturation limit or grow at substantially lower rates. This could be due to the increased fragmentation of the iron oxide phase observed for the 1.600 km-s^{-1} load case (cf. section 7.1), which causes higher growth rates of the number of reactant contact sites. Furthermore, recall the evolution of the number of contact sites (cf. Figure 7-16) for these corresponding 50 wt% mixtures. In Figure 7-16, the number of reactant contact sites in mixture (iv) exhibits dramatic increases, especially for U_P=1.600 km-s^{-1}; this translates to larger values of ζ during wave propagation. In mixture (v), moderate increases in the number of reactant contact sites ($N_c \to 30$) are observed for the 1.600 km-s^{-1} load case near t=4.5 ns. Mixture (vi) is an interesting case–the number of reactant contact sites remains fairly constant (N_c~5) for t<2.5 ns; this lead to a situation where ζ=0 for all loading conditions for t<2.5 ns. The onset of micro-initiation activity in mixture (vi) corresponds to increases in N_c around for t=2.5 ns.

The influence of the number of reactant contact sites on the number of micro-initiation events is illustrated in Figure 9-11 for two specific cases. Here, time histories of N_c and ζ are

plotted for the 20 wt% and 50 wt% mixture classes, i.e., mixtures (iii) and (iv). It is particularly clear for the 50 wt% mixture that the number of micro-initiation sites follows the number of reactant contact sites closely (such effects are most pronounced for the highest particle velocities). The same behavior is observed for the 20 wt% mixture, although it is not as dramatic. It appears that N_c grows faster than ζ for the 20 wt% mixture, whereas the growth rates of N_c and ζ are nearly identical for the 50 wt% mixture.

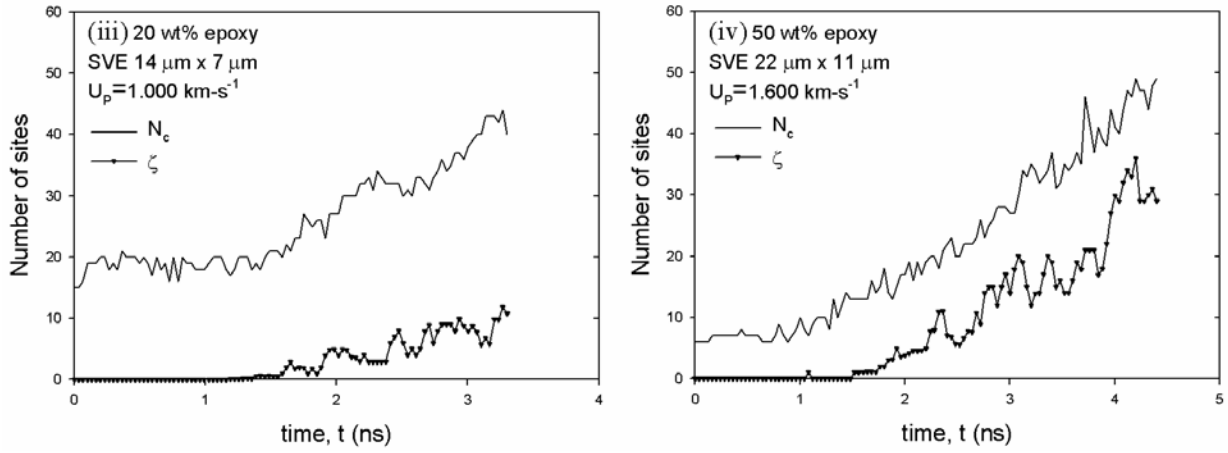

Figure 9-11. A comparison of the number of micro-initiation sites and the number of reactant contact sites for a 20 wt% mixture (U_P =1.000 km-s^{-1}) and a 50 wt% mixture (U_P =1.600 km-s^{-1}).

In Figure 9-12, the fraction of reactant contact sites that experience micro-initiation are plotted over a range of particle velocities for both the 20 wt% and 50 wt% mixture classes. The results presented here indicate that mixtures containing lower densities of particles (50 wt% mixtures) shocked with higher particle velocities (1.200–1.600 km-s^{-1}) are more effective in converting reactant contact sites to activated micro-initiation sites as compared to mixtures containing higher densities of particles (20 wt% mixtures) shocked with lower particle velocities (0.500–1.000 km-s^{-1}). An ideal comparison of the micro-initiation behavior of the 20 wt% and 50 wt% mixture classes would involve the same loading conditions; however, no micro-initiation events are observed in the 50 wt% mixtures for $U_P \leq 1.000$ km-s^{-1}, and the 20 wt% mixtures

cannot be simulated for U_P >1.000 km-s^{-1} due to numerical instabilities. Thus, the preceding observations of the micro-initiation are the most applicable comparisons that can be put forth for the data available.

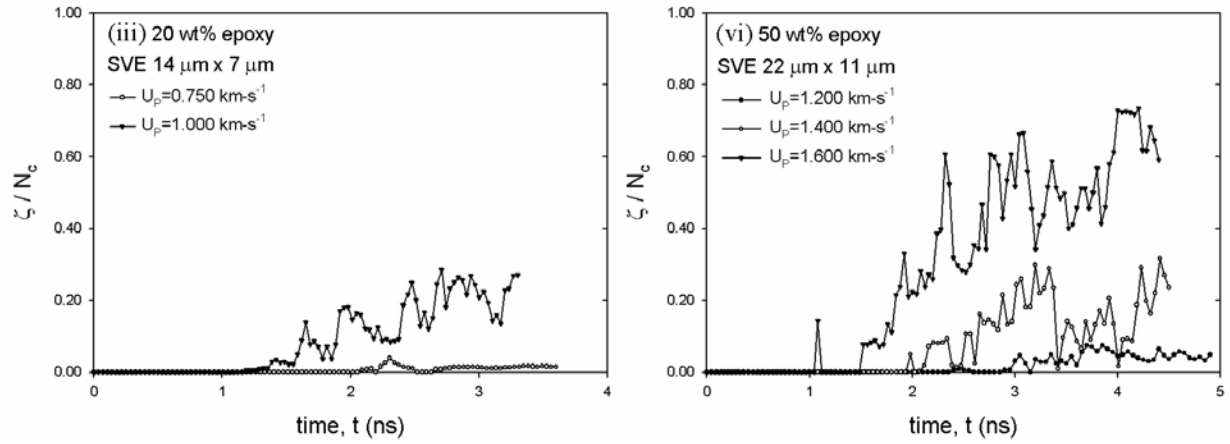

Figure 9-12. Evolution of the fraction of reactant contact sites that experience micro-initiation for the 20 wt% and 50 wt% mixture classes.

Additional factors beyond the number of reactant contact sites influence the number of micro-initiation events. The spatial configuration and morphology of the inclusion phases can have a significant effect on micro-initiation, e.g., any of the following scenarios may influence the number of micro-initiation sites:

1. The proximity of voids to reactant interfaces.
2. Arrangements of particles that induce large stress concentrations between contacting particles.
3. The surface area of particles, particularly in the Al phase.
4. The dispersion of Al particles in the SVE

Such factors are not considered explicitly in these calculations because they are difficult to quantify with automated techniques during shock simulation..

The micro-initiation sites observed in these calculations developed during mechanical equilibration, indicating that microscale reaction initiation (but not necessarily reaction

propagation) in the $Al+Fe_2O_3$ system is shock-induced (rather than shock-assisted). The experimental work of Boslough [14] showed that macroscale reaction initiation (i.e., reaction propagation) in the $Al+Fe_2O_3$ system was a shock-induced process. By implication, microscale reaction initiation in the $Al+Fe_2O_3$ system must also be shock-induced, as it precedes reaction propagation. Unfortunately, real-time predictions of micro-initiation cannot currently be validated by experimental methods due, in part, to a lack of spatial and temporal resolution.

CHAPTER 10

SUMMARY AND CONCLUSIONS

The goal of this research was to study the shock compression of micron-scale reactive particle systems by developing computational methods capable of resolving the coupled thermo-mechano-chemical responses at the particle level, and employing the concepts of microscale reaction initiation based on thermal explosion theory. This goal has been achieved for polymer-bonded thermite systems, with specific application to the Al+Fe_2O_3 system

The computational methods utilized in the shock compression of the reactive particle systems are described fully in this manuscript. First of all, techniques were developed for reconstructing microstructures based on a set of parameters that characterize the morphology of the mixture. Herein lies a set of approximations pertaining to these analyses–(i) the assumption of a 2-D microstructure geometry, and (ii) the reconstruction of Fe_2O_3 agglomerates (of subparticles) as single micron-scale particles. The former approximation is unavoidable due to the intense computational nature of fully 3-D calculations. The latter approximation is somewhat unavoidable due to the increased computational cost of resolving micron- and nano-scale particles simultaneously. Moreover, the objective of supporting the design of RPMMs is consistent with the aforementioned reductions of complexity. The computational methods of the Eulerian finite element method were expounded in detail and the constitutive models were derived for all phases. Herein lies another major approximation of these analyses–a simple elastic-plastic constitutive relation was used to model the deviatoric strength of the Fe_2O_3 phase; this assumption was necessary due to a lack of published data on the stress-strain responses of Fe_2O_3 over a range of strain rates and temperatures. The methods used to propagate ostensibly 1-D shock waves through the particle mixtures in the multi-material Eulerian finite element code, Raven [1], were contained in the definition of the initial value boundary problem.

Thermomechanical responses (e.g., post-shock microstructure morphologies, spatial profiles of pressure and temperature, melting behavior, and the evolution of reactant contact) were computed for each mixture class; it was found that the levels of reactant contact had a noticeable effect on the number of sites that experienced micro-initiation. Methods of calculating the Hugoniot for variable mixture compositions were implemented in the numerical

simulations. It was found that $P-U_P$ relations show excellent agreement with experimental data in the low-velocity regime; the U_S-U_P relations are preferable in the high-velocity regime. This suggests that costly impact experiments can be partially replaced by numerical simulations for the efficient characterization of mixture Hugoniots. Finally, algorithms were developed for predicting micro-initiation sites based on the Merzhanov criterion. A framework for calculating time histories of the number of micro-initiation sites during SVE wave propagation was implemented in the finite element simulations. The micro-initiation behavior of the Al+Fe_2O_3 system was investigated for a range of mixture compositions and shock load cases. Substantial micro-initiation activity was observed for the 50 wt% epoxy mixtures shocked with a particle velocity U_P=1.600 km-s^{-1}; sporadic micro-initiation activity was observed for the 20 wt% epoxy mixtures shocked with a particle velocity U_P=1.000 km-s^{-1}. Here, significant levels of variability were observed in the micro-initiation responses of the particle mixtures due, in part, to the levels of reactant contact. Unfortunately, the predictions of microscale reaction initiation cannot currently be validated by experimental methods.

The predictive capabilities established in this study provide opportunities for extension in future work:

1. The effects of porosity and phase morphology on micro-initiation could be evaluated through carefully designed parametric studies.
2. The dynamic finite element simulations could be augmented by algorithms that take into account the reaction kinetics and mass transfer at reactant interfaces during shock wave propagation (i.e., the effects of the chemical reactions).
3. Shock compression analyses could be extended to the nanoscale, where it will be necessary to develop constitutive models that respect pertinent size effects.
4. Finite element simulations could be performed at quasistatic loading rates to investigate stress states in shear and the tension-compression asymmetry of the yield surface of this granular material, neither of which may be resolved by simple mixture theories.

The pursuit of such research objectives, combined with future experimental work, will provide a deeper understanding of the complex, fully-coupled behavior of reactive particle systems at multiple length scales.

APPENDIX A
HUGONIOT DATA

Table A-1. Hugoniot Data calculated in numerical models for the 20 wt% epoxy mixtures

Particle Velocity U_P (km-s^{-1})	Shock Wave Velocity U_S (km-s^{-1})			Stationary Pressure P_{st} (GPa)		
	Mix.(i)	*Mix.(ii)*	*Mix.(iii)*	*Mix.(i)*	*Mix.(ii)*	*Mix.(iii)*
0.364	3.10	3.08	3.12	2.14	2.19	2.11
0.499	3.25	3.27	3.27	2.79	2.81	2.90
0.607	3.36	3.43	3.37	3.53	3.73	3.59
1.200	4.28	4.24	4.18	8.72	9.03	8.91
1.400	4.62	4.54	4.52	11.63	11.55	11.08
1.537	4.79	4.73	4.77	13.17	13.24	13.28
1.590	4.83	4.80	4.81	13.70	14.01	13.58
1.600	4.83	4.86	4.86	13.60	14.05	14.12
1.683	4.98	5.04	4.94	14.92	14.77	15.33

Table A-2. Hugoniot Data calculated in numerical models for the 50 wt% epoxy mixtures

Particle Velocity U_P (km-s^{-1})	Shock Wave Velocity U_S (km-s^{-1})			Stationary Pressure P_{st} (GPa)		
	Mix.(i)	*Mix.(ii)*	*Mix.(iii)*	*Mix.(i)*	*Mix.(ii)*	*Mix.(iii)*
0.500	3.24	3.20	3.19	3.78	3.76	3.81
0.625	3.35	3.34	3.35	5.15	5.00	4.97
0.750	3.50	3.50	3.48	6.16	6.07	6.22
0.875	3.76	3.71	3.76	7.74	7.97	8.02
1.000	3.91	3.93	3.86	9.72	9.83	9.23

Table A-3. Hugoniot Data measured in experiments for the 50 wt% epoxy mixtures

Particle Velocity U_P (km-s^{-1})	Shock Wave Velocity U_S (km-s^{-1})	Stationary Pressure P_{st} (GPa)	Experimental Group
0.364	3.465	2.00	Ferranti and Thadhani [30]
0.499	3.653	2.96	–
0.607	3.917	3.56	–
1.403	4.839	12.56 ± 4.62	Jordan et al. [86]
1.537	5.219	14.84 ± 2.41	–
1.590	4.973	14.62 ± 4.83	–
1.601	5.094	15.09 ± 2.10	–
1.683	5.063	15.71 ± 2.28	–

REFERENCES

1. Benson, D.J., *A multi-material Eulerian formulation for the efficient solution of impact and penetration problems.* Computational Mechanics, 1995. **15**: 558-571.

2. Thadhani, N.N., *Shock-induced chemical reactions and synthesis of materials.* Progress in Materials Science, 1993. **37**: 117-226.

3. Meyers, M.A., *Dynamic Behavior of Materials*, 1994 (New York: J. Wiley & Sons).

4. Thadhani, N.N., *Shock-induced and shock-assisted solid-state chemical reactions in powder mixtures.* J. Appl. Phys., 1994. **76** (4): 2129-2138.

5. Mutz, A.H. and T. Vreeland Jr., in *Shock Waves and High Strain-Rate Phenomena in Materials*, M.A. Meyers, L.E. Murr, and K.P. Staudhammer, eds., 1992 (New York: Dekker), 425-434.

6. Thadhani, N.N., et al., *Shock-induced chemical reactions in titanium-silicon powder mixtures of different morphologies: Time-resolved pressure measurements and materials analysis.* J. Appl. Phys., 1997. **82** (3): 1113-1128.

7. Vandersall, K.S. and N.N. Thadhani, *Time-resolved measurements of the shock-compression response of Mo + 2 Si elemental powder mixtures.* J. Appl. Phys., 2003. **94** (3): 1575-1583.

8. Thadhani, N.N., *Shock compression processing of powders.* Adv. Materials and Manufacturing Processes, 1988. **3** (4): 493-549.

9. Batsanov, S.S., et al., *Effect of an Explosion on Matter: Dynamic Compression of Potassium Nitrate.* Combustion, Explosion and Shock Waves, 1965. **1**: 47.

10. Batsanov, S.S. and A.A. Deribas, *Structural Changes in Neodymium Oxide in Shock-Loading Experiments.* Combustion, Explosion and Shock Waves, 1965. **1**: 77.

11. Graham, R., et al., Ann. Rev. Mater. Sci., 1986. **16**: 315.

12. Hammetter, W.F., et al., in *Shock Waves in Condensed Matter*, S.C. Schmidt and N.C. Holmes, eds., 1988 (Amsterdam: Elsevier Science).

13. Morosin, B., et al., *Shock-induced chemical synthesis of barium ferrites*, in *Shock Waves in Condensed Matter*, S.C. Schmidt and N.C. Holmes, eds., 1988 (Amsterdam: Elsevier Science).

14. Boslough, M.B., *A thermochemical model for shock-induced reactions (heat detonations) in solids.* J. Chem. Phys., 1990. **92** (3): 1839-1848.

15. Hornig, H., et al., in *Proceedings of the Eleventh International Pyrotechnics Seminar*, 1986, Vail, Colorado.

16. Krueger, B.R., A.H. Mutz, and T. Vreeland Jr., *Correlation of shock initiated and thermally initiated chemical reactions in a 1:1 atomic ratio nickel-silicon mixture.* J. Appl. Phys., 1991. **70** (10): 5362-5368.

17. Vecchio, K.S., L.H. Yu, and M.A. Meyers, *Shock Synthesis of Silicides - I. Experimentation and Microstructural Evolution.* Acta Metall. Mater., 1994. **42** (3): 701-714.

18. Meyers, M.A., L.H. Yu, and K.S. Vecchio, *Shock Synthesis of Silicides - II. Thermodynamics and Kinetics.* Acta Metall. Mater., 1994. **42** (3): 715-729.

19. Norwood, F.R. and R.A. Graham, *Numerical simulations of a sample recovery fixture for high velocity impact*, in *Shock-Wave and High-Strain-Rate Phenomena in Materials*, M.A. Meyers, L.E. Murr, and K.P. Staudhammer, eds., 1992: Elsevier Scientific), 989-996.

20. Dremin, A.N. and O.N. Breusov, Russ. Chem. Rev., 1968. **37**: 392.

21. Meyers, M.A., et al., *Effect of shock pressure and plastic strain on chemical reactions in Nb-Si and Mo-Si systems.* Materials Science and Engineering A, 1995. **201**: 150-158.

22. Nesterenko, V.F., et al., *Controlled high-rate localized shear in porous reactive media.* Appl. Phys. Lett., 1994. **65** (24): 3069-3071.

23. Yu, L.H., et al., in *Shock Compression of Condensed Matter - 1993*, 1994: American Institute of Physics.

24. Dunbar, E., N.N. Thadhani, and R.A. Graham, *High-pressure shock activation and mixing of nickel-aluminum powder mixtures.* J. Mater. Sci., 1993. **28**: 2903-2914.

25. Tamura, S. and Y. Horie, J. Appl. Phys., 1998. **84**: 3574.

26. Holman, G.T., et al., in *High-Pressure Shock Compression Science and Technology*, 1993: American Institute of Physics.

27. Thadhani, N.N., et al., *Shock compression of Al+Fe2O3 powder mixtures of different volumetric distributions*, in *Shock Compression of Condensed Matter - 1997*, 1998: AIP.

28. Wang, L.L., Z.A. Munir, and Y.M. Maximov, *Thermite reactions: their utilization in the synthesis and processing of materials.* J. Mater. Sci., 1993. **28** (14): 3693-3708.

29. Mei, J., R.D. Halldearn, and P. Xiao, *Mechanisms of the Aluminum-Iron Oxide Thermite Reaction.* Scripta Materialia, 1999. **41** (5): 541-548.

30. Ferranti, L. and N.N. Thadhani, *Dynamic Characterization of Epoxy-Cast Al+Fe2O3 Thermite Using the Taylor Anvil Test*, Georgia Institute of Technology, 2005 (in preparation).

31. Horie, Y. and A.B. Sawaoka, *Shock Compression Chemistry of Materials*, 1993 (Tokyo: KTK). 235.

32. Graham, R.A., in *High Pressure Explosive Processing of Ceramics*, R.A. Graham and A.B. Sawaoka, eds., 1987 (Aedermannsdorf, Switzerland: Trans Tech), 29.

33. Hwang, M.D. 1992, North Carolina State University: Raleigh, NC.

34. Bennett, L.S., Y. Horie, and M.M. Hwang, *Constitutive model of shock-induced chemical reactions in inorganic powder mixtures.* J. Appl. Phys., 1994. **76** (6): 3394-3402.

35. Gourdin, W.H., Met. Trans. A, 1984. **15A**: 1653.

36. Schwarz, R.B., et al., Acta Metall., 1984. **32**: 1243.

37. Williamson, R.L., *Parametric studies of dynamic powder consolidation using a particle-level numerical model.* J. Appl. Phys., 1990. **68**: 1287-1296.

38. Thompson, S.L., CSQII - An Eulerian Finite Difference Program for Two-Dimensional Material Response, Report Number: SAND77-1339, 1979: Sandia National Laboratories).

39. Wright, R.N., G.E. Korth, and J.E. Flinn, Met. Trans. A, 1989. **20A**: 2449.

40. Benson, D.J., *An analysis by direct numerical simulation of the effects of particle morphology on the shock compaction of copper powder.* Modelling Simul. Mater. Sci. Eng., 1994. **2**: 535-550.

41. Benson, D.J., *The calculation of the shock velocity - particle velocity relationship for a copper powder by direct numerical simulation.* Wave Motion, 1995. **21**: 85-99.

42. Benson, D.J., W. Tong, and G. Ravichandran, *Particle-level modeling of dynamic consolidation of Ti-SiC powders.* Modelling Simul. Mater. Sci. Eng., 1995. **3**: 771-796.

43. Benson, D.J., et al., *Quasistatic and Dynamic Regimes of Granular Material Deformation Under Impulse Loading.* J. Mech. Phys. Solids, 1997. **45**: 1955-1999.

44. Nesterenko, V.F., *Micromechanics of powders under strong impulse loading*, in *Computer Methods in Theory of Elasticity and Plasticity: Proc. Tenth All-Union Conference*, 1988, Novosibirsk, Russia.

45. Benson, D.J. and P. Conley, *Eulerian finite-element simulations of experimentally acquired HMX microstructures.* Modelling Simul. Mater. Sci. Eng., 1999. **7**: 333-354.

46. Merzhanov, A.G., *On Critical Conditions for Thermal Explosion of a Hot Spot.* Combustion and Flame, 1966. **10**: 341-348.

47. Batsanov, S.S., *Shock-induced chemical reactions in metal-silicon systems*, in *Metallurgical and Materials Applications of Shock-Wave and High Strain-Rate Phenomena*, L.E. Murr, K.P. Staudhammer, and M.A. Meyers, eds., 1995: Elsevier Science), 707-714.

48. Iyer, K.R., et al., *Solid state chemical reaction at the shock front*, in *High Pressure Science and Technology - 1993*, S.C. Schmidt, et al., eds., 1993 (New York: American Institute of Physics), 1337-1340.

49. Bowden, F.P. and A.D. Yoffe, *Ignition and Growth of Explosions in Liquids and Solids*, 1952 (Cambridge: Cambridge University Press).

50. Do, I.P.H. and D.J. Benson, *Modeling shock-induced chemical reactions.* International Journal of Computational Engineering Science, 2000. **1** (1): 61-79.

51. Do, I.P.H. and D.J. Benson, *Micromechanical modeling of shock-induced chemical reactions in heterogeneous multi-material powder mixtures.* International Journal of Plasticity, 2001. **17**: 641-668.

52. Torquato, S., *Random heterogeneous materials: microstructure and macroscopic properties*, 2002 (New York: Springer).

53. Granqvist, C.G. and R.A. Buhrman, *Ultrafine metal particles.* J. Appl. Phys., 1976. **47** (5): 2200-2219.

54. Ostoja-Starzewski, M., *Scale effects in plasticity of random media: Status and challenges.* International Journal of Plasticity, 2005. **21** (6): 1119-1160.

55. Kanit, T., et al., *Determination of the size of the representative volume element for random composites: statistical and numerical approach.* International Journal of Solids and Structures, 2003. **40**: 3647-3679.

56. Torquato, S., *Random heterogeneous media: microstructure and improved bounds on effective properties.* Applied Mechanics Review, 1991. **44**: 37-76.

57. Kirkpatrick, S., *Optimization by simulated annealing: quantitative studies.* Journal of Statistical Physics, 1984. **34** (5-6): 975-986.

58. Metropolis, N., et al., *Equation of state calculations by fast computing machines.* J. Chem. Phys., 1953. **21**: 1087-1092.

59. Benson, D.J., *Computational Methods in Lagrangian and Eulerian hydrocodes.* Computer Methods Appl. Mech. Eng., 1992. **99**: 235-394.

60. Asay, J.R. and M. Shahinpoor, eds. *High-Pressure Shock Compression of Solids*, 1993 (New York: Springer-Verlag).

61. Benson, D.J., *A mixture theory for contact in multi-material Eulerian formulations.* Computer Methods Appl. Mech. Eng., 1997. **140**: 59-86.

62. Van Leer, B., *Towards the ultimate conservative difference scheme. IV. A new approach to numerical convection.* J. Comput. Phys., 1977. **23**: 276-299.

63. Benson, D.J., *Momentum Advection on a Staggered Mesh.* Journal of Computational Physics, 1992. **100**: 143-162.

64. Youngs, D.L., *Time dependent multi-material flow with large fluid distortion*, in *Numerical Methods for Fluid Dynamics*, 1982, Reading, PA: Academic.

65. Benson, D.J., *Eulerian finite element methods for the micromechanics of heterogeneous materials: Dynamic prioritization of material interfaces.* Computer Methods Appl. Mech. Eng., 1998. **151**: 343-360.

66. Brandes, E.A., ed. *Smithells Metals Reference Book*, sixth ed., 1983 (Boston: Butterworth & Co.).

67. Marsh, S.P., ed. *LASL Shock Hugoniot Data*, 1980 (Berkeley, CA: University of California Press).

68. Shaffer, P.T.B., *Properties of High-Temperature Materials*, Plenum Press Handbooks of High-Temperature Materials, Vol. 1, 1964 (New York: Plenum Press).

69. Lee, H. and K. Neville, *Handbook of Epoxy Resins*, 1967 (New York: McGraw-Hill, Inc.).

70. Willett, J.C., Material Safety Data Sheet, Report Number: 23-12T, 1995 (Houston: Shell Oil Company).

71. Brydson, J.A., *Plastics Materials*, fifth ed, 1989 (Boston: Butterworths).

72. Klepaczko, J.R., T. Sasaki, and T. Kurokawa, *On Rate Sensitivity of Polycrystalline Aluminum at High Strain Rates.* Trans. Japan Soc. Aero. Space Sci., 1993. **36** (113): 170-187.

73. Kinslow, R., ed. *High-Velocity Impact Phenomena*, 1970 (New York: Academic Press).

74. Murnaghan, F.D., *Finite deformations of an elastic solid.* American Journal of Mathematics, 1937. **49**: 235-260.

75. Klopp, R.W. and R.J. Clifton, *Pressure-Shear Impact and Dynamic Viscoplastic Response of Metals*, in *Proc. of Workshop on Inelastic Deformation and Failure Modes*, 1984, Northwestern University, Evanston, IL.

76. Kocks, U.F., A.S. Argon, and M.F. Ashby, *Thermodynamics and Kinetics of Slip.* Prog. Mater. Sci., 1975. **19**.

77. Sakino, K. and J. Shioiri, *Dynamic Flow Stress Response of Aluminum to Sudden Reduction in Strain Rate at Very High Strain Rates*, in *Proc. Conf. DYMAT91, Journal de Physique, IV, Colloque C3*, 1991, Les Ulis.

78. Shioiri, J., et al., *Microscopic Aspects of Strain Rate Dependency of Dynamic Flow Stress in Metallic Materials*, in *Proc. 6th Conf. on Mechanical Behaviour of Materials*, 1991, Oxford: Pergamon Press.

79. Chen, W. and B. Zhou, *Constitutive Behavior of Epon 828/T-403 at Various Strain Rates.* Mechanics of Time Dependent Materials, 1998. **2** (2): 103-111.

80. Hasan, O.A. and M.C. Boyce, *A Constitutive Model for the Nonlinear Viscoelastic Viscoplastic Behavior of Glassy Polymers.* Polymer Engineering and Science, 1995. **35** (4): 331-344.

81. Lu, H., G. Tan, and W. Chen, *Modeling of Constitutive Behavior for Epon 828/T-403 at High Strain Rates.* Mechanics of Time Dependent Materials, 2001. **5**: 119-130.

82. Stevenson, M.E., M. Kaji, and C. Bradt, *Microhardness anisotropy and the indentation size effect on the basal plane of single crystal hematite.* Journal of the European Ceramic Society, 2002. **22**: 1137-1148.

83. Kreig, R.D. and S.W. Key, *Implementation of a time dependent plasticity theory into structural programs*, in *Constitutive Equations in Viscoplasticity: Computational and Engineering Aspects*, 1976, New York: ASME.

84. Ostoja-Starzewski, M., *Wavefront propagation in a class of random microstructures - I. Bilinear elastic grains.* Int. J. Non-Linear Mechanics, 1991. **26** (5): 655-669.

85. Ostoja-Starzewski, M., *Wavefront propagation in a class of random microstructures - II. Non-linear elastic grains.* Int. J. Non-Linear Mechanics, 1995. **30** (6): 771-781.

86. Jordan, L.J., et al., *Equation of State of Aluminum-Iron Oxide (Fe_2O_3)-Epoxy Composite: Modeling and Experiment*, Eglin Air Force Base and Georgia Institute of Technology, 2005 (in preparation).

87. Frank-Kamenetskii, D.A., *Diffusion and Heat Transfer in Chemical Kinetics*, second ed, 1969 (New York: Plenum Press).

88. van't Hoff, J.H., *Lectures on Theoretical and Physical Chemistry*, 1899 (London: Arnold).

89. Semenov, N.N., Z. Phys. Chem, 1928. **48**: 571.

90. Frank-Kamenetskii, D.A., Zh. Fiz. Khim., 1939. **13**: 738.

91. Barzykin, V.V., et al., Zh. prikl. Mekh. tekh. Fiz., 1964. **3**: 118.

92. Dvoryankin, A.V., A.G. Strunina, and A.G. Merzhanov, *Stability of combustion in thermite systems.* Combustion, Explosion, and Shock Waves (English Translation of Fizika Goreniya i Vzryva), 1985. **21** (4): 421-425.

93. Davis, L.C. and B.E. Artz, *Thermal conductivity of metal-matrix composites.* J. Appl. Phys., 1995. **77** (10): 4954-4960.